IMPACT DAMAGE RESISTANCE AND TOLERANCE
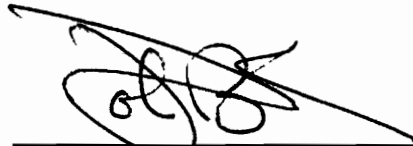# OF ADVANCED COMPOSITE MATERIAL SYSTEMS

by

Kuen Tat Teh

Dissertation submitted to the Faculty of the
Virginia Polytechnic Institute and State University
in partial fulfillment of the requirements for the degree of
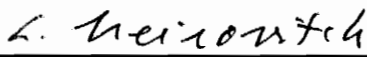
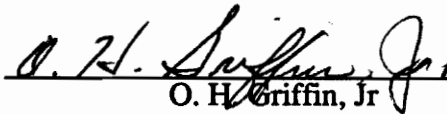DOCTOR OF PHILOSOPHY
in
Engineering Mechanics

APPROVED:

J. Morton, Chairman

L. Meirovitch   O. H. Griffin, Jr

R. W. Landgraf   Y. Renard

July, 1993

Blacksburg, Virginia

IMPACT DAMAGE RESISTANCE AND TOLERANCE
OF ADVANCED COMPOSITE MATERIAL SYSTEMS

by

Kuen Tat Teh

Committee Chairman: John Morton
Engineering Science and Mechanics

(ABSTRACT)

Experimental evaluations of impact damage resistance and residual compression strengths after impact are presented for nine laminated fiber reinforced composite material systems. The experiments employ a small scale specimen for assessing the impact damage resistance and impact damage tolerance of these materials. The damage area detected by C-scan is observed to develop linearly with the impact velocity for impact velocities higher than a threshold value. Brittle material systems have lower threshold velocities and higher damage area growth rates than toughened systems. The impact damage resistance of each material system can be characterized with threshold velocity V_c and damage area growth rate C. The residual compressive strength after impact was observed to decrease linearly with the damage area equivalent diameter. The rate of compressive strength reduction, K_d, has been observed to be independent of the material properties.

The impact damage can be simulated from quasi-static indentation test in which the damage due to these two loading conditions are quite similar. The residual compressive strength can also be simulated from specimens with similar *damage size* resulting from quasi-static indentation load.

Acknowledgments

The research study presented in this dissertation was carried out under the direction of Dr. John Morton and I would like to express great appreciation for his guidance and support throughout this research.

I would also like to express my sincere appreciation to Dr. Leonard Meirovitch, Dr. O. Hayden Griffin, Jr., Dr. Ronald Landgraf, and Dr. Yuriko Renardy for serving on my committee and reviewing this manuscript.

The funding for this research project provided by National Science Foundation Science and Technology Center for High Performance Polymeric Adhesives and Composites at Virginia Tech under Grant Number DMR 912004 is gratefully acknowledged.

In addition to the above noted, this work was made possible by:

- my parents and all the family members for their support and encouragement.

- the members of our research group, Diane Peters, Deanna Busick, David Johnson, Yanhong Zhang, Robert Bennett, Andre Lavoie, Ernst Lutz, Henjen Ho, and Ming-Yi Tsai.

- all my friends at Virginia Tech, especially Lei Wang, Min-Chung Li, and Yi-Chwan Chao.

Table of Contents

List of Figures

xiv

List of Tables

1 Introduction

The advantages of fiber reinforced composite materials over conventional metals in structural applications have been well recognized. The superior strength-to-weight and stiffness-to-weight ratios are two of the special features of advanced composite materials exploited by engineers to design and manufacture fuel efficient commercial aircraft or high performance military jets. The results are substantial weight saving in aircraft structure and increase in payload. Other advantages of advanced composite materials can be found in the new generation of business aircraft Starship manufactured by Beechcraft of Raytheon Company. This aircraft is an all-graphite fiber composite rivet-less construction in the fuselage and wings which affords a smooth surface for efficient operation unmatched by any other conventional materials.

Fiber reinforced composite materials have excellent mechanical performance when the loading is in the fiber direction. Various fiber stacking orientations of laminated composites have been used to achieve the optimum structural performance for inplane loadings. However, one of the drawbacks of laminated composites is weakness in the direction perpendicular to the laminate plane. Thus, laminates are highly susceptible to transverse impact damage [1]. Several examples of transverse impact by foreign objects on aircraft structures include the dropped tools during the repair work, runway debris during the take off and landing, and hailstones or birds strike in flight.

Numerous research studies have shown that significant reductions in strength can occur after impact, even when there is no visible damage on the laminate surface. Reviews of investigations on this subject can be found in recent papers by Abrate [2], and Cantwell and Morton [3]. The most commonly found types of damage, as a result of low energy impacts, are internal matrix cracks and delamination between plies. For laminated composites, delamination damage has a profound influence on the strength degradation of composite structures especially under compression loading where the load carrying plies lose the stabilizing structural support from the neighboring plies. The result is premature failure through buckling or crippling [3].

In the past few decades, several impact test devices using different test methods have been developed by researchers to simulate impact load on composite structures [2]. A few examples are drop weight [4-16], pendulum [17], cantilever [18, 19], and gas gun [9, 11, 17, 20-34]. The basic objective of these impact test devices is to control the velocity of the "impactor" through some mechanisms. For drop weight and pendulum, the impact velocity of the impactor is adjusted with the vertical free fall distance to the target. Whereas the impact velocity of cantilever impactor is controlled by the bending of the cantilever which acts like a "spring" to accelerate the impactor.

Although the drop weight, pendulum, and cantilever impact test devices are easy to construct, the range of impact velocities is quite limited. For example, a 5 m (16.4 ft) height of drop weight tower is needed for the impactor to travel at 10 m/s when hitting the target. The maximum impact velocity of the cantilever impactor designed by Lal was reported at 7.8 m/s [18, 19]. Therefore, these devices are suitable only for low velocity impact test, such as to simulate dropped tool on composite structure. For high velocity impact test, a gas gun is needed in which the impactor is propelled by the release of the compressed gas through a gun barrel toward the target. The impactor velocity can be controlled by the gas pressure and the length of the gun barrel.

By far, the drop weight and gas gun are the two most commonly used impact test devices. However, there are many variations in the design for different testing requirements. For the drop weight test device, the impactor can be guided inside a vertical tube [7, 14, 16] or sliding down along two vertical guiding rods [6, 8-10, 12, 13]. The later design is easier for the impactor to be instrumented [35] with load cell or accelerometer which is the design used in Dynatup impact tester [12], a commercially available impact test device.

For the gas gun, the impactor is fired directly from the gun barrel to the target. Since the impactor has to travel inside the gun barrel and the impact velocity depends on the impactor mass, a small impactor typically less than 50 g is usually used and is difficult to instrument. The instrumented gas gun impact test device designed by Delfosse et. el. [31] uses a 280 g impactor and the maximum impact velocity is about 50 m/s. The gun barrel used in Refs. 28 and 33 is the most unique one. Instead of

using a circular tube, a square tube is used as the barrel for a rectangular base impactor with line-nose to create a line impact on a beam specimen.

The dimensions of the composite material specimens used in impact tests are also not consistence for different researchers. The types of specimens include beam specimen for residual tensile strength measurement, plate specimen for residual compressive strength measurement, and composite sandwich specimens [30, 32]. Currently, no test methods have been standardized by the composite research community, such as ASTM, to characterize the impact damage resistance and tolerance in order to have a meaningful comparison for the impact performance of various composite material systems One of the testing standard used by composite manufacturer is the Boeing Specification Support Standard (BSSS). The impact specimen used in BSSS required the used of relatively thick 48-ply laminated plate with the dimensions of 150 mm X 100 mm (4 in X 6 in) [5, 12, 37]. The specimen is impacted with a 5.4 kg impactor at 30.5 J of incident energy using a drop weight tower. After impact, the specimen is then loaded in a special compression fixture to measure the residual compressive strength which is used to characterize the impact damage tolerance.

In cases when the material supply is limited such as new material systems are under development, it is not economical to use BSSS to evaluate the impact damage resistance and impact damage tolerance of these materials. Therefore, there is a need for a more efficient test procedure which only requires a minimum amount of material. The objectives of this study are to design and construct a gas gun which can be used for low to high velocity impact tests, and to develop a cost effective test procedure for determining the parameters which can be used to characterize the impact damage resistance and impact damage tolerance using small scale specimens

In Chapter 2, the design of the gas gun and the gas gun operating procedure are presented. In Chapter 3, the material systems used in this impact study program and the test procedure to characterize impact damage resistance are introduced. The impact damage observed from the specimen surface are also described in this chapter. Internal damage detected by ultra-sonic C-scan and penetrant enhanced X-ray are presented in Chapter 4. The C-scan images of the impacted specimens provide a

quantitative measurement of the damage area which can be used to characterize the impact damage resistance of each material system.

In Chapter 5, the experimental results of residual compressive properties after impact for each material system are presented. The limitation of the Caprino model which is used to model the residual strength is identified. A model to predict the residual compressive strength based on the damage size is developed in this chapter.

In Chapter 6, damage resulting from quasi-static indentation instead of impact is investigated. The objectives are to simulate the impact load with quasi-static indentation load and to study the effect on residual compressive strength due to these two loading conditions. In the final chapter, the accomplishments and conclusions of this research study are summarized. A few suggestions for possible future work are given at the end of the chapter.

2 Gas Gun Design and Impact Test Setup

2.1 Introduction

As mentioned in Chapter 1, a gas gun is needed for the high velocity impact tests which can be conveniently achieved by driving the impactor with pressurized gas. Although a relatively low impact velocity up to 30 m/s was envisioned for this study, it would still required at least a 45 m (150 ft) height drop weight tower to achieve the desired velocity. For this reason and possible need for even higher impact velocities in the future, a gas gun was designed by a team consisting of the author, his advisor Prof. John Morton, Dr. Publio Pintado, and Dr. Sotiris Kellas. Funding for the gas gun construction was provided by the NSF Science and Technology Center for High Performance Polymeric Adhesives and Composites.

2.2 Impact Testing Setup

A schematic arrangement of the impact testing device used in this study is shown in Fig. 2.1. The three main components are the gas gun system, data acquisition system, and high speed video camera system.

2.2.1 Gas Gun System

As shown in Fig. 2.1, the gas gun system consists of a nitrogen gas tank, a pressure chamber, a breech loading system, a 1.83 m (6 ft) long barrel, and a projectile. From the nitrogen gas tank, an air actuator to control the gas pressure in the pressure chamber is attached to the outlet of the gas tank main valve. A pressure release valve (integral bonnet needle valve) is connected next to the air actuated valve for releasing the gas pressure. Therefore, both air actuator and release valve are used to control the pressure in the pressure chamber. To prevent gas pressure in pressure chamber exceeding design limit, an externally adjustable relief valve (set at 6.3 MPa) is installed between air actuated valve and pressure release valve.

Nitrogen gas is delivered from the gas tank to pressure chamber through a 5.5 m (18 ft) long 20.6 MPa (3000 psi) rating stainless steel flexible hose. The pressure chamber is a modified 1000 cc sample cylinder with a pressure rating of 12.4 MPa

(1800 psi). The length and outside diameter of the cylinder are 27.6 cm (10.9 in) and 8.9 cm (3.5 in), respectively. One end of the sample cylinder is equipped with a rupture valve and served as nitrogen gas inlet from gas tank. The rupture valve is an additional safety device to protect sample cylinder from excessive pressure. On the other end of the sample cylinder, a 14 mm thick circular disk with inside diameter of 29 mm is force fitted to the end of the sample cylinder to form part of the breech loading system. Details of this design are presented in Fig. 2.2. The outside diameter of the disk is about 7.6 cm and is threaded on the outer surface. A 5 cm diameter circular groove is machined on the disk surface facing away from the sample cylinder for fitting an O-ring which is used to seal off pressure in pressure chamber. Two small holes are drilled through the thickness of the circular disk just outside the O-ring to allow passage of power supply wires to firing mechanism. The firing mechanism is made with two strands of chrome wires twisted together around pressure chamber outlet to form a heating element. A battery charger set at 12 V is used to provide the electric current for firing mechanism

Details of the breech loading system are shown in Figs. 2.3 and 2.4. By referring to Fig. 2.3, both pressure chamber (A) and gun barrel (J) are secured on top of a 3 m (10 ft) long aluminum channel. The only movable parts of this breech loading system are parts H and I which slide together along the barrel. Disposable diaphragm (D), gasket (E) and breech spacer (K) are removable pieces which are installed between pressure chamber and barrel. The disposable diaphragm is made by a layer of thin mylar film with cardboard paper backing to prevent wrinkling of the mylar film during the closing of breech collar (H) with pressure seal (B). The breech loading system was designed to minimize the time between tests by simplifying the procedure for replacement of the disposable diaphragm.

To seal off pressure chamber, the disposable diaphragm is positioned against O-ring (C) with the mylar film facing pressure chamber. A piece of laminated composite gasket (E) is used to support flexible diaphragm and a hollow cylindrical steel breech spacer (K) is used to secure all these three components together. The flexible diaphragm in this setting is in contact with the heating element. A 19 mm (0.75 in) diameter hole is cut at the center of diaphragm paper backing and composite washer to allow the flow of nitrogen gas from pressure chamber after the bursting of mylar film.

6

The composite washer serves to support diaphragm and maintain contact with heating element when pressure chamber is pressurized. The flexible diaphragm may be pushed away from heating element by high pressure gas without the support of stiff composite washer.

After the diaphragm is installed, breech collar (H) is slid along the barrel and locked in place with pressure seal (B). By tightening Breech collar (H) on pressure seal (B), the diaphragm is in full contact with O-ring (C) and seals the pressure chamber. A barrel flange (F) is forced fitted at the upper end of the barrel to hold the O-ring (G) in place. After tightening breech collar (H), breech pressure collar (I) is hand tightened on O-ring (G) to prevent the pressurized nitrogen gas from escaping through the space between part H and the barrel.

The gun barrel is fabricated from a smooth bore stainless steel tube. The outside and inside diameter of the barrel are 28.6 mm (1.125 in) and 19 mm (0.75 in), respectively. A projectile such as Teflon sabot or a steel ball can be placed in any position inside the barrel. An infrared light emitting diode (LED) and a photo-transistor are located near the nozzle of the barrel to measure the projectile velocity as it leaves the barrel.

The gas gun was tested by filling the pressure chamber with water for up to 10.34 MPa (1500 psi) to detect possible leaking around the breech loading system. As a safety precaution, a Plexiglas case was made to cover the area from the nozzle of gas gun to the specimen for low velocity impact tests. For high velocity impact tests, a similar case made of 12.7 mm (0.5 in) thick aluminum was used. In addition, a smaller aluminum case was also made to cover the pressure chamber and breech loading systems.

2.2.2 Data Acquisition System

The data acquisition system is a Macintosh computer with a National Instruments' NB-A2000 high-speed 12-bit resolution analog input plug-in board. The board has four analog input channels with the maximum scanning rate of one million samples per second. The board can be used for one, two, or four channels input. For

7

example, to use four channels input, the board can read in four analog signals simultaneously with the maximum scanning rate of 250,000 scans/sec.

The data acquisition board is driven by a software module called a virtual instrument. An icon-based graphical programming system called LabVIEW from National Instruments is used for building the software modules. The virtual instrument has a graphical front panel as the user interface and a block diagram as the program which allows users to customize their data acquisition systems for specific needs. A LabVIEW virtual instrument has been programmed to record LED and strain gage voltage outputs for this study.

2.2.3 High-Speed Video Camera System

The high-speed video camera system is the Kodak EktaPro EM Motion Analyzer. The seven main components of this systems are processor, intensified imager, intensified imager controller, video cassette recorder (VCR), video monitor, video printer, and multi-channel data link. The image recording rates of this system can be set at 50, 125, 250, 500, and 1000 frames per second in full screen recording. To use split screen recording, the highest recording rates are 2000, 3000, 4000, and 6000 pictures per second in 1/2, 1/3, 1/4, and 1/6 split, respectively. The use of the intensified imager reduces the need for extra lighting equipment.

2.3 Gas Gun Operation

The operating procedure of the gas gun are summarized in the following steps. First, set up specimen to be impacted and a sabot is placed at a predetermined position in the gun barrel. Second, a disposable diaphragm is installed in the breech loading system as shown in Fig. 2.3(b). After the breech loading system is closed and locked, the third step is to pressurize the pressure chamber by opening the gas tank main valve and adjusting the air regulator valve. The release valve is used to lower the pressure if it is higher than required. Once the predetermined pressure level is attained, both the main valve and the air regulator valve are closed and the gas gun is ready for action. The gun is fired by electrically bursting the mylar diaphragm with a switch to close the circuit between heating the element and battery charger.

The data acquisition and high-speed video camera is set up to record the impact event before the gas gun is pressurized. The recording of both systems can be triggered by the voltage drop in the photo-transistor as the impactor passes between the LED and photo-transistor.

2.4 Gas Gun Calibration

An example of the photo-transistor voltage output recorded by the data acquisition system as the impactor passed between the LED and photo-transistor is shown in Fig. 2.5(a). The photo-transistor voltage is at 0.8 V when both the infrared LED and photo-transistor can "see" each other. As the impactor passes between them, the infrared signal from LED is blocked by the impactor and the voltage drops to zero and remains low until the impactor has passed. Since the photo-transistor voltage is recorded at a certain rate, the time for this interval can be determined. By measuring the length of the impactor, the velocity can be calculated. The second drop of voltage between 14 and 23 millisecond is due to the rebound of impactor from the target.

The impactor velocity can be controlled by adjusting the pressure in the pressure chamber and/or the position of the impactor along the length of the barrel. The variation of the 35 g impactor velocity with the impactor position in the barrel is shown in Fig. 2.6. The pressure used for this calibration curve is 103 kPa (15 psi). The impactor position is measured from the nozzle of the barrel. A spring ruler is used to position the impactor into the barrel.

The calibration curves for higher pressures are shown in Fig. 2.7. Four impactor positions were used for each pressure level from 172 kPa (25 psi) to 5.52 MPa (800 psi) using a 35 g impactor. The highest impactor velocity is 264 m/s (590 mph) or 1.22 kJ of kinetic energy for 5.52 MPa (800 psi) pressure and placing impactor closest to the pressure chamber. Thus, the longer the distance for impactor to travel in the barrel, the higher the velocity that can be attained as the impactor leaves the barrel.

9

3 Impact Test and Surface Damage Observation

3.1 Introduction

In this chapter, the material systems selected for the impact study program and test procedure to characterize impact damage resistance are introduced. The characteristics of impact damage visually observed from the specimen surface after impact are described for each material system. More extensive impact damage observations such as internal matrix crack and delamination using X-ray and C-scan nondestructive techniques are described in chapter 4.

3.2 Material Systems

Nine composite material systems (Table 3.1) were available for this study. Quasi-isotropic laminates with the stacking sequence $[0/90/\pm45]_{2S}$ were fabricated for each system. These material systems are: AS4/3502 (A), a graphite/epoxy thermoset composite; AS4/PEEK (B), an aromatic polymer composite (APC-2) with AS4 graphite fibers in a semicrystalline polyetheretherketone (PEEK) thermoplastic matrix; G30-500/F185 (C), a graphite/epoxy thermoset composite where F185 denotes a 120°C (250°F) cure epoxy resin system; G30-500/F263-2 (D), a 175°C (350°F) cure epoxy resin system; IM7/F650 (E), a graphite/polyimide thermoset composite where F650 is Hexcel's first generation bismaleimide (BMI) system, a relatively brittle resin matrix; IM7/F655 (F) and IM7/F655-2 (G), Hexcel's second and third generation toughened BMI systems; IM7/8551-7A (H), a graphite/epoxy thermoset composite with IM7 graphite fibers in a rubber toughened amine-cured epoxy resin system; and S-2/8551-7A (I), a glass/epoxy thermoset composite. The Celion® G30-500 is a high strength carbon fiber with the tensile properties similar to the AS4 carbon fiber, the IM7 carbon fiber has a higher tensile strength and modulus than the AS4 fiber, and the S-2 is a glass fiber. The selection of these material systems provides the basis for comparing the material impact damage resistance and impact damage tolerance of the same fiber in different matrix materials (A-B, C-D, E-F-G-H), and different fibers with the same toughened epoxy matrix (H-I). Material systems B, E, F and G were provided by the manufacturers as cured panels and the rest were cured from the prepreg tapes in the manufacturing facility of the Center for Composite Materials and

Structures at Virginia Tech. All panels were cured with dimensions 35 cm x 35 cm. The thickness of the cured materials varied from panel to panel, as indicated in Table 3.1.

3.3 Impact Test and Damage Assessment

Each panel was inspected using the ultra-sonic C-scan facility to ensure its quality prior being cut into several square specimens (65 mm x 65 mm) for the impact test. Specimens were clamped in a fixture (Fig. 3.1) which provided support between cylindrical rings during the impact. The inside diameter of the cylindrical supports was 50.8 mm (2 in) (Fig. 3.2).

A 12.7 mm (0.5 in) diameter hemispherical steel head mounted in a Teflon sabot (32 mm length and 19 mm diameter) was used as the impactor (Fig. 3.1). The total mass of the impactor was 35 g. The impact velocity or energy of the impactor was selected to lie in the range which caused damage in the specimen ranging from barely visible to visible but without fully extending to the ring support, based on the damage observed from the surface of the specimen. These impact velocities can be divided into four levels. At least five specimens were tested for each impact velocity level and a total of at least 20 specimens were impacted for each material system. A photo-transistor was used to trigger the data acquisition system recording process and to measure the impactor velocity. The location of the infrared LED and photo-transistor with respect to the barrel end and the specimen support is shown in Fig. 3.3.

3.4 Surface Damage Observation after Impact

After the impact test, the front (impacted side) and back surfaces of each specimen were inspected. As the impact velocity increases, the impact damage created can be classified into three stages:
   a) non-visible damage,
   b) barely visible damage, and
   c) visible damage.

In the non-visible damage stage, no dimple or crack can be seen. A *dimple* is the surface indentation caused by the impression of impactor onto the specimen front

surface and a *crack* is the matrix crack along the surface 0° ply unless it is stated otherwise. Microcracks and the internal cracks are, of course, not detected with the naked eye. Nondestructive techniques such as C-scan and X-ray are then needed. In some cases, there may be no damage in the specimen after being impacted.

The impact damage associated with the barely visible damage stage is usually in the form of a shallow dimple and delamination associated with a crack. In order to see these type of damages more clearly, the specimen may be observed under sufficient illumination. The dimple can be felt by rubbing the specimen surface lightly with the finger.

For the visible damage stage, the dimple and crack with delamination can be easily observed. Broken fibers on the back surface ply are observed in some material systems. For some material systems such as AS4/PEEK, creases associated with a dimple [8] are observed. The size and location of these creases varied from one specimen to another even for similar impact velocities. The four most commonly observed creases are illustrated in Fig. 3.4. At higher impact velocities, fiber breakage in the front surface ply can also be created and the broken fibers of the ply beneath the back surface ply may protrude outside the back surface.

The depths of the dimple and the height of the crease were measured by using the Rank Taylor Hobson 'Talysurf' 4, an instrument for the evaluation of surface texture. The dimple and crease measurement profiles for an AS4/PEEK specimen after impact are shown in Figs. 3.5 and 3.6. The vertical and horizontal magnifications of these output traces are 500X and 20X, respectively. The maximum horizontal measurement of the 'Talysurf' 4 was the traversing length of the stylus, whereas the maximum vertical measurement was the height of the graph paper used for recording. Since 500X magnification was used for the measurement, the maximum depth of a dimple or the maximum height of a crease that can be measured continuously on a graph paper as shown in Fig. 3.5(a) was 0.05 mm. To measure the depth of a dimple deeper than 0.05 mm, the gearbox of the 'Talysurf' 4 was turned off temporarily when the recording pen reached the bottom of the graph paper. The gearbox, together with stylus, was raised manually until the recording pen was on top of the graph paper and the measurement continued. The same procedure was used

when the recording reached the top of the graph paper, the gearbox was lowered manually in this case. The graph paper was cut and the traces were joined together as shown in Fig. 3.5(b) for complete measurement after the recording was completed. An example of a crease measurement on an AS4/PEEK specimen surface is shown in Fig. 3.6(a). This crease was created away from the point of impact, that is outside the dimple, and a crease which extended into the dimple is shown in Fig. 3.6(b).

3.4.1 AS4/3502

The range of impact velocities tested on AS4/3502 was between 4.9 and 14.2 m/s. No visible damage was observed on the specimen surface for impact velocities less than 6 m/s. Between impact velocities of 7.3 to 8.1 m/s, a barely visible dimple was observed. A dimple and crack were created in the velocity range from 10.3 to 11.4 m/s. The dimple was barely visible but can be felt by rubbing the surface. The crack was not formed directly under the point of impact but a few millimeters away from it. As the velocities increased to the range from 12.8 to 13.5 m/s, the dimple was still barely visible but the crack was quite visible. The crack length parallel to the 0° surface ply was about 35 mm and the width of the cracked region was about 5 mm. Delamination associated with these surface cracks was observed but no fiber breakage could be seen on either the front or the back surface of the specimen for impact velocities up to 14.2 m/s.

No measurement of dimple depth was performed on this material system.

3.4.2 AS4/PEEK

The range of impact velocities for AS4/PEEK was between 7.5 and 19.3 m/s. For the impact velocities between 7.5 and 7.9 m/s, an approximately 2 mm diameter circular pan shaped dimple was created. The 0.02 mm deep dimple was visible and well defined. On the back surface, a barely visible protrusion was created.

At 11.7 m/s impact velocity, the diameter and the depth of the dimple increased to about 3 and 0.12 mm, respectively. On the back surface, an elliptical shaped protrusion with the major axis parallel to the back surface ply fiber direction was observed. A single crack was also created right along the major axis of the elliptical

protrusion. The surface damage created by 12.0 and 12.1 m/s impact velocities were similar to those created by 11.7 m/s impact velocity. In addition, a single crack extended outside the elliptical protrusion with the crack length about 15 to 30 mm. As the impact velocity increased to 12.3 m/s, a 1.5 mm length crease was created at the front surface just outside the edge of the circular dimple. The height of the crease was about 0.04 mm and its length was perpendicular to the surface ply fiber direction. The location of the crease relative to the dimple is illustrated in Fig. 3.4(a). A few more cracks were also created. At 12.9 m/s impact velocity, two creases as in Fig. 3.4(b) were formed on the front surface with the length of about 2 mm.

By increasing the impact velocities to the range between 15.2 and 16.2 m/s, the diameter and depth of the dimple was increased to about 4 and 0.16 mm, respectively. On the back surface, the length of the cracks was about 30 to 40 mm. In this velocity range, front surface creases with the length of 3 to 4.5 mm were formed in some specimens and were similar to the one shown in Fig. 3.4(b). For higher impact velocities, the depth of the surface dimple was deeper and its circular edge was no longer well defined as those created at lower impact velocities.

At 17.5 m/s impact velocity, the diameter and depth of the dimple were about 4 and 0.2 mm, respectively. A single crease about 4.5 mm long similar to the crease shown in Fig. 3.4(a) was created. The shape of the back surface protrusion was resemble to a diamond with several cracks on the protrusion surface. The crack length was about 35 mm long. For the impact velocities of 17.6 and 18.1 m/s, two 5 mm long creases as shown in Fig. 3.4(b) were created close to the dimple. The visible crack length on the back surface was about 35 to 40 mm. At 18.9 m/s impact velocity, the dimple was about 5 mm in diameter and 0.28 mm deep. Two creases with 3.5 and 5 mm long were also created. On the back surface, the crack length was about 45 mm and fiber breakage was also observed where the broken fibers were right under the point of impact. As the impact velocity increased up to 19.3 m/s, front surface crack was created inside a 0.54 mm deep dimple. Two creases 4 and 5 mm long were also created. The length of the crack was shorter (about 25 mm long) than the surface crack created with a lower impact velocity and the fiber breakage across the back surface right under the point of impact was more extensive. The fiber breakage was

straight across the back surface perpendicular to the back surface ply fiber direction with the length of about 10 mm.

For all the specimens with a crack, back surface ply delamination was barely visible. The delamination can, however, be detected by tapping the specimen surface around the crack with a sharp solid object such as a dental probe.

3.4.3 G30-500/F185

The range of impact velocities tested for G30-500/F185 was between 7.3 and 20.5 m/s. For the impact velocities between 7.3 and 8.1 m/s, only a front surface circular pan shaped dimple about 0.02 mm deep was created. The diameter of the dimple was about 2 to 3 mm. Its shape was well defined and visible in reflected light. No crack was observed in this velocity range.

In the impact velocity range from 11.4 to 12.4 m/s, a dimple about 3 mm in diameter and 0.07 mm deep was created. One or two creases were also created with a length of about 0.5 to 1.5 mm. The crease formation on the specimen impacted with 12.0 m/s impact velocity is illustrated in Fig. 3.4(c) and was different from any crease formation observed in AS4/PEEK specimens. As the impact velocities increased to between 12.5 and 12.7 m/s, the diameter of the dimple was about 3.5 to 4 mm. No crease was formed except on the specimen with 12.7 m/s impact velocity where a 1 mm length crease was observed. No crack was observed on the specimen for the 11.4 to 12.4 m/s impact velocity range. However, a highly reflective spot was observed on the back surface right under the point of impact.

As the impact velocities increased to the range between 16.0 and 16.4 m/s, the dimple was about 4 mm in diameter and 0.14 mm deep. At 16.0 m/s impact velocity, two creases were created with a length of about 3 and 3.5 mm (as shown in Fig. 3.4(b)). The crack, with no fiber breakage, was also created. At a 16.2 m/s impact velocity, two 4 mm length creases as shown in Fig. 3.4(b) were created on the front surface. On the back surface, a crack and fiber breakage were visible. The crack was shorter than that created with the 16.0 m/s impact velocity. The back surface damage was confined to a small region in a starlike shape right under the point of impact. For the specimen impacted with 16.2 m/s velocity, two creases as shown in Fig. 3.4(c)

were created with a length about 3 and 4 mm. Crack and fiber breakage were visible. The starlike shape damage region was about 10 mm long along the back surface ply fiber direction and the width was about 6 mm. At 16.3 m/s impact velocity, three creases as shown in Fig. 3.4(d) were created. By referring to Fig. 3.4(d), the length of the two right side creases were about 4 mm and the shortest crease on the left side was about 1.5 mm long. The crack and fiber breakage were visible within a 5 mm x 5 mm region. As the impact velocity increased to 16.4 m/s, two smaller creases as shown in Fig. 3.4(c) were created with a length of about 2 and 3 mm. On the back surface, the damage was mainly in the form of a surface crack about 5 mm long and without visible fiber breakage.

For the range of impact velocities between 19.0 and 20.5 m/s, the edge of the front surface circular dimple was no longer visually well defined as its depth increased. Between 19.0 and 19.1 m/s impact velocities, the dimple was about 4 mm in diameter and 0.16 mm deep, two creases as shown in Fig. 3.4(b) were created with a length of about 5 mm each. The back surface cross shaped damage was mainly fiber breakage developed across the back surface ply fiber direction. Surface cracks along the fiber direction were also observed but with shorter lengths. The length of the fiber breakage was about 10 mm for 19.0 m/s and 6 mm for 20.5 m/s impact velocity. At 19.7 m/s impact velocity, the dimple was about 5 mm in diameter and 0.24 mm deep. Two 5 mm length creases as shown in Fig. 3.4(b) were also created. The cross shaped damage on the back surface was mainly fiber breakage (about 12 mm long) across the fiber direction and some surface matrix cracks along the fiber direction. At 19.8 m/s impact velocity, the front surface damage was similar to the damage created with 19.8 m/s impact velocity, but the back surface damage was smaller in the form of the fiber breakage and surface matrix crack. For an impact velocity of 19.9 m/s, the dimple was about 5 mm in diameter and 0.18 mm deep. Two creases about 7 mm as shown in Fig. 3.4(c) were created. On the back surface, cross shaped fiber breakage and crack were created. The length of the fiber breakage across the back surface ply fiber direction was about 9 mm and the surface matrix crack along the fiber direction was about 18 mm. Similar front surface damage was observed for the specimen impacted with 20.5 m/s impact velocity. On the back surface, the damage was mainly fiber

breakage about 5 mm long and had less surface matrix crack than the specimen impacted with 19.9 m/s impact velocity.

3.4.4 G30-500/F263-2

The range of impact velocities tested on this material system was between 4.4 and 20.7 m/s. No surface damage was observed for the range of impact velocities between 4.4 and 5.5 m/s. For the impact velocities between 7.5 and 8.0 m/s, no visible damage on the specimen surface was observed. Only a dimple was detected by rubbing the specimen surface with a finger.

As the impact velocities increased to the range between 10.7 and 11.4 m/s, the matrix cracks along the back surface ply fiber direction were visible. The length of the cracks was about 20 mm. On the front surface, no dimple was visible but could be felt by rubbing the specimen surface with a finger.

At the impact velocity of 12.9 m/s, the front surface condition remained the same and the back surface matrix crack length was about 30 mm long. Delamination around the cracks was detected by tapping the surface with a finger.

Between impact velocities of 13.9 and 14.9 m/s, the front surface condition again remained the same, On the back surface, the matrix cracks along the fiber direction were extended almost to the ring support and the width of the cracked region was about 7 mm. Delamination within this region was visible.

For the 16.2 m/s impact velocity, a dimple and a small matrix crack within the dimple along the front surface fiber direction were visible. On the back surface, a delaminated roof shaped protrusion about 10 mm wide was created along the back surface fiber direction. Several matrix cracks along the back surface fiber direction were visible within the protrusion and a single crack was apparent right on top of the protrusion with the crack extending to the ring support.

For the impact velocity of 20.7 m/s, a dimple with matrix cracks and fiber breakage were observed on the front surface in an approximately 12 mm x 12 mm region. On the back surface, the delamination and the matrix cracks along the fiber

direction of the back surface ply had extended outside the ring support to the edge of the specimen. Broken fibers in the back surface ply were observed at the ring support. The broken fiber and matrix cracks in the 90° ply beneath the back surface 0° ply were visible right under the point of impact.

No measurement of dimple depth was performed on this material system.

3.4.5 IM7/F650

The range of impact velocities tested on IM7/F650 material system was between 4.4 and 20.6 m/s. No front and back surface damage were observed the velocities up to 5.0 m/s. At 5.5 m/s impact velocity, a barely visible dimple was observed. The shape of the dimple was not well defined. On the back surface, an elliptical protrusion about 11 mm long along the back surface fiber direction and about 5 mm wide was created. No delamination was detected by tapping the protrusion with a dental probe.

For impact velocities from 7.8 to 8.3 m/s, a barely visible dimple was observed. On the back surface, a double-wing shaped protrusion with no surface crack was observed. Each wing resembled the shape of a heart with the tip pointing outward along the back surface fiber direction from the center of the specimen. No damage was observed right under the point of impact (center of the specimen). By tapping the surface of the "wing," delamination under the back surface ply was detected. The total length of this double-wing shape protrusion was about 20 mm for the specimen impacted with 7.8 and 7.9 m/s impact velocities, and about 22 mm for the specimens impacted with 8.1 to 8.3 m/s impact velocities. The width of these wing regions was about 10 mm.

For impact velocities from 10.7 to 11.0 m/s, a visible dimple was created. On the back surface, the length of the wings from tip to tip was about 27 to 32 mm long. No surface crack was observed in the wing region except a few tiny cracks were observed on the specimens impacted with 10.9 and 11.0 m/s impact velocities. No damage was detected right under the point of impact.

As the impact velocities increased to the range between 13.9 and 14.3 m/s, visible dimple was observed on the front surface. On the back surface, the length of

18

the wings from tip to tip was about 40 to 45 mm, and the width was about 10 mm. Cracks along the back surface fiber direction were observed on the wing surface and at the edges of the wing. Similar to the specimens impacted with lower impact velocities, no damage was observed right under the point of impact.

For the specimen impacted with 17.8 m/s impact velocity, one side of the wing had reached the ring support with two parallel surface matrix cracks formed on both edges of the wing section. Cracks were observed to extend to the ring support but did not go through the center of the specimen and propagate to the wing section on the other side. As before, no damage was observed at the center of the specimen right under the point of impact.

At 20.6 m/s impact velocity, a dimple with matrix cracks and fiber breakage inside the dimple region were observed on the front surface. On the back surface, a rectangular shaped delamination with both ends reaching the ring support was observed. Cracks on the surface and on both edges of the rectangular region were observed along the back surface fiber direction. The width of this delamination region was about 8 mm. At the location under the point of impact, surface matrix cracks and delamination were observed. For all the specimens impacted with up to 20.6 m/s impact velocity, no back surface ply fiber breakage was observed.

No measurement of dimple depth was performed on this material system.

3.4.6 IM7/F655

The range of impact velocities tested for IM7/F655 was between 5.4 and 20.1 m/s. No front and back surface damage was observed for the impact velocities up to 9.3 m/s. Between 13.8 and 14.3 m/s impact velocities, a pan shape dimple about 2 mm in diameter and 0.06 mm deep was created. On the back surface, an elongated protrusion along the 0° back surface ply direction was observed with cracks from 2.2 to 2.4 cm long. Delamination under the protrusion surface was detected by tapping the surface with sharp object.

For the impact velocities between 17.6 and 18.1 m/s, similar front and back surface damage was observed as those created with lower impact velocities. The

depth of the dimple was about 0.09 mm. The length of the cracks on the protrusion surface were from 3.5 to 4.2 cm. In addition to a dimple, a 7 mm long crease as in Fig. 3.4(a) was created for impact velocities of 18.6 and 18.8 m/s. The length of the cracks on the back surface was about 4 cm. No crease was observed on the specimen impacted with 18.9 m/s impact velocity.

For 19.1 m/s impact velocity, front surface cracking at the edge of the dimple was observed and the back surface cracks about 4.4 cm long were observed on the protrusion surface. Broken fibers along with cracks inside the dimple were observed for 20.1 m/s impact velocity. The back surface cracks fully extended to the edge of the support. At this impact velocity, the width of the protrusion was about 12 mm. No back surface fiber breakage was observed up to this impact velocity.

3.4.7 IM7/F655-2

The range of impact velocities tested for IM7/F655-2 was between 8.0 and 22.3 m/s. No front and back surface damage was observed for impact velocities up to 8.3 m/s. Between 12.7 and 13.3 m/s impact velocities, a pan shape dimple about 3 mm in diameter and 0.05 mm deep was created. Two 3 mm long creases as in Fig. 3.4(c) were also observed on the specimen impacted with 13.1 m/s impact velocity. On the back surface, an elliptical shape protrusion about 8 to 12 mm long was observed. A barely visible crack was also observed on the specimen impacted with 13.0 m/s impact velocity.

For impact velocities between 16.3 and 16.7 m/s, a 0.08 to 0.1 mm deep dimple and one or more associated creases were observed. Three creases as in Fig. 3.4(d) with the length of 3, 3.5, and 5 mm were created on the specimen impacted with 16.3 m/s impact velocity. The creases created on four specimens impacted with 16.7 m/s impact velocity varied from specimen to specimen. One crease from 1 to 5 mm long was observed on three of these specimens and two creases as in Fig. 3.4(b) with the length of 2.5 and 5 mm were observed on one specimen. On the back surface, a 2.3 to 3 cm long protrusion with cracks was observed for this range of impact velocities.

For the impact velocities between 19.5 and 22.3 m/s, a 0.1 to 0.16 mm deep dimple with two creases as in Fig. 3.4(b) or (c) were created on most specimens. The

lengths of these creases were from 6 to 9 mm. No crease was created on the specimen impacted with 19.5 m/s impact velocity. On the back surface, a 3.7 to 5 cm long protrusion with cracks were observed. The cracks were extending to the edge of the support on some specimens. Broken fibers were observed on the specimen impacted with 22.28 m/s impact velocity.

3.4.8 IM7/8551-7A

The range of impact velocities tested for IM7/8551-7A was between 7.0 and 20.6 m/s. No front and back surface damage was observed on the specimen impacted with impact velocities up to 8.5 m/s. A dimple could be detected by rubbing the front surface with a finger.

For impact velocities between 12.3 and 13.1 m/s, a dimple about 0.06 mm deep was observed on the front surface. On the back surface, matrix cracks and protrusion about 2 cm long were created. For impact velocities between 16.5 and 16.7 m/s, a 0.08 mm deep dimple on the front surface was observed. A crease about 5 mm long was also observed on the specimen impacted with 16.6 m/s impact velocity. On the back surface, matrix cracks and protrusion about 30 mm long were created.

For impact velocities between 19.1 and 20.6 m/s, a 0.3 to 0.4 mm deep dimple with matrix cracks within the dimple were observed on the front surface. On the back surface, the protrusion with matrix cracks extended to the edge of the support were created. Broken fibers were observed from the surface 0° ply and the 90° ply beneath the surface ply under the point of impact. The width of the protrusion was about 10 mm.

3.4.9 S-4/8551-7A

The range of impact velocities tested for S-2/8551-7A was between 7.6 and 27.2 m/s. For the impact velocities between 7.6 and 8.4 m/s, a 2 mm diameter circular shaped white ring around a 0.01 mm deep dimple was observed on the front surface at the point of impact. On the back surface, several microcracks along the back surface fiber direction in a region about 2.5 cm long and 1.5 cm wide were created. Due to the semi-transparent nature of this material system, matrix cracks and delamination were

opaque against the yellowish semi-transparent background when the specimen was observed in front of a light source. From the front surface, a circular shape opaque region was apparent (Fig. 3.4(a)). From the back surface, a larger opaque region about 4 mm in diameter could be seen (Fig. 3.4(b)). The matrix cracks were easily visible with a spacing of about 0.5 mm. No damage was observed at the center of the opaque region which remained semi-transparent.

For impact velocities between 14.0 and 14.4 m/s, a 0.07 mm deep dimple with matrix cracks around the dimple were observed on the front surface. On the back surface, delaminations and matrix microcracks were created. The delaminations were on both side of the point of impact about 2 mm apart. The length and width of the largest delamination were about 5 and 3 mm, respectively. By observing the specimen in front of a light source (Fig. 3.4(c), (d)), the opaque region was rectangular in shape, about 13 mm long and 11 mm wide. Surface matrix cracks outside the opaque region were visible. No damage except back surface matrix cracks was apparent at the center of the opaque region.

For impact velocities between 19.4 and 19.9 m/s, similar damage was observed on front and back surfaces as created with lower impact velocities. The depth of the dimple was about 0.09 mm. The largest delamination created was about 14 mm long and 5 mm wide. The opaque region was about 15 mm in both length and width (Fig. 3.8(a), (b)). The delaminations extended outside this opaque region (Fig. 3.8(b)).

For impact velocities between 24.5 and 27.2 m/s, similar damage was again observed on front and back surfaces (Fig. 3.8(c), (d)). The depth of the dimple created at these velocities was about 0.1 mm. The delamination in some specimens extended to the edge of the support. As for the specimens impacted with lower impact velocities, the point of impact at the middle of the opaque region still remained semi-transparent.

4   Impact Damage Resistance

4.1 Introduction

In chapter 3, the impact damage visually observed from the specimen front and back surfaces for each material system was described. For laminated composites, internal damage such as matrix crack and delamination may exist as a result of transverse impact even when there is no visible damage from the specimen surface. Therefore, to account fully for the impact damage in the specimen, ultra-sonic C-scan and penetrant enhanced X-ray techniques were used to detect these types of damage. In this chapter, the impact damage detected by these two non-destructive techniques are presented. The ultra-sonic C-scan image of the damage specimen provides a quantitative measurement of the damage area which can be used to characterize the impact damage resistance of each material system.

4.2 Non-destructive Inspection of Impact Damage

Zinc-iodide solution (60 g zinc iodide + 10 ml water + 10 ml alcohol + 10 ml photo flo) was used to penetrate the internal cracks as an X-ray opaque liquid to enhance the detection of delamination and matrix cracking in the impacted specimen. The solution was applied to the specimen back surface for at least 12 hours. The open matrix crack on the specimen back surface provided the "entrance" for the zinc-iodide solution to penetrate into the internal crack network. Unless there is a "path" for the zinc-iodide to reach all the internal damage, isolated cracks will not be detected without the presence of zinc-iodide. A hole may be drilled through the point of impact to expose the isolated cracking. Since the impacted specimens have to be preserved for residual strength measurement and isolated cracks are assumed to be smaller than the "exposed" cracks, this method is not used to detect the isolated cracking.

Before the impacted specimen was placed inside the cabinet X-ray equipment, the residual zinc-iodide solution remaining on the specimen surface was thoroughly washed away with running water. A Hewlett-Packard HP 43805 N X-ray system was used to expose the impacted specimen on an X-ray film. In addition to use the X-ray technique for impact damage detection, ultra-sonic C-scan method was also utilized.

The impacted specimen was fully submerged in water and scanned with a Panametrics' videoscan immersion transducer (10 MHz, 1.5 inch focal length).

The ultra-sonic C-scan images and X-ray radiographs of four selected specimens impacted with four different velocities for each material system are shown in Figs. 4.1-18. The impact damage revealed by penetrant enhanced X-ray provides more detail than the ultra-sonic C-scan. The white area in the C-scan images represents the region of impact damage. This area is the projection of the damage area through the thickness of the specimen and does not, therefore, represent the total ply by ply damage or crack surface area that has been created after impact. Delamination and matrix cracking can be differentiated in the X-ray radiographs but these details are lost in ultra-sonic C-scan images. For most of the material systems impacted with higher velocities, the region of damage detected by both C-scan and X-ray are almost identical. Due to the low resolution of the ultra-sonic C-scan compared to X-ray, matrix cracks in AS4/PEEK from the X-ray radiographs in Fig. 4.4 were not detected by C-scan (Fig. 4.3). Similar results are also observed in IM7/F655-2 (Figs. 4.13 and 4.14).

From Fig. 4.5(a), the damage in the G30-500/F185 specimen with 12.6 m/s velocity impact detected by ultra-sonic C-scan was not apparent in X-ray radiographs (Fig. 4.6(a)). As mentioned in section 3.4.3, no surface cracks were observed in this specimen. Therefore, the damage detected by C-scan was, apparently, an isolated internal crack. Another advantage of ultra-sonic C-scan over X-ray on damage detection is in the case of glass fiber laminates. Unlike the details of damage shown in X-ray radiographs for graphite fiber laminates, the X-ray radiographs of S-2/8551-7A specimen (Fig. 4.18) do not provide any useful representation of the impact damage. This is apparently due to the scattering of X-ray by the glass fibers. By observing the specimen in front of a light source as described in section 3.4.9, the impact damage can be seen in greater details as shown in Figs. 3.7 and 3.8 and the region of damage is identical to that shown in C-scan image. Thus, both ultra-sonic C-scan and penetrant enhanced X-ray techniques have their own advantages and limitations in detecting the impact damage of laminated composites.

By comparing the size of surface cracks as described in chapter 3 with the damage observed from X-ray radiographs and C-scan images, the length of surface protrusion, delamination, or cracks for most of the material systems is almost identical to those detected by C-scan and X-ray except for G30-500/F185 system where less damage was visually observed from the specimen surface. Thus, the largest delamination for most material systems was created between the two layers of the back surface 0° ply and 90° ply. This delamination resembles a pair of wings along the surface fiber direction is clearly shown in most X-ray radiographs.

4.3 Impact Damage Resistance Characterization

The impact damage resistance of a material system is a measure of its ability to withstand the impact without sustaining significant damage. Material systems which have smaller impact damage for a given impact velocity or energy have higher impact damage resistance than those sustaining larger impact damage. For some material systems, direct comparison of impact damage may be difficult especially if the dominated modes of damage are different, e.g. delamination versus fiber breakage.

To measure the impact damage of a specimen, Liu and Hong [23, 26] measured the total delamination area by slicing the impacted plate into strips 5 mm in width. The delamination length on each ply interface of the strips was measured and the areas of delamination at the interfaces were obtained by assembling the individual crack lengths. The main drawback of this measuring method is the destruction of the specimen which could otherwise be used for residual strength measurement. Therefore, instead of measuring the total delamination area, the area of damage region from ultra-sonic C-scan image was used to characterize the impact damage resistance in this investigation. Implicit in this approach is that the through the thickness damage development is similar in each system.

The C-scan detected damage area for each specimen was measured using the Claris CAD graphic software. The ultra-sonic C-scan images were scanned into the Macintosh computer using Apple Scanner and transferred into Claris CAD. A closed polygon was drawn along the edges of the damage region and the area of the polygon,

which represented the C-scan detected damage area, was calculated by computer with greater accuracy and consistency than hand measurement.

For the rest of this section, the variations of C-scan detected damage area with impact velocity, incident energy, and absorbed energy are investigated. Since the impact velocity was the only variable for the impact test, the incident energy is proportional to the square of impact velocity. The relation of damage area with incident energy has been used by most researchers to study the impact damage resistance due to the use of energy release to explain the damage created in the specimen.

A summary of the experimental results of the C-scan detected damage area for given impact velocities for each material systems is presented in Fig. 4.19. The data shown in this figure are only from the specimens with damage areas less than 600 mm^2. These are the complete data for all of the material systems except G30-500/F263-2 and IM7/F650. The data from all the impacted specimens for these two systems are shown separately in Fig. 4.20. From Fig. 4.19, the data appear to be divided into two major groups with the AS4/3502, G30-500/F263-2, and IM7/F650 towards the left (brittle) side and the rest of the material systems towards the right (tough) side. The damage area detected in IM7/F650 is the largest compared to the rest of the material systems which indicates IM7/F650 has the lowest impact damage resistance, for velocities up to 12 m/s. For the AS4/3502 and G30-500/F263-2, the damage areas are almost identical for impact velocities up to 15 m/s. At about 11 m/s, the damage area of these materials is about half of the damage area detected in IM7/F650.

The damage areas in both 8551-7A systems, which are on the right (tough) side of Fig. 4.19, are almost identical for impact velocities up to 16 m/s. For impact velocities higher than 16 m/s, a higher impact velocity for S-2/8551-7A is needed to create the same damage area as in the graphite fiber IM7/8551-7A system. This indicates that glass fiber S-2/8551-7A system has a higher impact damage resistance than the IM7/8551-7A. For the IM7/F655, the damage area detected is almost identical with that in IM7/8551-7A for velocities up to 20 m/s, except at a lower impact velocities between 7 and 10 m/s. For the AS4/PEEK, G30-500/F185, and

IM7/F655-2, damage was detected only for impact velocities higher than 10 m/s. The results for both AS4/PEEK and IM7/F655-2 are almost identical and slightly greater than the damage detected in G30-500/F185, for impact velocities between 10 and 20 m/s.

From the data in Fig. 4.19, the damage area appeared to develop linearly up to 600 mm^2 with impact velocity once the damage was initiated for most material systems. Thus, the data can be fitted with a linear equation to measure the impact damage resistance for each material system. The non-zero damage area data points up to 600 mm^2 were used for line fitting only. Therefore, the data of IM7/F650 (Fig. 4.20(b)) with higher than 12 m/s of impact velocities were neglected. The reasons were due to the nonlinear appearance of the data and to minimize the influence of ring support on the damage development by considering only the damage area less than 30% of the total specimen area inside the support. The data with less than 600 mm^2 of damage area was also discarded for line fitting if the delamination extended as far as the support, such as the damage shown in Fig. 4.16(d).

In Fig. 4.21, the data for AS4/3502 are taken as an example, and fitted with a linear equation

$$A_d = CV_i + C_o \qquad (4.1)$$

where A_d = damage area
$\quad\quad\quad$ V_i = impact velocity

The constant C, the slope of the line, is a measure of the growth rate of the damage area with respect to the impact velocity. The threshold velocity V_c, where the line intersects with the x-axis, can be calculated by simply setting $A_d = 0$ in Eq. (4.1)

$$V_c = -\frac{C_o}{C} \qquad (4.2)$$

The threshold velocities V_c for the nine material systems are shown in Fig. 4.22 and the damage growth rates C are shown in Fig. 4.23. In general, material systems which have a high V_c and a low C value have the best resistance to impact damage.

27

Thus, both V_c and C can be used as the parameters in characterizing the impact damage resistance of composite material systems.

From the results in Fig. 4.22, the threshold velocity V_c of AS4/PEEK is twice the V_c value of AS4/3502. Thus, the thermoplastic composite system can sustain impact velocities twice as great as the thermoset composite system with the same AS4 fibers, before damage is induced. For the epoxy systems cured at different temperatures, the V_c value of G30-500/F185 is almost twice the V_c value of G30-500/F263-2.

For the three BMI systems with IM7 fibers, the brittle IM7/F650 bismaleimide has the lowest V_c value and is almost identical to the V_c value of AS4/3502. By toughening the bismaleimide, the V_c value is increased by almost 90% for IM7/F655 and 130% for IM7/F655-2 compared to IM7/F650. The V_c value of IM7/F655-2 is almost identical to AS4/PEEK and G30-500/F185.

Both IM7/8551-7A and S-2/8551-7A have almost identical V_c values which seems to indicate the threshold velocity to initiate the impact damage in the laminated composites depends only on the matrix material.

From the results in Fig. 4.23, the AS4/PEEK thermoplastic system has about half the damage area growth rate C than the AS4/3502 thermoset system. Together with the high V_c value of this material system, AS4/PEEK is significantly better in resisting the impact damage than the AS4/3502.

For the epoxy systems cured at different temperatures, the C value of G30-500/F185 is also about half the C value of G30-500/F263-2. Which again indicates that G30-500/F185 has a better impact damage resistance. Compared to AS4/PEEK, G30-500/F185 appears to have better impact damage resistance with almost identical V_c value but 40% lower C value. However, the G30-500/F185 laminate is 36% thicker than the AS4/PEEK laminate, see Table 3.1. Further investigation of the laminate thickness effect on threshold velocity and impact damage growth rate is required. In addition to having similar V_c values, both G30-500/F263-2 and AS4/3502 systems also have similar C values which indicates that both systems have almost identical impact damage resistance.

For the three BMI systems, the brittle IM7/F650 bismaleimide system has the highest C of all the material systems chosen for this investigation. Although the V_c of IM7/F650 is almost identical to that of AS4/3502, the C value of IM7/F650 is about 90% higher than AS4/3502. This system has the lowest in impact damage resistance. By toughening the bismaleimide, the C values of both IM7/F655 and IM7/F655-2 systems can be reduced to half the C value of IM7/G650. The toughening of the bismaleimide improved the impact damage resistance of IM7/F655-2 to a level almost identical to that of the AS4/PEEK thermoplastic system.

For the rubber toughened 8551-7A systems, the C value of S-2/8551-7A is also almost identical to IM7/8551-7A. This is a further indication that the impact damage resistance is highly dependent upon the matrix material.

In addition to investigate the variation of damage area with impact velocity, the damage area can also be related to *incident energy* and *absorbed energy*. The *incident energy* of the impactor, U_i, is the kinetic energy of the impact before the contact of impactor with specimen.

$$U_i = \frac{1}{2}mV_i^2 \tag{4.3}$$

where   m   = mass of the impactor (=35 g)

The *absorbed energy*, U_a, is the difference of incident energy (U_i) and residual energy (U_r).

$$U_a = U_i - U_r \tag{4.4}$$

The residual energy, U_r, of the impactor is the kinetic energy of the impact after the rebounding of impactor from the specimen.

$$U_r = \frac{1}{2}mV_r^2 \tag{4.5}$$

where V_r = impactor rebound velocity

The absorbed energy (U_a) includes the energy that goes into matrix cracking, delamination, fiber fracture, elastic response, permanent local deformation, etc. [9] The term *absorbed energy* is also called the *impact energy* by other authors such as Liu and Hong [23, 26].

The variation of the damage area with *incident energy* for each material system is summarized in Fig. 4.24. The damage area also appeared to develop linearly with incident energy except at lower incident energies. From Fig. 4.25(a), although a straight line seems to be the best fit to the AS4/3502 data points with impact damage detected, the extension of the linear curve fit line in Fig. 4.25 would suggest the existence of damage in the specimen even before impact. Thus, the data between 0.6 and 1 J of incident energy have to be correlated with another mechanism and more data are needed to determine the damage initiation incident energy or critical incident energy. However, for the data of AS4/PEEK in Fig. 4.25(b), the critical incident energy U_{ic} can be determine by fitting a straight line through the data of the specimens with damage detected. Therefore, by fitting the data of each material system with a linear equation, at least one parameter, the slope of the line, can be obtained to characterize the damage area growth rate with respect to incident energy.

The critical incident energy U_{ic} and damage area growth rate with respect to incident energy C_{ui} for the nine material systems are shown in Figs. 4.26 and 4.27, respectively. Since the critical incident energy values of AS4/3502, G30-500/F263-2, and S-2/8551-7A could not be determined directly, it was left blank for these three material systems in Fig. 4.26. From Figs. 4.26 and 4.27, the comparisons of U_{ic} and C_{ui} values of each material system are quite similar to the comparisons of V_c and C values shown in Fig. 4.22 and 4.23 except for the IM7/8551-7A and S-2/8551-7A.

The variations of damage area with incident energy for both IM7/8551-7A and S-2/8551-7A are shown in Fig. 4.28. The reason for the low value of damage area growth rate of S-2/8551-7A is because the data with less than 2 J of incident energy in Fig. 4.28 were not actually in linear relation with the rest of the data. Compared to the variation of damage area with impact velocity for the same material systems shown in Fig. 4.29, the relation of damage area with impact velocity are linear for all the data and have much better linear correlation than the variation of damage area with incident

energy. For those material systems in which the U_{ic} could be determined from the linear curve fit, the critical velocity calculated from U_{ic} was lower than the V_c value. Therefore, there is no real physical meaning for U_{ic} calculated from the curve fitting.

A summary of the damage area for given *absorbed energy* for each material system is shown in Fig. 4.30. Unlike the impact velocity, V_i, of the impactor which can be measured accurately from photo-transistor voltage output, the impactor may rotate with an angle of few degrees after rebounding form the specimen. Since the same impactor length was used for calculating the approximately rebound velocity V_r, the absorbed energy is, therefore, an approximate value.

The data of AS4/3502 used as an example shown in Fig. 4.31 can be fitted with a second degree polynomial curve. Therefore, a linear variation of damage area with square root of absorbed energy can be obtained and the results are summarized in Fig. 4.32. The data of AS4/3502 are again used as an example in Fig. 4.33 to be fitted with a linear equation similar to Eq. (4.1)

$$A_d = C_1\sqrt{U_a} + C_2 \qquad (4.6)$$

The constant C_1, slope of the line, is a measure of the damage area growth rate with respect to the square root of absorbed energy. The minimum energy absorbed or threshold absorbed energy U_{at} to initiate the impact damage can be calculated as before by simply setting $A_d = 0$ in Eq. (4.6)

$$U_{at} = \left(\frac{C_2}{C_1}\right)^2 \qquad (4.7)$$

The threshold absorbed energy U_{at} and the damage area growth rate C_1 are summarized in Figs. 4.34 and 4.35, respectively. The results are quite similar to the threshold velocity V_i and damage area growth rate C shown in Figs. 4.22 and 4.23. The material system which has low value of threshold velocity also absorb less energy to initiate impact damage such as AS4/3502 and G30-500/F263-2. Both AS4/PEEK and IM7/F655-2 which have high value of threshold velocity also absorb the highest amount of energy to initiate the damage. For IM7/F650, although this material system

31

has one of the lowest threshold velocity, more energy is absorbed to initiate the impact damage compared to AS4/3502 and G30-500/F263-2. As indicated in Fig. 4.35, IM7/F650 again has the highest impact damage growth rate compared to other material systems.

Although a linear relation of damage area with *incident energy* or *absorbed energy* would have the physical meaning to characterize the damage area through energy release per unit area of damage area of matrix cracking and delamination, the experimental results indicated the damage area is in linear relation with impact velocity even though it has no any significant physical meaning. The reason may be due to the use of projected area rather than the "total damage area" in all ply interfaces. The "total damage area" of delamination after impact measured by Hong and Liu [26] has been shown to be in linear relation with the absorbed energy.

The variations of damage length and damage width with impact velocity for each material system are summarized in Fig. 4.36. The length and width are measured from the ultra-sonic C-scan image of the damage region along and transverse to the surface 0° ply, respectively. Both brittle and tough material systems are less distinctive in these figures compared to the data shown in Fig. 4.19.

4.4 Comparison with Other Test Method

To compare the experimental results that have been presented in Section 4.3 with the data obtained by using different impact test method, the data of the three bismaleimide systems published in Ref. 37 are available for verification. The data for compression strength after impact (CAI strength) and the equivalent damage diameter of three bismaleimide systems impacted with 30.5 J of incident energy are tabulated in Table 4.1. The impact test method used in Ref. 37 is by dropping a 5.4 kg mass through a guide tube onto a 32-ply quasi-isotropic laminate following the Boeing Specification Support Standard (BSSS). The impact velocity is about 3.4 m/s for 30 J of incident energy. The damage area can be calculated from the equivalent damage diameter and are also tabulated in Table 4.1. The damage area ratios of IM7/F650 and IM7/F655 to IM7/F655-2 are 10.5:1 and 1.4:1, respectively. From Fig. 4.19, the damage areas of these three bismaleimide systems calculated using Eq. (4.1) at 20 m/s

of impact velocity or 7 J of incident energy are 1264 mm^2 for IM7/F655-2, 390 mm^2 for IM7/F655, and 279 mm^2 for IM7/F650. The comparison of IM7/F650 data is meaningless since the ratio of 10.5:1 would require the damage area to be 2929 mm^2 which is far greater than the area of specimen inside the ring support. Also, the damage area of 1264 mm^2 is beyond the 600 mm^2 limit that has been used to correlate the data using Eq. (4.1). For the toughened bismaleimide systems, the damage area ratio of IM7/F655 to IM7/F655-2 is 1.4:1 which agrees with the data in Ref. 37. Thus, the results indicate the same impact damage resistance information can be obtained with a much smaller specimen.

5 Impact Damage Tolerance

5.1 Introduction

In this chapter, the test procedure to characterize the impact damage tolerance of composite materials through a residual compression test is described. The experimental results of compressive moduli, strengths, and ultimate strains from specimens before and after impact are presented. Since the use of strain gages on damaged specimens is not practical, a procedure is developed by which the crosshead displacement of the testing machine during the compression test is used for specimen strain measurement. The two parameter residual strength model proposed by Caprino is investigated for its applicability in modeling the residual compressive strength of different composite material systems. Finally, an improved model based on experimental observation is proposed to characterize the residual compressive strength, and ultimate strain after impact.

5.2 Compression Test

The coupon specimens for the compression after impact tests were cut from the impacted specimen along the dashed line shown in Fig. 5.1(a) with the impact location at the center of the coupon. The dimensions of the coupon were 51.8 mm X 25.4 mm (2.04 in X 1.00 in) with the surface 0° ply parallel to the long side of the coupon (Fig. 5.1(b)). The compression coupon specimens before impact were also prepared with the same dimensions.

The compressive properties of these coupons before and after impact were measured using the compression fixture (Fig. 5.2) developed by Gurdal [38]. During the compression loading, the vertical edges of the coupon were laterally supported by four vertical steel pins as shown in Fig. 5.2(a) to prevent premature buckling of the specimen. The length of the coupon (51.8 mm) allowed the specimen to be compressed by 2.03 mm (0.08 in) or 4% strain without the four vertical steel pins being compressed at the same time. The top and bottom end of the specimen were clamped supported by tightening the screws located on the top and bottom compression platens of the fixture.

An Instron 4204 screw driven testing machine was used to apply the compression load on the specimen, through a spherical steel ball on top of the fixture (Fig. 5.2(b)), with a constant crosshead displacement rate of 0.254 mm/min (0.01 in/min). The load and crosshead displacement during the compression loading were recorded. One specimen without impact from each material system, except G30-500/F263-2 and AS4/3502, was instrumented with back to back strain gages to measure the compressive strain and to check the premature buckling of the specimen during the compression loading did not occur.

5.3 Compressive Stress-Strain Measurement

The damage to the surface of the impacted specimen prevented the use of strain gages to measure the compressive strain in the specimen. In addition, the steel pins used as a lateral support of the specimen made it difficult to employ an extensometer. Since the specimen was axially loaded between two steel platens which eliminated the slipping that had been observed in some tensile tests, it is possible to calculate the specimen compressive strain from the crosshead displacement of the testing machine.

A typical trace of compression test data is shown in Fig. 5.3 for the curve labeled "Original Test Data." During the compression loading, the crosshead of the testing machine moved downward to compress the specimen. Because of the possible slack between the crosshead and the driving screws, the initial nonlinear portion of the load-displacement curve up to about 0.8 mm crosshead displacement of the "Original Test Data" was apparently due to the movement of the crosshead as it seats on the driving screws under its own weight to the point when the crosshead was completely seated. This is based on the observation from the strain data shown in Fig. 5.4 measured from the strain gages which represents the actual strain of the specimen. Between 0.8 and 1.5 mm of crosshead displacement, the compression load increases almost linearly. Thus, by drawing a straight line tangent to this portion of the curve and extended to the x-axis at d_o (Fig. 5.3), the data can be adjusted by shifting to the left linearly with the equation

$$d = d_{ch} - d_o \qquad\qquad (5.1)$$

where   d   = shifted crosshead displacement

$$d_{ch} \quad = \text{ original crosshead displacement.}$$

The shifted test data are shown in Fig. 5.3 and the initial non-linear portion of the data are ignored.

The compression stress-strain relations of an AS4/3502 specimen before impact with the strains measured from strain gages (Gage) and crosshead displacement (S-CH) are shown in Fig. 5.4. The compressive stress σ is calculated as

$$\sigma = \frac{F}{A} \tag{5.2}$$

where   F   = compressive load

         A   = cross section area of the compression specimen

and the strain from the crosshead displacement is

$$\varepsilon_{ch} = \frac{d}{L} \tag{5.3}$$

where   L   = length of the compression specimen

The results shown in Fig. 5.4 indicate the strains measured from crosshead displacement are much higher than the actual strain measured from strain gages. Therefore, the crosshead displacement is not equal to the actual axial deformation of the specimen but the total deformation of the specimen, crosshead, load cell, compression fixture, etc.

In order to obtain the strain value from the crosshead displacement, it is necessary to calculate the deformation of the specimen. The series springs model in Fig. 5.5(a) is used to model the total deformation as measured by the crosshead displacement. The spring constant k_s represents the axial stiffness of the specimen and k_m is the equivalent spring constant of the crosshead, load cell, compression fixture, etc. The objective is to determine the expression of k_m in terms of known variables. In Fig. 5.5(b), the crosshead displacement, d, due to compression force, F, is

$$d = d_m + d_s \tag{5.4}$$

36

where d_m = total deformation of the crosshead, load cell, compression fixture, etc.

d_s = deformation of the compression specimen

Since the springs are in series, the axial force F can be expressed as

$$F = k_m d_m = k_s d_s \tag{5.5}$$

and the strain of the specimen is

$$\varepsilon = \frac{d_s}{L} \tag{5.6}$$

Multiplying Eq. (5.4) with k_m and substituting d_m and d_s from Eqs. (5.5) and (5.6), the equivalent spring constant k_m is

$$k_m = \frac{F}{d - L\varepsilon} \tag{5.7}$$

Both F and d are the experimental data from the compression test and ε can be measured using the strain gages. Since one specimen from each of the seven material systems was instrumented with strain gages, k_m was measured to be about 60 kN/mm using Eq. (5.7). Once k_m is determined, Eq. (5.7) can be rearranged to express ε as

$$\varepsilon = \frac{1}{L}\left(d - \frac{F}{k_m}\right) \tag{5.8}$$

which is used to obtain the strain data from the crosshead displacement d.

The corrected strain data from crosshead displacement are shown in Figs. 5.4, 5.6-8 labeled with (C-CH). Although most of the C-CH strain data are not exactly the same as the strain data from strain gages (Gage), the C-CH strain data are at least parallel to most of the Gage strain data such as in Figs. 5.6(b), 5.7(a), and 5.8(a). In fact, the Gage strain data appeared to be slightly shifted upward in these figures where the initiation of strain in the specimen is at a slightly higher loading. This may due to the friction in the compression fixture between the top compression plate with the vertical guiding rods and the steel pins which were used as the specimen lateral

support. The only Gage strain data initiated from zero load is in Fig. 5.6(a) where both Gage and C-CH strain data are almost identical up to 1% of compressive strain.

Since the strains measured from both back to back strain gages are almost identical, which indicates no premature buckling in the specimen during the compression loading.

5.4 Residual Compressive Modulus

After the compressive strain data for each specimen were obtained, the compressive modulus can be measured from the compressive stress-strain curves. In order to maintain the consistency of the modulus measurement, the compressive moduli presented were measured from the C-CH strain data, which is calculated from the crosshead displacement using Eq. (5.8). The compressive moduli of the specimens before impact are presented in Table 5.1 and summarized in Fig. 5.9. At least two specimens from each material system were tested. One datum point from IM7/F650 was found to be too low and was not used to calculate the average value of compressive modulus for this material system. This error may due to the misalignment of the compression fixture with the load cell during the compression loading. The variation of the compressive moduli of each material system was within ±8% of the average value. The modulus of each material system calculated from Classical Lamination Theory (CLT) using the material tensile properties is also shown in Table 5.1. In general, the compression modulus of each material system was 15 to 20% lower than the tensile modulus calculated from CLT. This was due to the weakness of the fibers which were susceptible to bending and buckling in compression.

From Fig. 5.9, the compressive moduli of material systems with AS4 and IM7 fibers are between 40 and 50 GPa with the exception of IM7/8551-7A which has slightly higher compressive modulus due to its higher fiber volume fraction (Fig. B.3(a)). This seems to indicate the compressive modulus depends on fiber material which was consistent with the prediction of CLT. For the two material systems with G30-500 fiber, G30-500/F185 has lower compressive modulus than G30-500/F263-2 due to the effect of lower fiber volume fraction. For the three BMI systems, the

toughening of the bismaleimide does not result in any significant improvement in compressive modulus. The compressive modulus of S-2/8551-7A is about 50% lower than IM7/8551-7A in which both material systems have the identical matrix material. In addition, the compressive moduli of both AS4/3502 and AS4/PEEK are almost identical even though both matrix materials are quite different to each other. Therefore, the results strongly suggest the matrix material has less effect on compressive modulus than the fiber material and were consistent with the prediction of CLT.

The variation of the residual compressive modulus with impact velocity and the normalized data for each material system are shown in Figs. 5.10-13. The compressive moduli before impact are plotted on y-axis. The normalized residual compressive modulus $\overline{E}$ and normalized impact velocity $\overline{V}$ are calculated as

$$\overline{E} = \frac{E_r}{E_o} \tag{5.9}$$

$$\overline{V} = \frac{V_i}{V_c} \tag{5.10}$$

where E_r = residual compressive modulus after impact
        E_o = compressive modulus before impact

and V_i and V_c are impact velocity and threshold velocity as defined in Eqs. (4.1) and (4.2). These normalized data are shown in Figs. 5.10(b)-13(b) which give better visualization of the test data in terms of the magnitude of modulus reduction at a given impact velocity with respect to threshold velocity.

From Figs. 5.11 and 5.13, the residual compressive moduli of G30-500/F185 and S-2/8551-7A remain unchanged at pre-impact level. For the rest of the material systems except AS4/PEEK, the reduction of compressive modulus is generally observed at impact velocity at least 50% or higher than the threshold velocity of each material system. Since the damage modes for impact velocities up to about 50% above the threshold level of each material system were matrix cracking and delamination, small amount of matrix cracking and delamination would have no

significant effect on the residual compressive modulus which had been shown to be highly dependent upon the fiber material. For AS4/PEEK, the compressive modulus reduction for as much as 20% were observed even at impact velocities lower than the threshold velocity of this material system. The reason may due to the bent fibers between the dimple and protrusion on the specimen front and back surfaces. These types of surface damage were observed at impact velocities below the threshold level.

The variation of the residual compressive modulus with C-scan detected damage area are shown in Figs. 5.14 and 5.15. The results indicate the residual compressive modulus remains unchanged up to 200 mm^2 for most material systems due to the small amount of matrix cracking and delamination which had little effect on residual compressive modulus. For S-2/8551-7A, no effect on compressive modulus was observed even with damage area closed to 500 mm^2. This was due to the low compressive modulus of S-2/8551-7A in which the fibers would be less effective in carrying compressive load In addition, no excessive bending of each individual ply and only small amount of matrix cracking were observed in the impacted specimens with damage area closed to 500 mm^2.

5.5 Residual Compressive Strength

The maximum load from each compression test recorded by the Instron testing machine was used to determine the compressive strength σ_o of specimens before impact and residual compressive strength σ_r of specimens after impact with Eq. (5.2). For the specimens after impact, the specimen original thickness before impact was used to measure the crosssectional area A used in Eq. (5.2).

The compressive strengths measured from the specimens of each material system before impact are presented in Table 5.2 and summarized in Fig. 5.16. The first compressive strength datum for IM7/F650 in Table 5.2 was obtained from the same specimen with the lowest compressive modulus in Table 5.1. The compressive strength of this specimen was also the lowest for this material system. The variation of the compressive strengths of each material system was within ±7% from the average value except for the IM7/F650 with ±11.2% variation.

From Fig. 5.16, the compressive strengths of most material systems are between 500 to 600 MPa. Both G30-500 fiber material systems have the lowest compressive strengths at about 400 MPa. As with compressive modulus, the toughening of the bismaleimide for the three BMI systems does not result in any significant improvement in compressive strength. For both material systems with AS4 fiber, the compressive strength of AS4/3502 is 21% lower than AS4/PEEK in which both material systems have the identical fiber. In addition, the compressive strengths of both IM7/8551-7A and S-2/8551-7A rubber toughened epoxy systems are almost identical even with two completely different fiber materials. Therefore, the results indicate that the compressive strength, like impact damage resistance, is highly dependent upon the matrix material. This is opposite to the compressive modulus which was observed to be highly dependent upon the fiber material.

The variation of the compressive strength with impact velocity and the normalized data for each material system are shown in Figs. 5.17-20. As before, the compressive strengths before impact are plotted on y-axis. The normalized residual compressive strength $\overline{\sigma}$ is calculated as

$$\overline{\sigma} = \frac{\sigma_r}{\sigma_o} \tag{5.11}$$

where σ_r = residual compressive strength after impact
        σ_o = compressive strength before impact

Unlike the residual compressive moduli after impact of most material systems which remain mostly unchanged at some impact velocities above their respective threshold velocities, the residual compressive strengths of all material systems are lower than their pre-impact levels at impact velocities higher than their respective threshold velocities. For AS4/PEEK (Fig. 5.17(b)) and G30-500/F185 (Fig. 5.18(b)), compressive strength reduction as much as 20% was observed even at impact velocities below the threshold velocity. From Fig. 5.20, the reduction in compressive strength for both IM7/8551-7A and S-2/8551-7A are identical for a given impact velocity. This is a further indication that the compressive strength is dependent upon the matrix material.

The variation of the residual compressive strength with impact velocity and the normalized data for all material systems are shown in Fig. 5.21. As in Fig. 4.19, the results in Fig. 5.12(a) also appear to fall into two groups with the same material systems AS4/3502, G30-500/F263-2, and IM7/F650 with higher compressive strength reduction than the rest of the material systems for a given impact velocity. From Fig. 5.21(b), the variation of the normalized residual compressive strength with normalized impact velocity for each material system appears to be quite similar. However, the data of each individual material system as shown in Figs. 5.17(b)-20(b) indicate the reduction of compressive strength may develop linearly or nonlinearly for different material systems.

In Fig. 5.22, the residual compressive strengths of each material system are plotted with respect to incident energy U_i. This variation has been modeled by Caprino [6], based on linear elastic fracture mechanics concepts. The original model was developed to predict the residual tensile strength of impacted carbon fiber reinforced plastic (CFRP) laminates which was also found to be effective in predicting the residual compressive strength due to impact.

Eq. (5.12) is the model for modeling the residual compressive strength of impacted CFRP laminates developed by Caprino.

$$\frac{\sigma_r}{\sigma_o} = \left(\frac{U_o}{U_i}\right)^{\alpha} \tag{5.12}$$

where U_o and α are experimentally determined parameters In deriving Eq. (5.12), the model previously proposed by Caprino [39] for predicting the residual strength σ_n of a notched laminate was used

$$\frac{\sigma_n}{\sigma_{no}} = \left(\frac{D_o}{D}\right)^{m}, \qquad D \geq D_o \tag{5.13}$$

where σ_{no} = strength of unnotched specimen
         D_o = characteristic defect of the material
         D = dimension of the notch

42

To apply Eq. (5.13) for predicting residual strength after impact, the assumption made by Caprino was the relation between D and incident energy U_i can be expressed by

$$D_o = \beta U_i^n, \qquad\qquad n > 0 \qquad\qquad (5.14)$$

Finally, Eq. (5.12) is obtained by substituting Eq. (5.14) into Eq. (5.13) with

$$\alpha = mn \qquad\qquad (5.15)$$

$$D_o = \beta U_o^n \qquad\qquad (5.16)$$

and replacing σ_n and σ_{no} by σ_r and σ_o, respectively.

To model the data in Fig. 5.22(b) with Eq. (5.12) where the left hand side of this equation is the normalized residual compressive strength as defined in Eq. (5.11), the data with impact damage were fitted with Eq. (5.12) as shown in Figs. 5.23 and 5.24. The solid symbols in these figures are the data used for curve fitting the Caprino model. Although the data of AS4/PEEK and G30-500/F185 in Fig. 5.23 can be fitted with a straight line with better correlation, the data at around 1 J of incident energy were not used for fitting the Caprino model since no damage was detected in the specimens producing these data points.

As a result of fitting the data of each material system with Eq. (5.12), the parameters U_o and α can be determined. Since Eq. (5.13) is valid for $D \geq D_o$, Eq. (5.12) is applicable only for $U_i \geq U_o$. When $U_i = U_o$, Eq. (5.12) yields $\sigma_r = \sigma_o$. Therefore, the physical meaning of U_o is clearly the lowest incident energy to initiate impact damage and compressive strength reduction whereas α represents the magnitude of strength reduction. The effects of U_o and α of Caprino model are demonstrated in Fig. 5.25. For material systems with identical U_o and different α values, the one with higher α has higher reduction in residual compressive strength for a given incident energy. The prediction of U_o by measuring the residual compressive strengths of several specimens impacted at various incident energies was close to the experimental results of AS4/3502 (Fig. 5.23(a)), G30-500/F263-2 (Fig. 5.23(B)), IM7/F650 and IM7/F655 (Fig. 5.24(a)).

43

The values of experimentally determined parameters U_o and α are summarized in Fig. 5.26. The α of each material system varies between 0.3 and 0.5. Since the incident energy used in Eq. (5.12) was the kinetic energy of the impactor (Eq. (4.3)), an equivalent threshold velocity of each material system can be calculated from U_o. The results are summarized in Fig. 5.27 and are very similar to the results in Fig. 4.22 which were determined from the impact damage size.

The variation of the residual compressive strength and the normalized strength with absorbed energy U_a for each material system are shown in Fig. 5.28. The results indicate there is no unique relation between the reduction in residual compressive strength and the amount of energy absorbed in different material systems.

Having examined the residual compressive strength as a function of impact threat, the effects on residual compressive strength as a result of impact damage can also be investigated. The variation of the residual compressive strength with C-scan detected damage area and their normalized relations are summarized in Fig. 5.29. The normalized C-scan detected damage area is calculated as

$$\overline{A}_d = \frac{A_d}{wL} \tag{5.17}$$

where   w   = width of the compression specimen

A_d and L are the damage area and the length of the specimen as defined in Eqs. 4.1 and 5.3, respectively. From Fig. 5.29(b), the relations of normalized residual compressive strength with damage area are identical for each material system except for one data point from each AS4/PEEK and G30-500/F263-2 are found to deviate from the rest. The reason for these anomalous data is not known. About 50% of original compressive strength is lost as a result of 20% damage of the specimen normal projection area. As indicated in this figure, the percentage of compressive strength reduction decreases as the damage area increases. The data can be fitted with a second degree polynomial curve and a linear relation between the residual compressive strength and the square root of damage area is expected.

Instead of relating the residual compressive strength with the square root of damage area, a more physical approach is to relate the residual compressive strength with the damage area equivalent diameter d_{eq}

$$d_{eq} = \sqrt{\frac{4A_d}{\pi}} \qquad (5.18)$$

which is the diameter of an equivalent circle with the area equal to the C-scan detected damage area A_d of a specimen.

The variation of the residual compressive strength with damage area equivalent diameter and the normalized data for each material system are shown in Fig. 5.30. The normalized damage area equivalent diameter $\bar{d}_{eq}$ is calculated as

$$\bar{d}_{eq} = \frac{d_{eq}}{w} \qquad (5.19)$$

which is the ratio of the d_{eq} to the width of the compression specimen w. Thus, the damage size was as wide as the width of the compression specimen at $\bar{d}_{eq} = 1$. As indicated in Fig. 5.30(b), the overall variation of normalized residual compressive strength $\bar{\sigma}$ with $\bar{d}_{eq}$ for all material systems is linear as expected.

In Figs. 5.31 and 5.32, the data of each material system are plotted separately for detail examination. Except for the deviation of one data point from each AS4/PEEK (at $\bar{d}_{eq} \approx 0.6$ in Fig. 5.31(a)) and G30-500/F263-2 (at $\bar{d}_{eq} \approx 0.5$ in Fig. 5.31(b)) which have been identified before, the residual compressive strength for each material system decreases linearly with the increase of damage area equivalent diameter for $\bar{d}_{eq}$ up to 1. Some data deviation from the linear line are found in AS4/PEEK and both 8551-7A material systems. In Fig. 5.31(a), residual compressive strength reduction as much as 20% was found for two AS4/PEEK specimens with no impact damage detected by either C-scan or X-ray. However, a dimple was created on these specimen surface and a protrusion on the back surface which may be the cause for the compressive strength reduction. An opposite situation was found in both 8551-7A systems where the residual compressive strengths of some specimens remain

unchanged at the pre-impact level even with the equivalent damage diameter between 20 to 30% of the specimen width (Fig. 5.32(b)). The reason may due to the different modes of damage created on these specimens. From the X-ray radiographs of IM7/8551-7A in Fig. 4.16(a) and the specimen image of S-2/8551-7A observed in front of a light source in Figs. 3.7(a) and (b), only matrix cracking without delamination was observed in these specimens. Since delamination would have greater effect on residual compressive strength [3], these specimens without the presence of delamination were able to carry the compression load up to the pre-impact level.

From Fig. 5.32(a), the residual compressive strengths of IM7/F650 specimens with $\overline{d}_{eq} \approx 1.8$ remain almost unchanged compared to those with $\overline{d}_{eq} \approx 1$. Although the specimens with $\overline{d}_{eq} \approx 1.8$ have larger damage area than those with $\overline{d}_{eq} \approx 1$, the width of the damage size in both compression specimens are almost identical as indicated in Fig. 5.33. Since the damage in the specimen away from the point of impact, which is the center of the specimen, is mainly delamination, the damage in compression specimen impacted with lower velocity (Fig. 5.33(a)) would be quite similar with the one impacted with higher velocity (Fig. 5.33(b)) after being cut from the impacted specimens.

Based on this observation, the residual compressive strengths of all material systems decrease linearly to about 40% of their pre-impact strength for $\overline{d}_{eq}$ up to 1 and remain at that level for damage equivalent diameter larger than the width of the compression specimen. Therefore, the variation of the residual compressive strength σ_r with damage equivalent diameter d_{eq} can be expressed as

$$\frac{\sigma_r}{\sigma_o} = 1 - K_d \frac{d_{eq}}{w}, \qquad\qquad d_{eq} \leq w \qquad\qquad (5.20)$$

or

$$\overline{\sigma} = 1 - K_d \overline{d}_{eq}, \qquad\qquad \overline{d}_{eq} \leq 1 \qquad\qquad (5.20a)$$

and

46

$$\sigma_r = \sigma_o\left(1 - K_d\right), \qquad\qquad d_{eq} \geq w \qquad\qquad (5.21)$$

where K_d is the rate of residual compressive strength reduction with respect to the damage area equivalent diameter. From Fig. 5.30(b), K_d is 0.625 for the testing conditions used in this investigation. In general, K_d is considered to depend on the laminate stacking sequence, impact conditions, compression specimen dimensions, and possibly mode of impact damage. However, it has been shown to be independent of the material properties.

As described in Chapter 4, the damage area of any material system can be modeled with Eq. (4.1). Substituting Eq. (4.2) into Eq. (4.1), the damage area A_d can be expressed as

$$A_d = CV_i - CV_c \qquad\qquad (5.22)$$

Since the damage area equivalent diameter d_{eq} in Eq. (5.20) is determined from the damage area A_d using Eq. (5.18), Eq. (5.20) can be expressed in terms of impact velocity V_i by substituting Eqs. (5.18) and (5.22) into Eq. (5.20).

$$\frac{\sigma_r}{\sigma_o} = 1 - K_v\sqrt{V_i - V_c}, \qquad\qquad V_i \leq V_c + \frac{\pi w^2}{4C} \qquad\qquad (5.23)$$

where $\quad K_v = \dfrac{2K_d}{w}\sqrt{\dfrac{C}{\pi}} \qquad\qquad (5.24)$

The residual compressive strength can also be expressed in terms of incident energy by substituting Eq. (4.3) into Eq. (5.23).

$$\frac{\sigma_r}{\sigma_o} = 1 - K_u\sqrt{\sqrt{U_i} - \sqrt{U_c}}, \qquad\qquad U_i \leq \left[\sqrt{U_c} + \frac{\pi w^2}{4C}\sqrt{\frac{m}{2}}\right]^2 \qquad\qquad (5.25)$$

where $\quad K_u = \dfrac{2K_d}{w}\sqrt{\dfrac{C}{\pi}}\left(\dfrac{2}{m}\right)^{\frac{1}{4}} \qquad\qquad (5.26)$

$$U_c = \frac{1}{2}mV_c^2 \tag{5.27}$$

For V_i and U_i higher than the limits stated in Eqs. (5.23) and (5.25), Eq. (5.21) is valid as long as the dominant damage mode is delamination. The residual compressive strength of a specimen impacted with perforation velocity of the same impactor would be much lower than a specimen impacted with low velocity even if the "damage area" of both specimens were identical.

The data for each material system modeled with Eqs. (5.21) and (5.25) are shown in Figs. 5.34 and 5.35. Compared to the Caprino model (Eq. 5.12), there are four parameters (V_c, C, σ_o, K_d) that need to be determined experimentally in Eq. (5.20) instead of three parameters (U_o, α, σ_o) in Caprino model. However, there are several improvements made in Eq. (5.20) over the Caprino model. First, once K_d is determined from a material system, the residual compressive strength of other material systems with the same testing conditions can be predicted; second, Eq. (5.20) can be used to predict the residual compressive strength based on the impact damage resistance and the compressive strength before impact whereas in Caprino model, the residual strength is predicted by measuring the residual compressive strength experimentally from several impacted specimens in addition to compressive strength before impact; third, the residual strength is not "over predicted" in Eq. (5.25) since no real number exists for $U_i < U_c$; and fourth, the effect of specimen width was considered in Eq. (5.20) to model the residual compressive strength.

In Section 4.4, the experimental results of impact damage resistance were compared with the test data available in Ref. [37]. The residual compressive strength of the same BMI systems were also published in Ref. [37] and are tabulated in Table 4.1. Since the testing methods employed in Ref. [37] were different from the methods used in this study, it is difficult to make direct comparison on residual compressive strength. However, the experimental results in Fig. 5.35(a) do indicate the residual compressive strength of IM7/F650 is much lower than both IM7/F655 and IM7/F655-2 at around 7 J of incident energy, which is the same incident energy used for damage area comparison in Section 4.4. Also, the residual strength of IM7/F655 is slightly lower than IM7/F655-2 which "agrees" with the magnitudes of residual compressive

strength shown in Table 4.1. Therefore, the residual compressive strength is highly dependent upon the dimension of the compression specimen and K_d needs to be adjusted accordingly.

The variation of the residual compressive strength with C-scan detected damage width and length, together with their normalized data, are shown in Figs. 5.36 and 5.37, respectively. The normalized C-scan detected damage width w_d and length L_d are calculated as

$$\overline{w}_d = \frac{w_d}{w} \tag{5.28}$$

$$\overline{L}_d = \frac{L_d}{L} \tag{5.29}$$

where w_d = C-scan detected damage width of the impacted specimen
           L_d = C-scan detected damage length of the impacted specimen

Unlike the variation of $\overline{\sigma}$ with $\overline{d}_{eq}$ shown in Fig. 5.30(b), the normalized data shown in Figs. 5.36(b) and 5.37(b) are more scattered for a given $\overline{w}_d$ and $\overline{L}_d$.

5.6 Residual Compressive Strain

The maximum compressive strain from the specimens of each material systems before impact are presented in Table 5.3 and summarized in Fig. 5.38. System S-2/8551-7A was found to have the highest compressive strain up to 2.7% compared to about 1.5% strain for most of the other material systems, which seems to indicate the compressive failure strain is dependent upon the fiber material rather than matrix material.

The variation of the residual compressive strain with impact velocity, incident energy, and absorbed energy are shown in Figs. 5.39-41. Since the stress-strain relations for most impacted specimens are almost linear up to the failure load, the results of residual compressive strain would be very similar to residual compressive strength as indicated in Fig. 5.39(b) compared to Fig. 5.21(b).

For the residual compressive failure strain as a function of the damage size, the variation of the residual compressive strain with damage area, equivalent diameter, damage width, and damage length are shown in Figs. 5.42-45. Again, linear relations between residual compressive failure strain with damage equivalent diameter are indicated in Fig. 5.43(b) for all material systems with equivalent diameter almost up to the width of the compression specimen. Thus, by calculating the rate of failure strain reduction with equivalent diameter, Eq. (5.20) can be modified to predict the residual compressive failure strain.

6   Quasi-Static Indentation Test

6.1 Introduction

In Chapter 5, the residual compressive strengths of all composite material systems were found to decrease linearly with respect to the damage area equivalent diameter and Eq. (5.20) was developed based on this observation to model the residual compressive strength after impact. In Eq. (5.20), K_d is an experimentally determined parameter which has been found to be independent of the material properties. Therefore, the residual compressive strength of any composite material system can be predicted by measuring the equivalent diameter of the damage area in a laminate following the same impact and compression test procedures. In this chapter, damage resulted from quasi-static indentation instead of impact was investigated. For impact test, the contact time of impactor with impacted specimen was typically in less than 1 millisecond. The objectives are to simulate the impact test with quasi-static indentation test and to study the effect on K_d due to these two loading conditions so that the residual compressive strength can be predicted with Eq. (5.20) using the equivalent diameter of the damage area created by quasi-static indentation.

6.2 Quasi-Static Indentation Test

A schematic diagram of the quasi-static indentation test setup is shown in Fig. 6.1. Essentially, the testing arrangement was identical to the setup for impact test except for the impactor which was, in this case, attached to the load cell of the testing machine as an indentor. A 16-ply quasi-isotropic laminate specimen with the dimensions same as impact specimen (Fig. 3.2) was clamped supported in the same fixture (Fig. 3.1) for holding the impact test specimen. Only one specimen from each composite material system was tested.

An Instron 4204 screw driven testing machine with a 1000-lb load cell was used to apply the indentation load at the center of the specimen, through a 12.7 mm (0.5 in) diameter hemispherical indentor, with a constant crosshead displacement rate of 0.254 mm/min (0.01 in/min). The load and crosshead displacement during the indentation loading were recorded. A typical trace of quasi-static indentation test data is shown in

Fig. 6.2. The maximum indentation load applied on each specimen before unloading is shown in Table 6.1. Since the maximum indentation load was up to 3.1 kN, the crosshead displacement was within the nonlinear range as indicated in Fig. 5.3 for compressive loads up to 5 kN. Therefore, the procedure to correct the crosshead displacement developed in Section 5.3 could not be applied to measure the indentation of the specimen.

6.3 Damage Assessment after Indentation Test

After the indentation test, the front (indented side) and back surfaces of each specimen were visually inspected. The depth of the front surface dimple was measured using 'Talysurf' 4 as described in Section 3.4. Ultra-sonic C-scan and penetrant enhanced X-ray techniques as described in Section 4.2 were also used to detect matrix crack and delamination in the specimen. The C-scan images and X-ray radiographs for all specimens are shown in Figs. 6.3-11. The method described in Section 4.3 was used to measure the damage area from C-scan image and the results are shown in Table 6.1. Since the objective of the quasi-static indentation test is to simulate the impact test for creating a similar damage in the specimen, the equivalent impact velocity for a given damage area after indentation test was calculated with Eq. (4.1) by assuming the damage due to quasi-static indentation was similar to impact damage. The equivalent impact velocities for all specimens were found to be between 13 and 18 m/s which are also shown in Table 6.1.

For AS4/3502, a 0.33 mm deep dimple was created on the front surface as a result of 2.4 kN indentation load. On the back surface, the crack length parallel to the 0° surface ply was about 30 mm. This surface damage was similar to the damage on the specimen impacted with 13 m/s impact velocity. The damage detected by C-scan and X-ray as shown in Fig. 6.3 was also similar to the damage shown in Figs. 4.1(b) and 4.2(b) resulted from impact velocity of 12.8 m/s. Therefore, the impact damage in an AS4/3502 specimen impacted with velocity of 12.7 m/s can be simulated by quasi-static indentation load of 2.4 kN.

Compared to the impact damage in AS4/PEEK specimens, the surface damage due to 3.1 kN of quasi-static indentation load was quite different. On the front

52

surface, the diameter and depth of the dimple were about 4 and 0.33 mm, respectively. In addition to the creases shown in Fig. 3.4(b), two creases in opposite sides of the dimple were formed with their lengths along the surface ply fiber direction. These types of creases were not found on any impacted specimen. On the back surface, fiber fracture and matrix cracks were observed. The length of the fiber fracture perpendicular to the back surface ply fiber direction was about 9 mm. The damage detected by C-scan and X-ray as shown in Fig. 6.4 was also different to those in impacted specimens shown in Figs. 4.3 and 4.4. The damage was mainly matrix cracks without significant delamination.

The damage in G30-500/F185 due to quasi-static indentation load was also quite different compared to those specimens due to impact. The dimple created by 3.1 kN indentation load was about 0.24 mm deep and 4 mm in diameter, which was deeper than the dimple on the specimen impacted with velocity of 12.7 m/s. The creases on each side of the dimple about 3 and 4 mm long were created on the front surface as shown in Fig. 3.4(c). On the back surface, fiber fracture about 4 mm long perpendicular to the surface ply fiber direction without significant matrix crack was observed. Compared to the impacted specimen with the same damage area in C-scan images, no damage was detected by X-ray in the specimen impacted with velocity of 12.6 m/s (Fig. 4.6(a)) and matrix cracks along the surface ply direction was the dominant damage mode observed on specimens impacted with higher velocities as shown in Fig. 4.6.

For G30-500/F263-2, a 0.12 mm deep dimple was created on the front surface as a result of 2.9 kN indentation load. On the back surface, matrix crack about 37 mm long was created along the surface ply fiber direction. This type of damage was very similar to the damage on specimen impacted with velocity of 14.9 m/s. In addition, the damage detected by C-scan and X-ray as shown in Fig. 6.6 was also similar to the impact damage shown in Figs. 4.7(c, d) and 4.8(c, d). Therefore, the impact damage in an G30-500/F263-2 specimen impacted with velocity of 14.5 m/s can be simulated by quasi-static indentation load of 2.9 kN.

For the three BMI systems, the damage observed on the specimen surface and the internal damage detected by C-scan and X-ray (Figs. 6.7-9) due to quasi-static

indentation load were quite similar to the impact damage (Figs. 4.9-14) of the same composite material systems impacted with velocities closed to the equivalent impact velocities shown in Table 6.1. Similar damage between quasi-static indentation (Figs. 6.10 and 6.11) and impact (Figs. 4.15-18) were also observed for the two rubber toughened epoxy systems. Therefore, the impact damage of most composite material systems can be simulated by quasi-static indentation test except AS4/PEEK and G30-500/F185. The differences in damage modes in these two composite material systems seems to indicate these materials were sensitive to loading rate.

6.4 Residual Compressive Strength

After the quasi-static indentation test followed by damage assessment, the residual compressive strength of each specimen was measured with the same procedure described in Section 5.2. An Instron 4206-006 screw driven testing machine with a 100-kN load cell was used to performed the compression test. A typical trace of compression test data is shown in Fig. 6.12. The data of crosshead displacement in Fig. 6.12 were not adjusted to measure the actual deformation of the specimen. The equivalent spring constant k_m need to be determined due to the different testing machine used for these compression tests. Since the main objective for this study is to measure the residual compression strength, no attempt has been made to evaluate k_m for compressive strain measurement.

The residual compressive strengths of all specimens are shown in Table 6.2 together with the damage area equivalent diameter. Due to an experimental error, the four vertical pins for specimen lateral support in the compression fixture were not used during the compression test of G30-500/F185 and G30-500/F263-2 specimens. In Figs. 6.13 and 6.14, the residual compression strength of each specimen was plotted with the residual compressive strengths after impact of each corresponding composite material system and compared to the prediction of the model (Eqs. 5.21 and 5.21). The residual compressive strengths due to quasi-static indentation load for most composite material systems, except for G30-500/F185 and S-2/8551-7A, were identical to the residual compressive strength after impact for a given damage area equivalent diameter.

In Fig. 6.13(a), even though the modes of damage were quite different in AS4/PEEK, the residual compressive strength due to quasi-static load was within the prediction of the model and the experimental results of impacted specimens. More tests are needed to determine whether the residual compressive strength can be predicted for higher damage area equivalent diameter in a specimen. The lower than expected residual compressive strength of G30-500/F185 shown in Fig. 6.13(b) might be due to premature buckling of the specimen since it was not lateral supported during the compression test. However, the residual compression strength of G30-500/F263-2 was not effected by the same testing condition.

The test result of IM7/F650 in Fig. 6.14(a) was a further indication of the applicability of Eq. 5.21 to predict the residual compressive strength for the equivalent diameter larger than the width of the compression specimen. In Fig. 6.14(b), the residual compressive strength of S-2/8551-7A was lower than the predicted strength of the model. However, it was just slightly lower than the residual compressive strength of the impacted specimen for a given equivalent diameter. More data are needed for further investigation

The experimental results from this study indicated the residual compressive strength after impact can also be simulated from a specimen with similar damage size resulted from quasi-static indentation load. It also appears that K_d was not effected by the mass of impactor since a specimen under quasi-static indentation load could also be considered to be impacted by a high mass impactor traveling at extremely low velocity.

7   Conclusions

7.1 Accomplishments

The three main objectives accomplished in this research work can be summarized as follows:

1.   An impact testing device has been set up which consists of three main components: the gas gun system, high speed data acquisition system, and high speed video camera system. The design of the gas gun system allows the performing of impact tests with the impact velocity ranging from a few meters per second to at least 264 m/s (590 MPH) using a 35 g impactor. This range of impact velocities allows the simulation of impact to aircraft structures such as dropped tool (low impact velocity), runway debris (medium impact velocity), and bird strike on rotating jet engine fan blades (high impact velocity). The main feature of the gas gun was the design of the breech loading system to minimize the time between tests by simplifying the procedure for replacement of the disposable diaphragm.

2.   A test procedure has been developed to determine the impact damage resistance of laminated composite material systems by using a small scale specimen to minimize the amount of material used in the impact test. This test procedure is suitable for testing materials which are in limited supply such as new materials under development. The impact damage resistance of a material system is characterized by the threshold impact velocity to initiate the impact damage and the damage area growth rate of the specimens.

3.   A test procedure has also been developed to determine the impact damage tolerance of laminated composite material systems by measuring the residual compressive properties after impact using a compression test fixture designed by Gurdal. The impact damage tolerance can be characterized by the reduction of residual compressive strengths after impact with the damage area equivalent diameter. These relations have been found to be linear and independent of the material properties for each composite material systems investigated in this study. A procedure

has also been developed to convert the crosshead displacement to measure the compressive strain of the specimen.

7.2 Conclusions

The conclusions may be summarized as follows:

1.   Dimple and creases were two types of impact damages observed on the front surface of the specimen after impact, whereas delamination associated with matrix cracks along the surface ply fiber direction were observed on the back surface for most material systems. Fiber fracture was the main damage mode observed on the back surface in G30-500/F185 where no delamination could be detected from the specimen surface.

2.   Matrix cracking and delamination were the main internal damage modes revealed by using penetrant enhanced X-ray and ultrasonic C-scan techniques. The matrix cracks were concentrated around the point of impact and the damage away from the point of impact was mainly delamination. Since the length of the surface matrix crack with delamination observed from the back surface was identical to the length of the delamination detected by X-ray and C-scan, the largest delamination was between the back surface $0°$ ply and the $90°$ ply beneath the surface ply. The width of the delamination could not be determined from the surface of the specimen which had to be measured from the X-ray radiograph or C-scan image.

3.   The projected area of the impact damage detected by C-scan can be used to characterize the impact damage resistance of laminated composite material systems. The damage area was observed to develop linearly with impact velocity above a certain threshold velocity. Therefore, the impact damage resistance of each material system can be ranked by the threshold velocity V_c and the damage area growth rate C. The experimental results indicated the brittle material systems had lower threshold velocity and higher damage area growth rate than the toughened material systems. The impact damage resistance was also observed to be highly dependent upon the matrix material.

4.   By measuring the equivalent spring constant of the testing machine used for compression test, the compressive strain of an impacted specimen can be calculated from the crosshead displacement using Eq. (5.8). Thus, the residual compressive modulus and the residual compressive failure strain can be determined.

5.   The compressive modulus measured from the compression test on each material system was in general 15 to 20% lower than the tensile modulus calculated from Classical Lamination Theory using the material tensile properties. This was due to the weakness of the fibers which were susceptible to bending and buckling in compression. Therefore, the compressive modulus was highly dependent upon the fiber material. For this reason, small amount of matrix cracking and delamination have been observed to have little effect on the residual compressive modulus after impact .

6.   The residual compressive strength was observed to decrease linearly with the damage area equivalent diameter which can be modeled with Eqs. (5.20) and (5.21). K_d, the rate of compressive strength reduction with respect to the damage area equivalent diameter, in Eq. (5.20) was determined to be 0.625 for the testing condition employed in this investigation, and was found to be independent of the material properties.

7.   Since the residual compressive strength in Eq. (5.20) was modeled in terms of damage size rather than the incident energy as in Caprino model, the residual compressive strength can be predicted based on the impact damage resistance and the compressive strength before impact. The effect of specimen width was also incorporated into the model where K_d was also a function of the specimen dimensions..

8.   Eq. (5.20) can also be used to model the residual compressive failure strain. Linear relations between residual compressive failure strain with damage equivalent diameter were observed for each material system.

9.   For the laminated composite material systems which are insensitive to the loading rate, the modes of damage observed on both specimens with the same *damage size* after impact and quasi-static indentation load were almost identical. Therefore,

the impact damage can be simulated by quasi-static indentation test on these material systems.

10.   The residual compressive strength after impact can also be simulated from a specimen with similar *damage size* resulting from quasi-static indentation load even if the damage in both loading conditions were quite different. Therefore, K_d was not affected by the mass of impactor in the same testing conditions since a specimen under quasi-static indentation load can be considered to be impacted by high mass impactor traveling at extremely low velocity.

7.3 Suggestions for Future Work

The experimental work presented in this dissertation was focused on the effect of different material properties on impact damage resistance and tolerance. The parameters V_c and C used to characterize impact damage resistance, and K_d to model residual compressive strength were determined from the specimens with identical stacking sequence and geometric dimensions except for some variation in laminate thickness. Further research is needed to investigate the effects on V_c, C, and K_d for different laminate stacking sequences, support conditions of the impact specimen, specimen sizes or scale effect for impact test and residual compressive strength measurement, etc.

Some preliminary experiments have been performed to investigate the thickness effects on impact damage resistance and tolerance. The laminate stacking sequences used in this investigation were base scale $[0/90/\pm45]_{2S}$, ply level scale $[0_2/90_2/45_2/-45_2]_{2S}$, and sublaminate level scale $[0/90/\pm45]_{4S}$. Both ply and sublaminate level scale laminates were used to study the thickness effects due to ply thickness and stacking sequence, respectively.

In addition to measuring the impact damage tolerance parameter through compression test, other damage tolerance parameters can also be determined by measuring the residual laminate properties with other test methods. Several possible future works include the residual tensile, flexural, and fatigue strength characterizations.

59

The test procedures developed in this research work can also be applied to other types of material systems which are not laminates. For example, the impact damage resistance of in-situ composite materials such as PEKK/HX1000, a LCP/polymer blend material, with different percentage of HX1000 concentrations has been characterized with the same testing procedure [40].
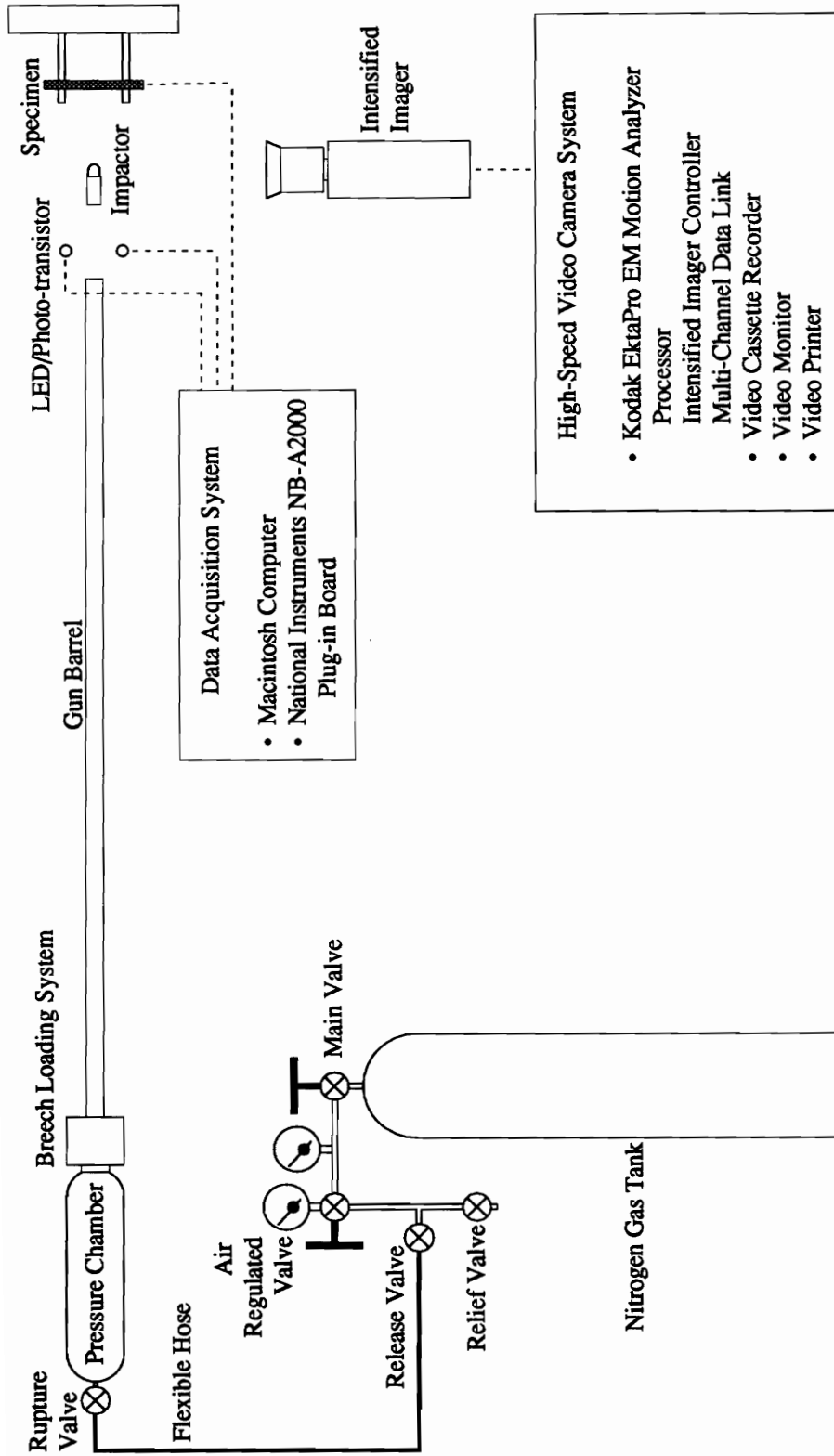
Fig. 2.1 Schematic diagram of the impact testing setup.
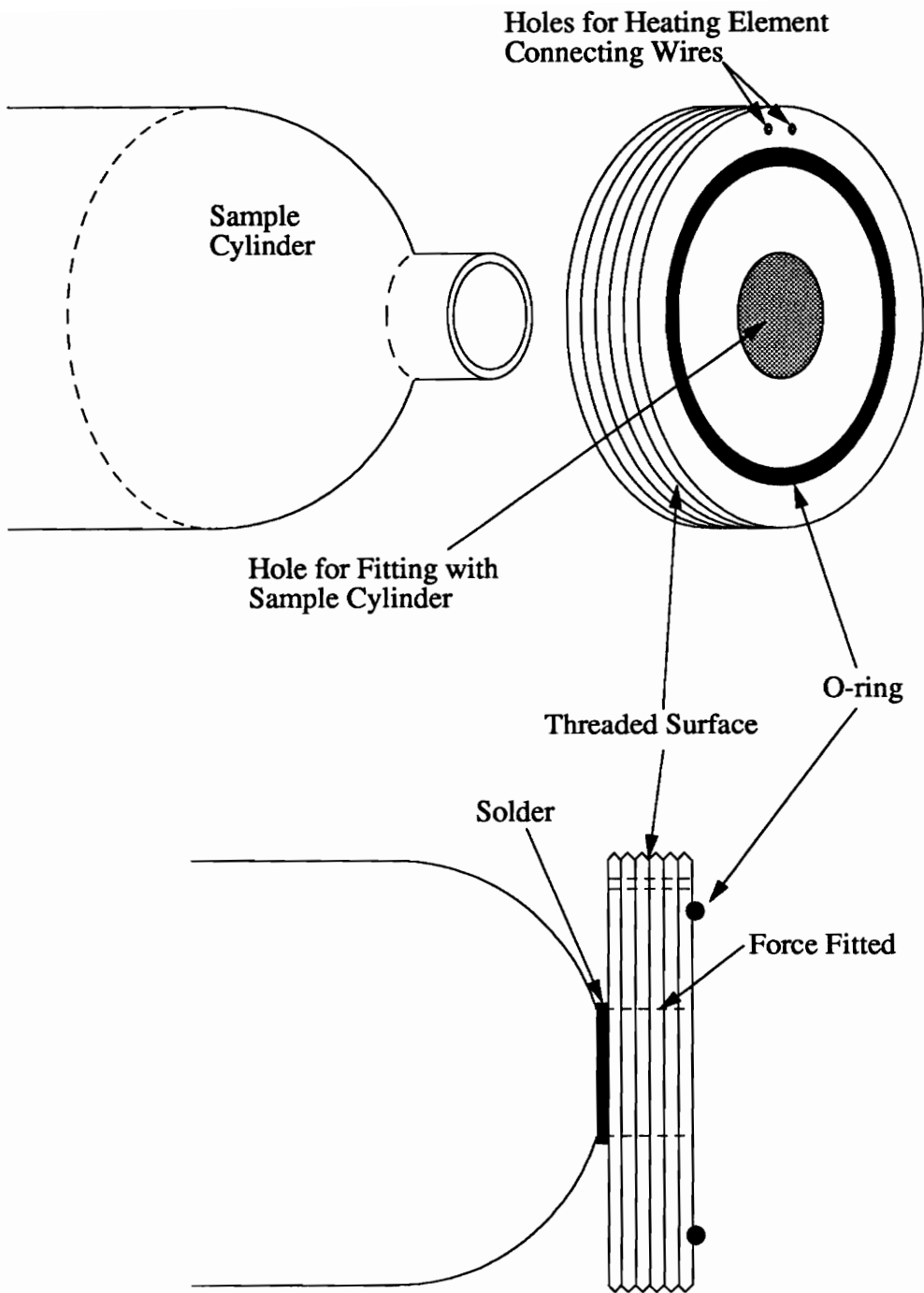
Fig. 2.2 Modification of sample cylinder for portion of breech loading system.

62

Fig. 2.3 Design of breech loading system. (a) Opened and (b) closed positions.

A   Pressure chamber
B   Heating element seat and pressure seal
C   O-ring seal
D   Disposable diaphragm
E   Gasket (Graphite/epoxy plate)
F   Barrel flange
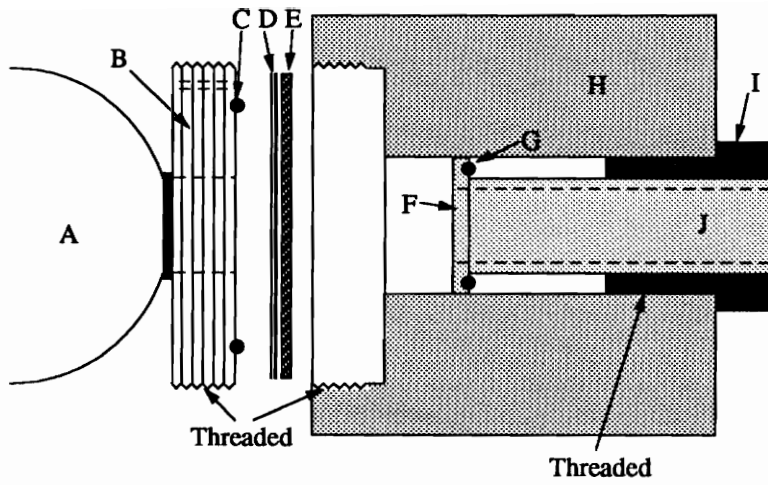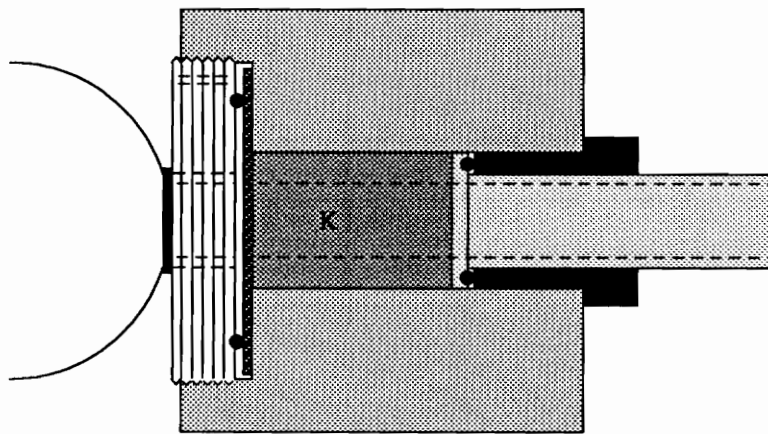
G   O-ring seal
H   Breech collar
I   Barrel pressure collar
J   Gun barrel
K   Breech spacer
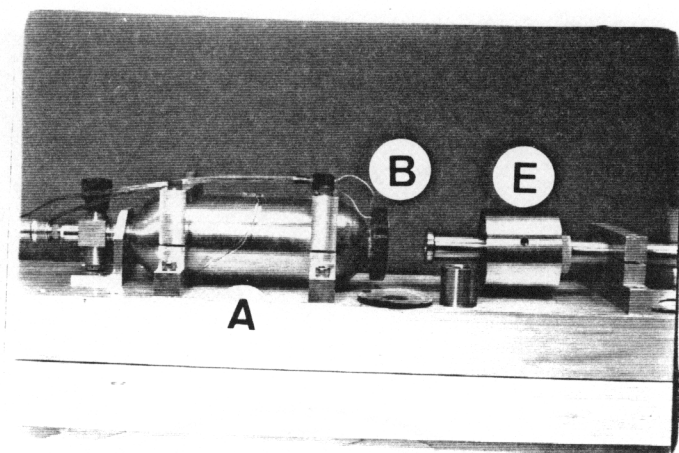
(a)
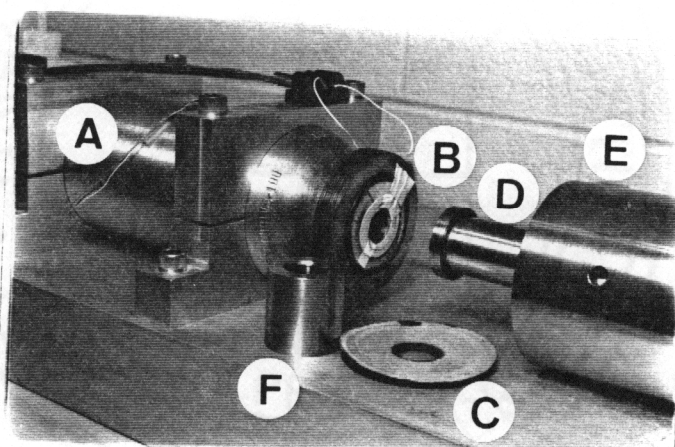
(b)

A   Pressure Chamber   D   Gun barrel
B   Heating element seat and pressure seal   E   Breech collar
C   Disposable diaphragm   F   Breech spacer

Fig. 2.4 Details of the breech loading system.
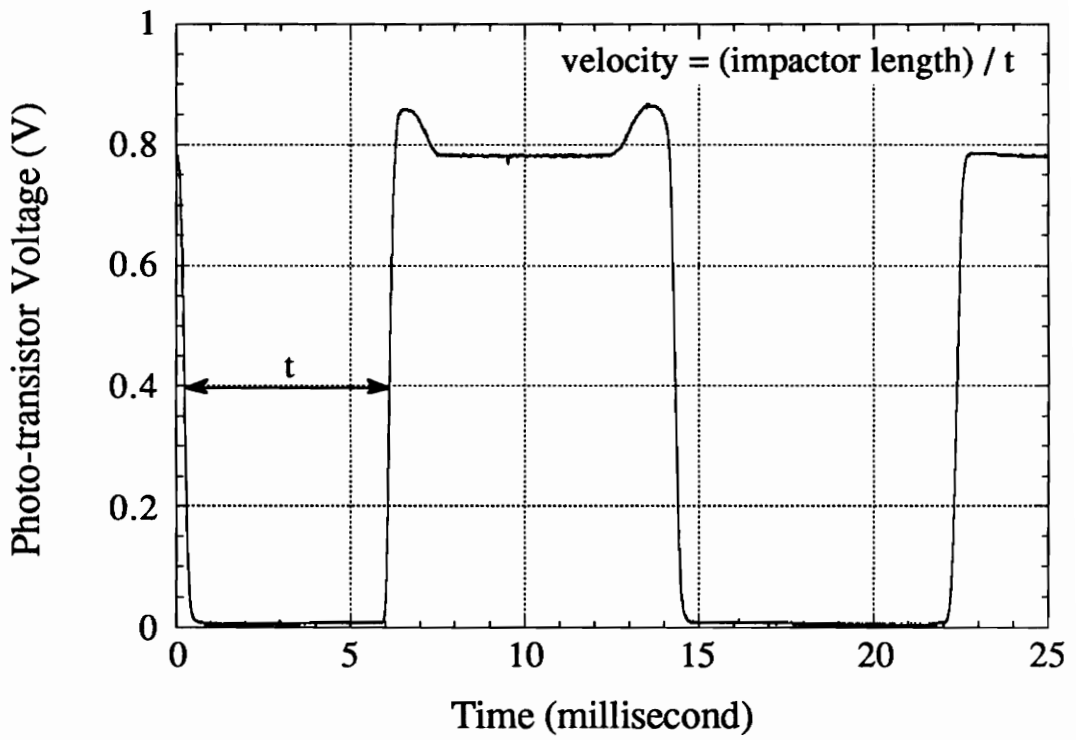
Fig. 2.5 Impactor velocity measurement. A typical photo-transistor voltage output as the impactor passed between the LED and photo-transistor.
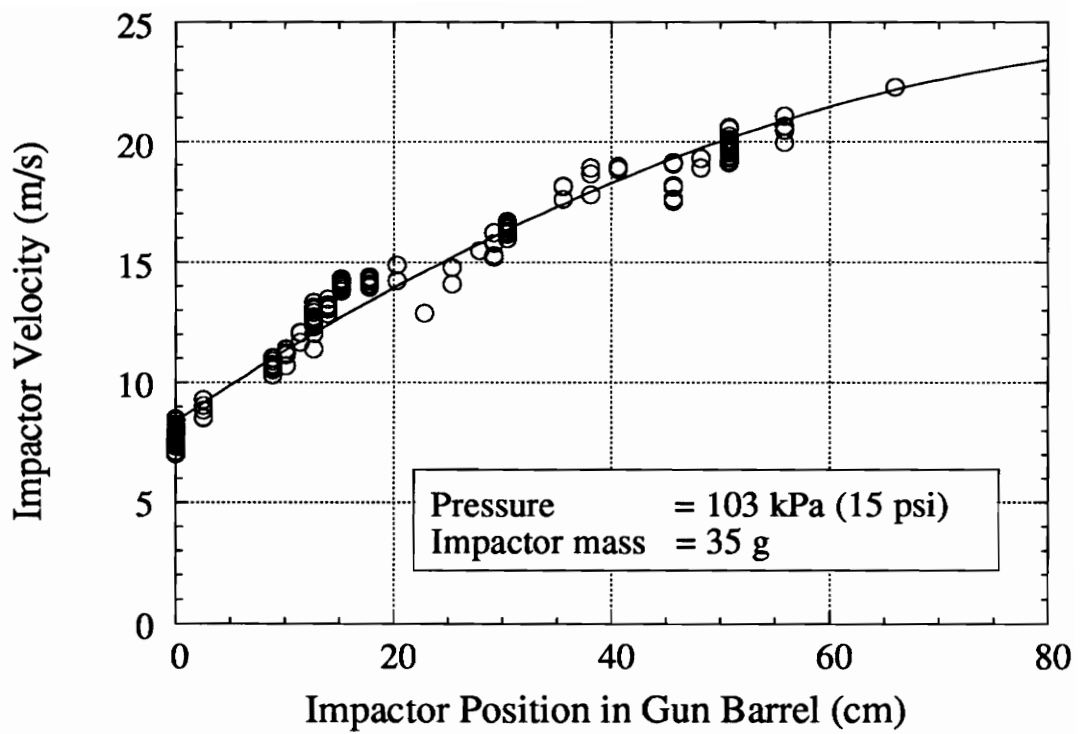
Fig. 2.6 Velocity calibration curve using 103 kPa of pressure in pressure chamber.
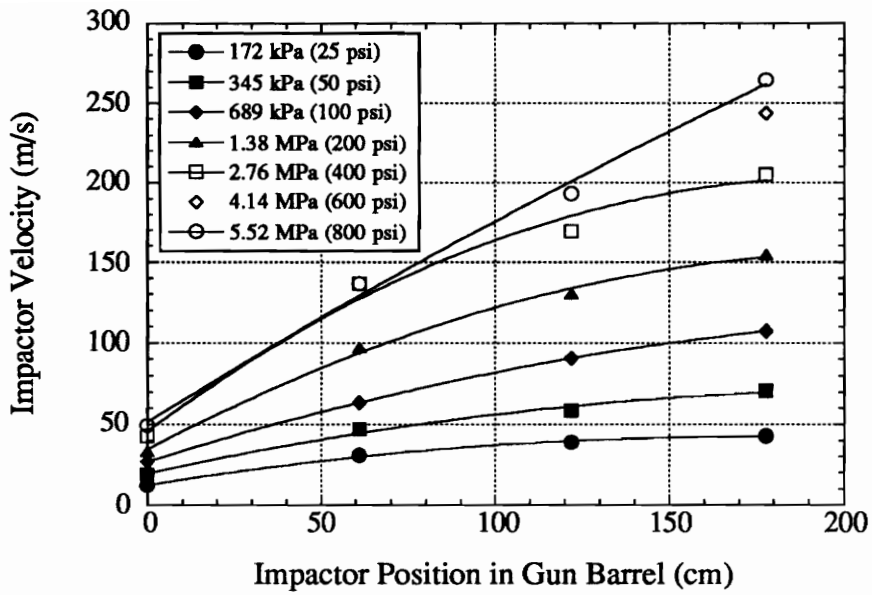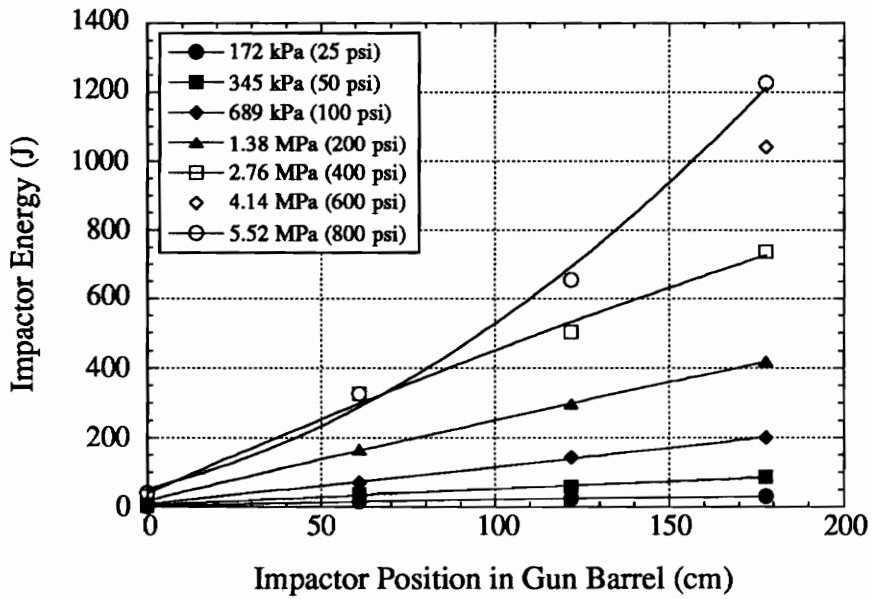
Fig. 2.7 High velocity gas gun calibration curves: Variation of (a) impactor velocity and (b) kinetic energy with impactor position in gun barrel for various pressure level.
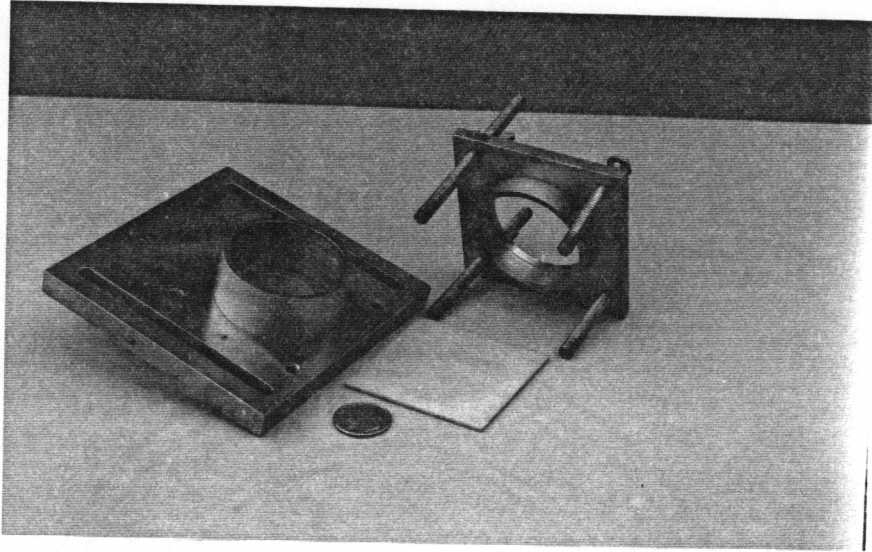
(a)
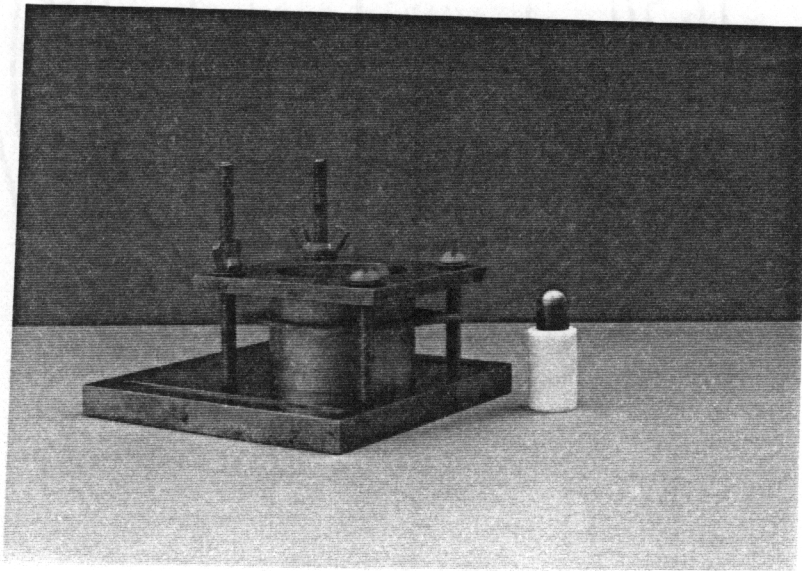
(b)

Fig. 3.1 Fixture for holding the impact test specimen. The impactor is shown to the right of the fixture in photograph (b).
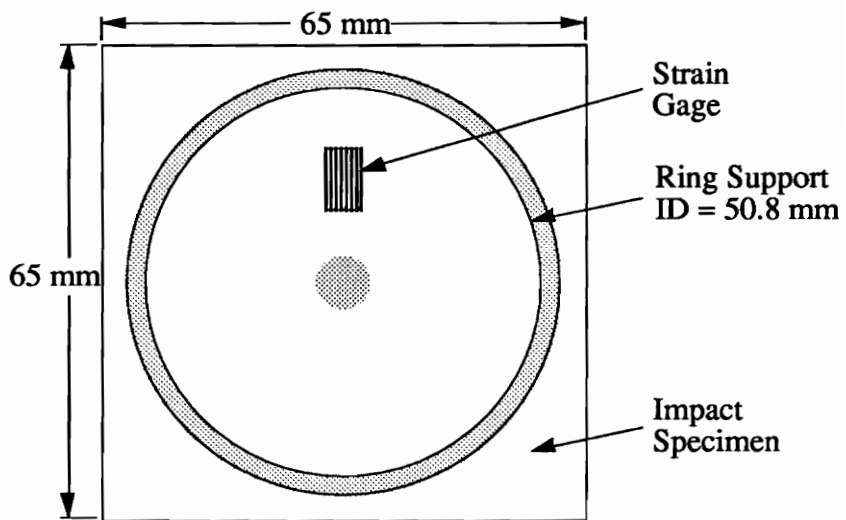
Fig. 3.2 Dimensions of the impact specimen.
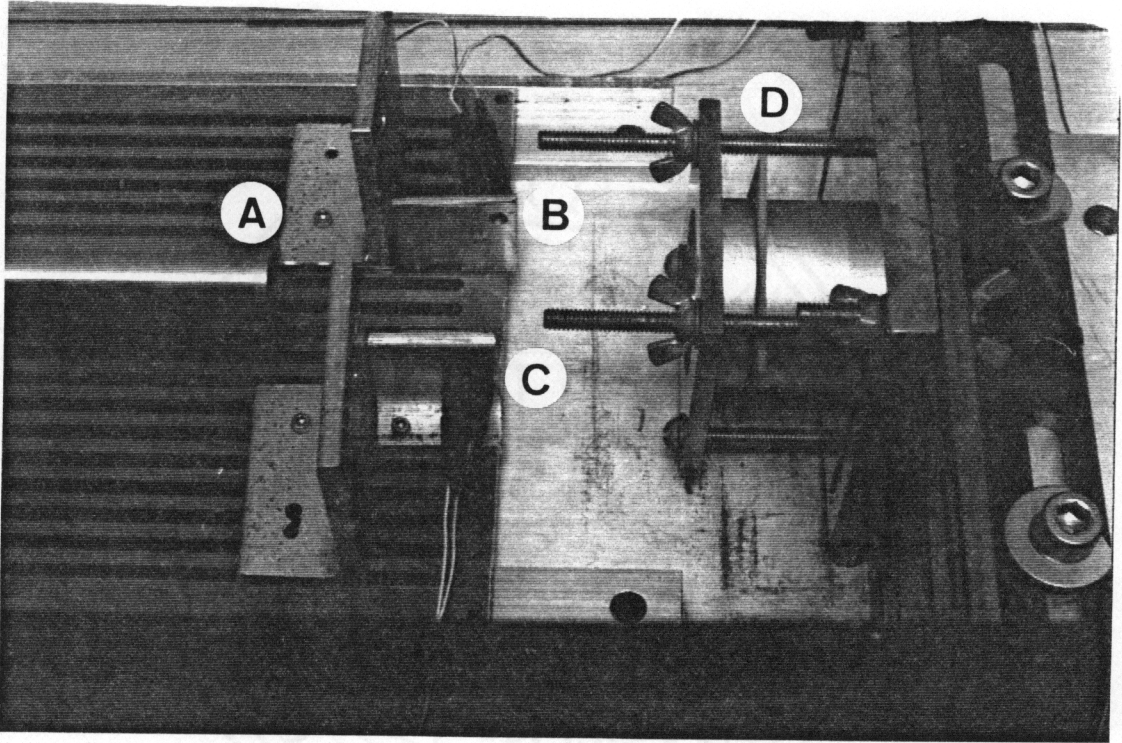
A Barrel end
B LED

C Photo-transistor
D Specimen

Fig. 3.3 Impact test specimen setup.
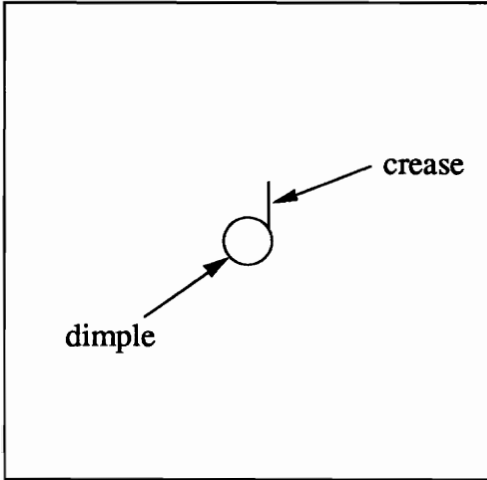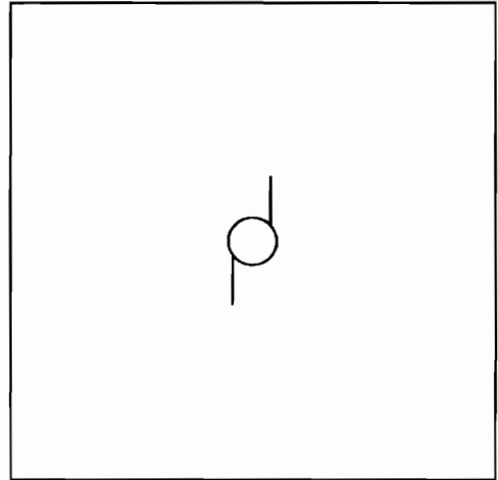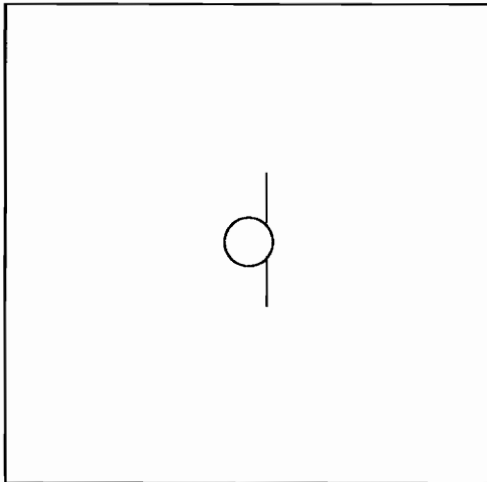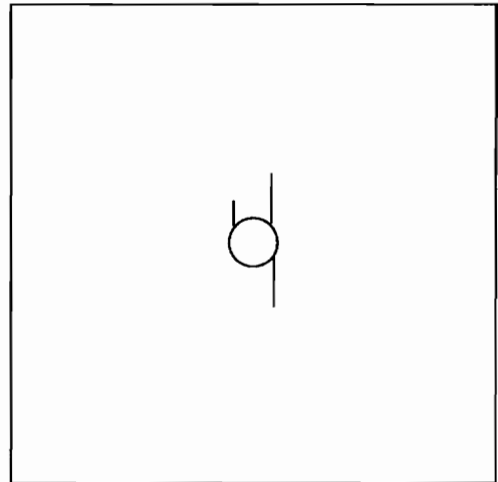
Fig. 3.4 Front surface creases formation around the indentation of the impacted specimen. Surface ply fiber orientation is in horizontal direction.

71
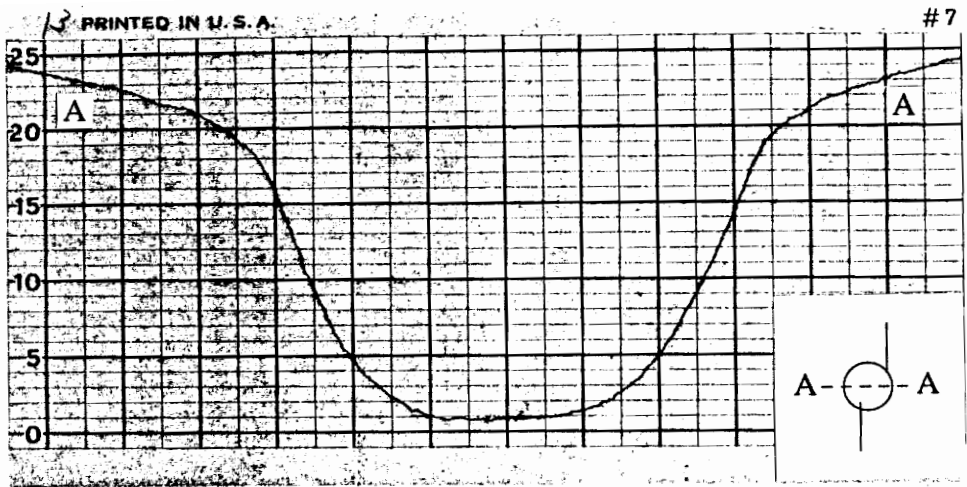
(a)
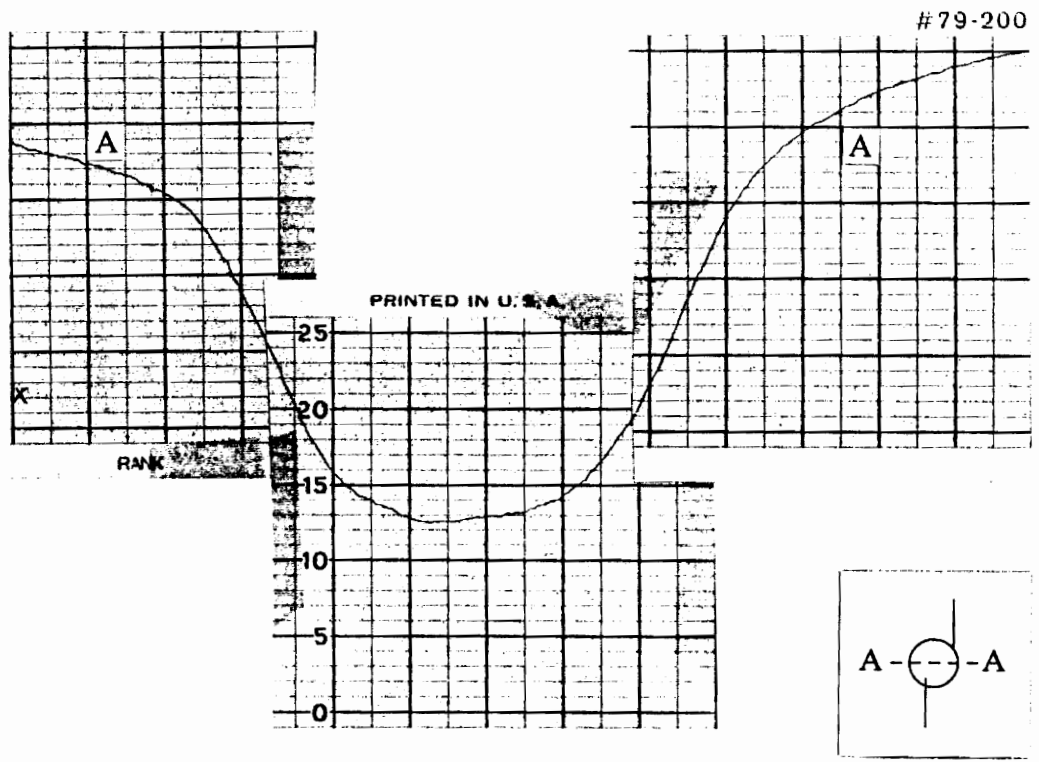
(b)

Fig. 3.5 Talysurf measurement of a dimple on AS4/PEEK specimen surface after impact. Impact velocity = (a) 12.0 m/s, (b) 12.1 m/s. (Vertical magnification: 500X, horizontal magnification: 20X)
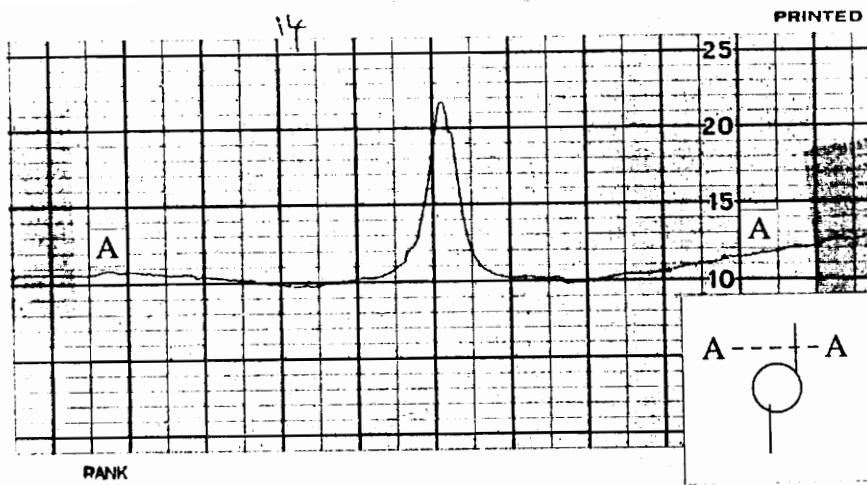
(a)
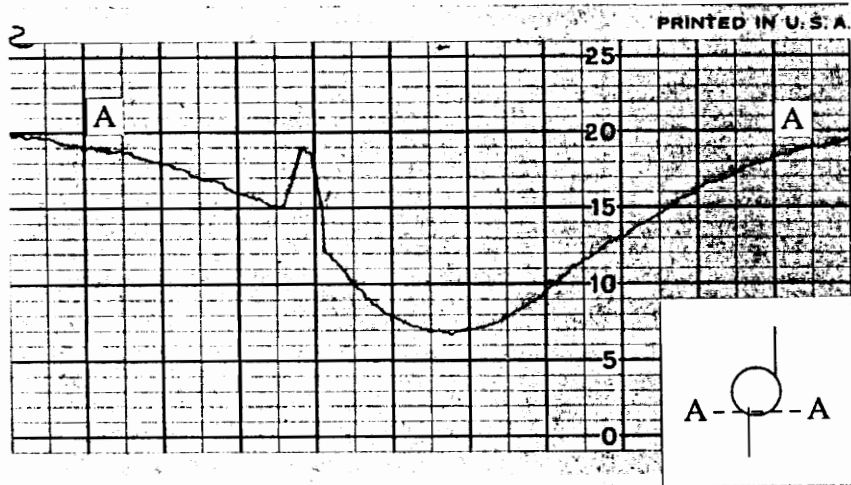
(b)

Fig. 3.6 Talysurf measurement of a crease (a) outside and (b) inside the dimple on AS4/PEEK specimen after impact. Impact velocity = (a) 17.5 m/s, (b) 12.9 m/s. (Vertical magnification: 500X, horizontal magnification: 20X)
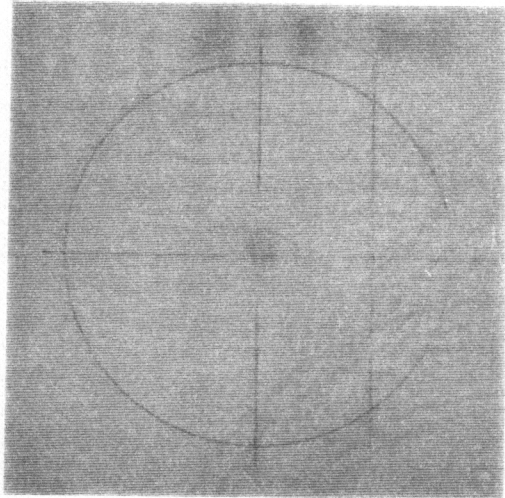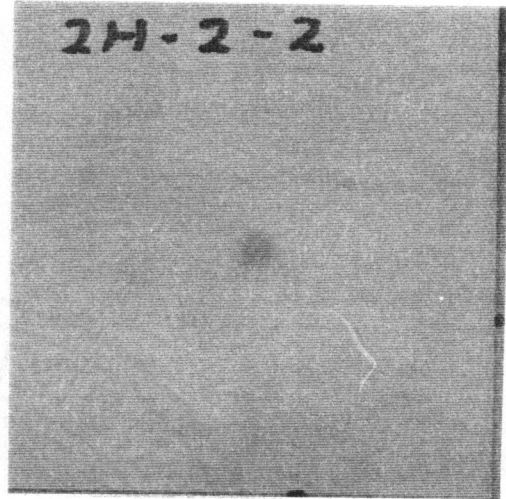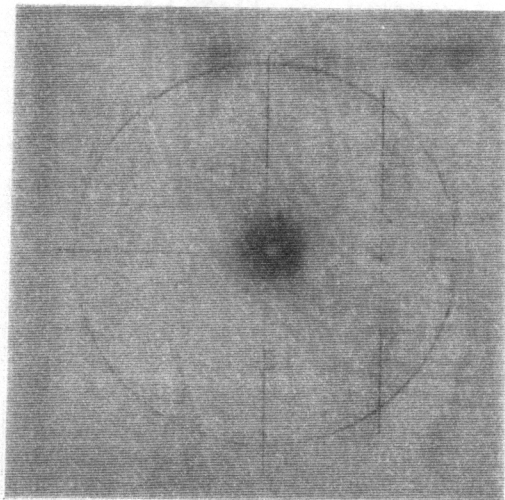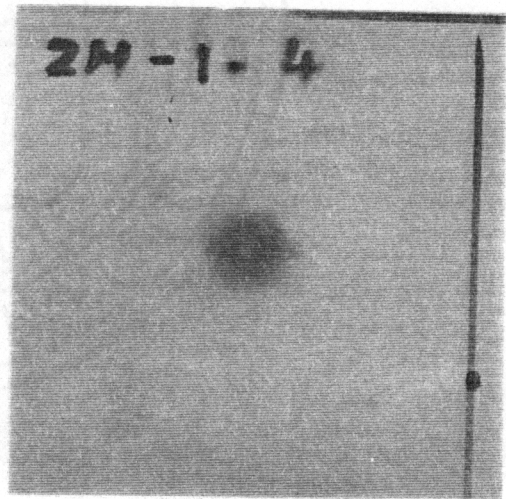
Fig. 3.7 Impact damage in S-2/8551-7A specimens observed in front of a light source.
Impact velocity = 8.1 m/s : (a) front view, (b) back view;
Impact velocity = 14.4 m/s : (c) front view, (d) back view.
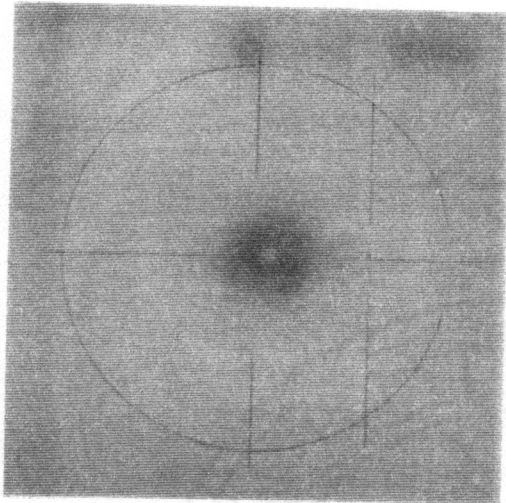
(a)
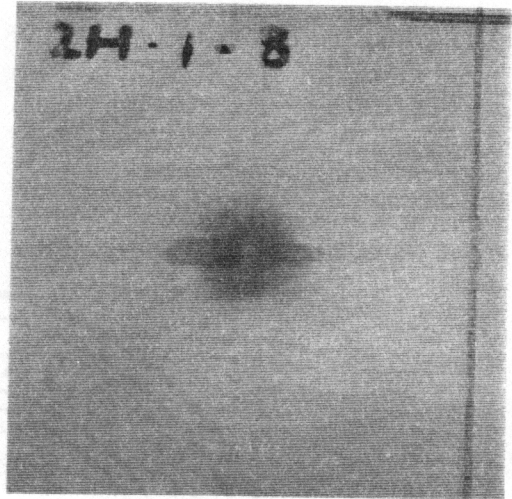
(b)
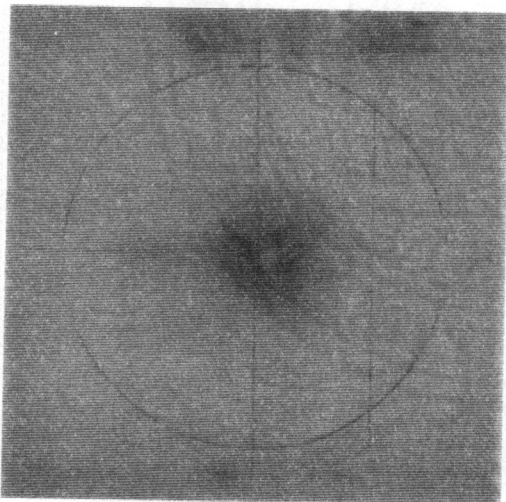
(c)
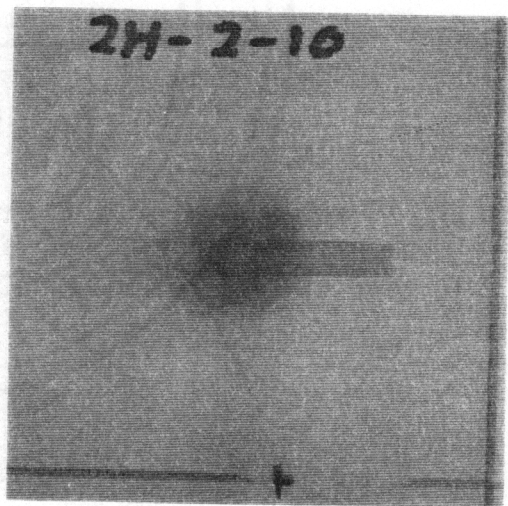
(d)

Fig. 3.8 Impact damage in S-2/8551-7A specimens observed in front of a light source.
Impact velocity = 19.9 m/s : (a) front view, (b) back view;
Impact velocity = 25.9 m/s : (c) front view, (d) back view.

75
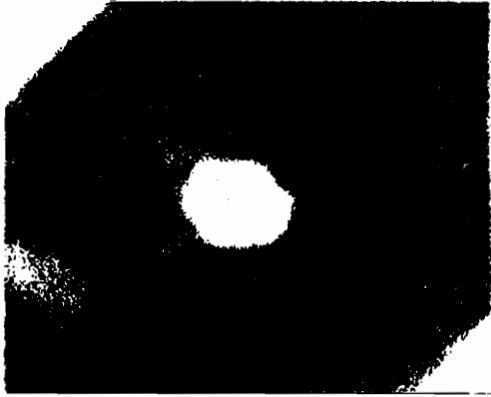
(a)

(b)

(c)

(d)

Fig. 4.1 Ultra-sonic C-scan images of AS4/3502 specimens impacted with velocities of (a) 7.3 m/s, (b) 10.3 m/s, (c) 12.8 m/s, and (d) 14.2 m/s.
The surface 0° ply is in horizontal direction.
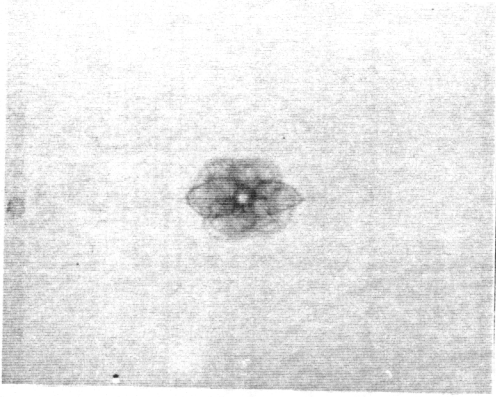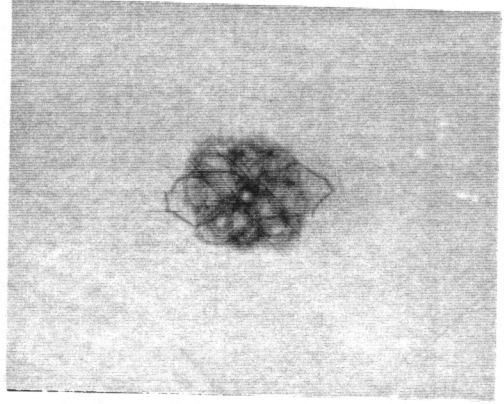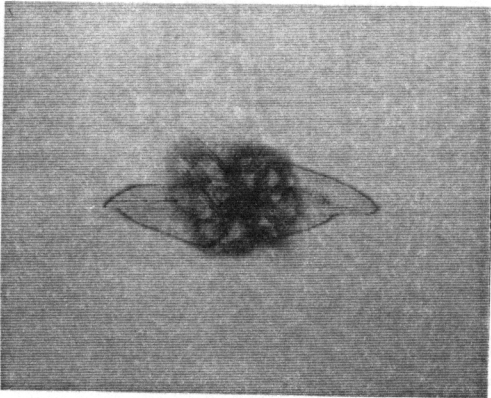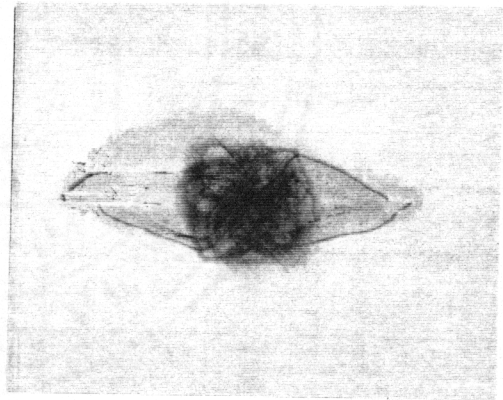
Fig. 4.2 X-ray radiographs of AS4/3502 specimens impacted with velocities of (a) 7.3 m/s, (b) 10.3 m/s, (c) 12.8 m/s, and (d) 14.2 m/s. The surface 0° ply is in horizontal direction.
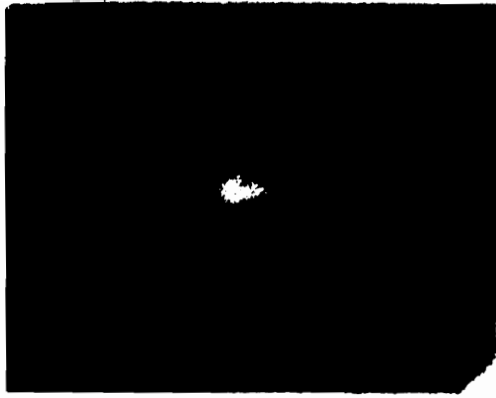
(a)
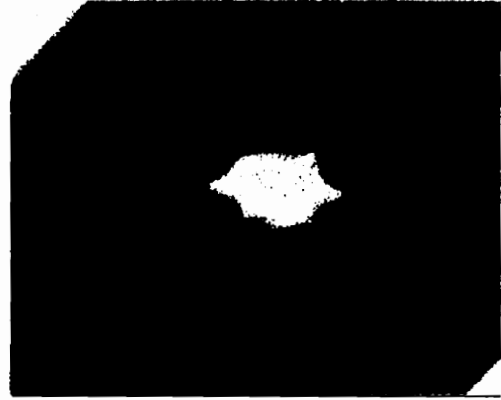
(b)
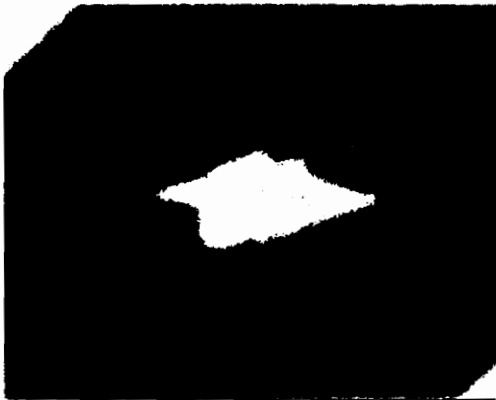
(c)
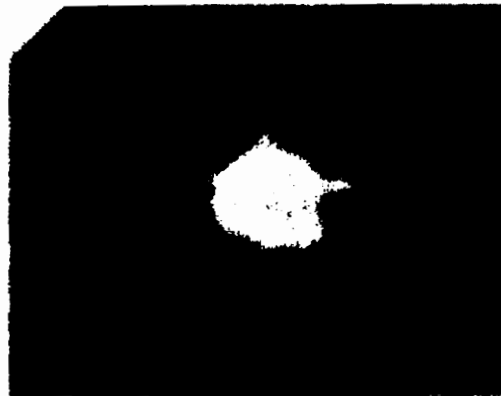
(d)

Fig. 4.3 Ultra-sonic C-scan images of AS4/PEEK specimens impacted with velocities of (a) 12.0 m/s, (b) 15.3 m/s, (c) 18.1 m/s, and (d) 19.3 m/s. The surface 0° ply is in horizontal direction.
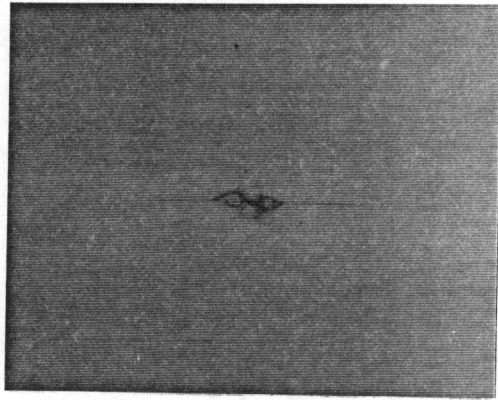
(a)
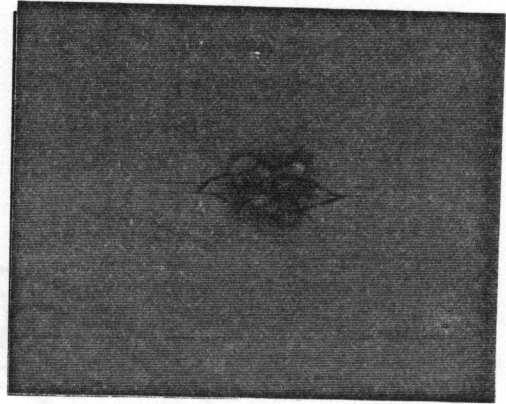
(b)
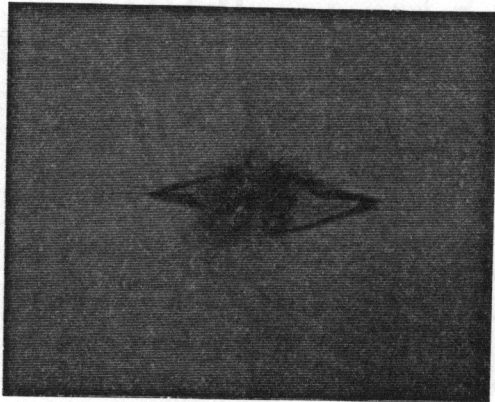
(c)
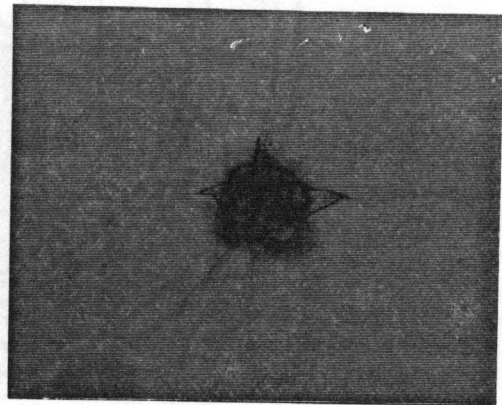
(d)

Fig. 4.4 X-ray radiographs of AS4/PEEK specimens impacted with velocities of (a) 12.0 m/s, (b) 15.3 m/s, (c) 18.1 m/s, and (d) 19.3 m/s. The surface 0° ply is in horizontal direction.

(a)

(b)

(c)

(d)
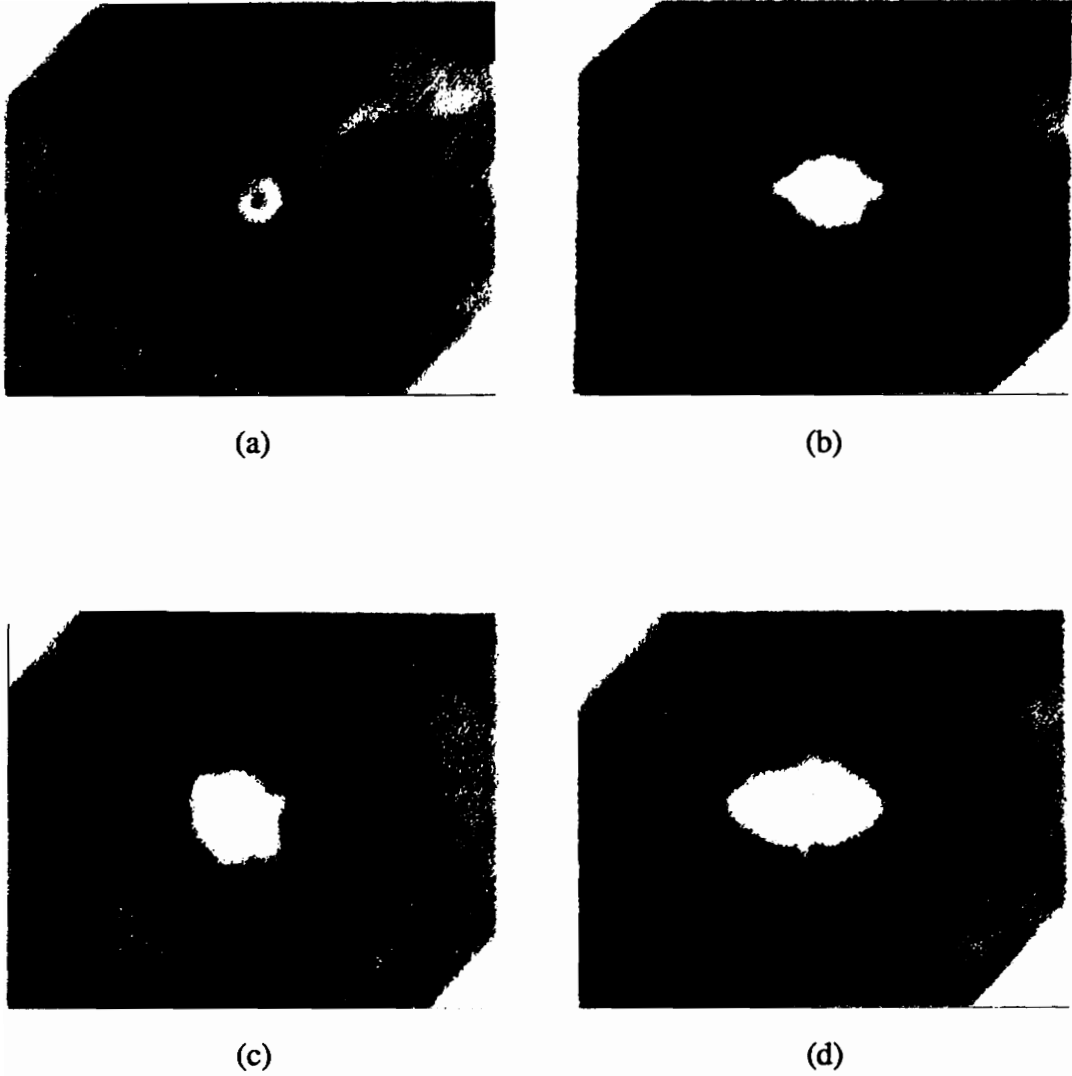
Fig. 4.5 Ultra-sonic C-scan images of G30-500/F185 specimens impacted with velocities of (a) 12.6 m/s, (b) 16.0 m/s, (c) 19.0 m/s, and (d) 20.5 m/s. The surface 0° ply is in horizontal direction.
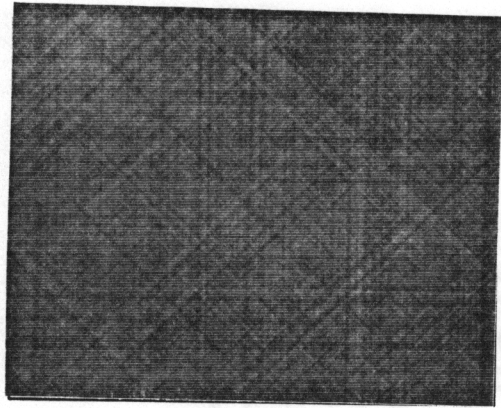
(a)
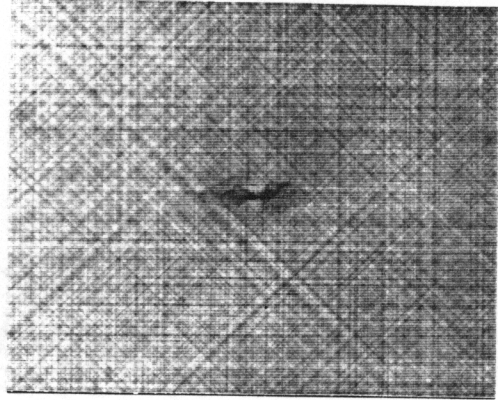
(b)
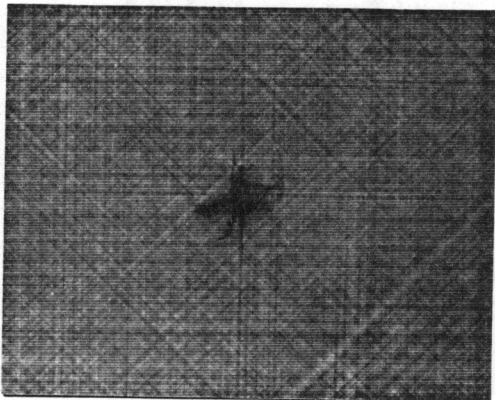
(c)
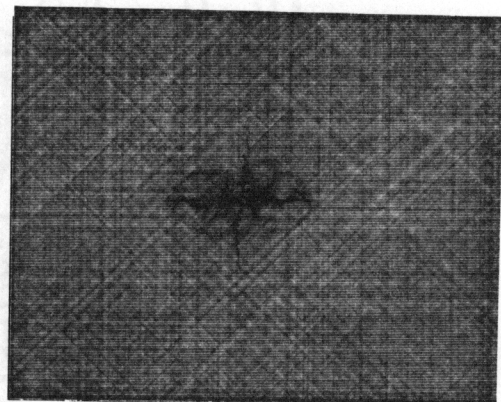
(d)

Fig. 4.6 X-ray radiographs of G30-500/F185 specimens impacted with velocities of
(a) 12.6 m/s, (b) 16.0 m/s, (c) 19.0 m/s, and (d) 20.5 m/s.
The surface 0° ply is in horizontal direction.
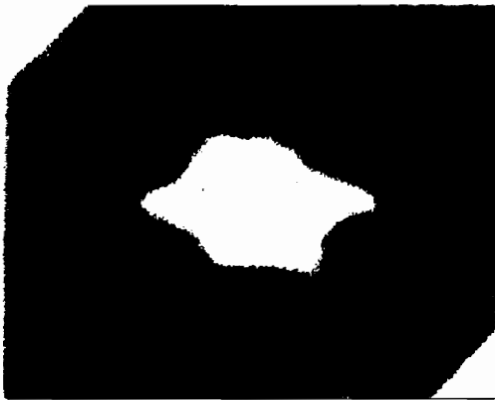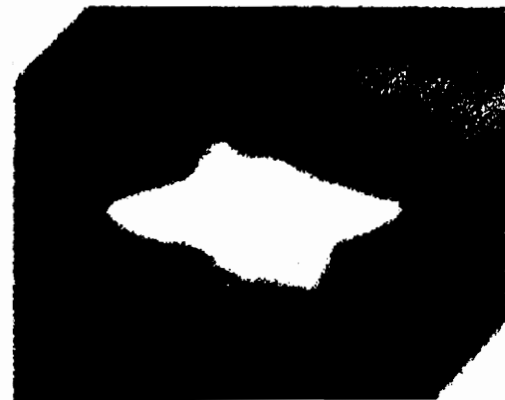
Fig. 4.7 Ultra-sonic C-scan images of G30-500/F263-2 specimens impacted with velocities of (a) 7.5 m/s, (b) 10.7 m/s, (c) 12.9 m/s, and (d) 14.9 m/s. The surface 0° ply is in horizontal direction.
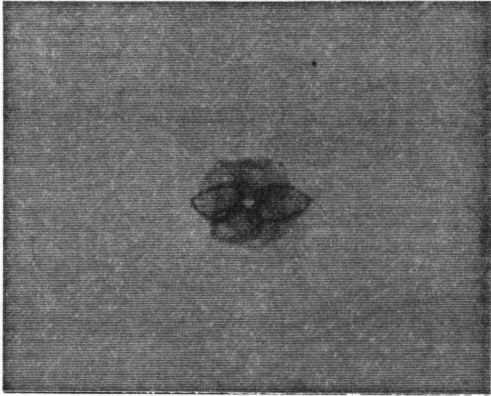
(a)
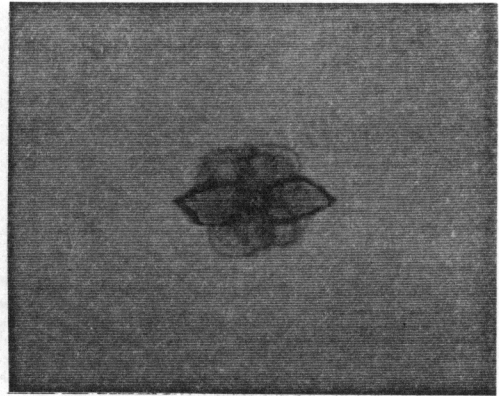
(b)
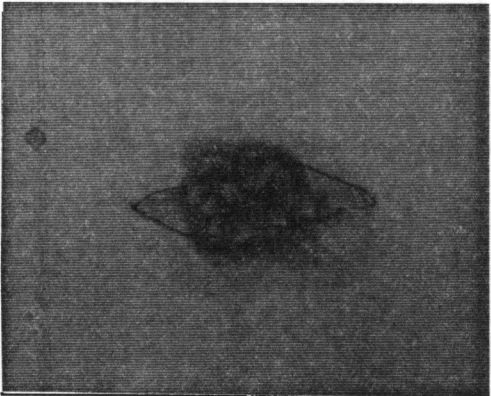
(c)
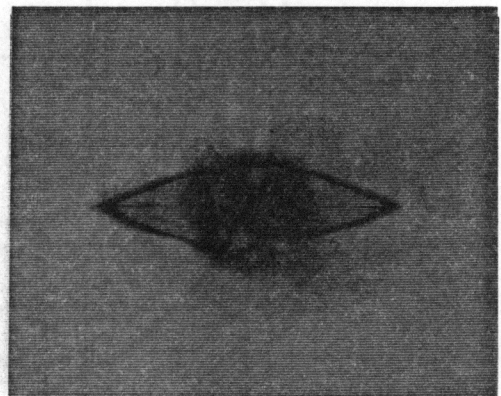
(d)

Fig. 4.8 X-ray radiographs of G30-500/F263-2 specimens impacted with velocities of (a) 7.5 m/s, (b) 10.7 m/s, (c) 12.9 m/s, and (d) 14.9 m/s. The surface 0° ply is in horizontal direction.

83
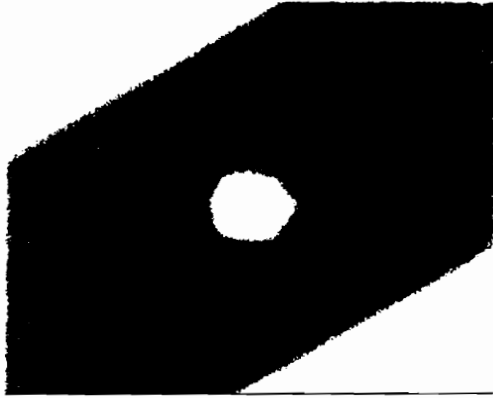
(a)
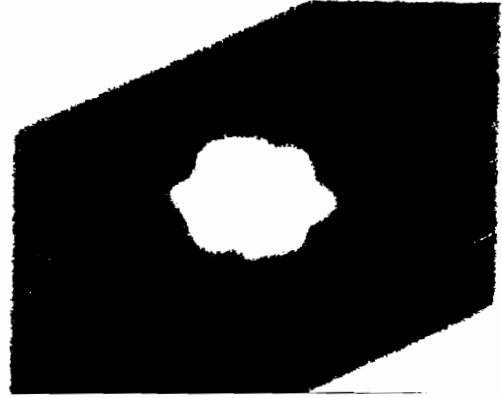
(b)

(c)

(d)

Fig. 4.9 Ultra-sonic C-scan images of IM7/F650 specimens impacted with velocities of (a) 5.5 m/s, (b) 7.8 m/s, (c) 11.0 m/s, and (d) 13.9 m/s.
The surface 0° ply is in horizontal direction.

84

(a)
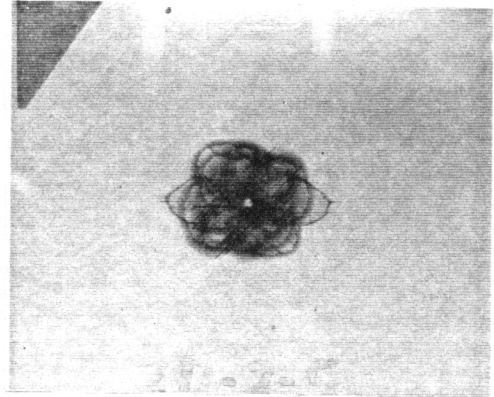
(b)
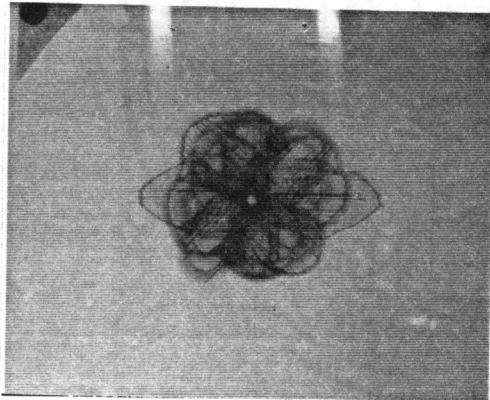
(c)
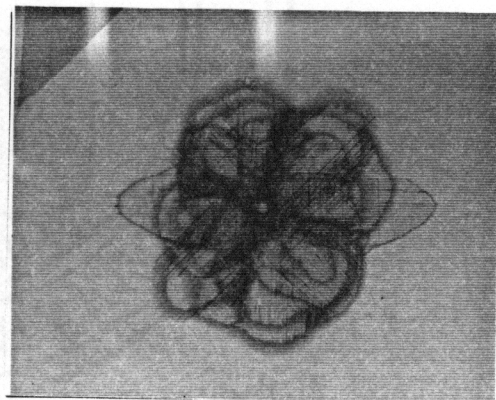
(d)

Fig. 4.10 X-ray radiographs of IM7/F650 specimens impacted with velocities of (a) 5.5 m/s, (b) 7.8 m/s, (c) 11.0 m/s, and (d) 13.9 m/s. The surface 0° ply is in horizontal direction.
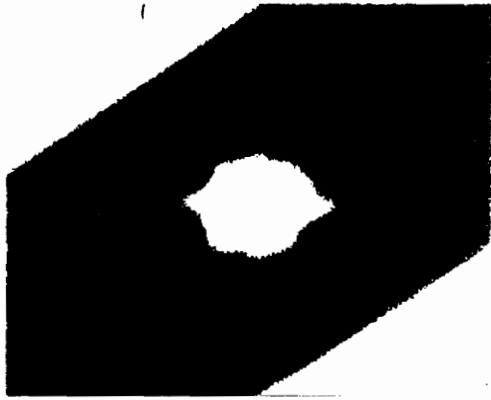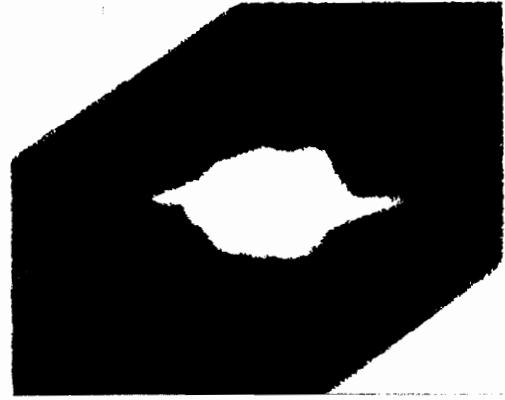
Fig. 4.11 Ultra-sonic C-scan images of IM7/F655 specimens impacted with velocities of (a) 13.8 m/s, (b) 17.6 m/s, (c) 18.8 m/s, and (d) 20.1 m/s. The surface 0° ply is in horizontal direction.
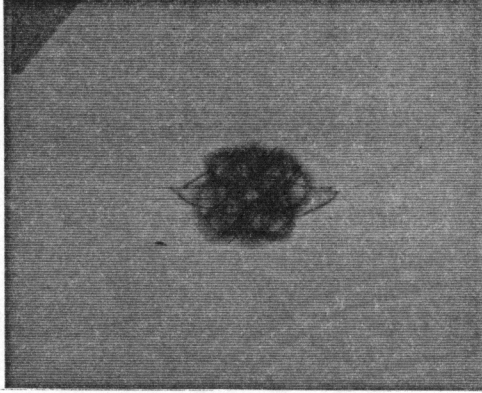
(a)
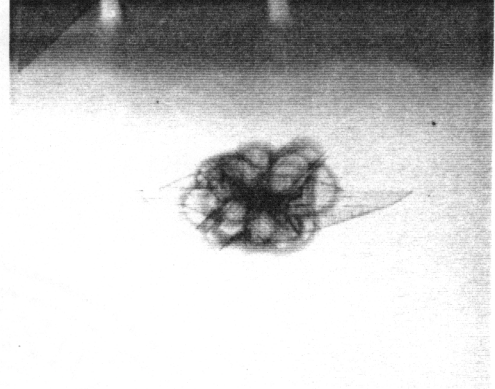
(b)
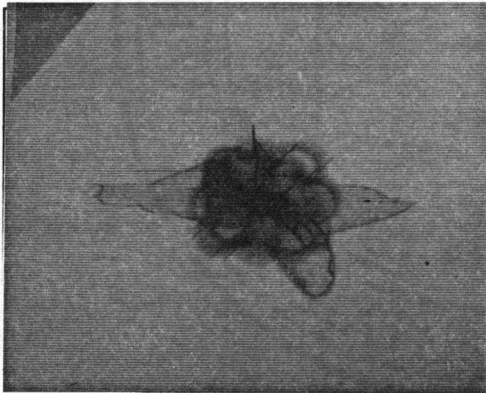
(c)
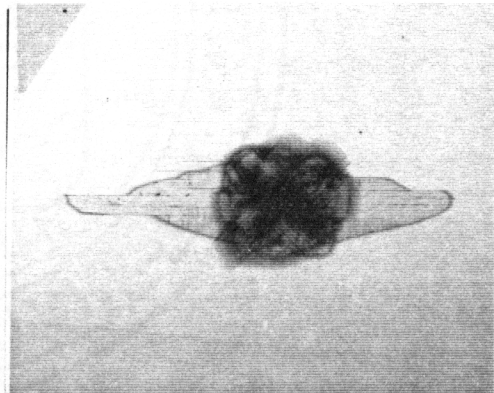
(d)

Fig. 4.12 X-ray radiographs of IM7/F655 specimens impacted with velocities of (a) 13.8 m/s, (b) 17.6 m/s, (c) 18.8 m/s, and (d) 20.1 m/s. The surface 0° ply is in horizontal direction.
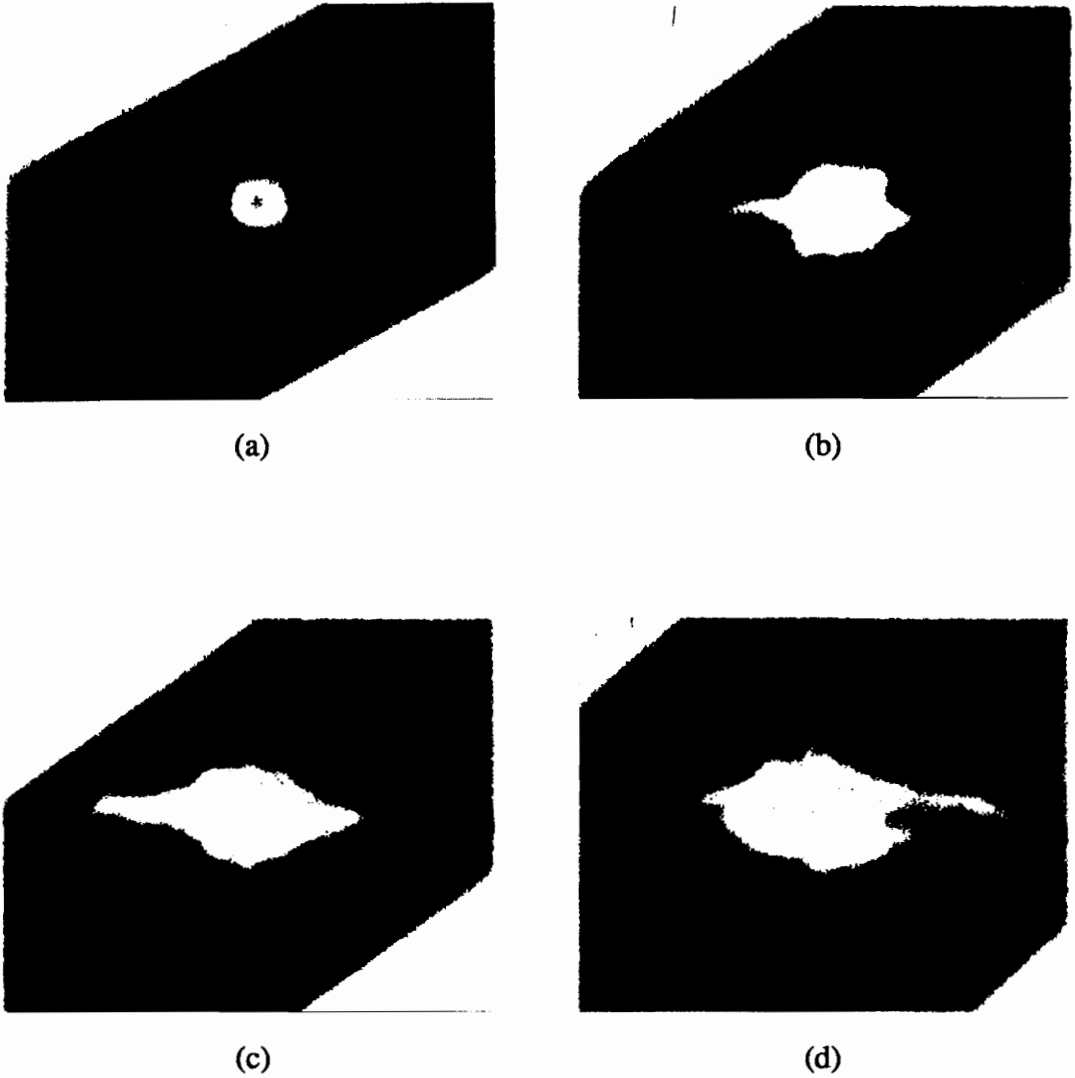
Fig. 4.13 Ultra-sonic C-scan images of IM7/F655-2 specimens impacted with velocities of (a) 12.7 m/s, (b) 16.7 m/s, (c) 19.5 m/s, and (d) 22.3 m/s. The surface 0° ply is in horizontal direction.
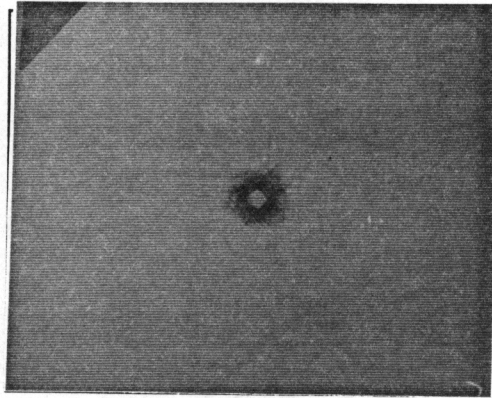
(a)
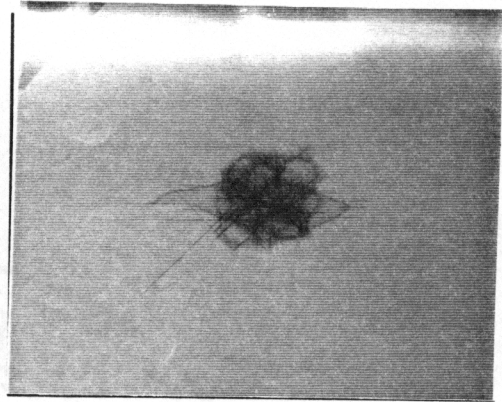
(b)
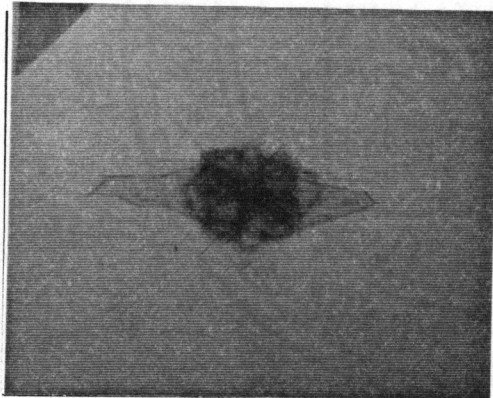
(c)
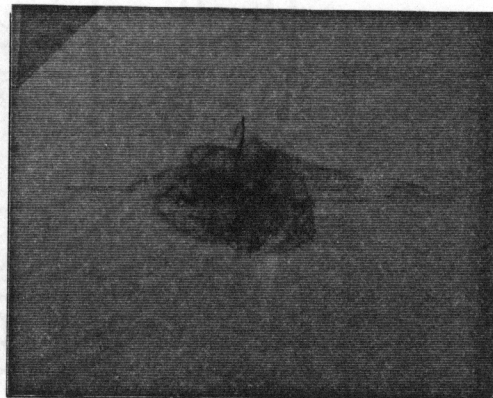
(d)

Fig. 4.14 X-ray radiographs of IM7/F655-2 specimens impacted with velocities of (a) 12.7 m/s, (b) 16.7 m/s, (c) 19.5 m/s, and (d) 22.3 m/s. The surface 0° ply is in horizontal direction.
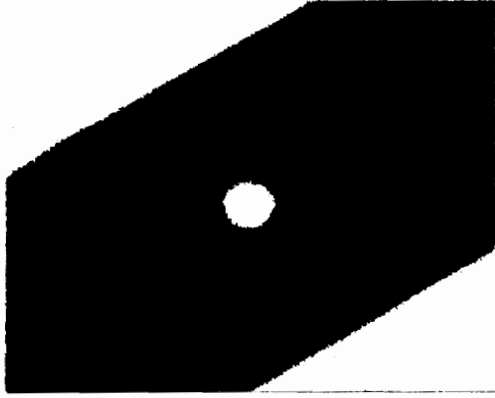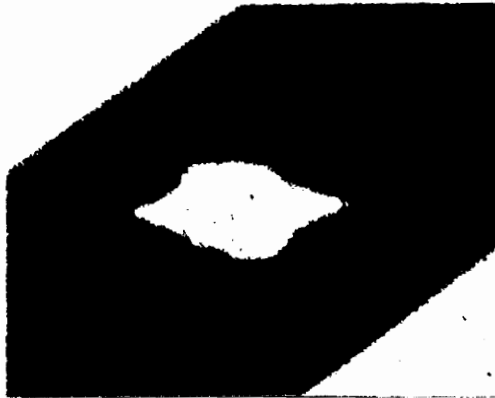
Fig. 4.15 Ultra-sonic C-scan images of IM7/8551-7A specimens impacted with velocities of (a) 8.3 m/s, (b) 12.7 m/s, (c) 16.5 m/s, and (d) 20.6 m/s. The surface 0° ply is in horizontal direction.
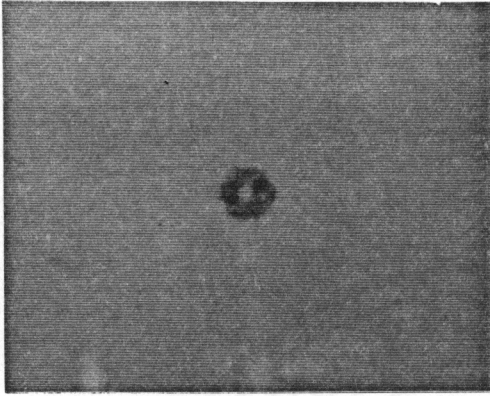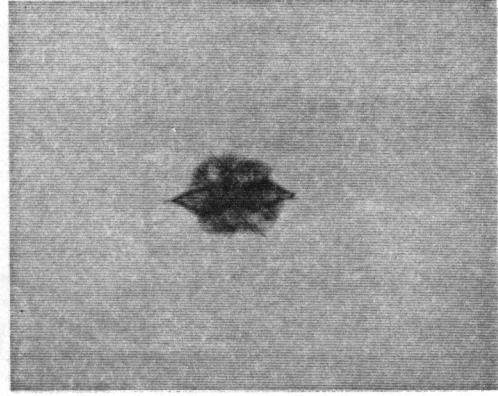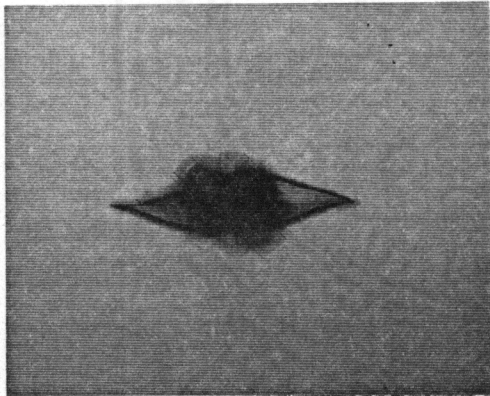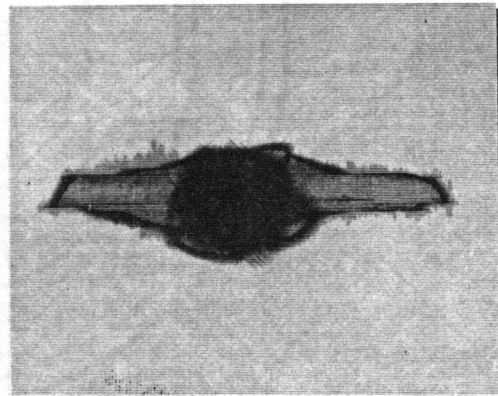
Fig. 4.16 X-ray radiographs of IM7/8551-7A specimens impacted with velocities of (a) 8.3 m/s, (b) 12.7 m/s, (c) 16.5 m/s, and (d) 20.6 m/s. The surface 0° ply is in horizontal direction.

(a)

(b)

(c)

(d)
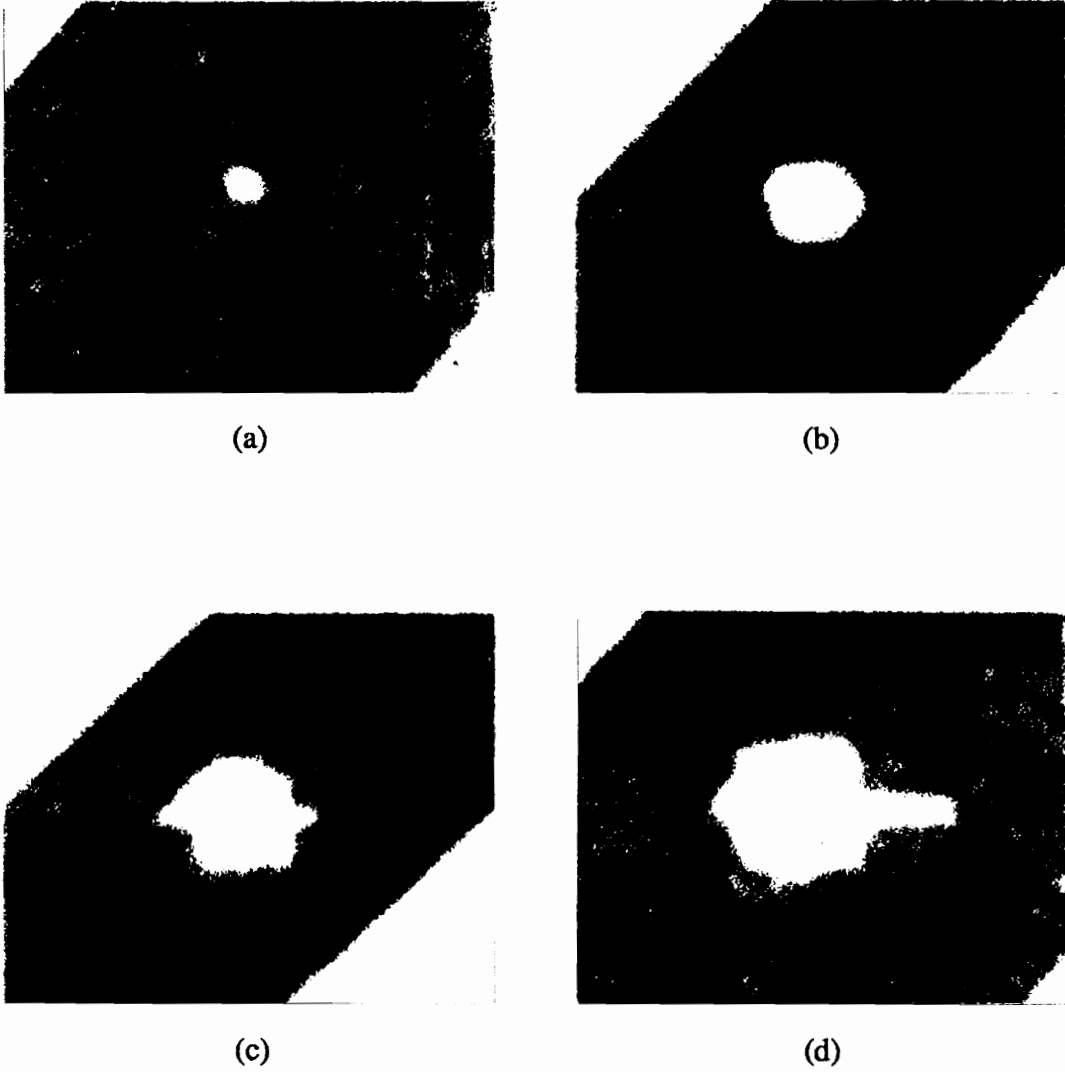
Fig. 4.17 Ultra-sonic C-scan images of S-2/8551-7A specimens impacted with velocities of (a) 8.1 m/s, (b) 14.4 m/s, (c) 19.9 m/s, and (d) 25.9 m/s. The surface 0° ply is in horizontal direction.
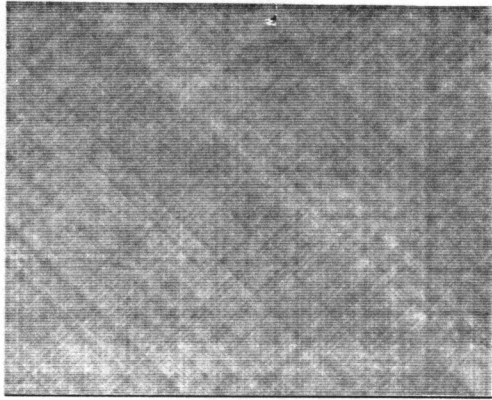
(a)
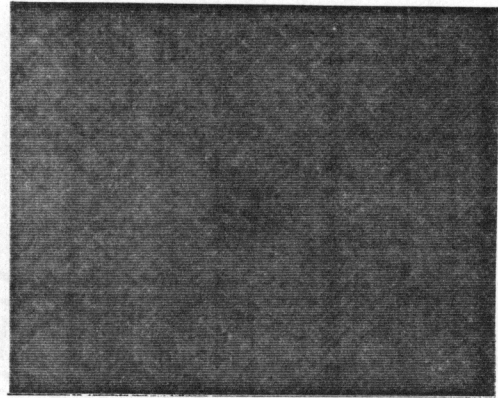
(b)
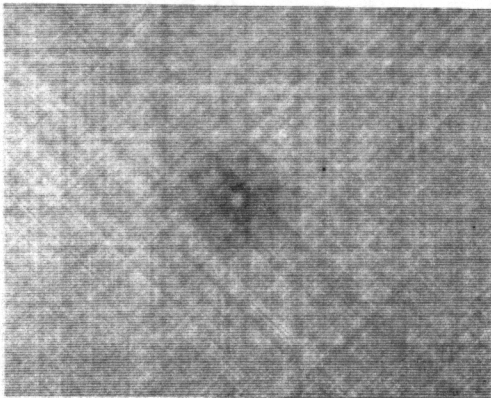
(c)
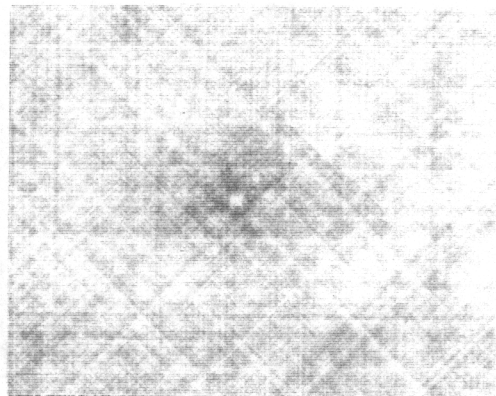
(d)

Fig. 4.18 X-ray radiographs of S-2/8551-7A specimens impacted with velocities of (a) 8.1 m/s, (b) 14.4 m/s, (c) 19.9 m/s, and (d) 25.9 m/s. The surface 0° ply is in horizontal direction.
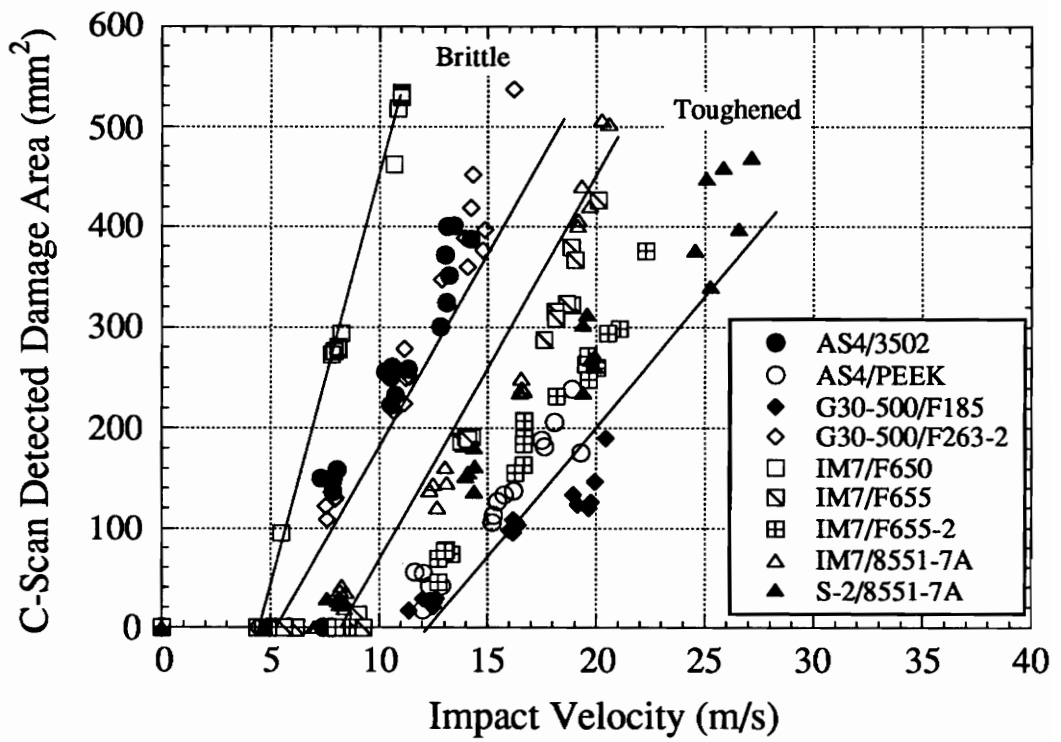
Fig. 4.19 Variation of C-scan detected damage area with impact velocity for each material system.
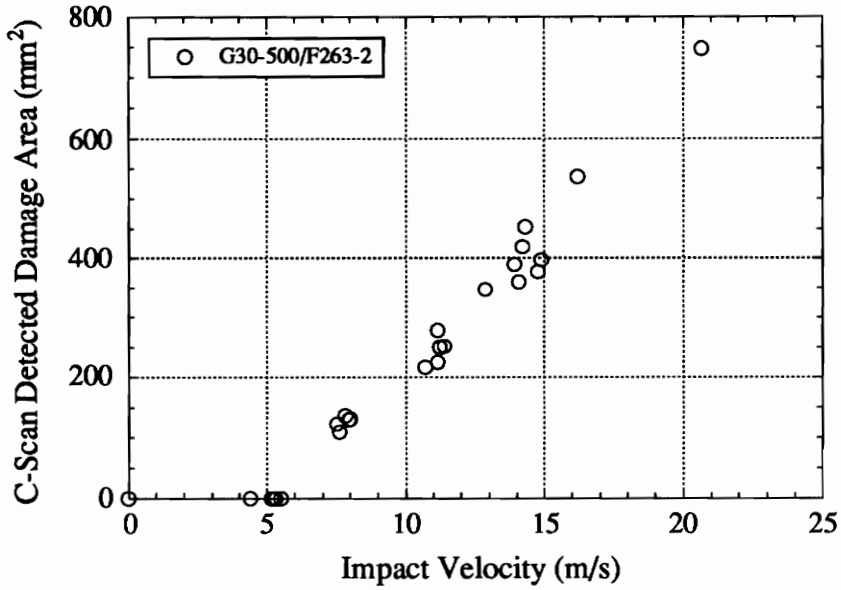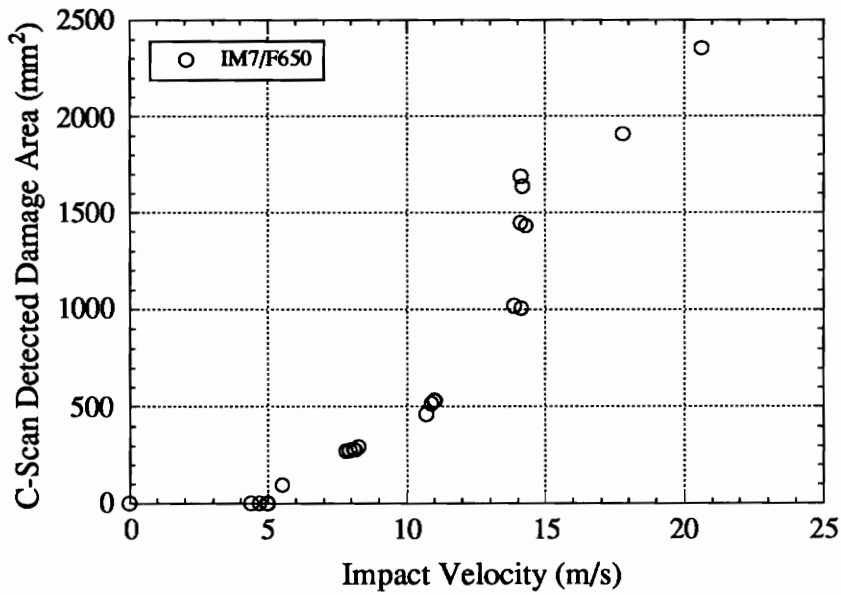
Fig. 4.20 Variation of C-scan detected damage area with incident energy for (a) G30-500/F263-2 and (b) IM7/F650.
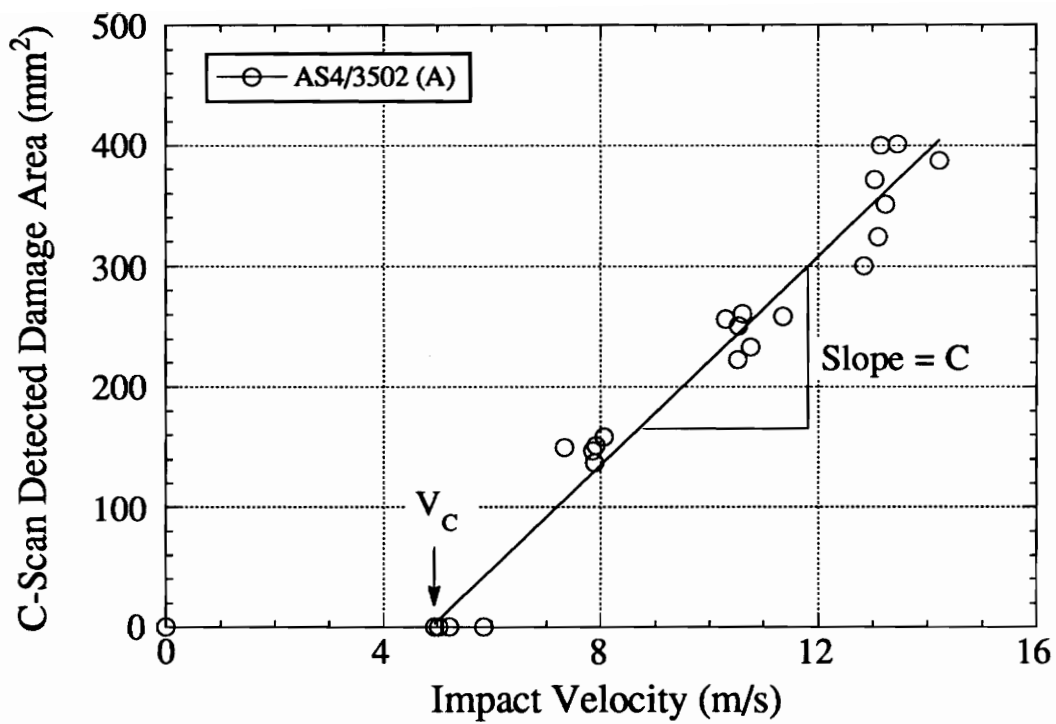
Fig. 4.21 Example of linear curve fitting to the damage area - impact velocity data for AS4/3502.
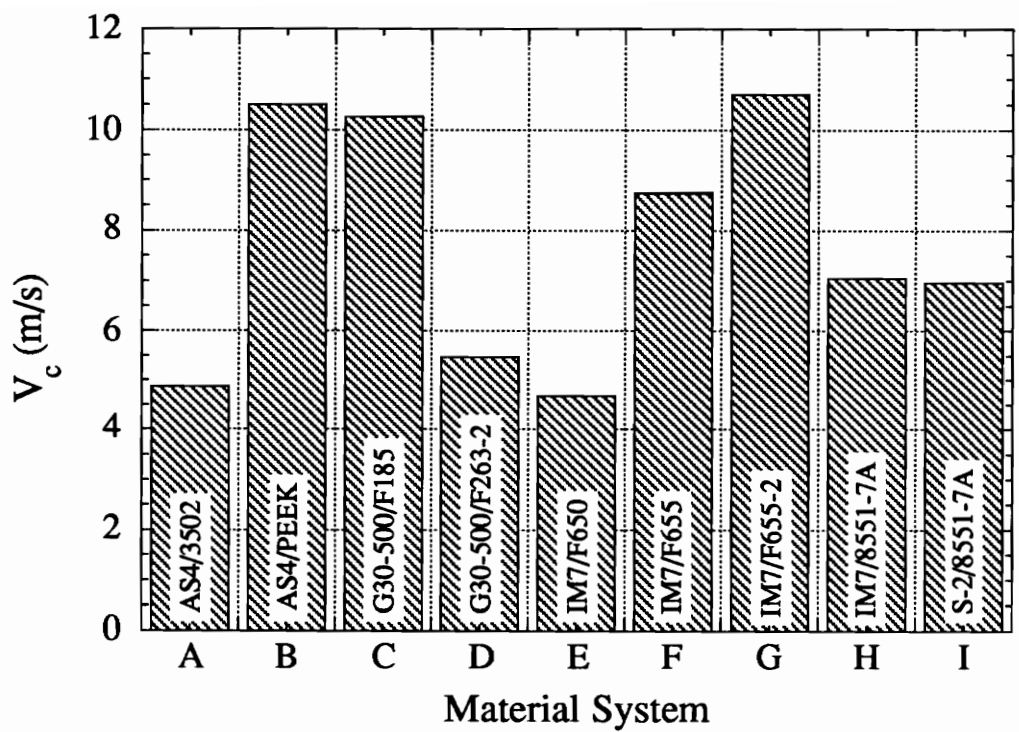
Fig. 4.22 Damage initiation impact velocity or threshold velocity of each material system.
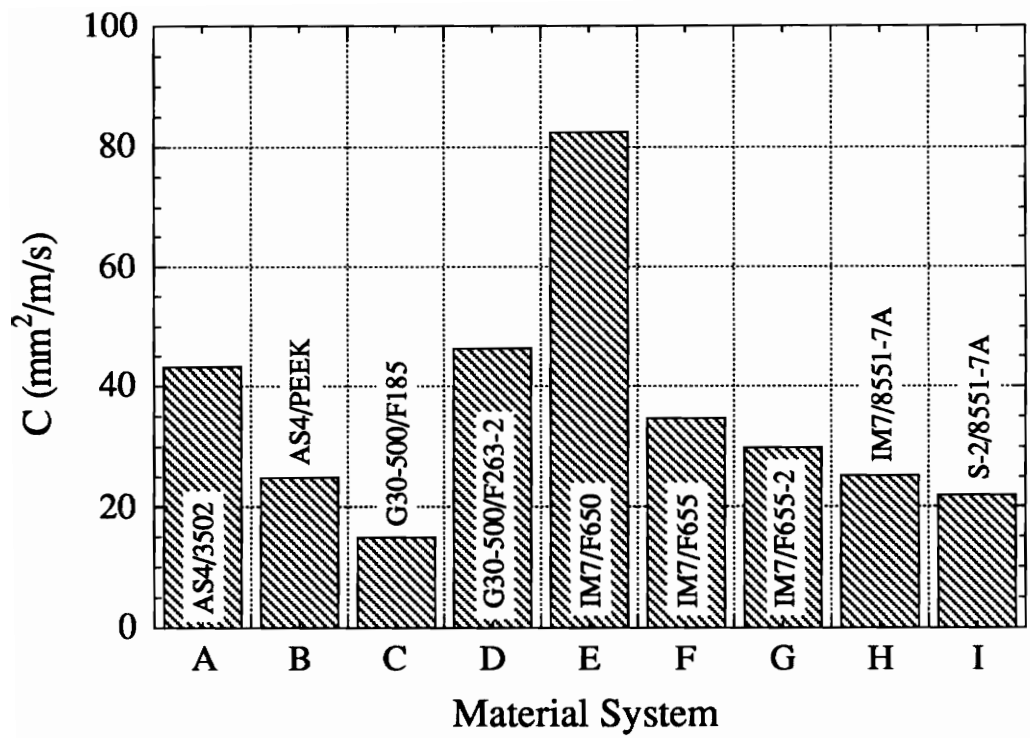
Fig. 4.23 Impact damage growth rate of each material system.
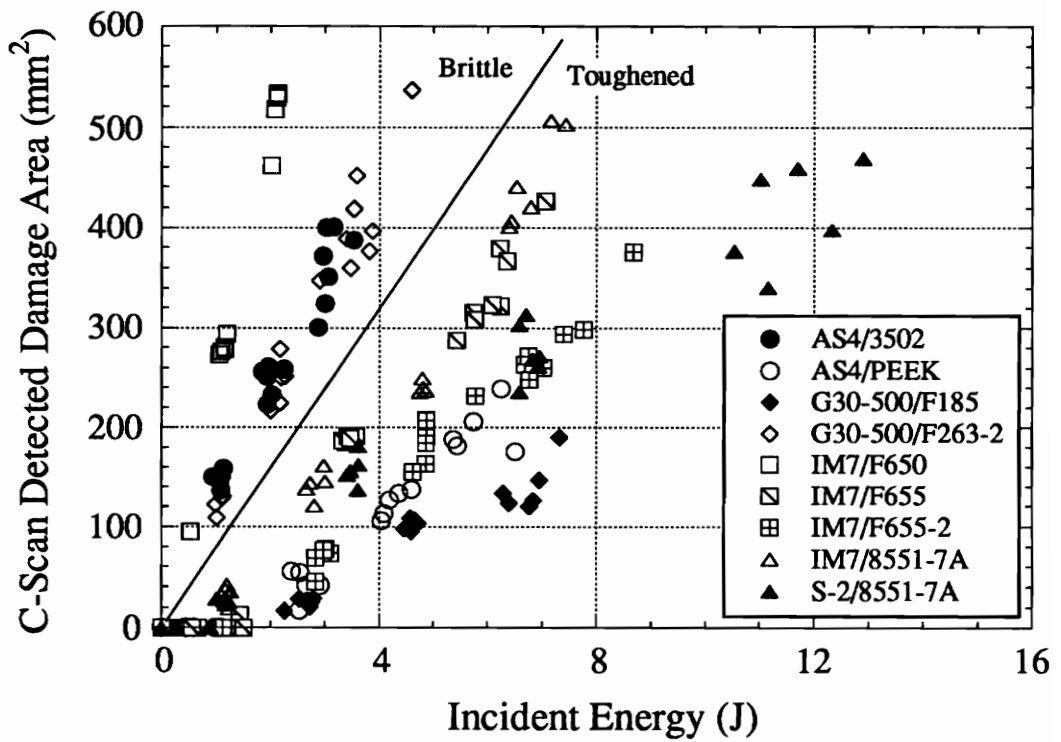
Fig. 4.24 Variation of C-scan detected damage area with incident energy for each material system.
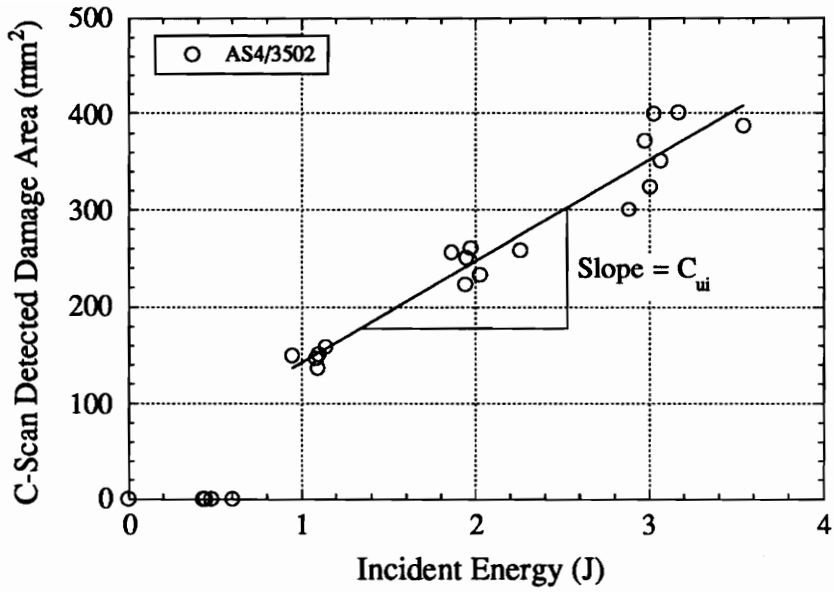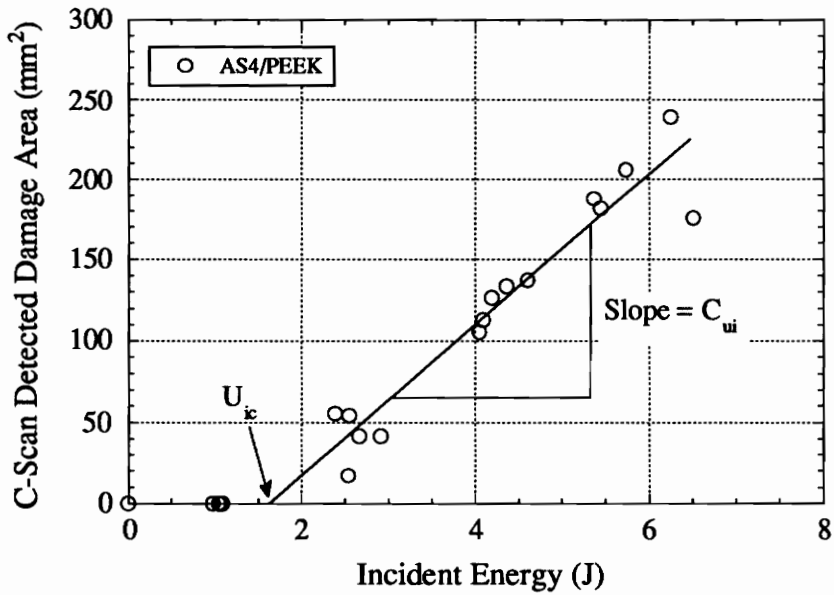
Fig. 4.25 Example of linear curve fitting to the damage area - incident energy data for (a) AS4/3502 and (b) AS4/PEEK.
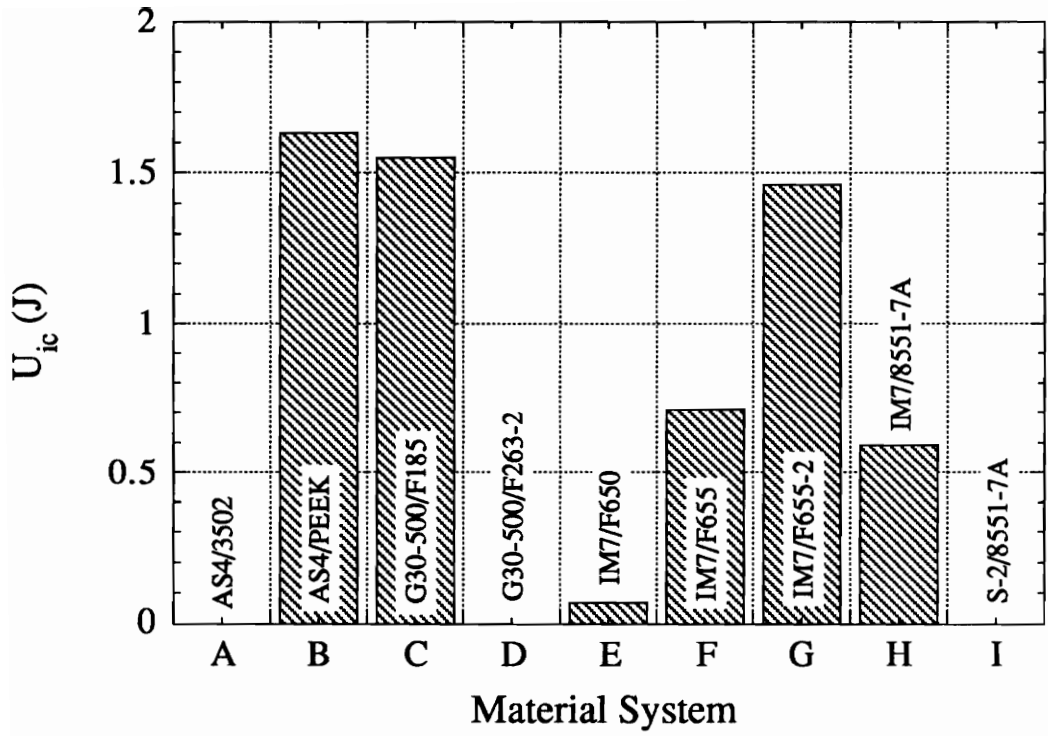
Fig. 4.26 Damage initiation incident energy of each material system.
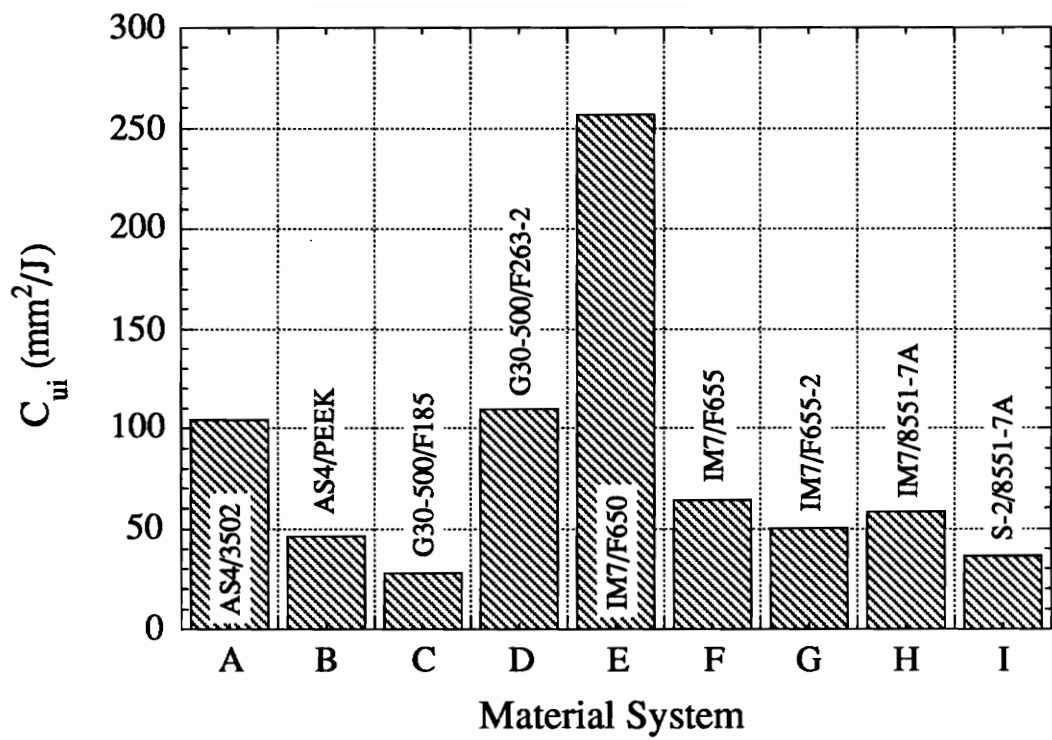
Fig. 4.27 Impact damage growth rate with respect to incident energy of each material system.
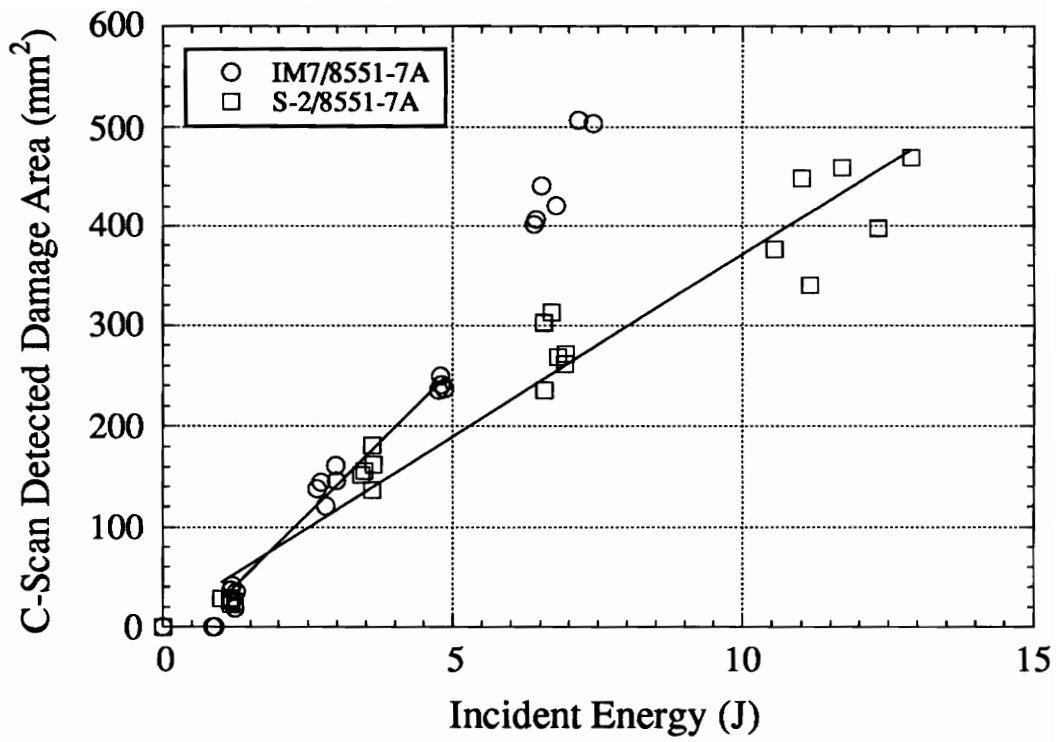
Fig. 4.28 Variation of C-scan detected damage area with incident energy for IM7/8551-7A and S-2/8551-7A.
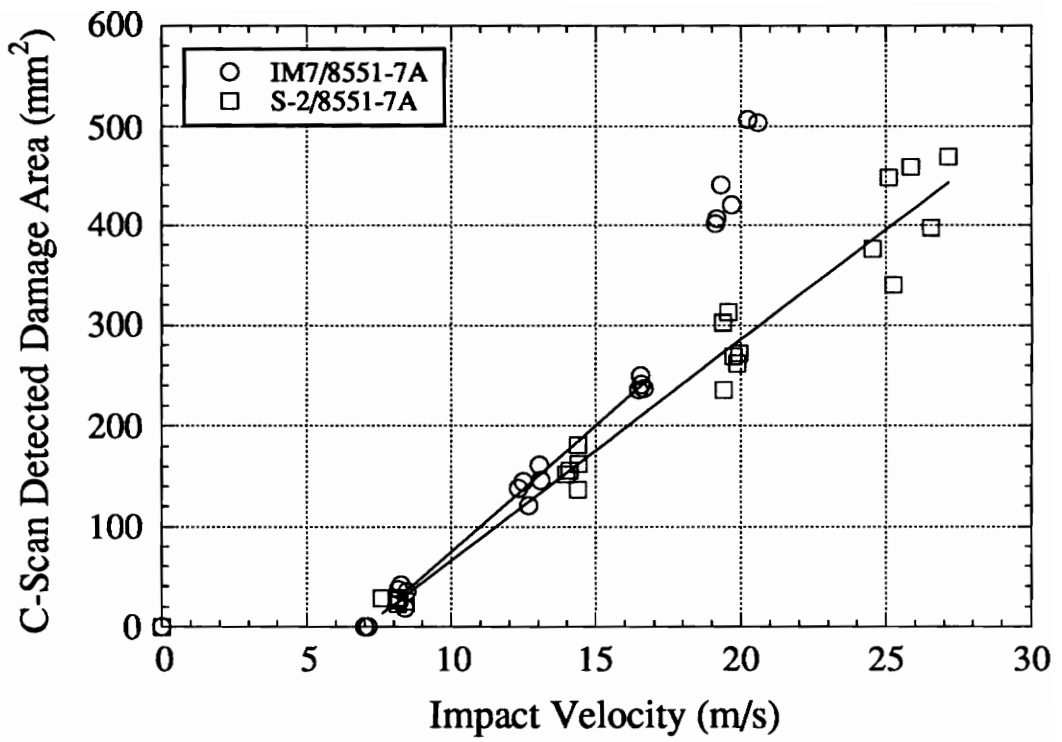
Fig. 4.29 Variation of C-scan detected damage area with impact velocity for IM7/8551-7A and S-2/8551-7A.
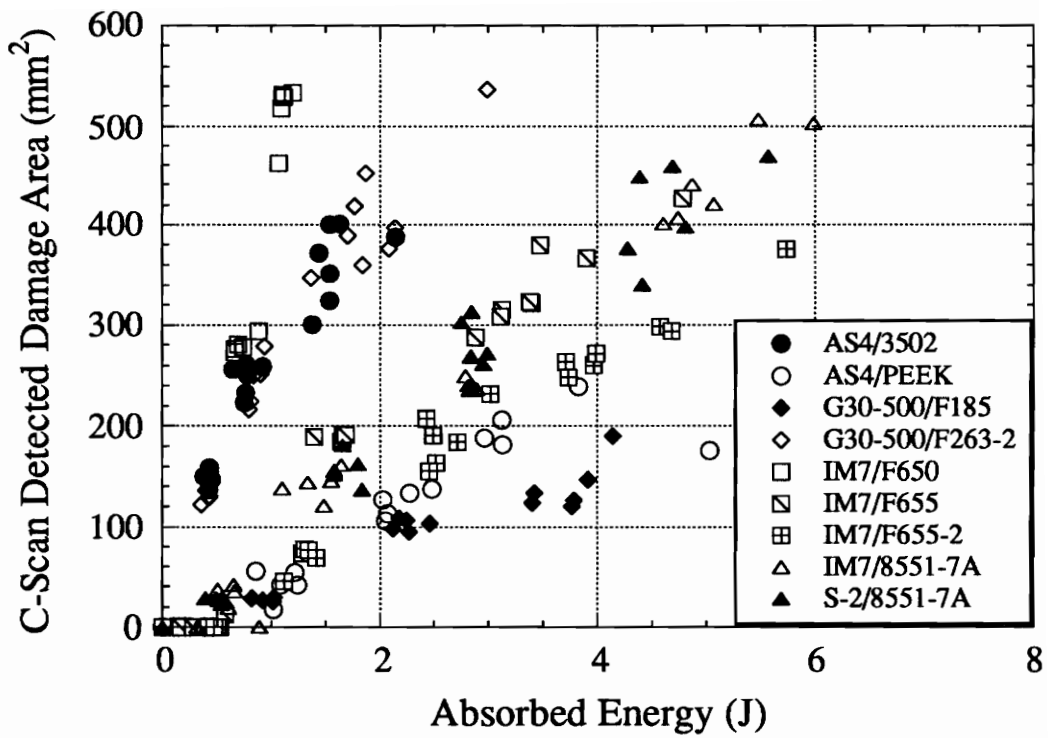
Fig. 4.30 Variation of C-scan detected damage area with absorbed energy (U_a) for each material system.
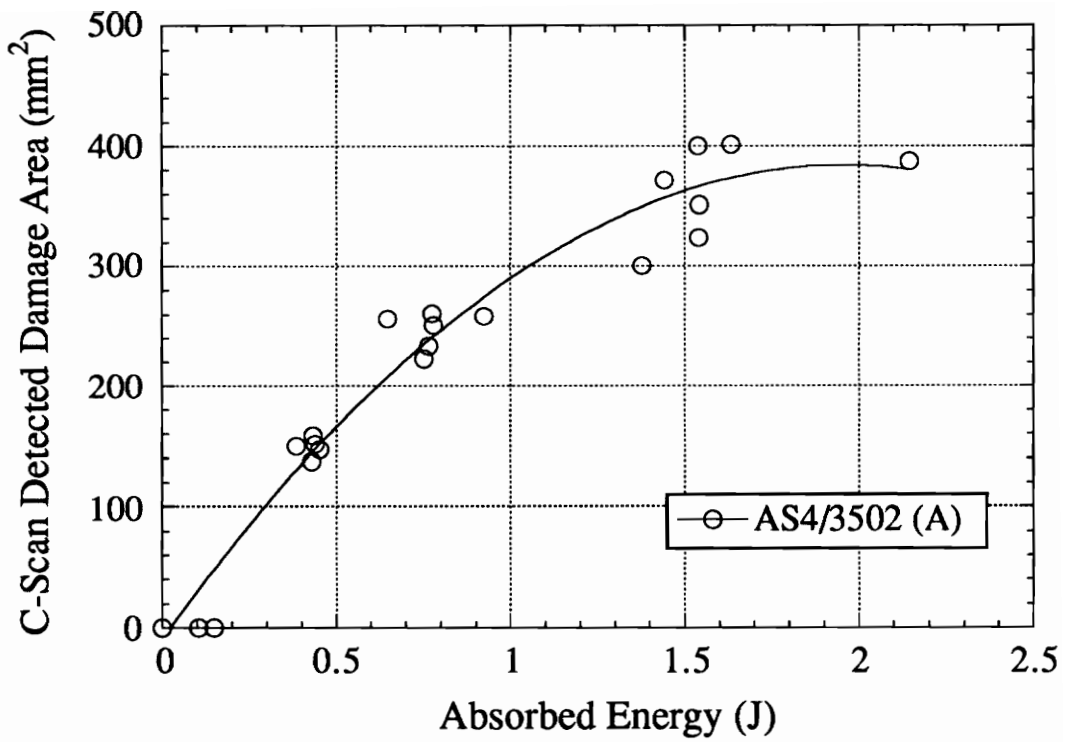
Fig. 4.31 Example of second degree polynomial curve fitting to the damage area - absorbed energy data for AS4/3502.
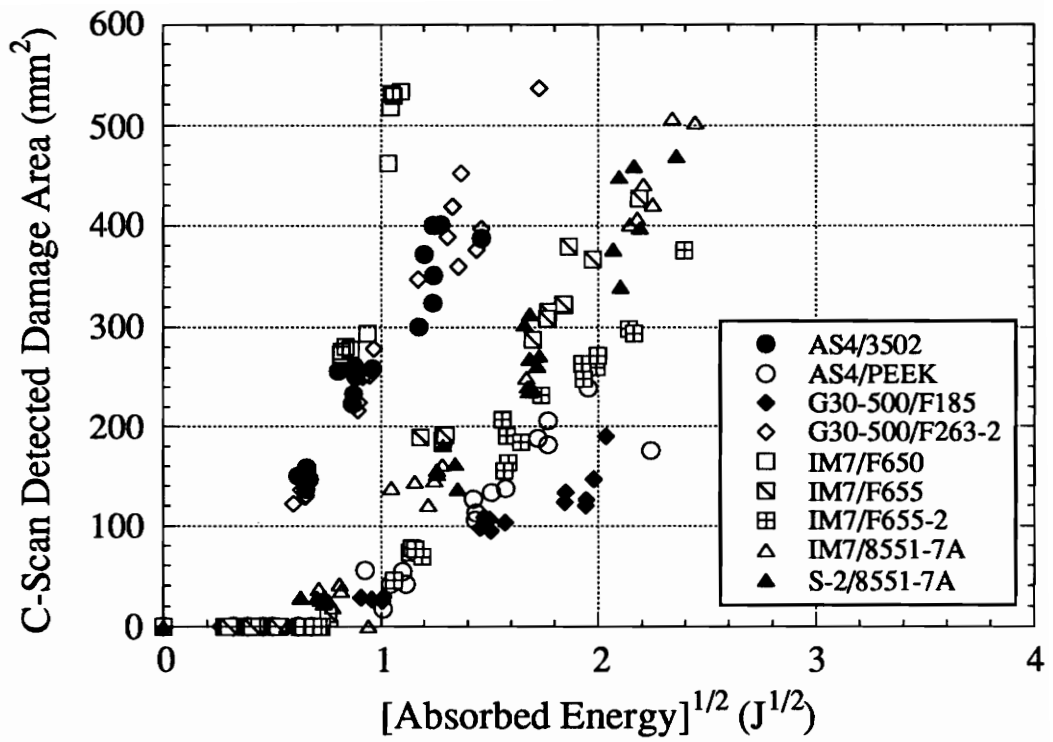
Fig. 4.32 Variation of C-scan detected damage area with [absorbed energy]$^{1/2}$ for each material system.
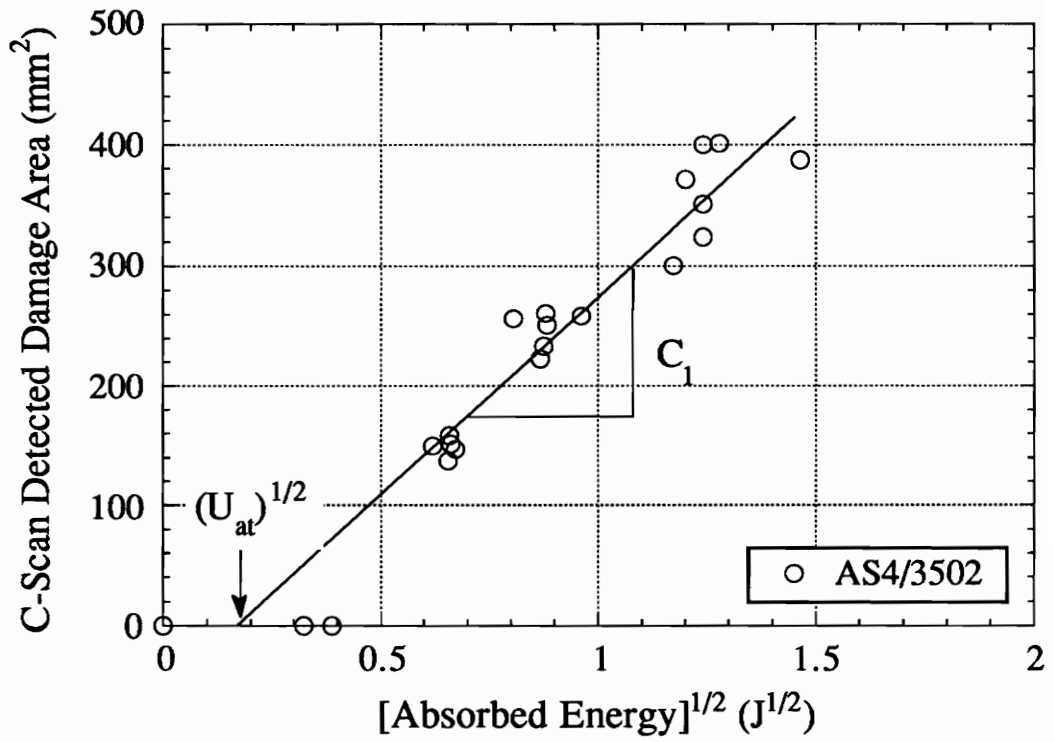
Fig. 4.33 Example of linear curve fitting to the damage area - [absorbed energy]$^{1/2}$ data for AS4/3502.
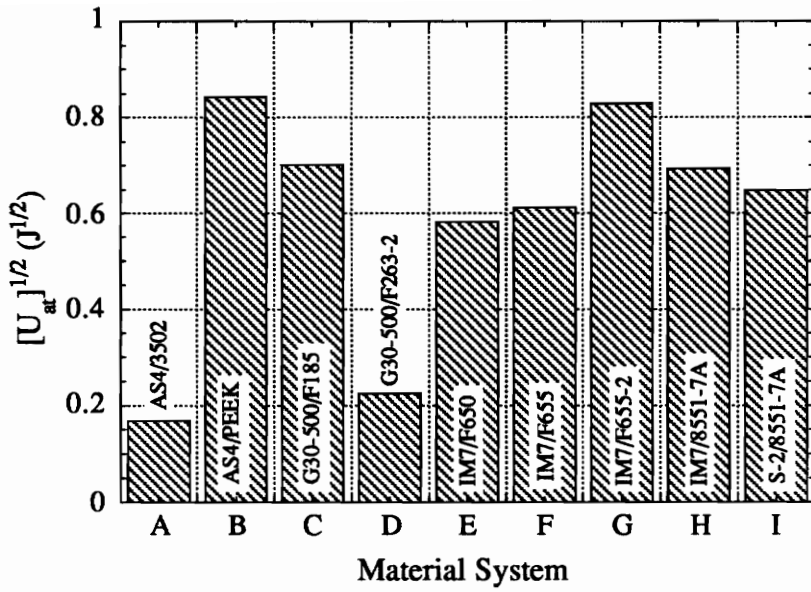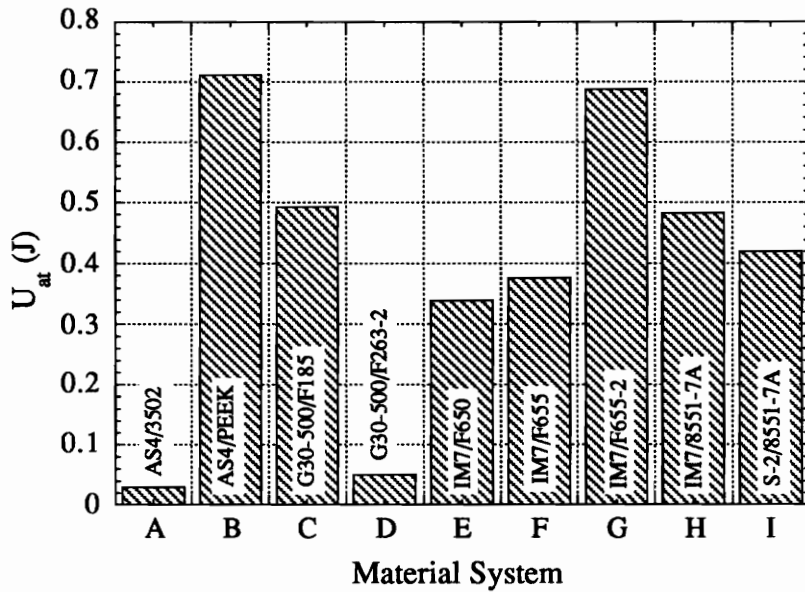
Fig. 4.34 Damage initiation absorbed energy of each material system.
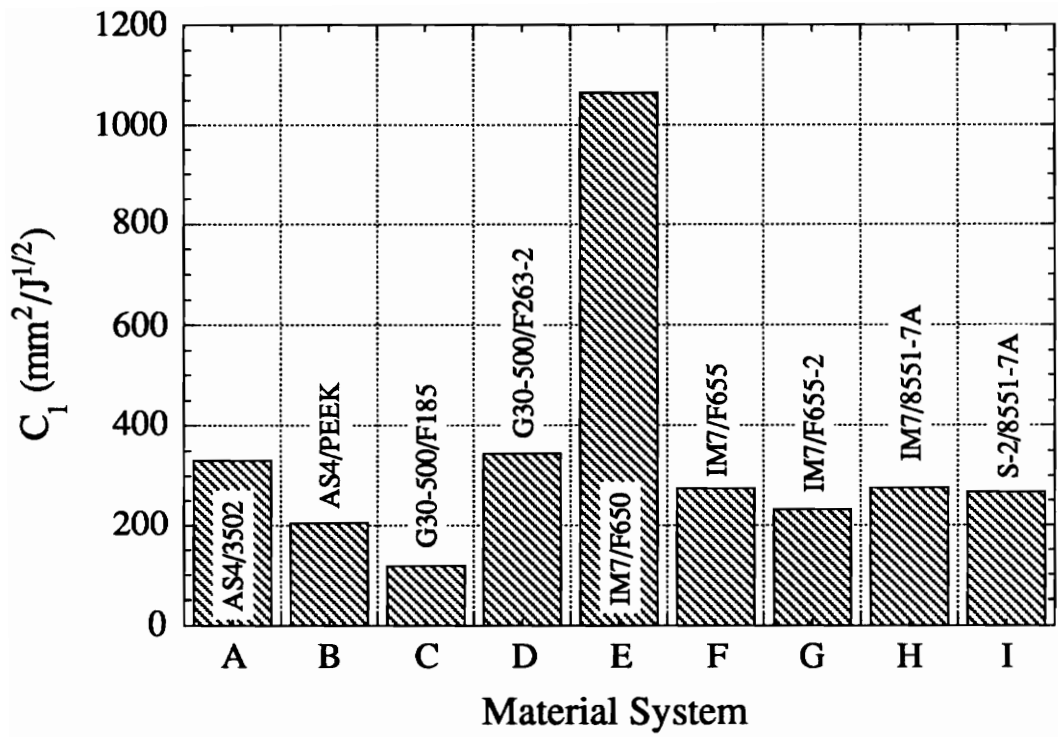
Fig. 4.35 Impact damage growth rate of each material system.
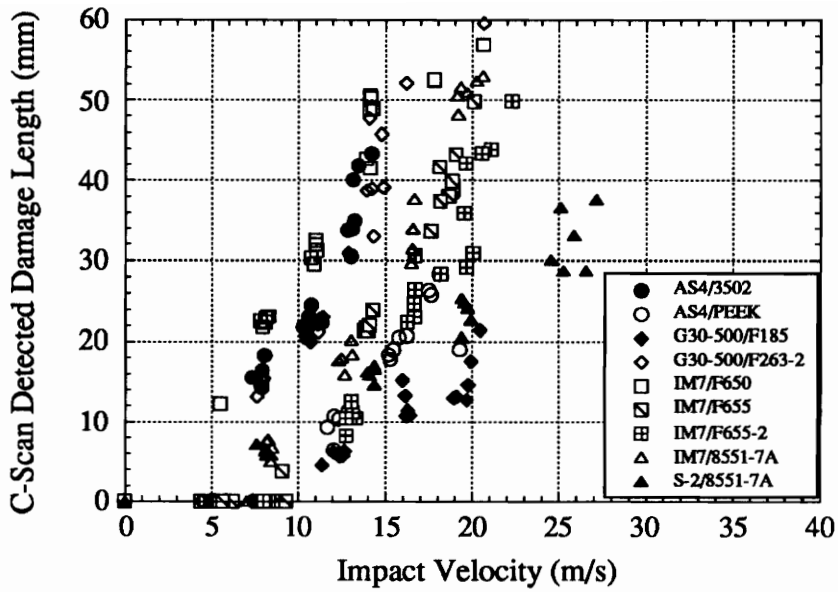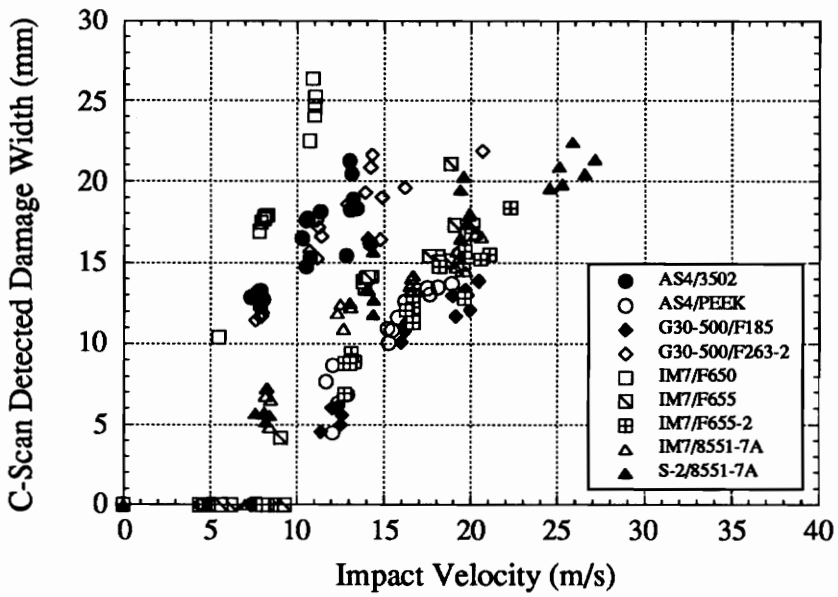
Fig. 4.36 Variation of (a) C-scan detected damage length and (b) width with impact velocity for each material system.

111
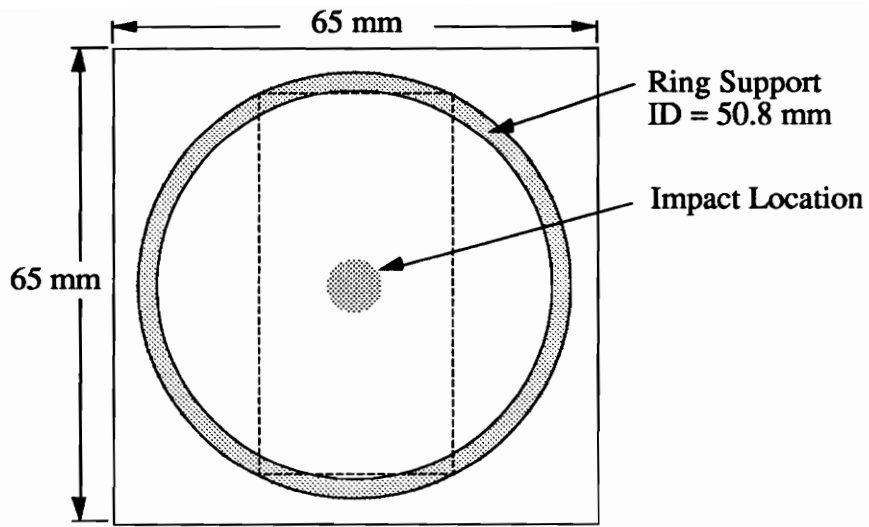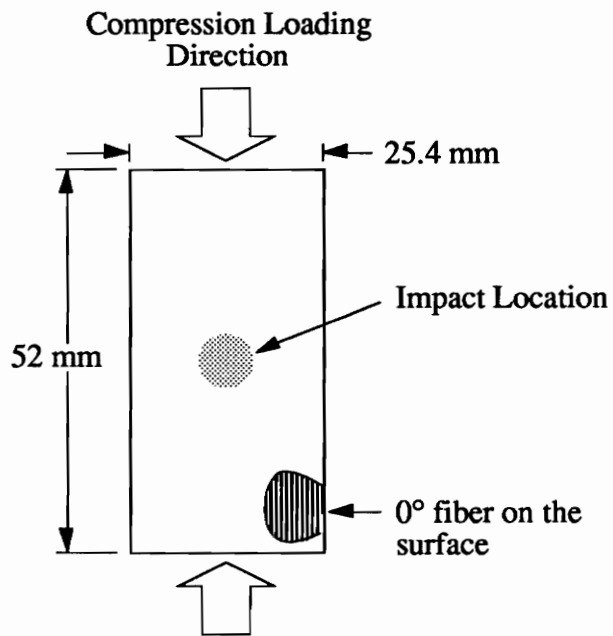
Fig. 5.1 Dimensions of the compression after impact test coupon.
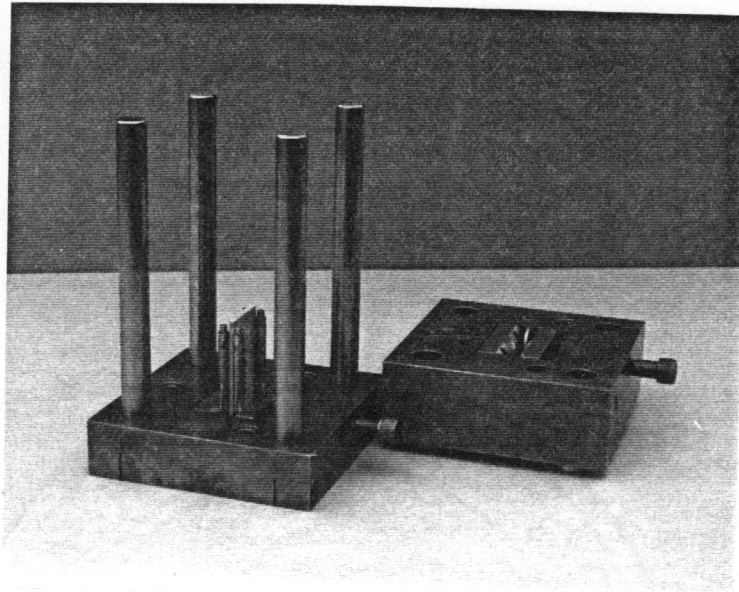
(a)
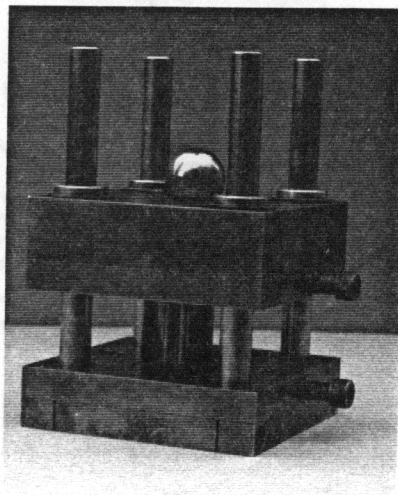
(b)

Fig. 5.2 Compression test fixture for measuring compressive strength of the specimen.

113
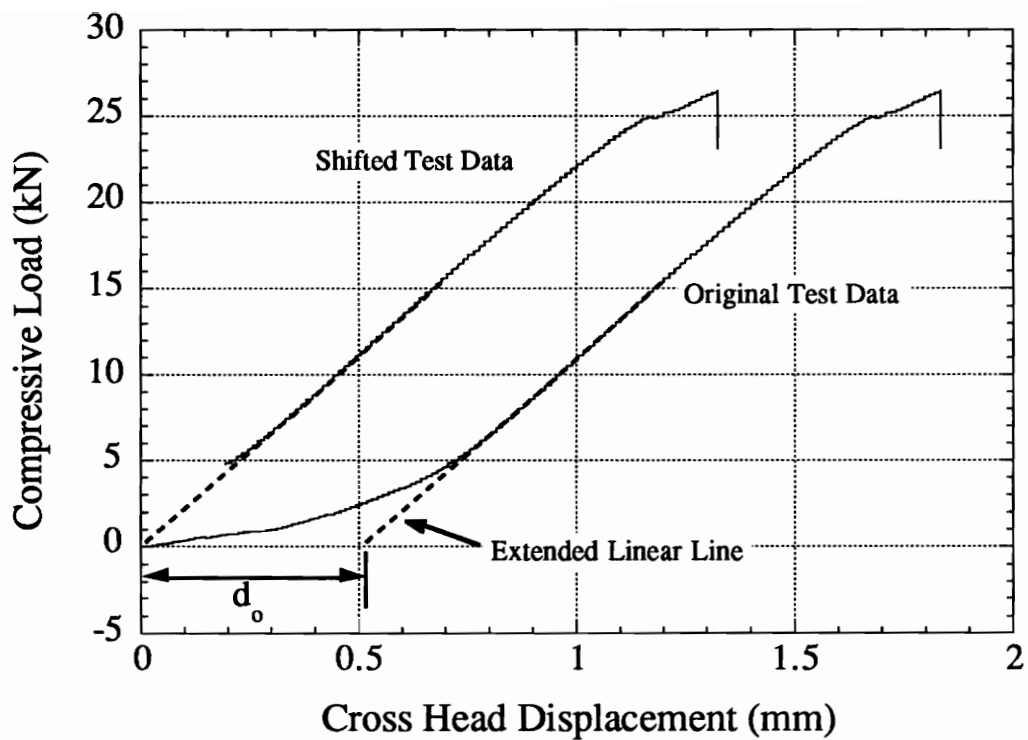
Fig. 5.3 Example of correcting the crosshead displacement to actual deformation measurement from original test data to shifted test data on the load-displacement curve of an AS4/PEEK specimen impacted with velocity of 7.5 m/s.
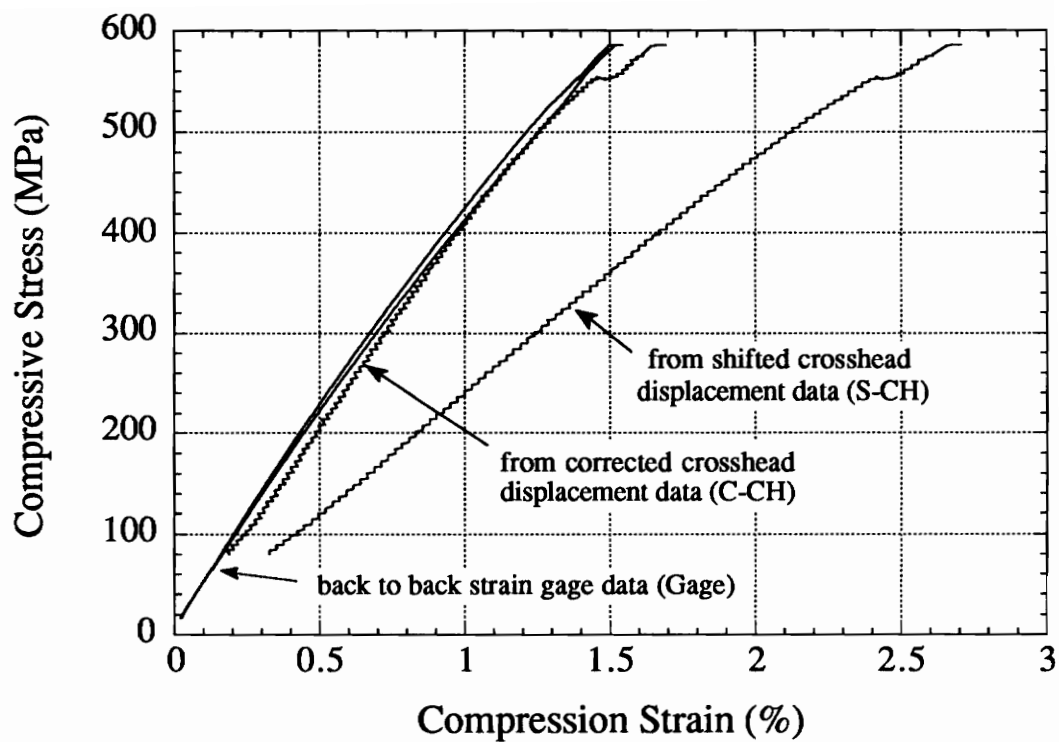
Fig. 5.4 The compressive stress-strain curves of an AS4/PEEK specimen before impact with strains measured from strain gages (Gage), and both shifted (S-CH) and corrected (C-CH) crosshead displacement.
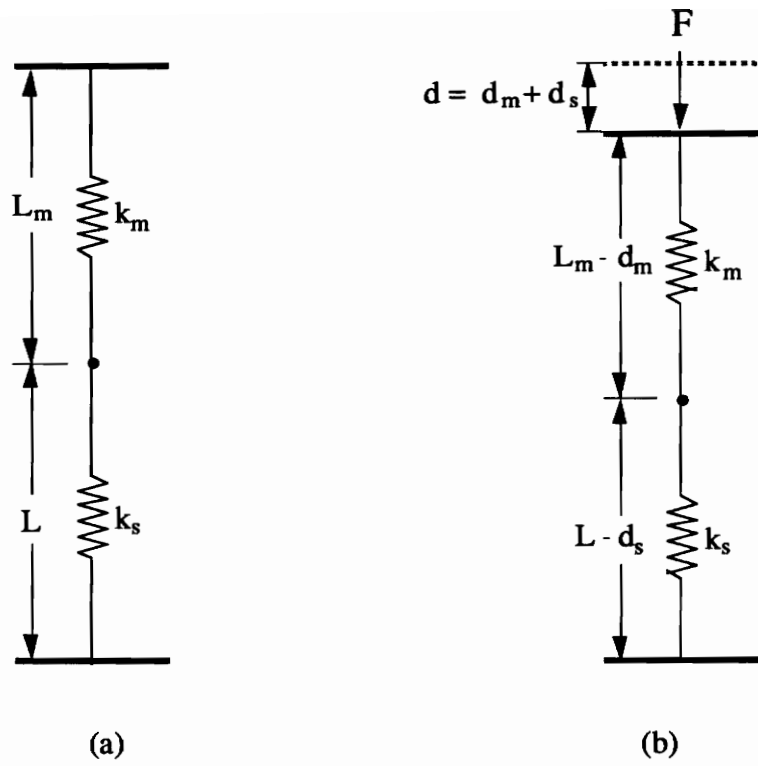
Fig. 5.5 The series spring model for the compression test loading condition.
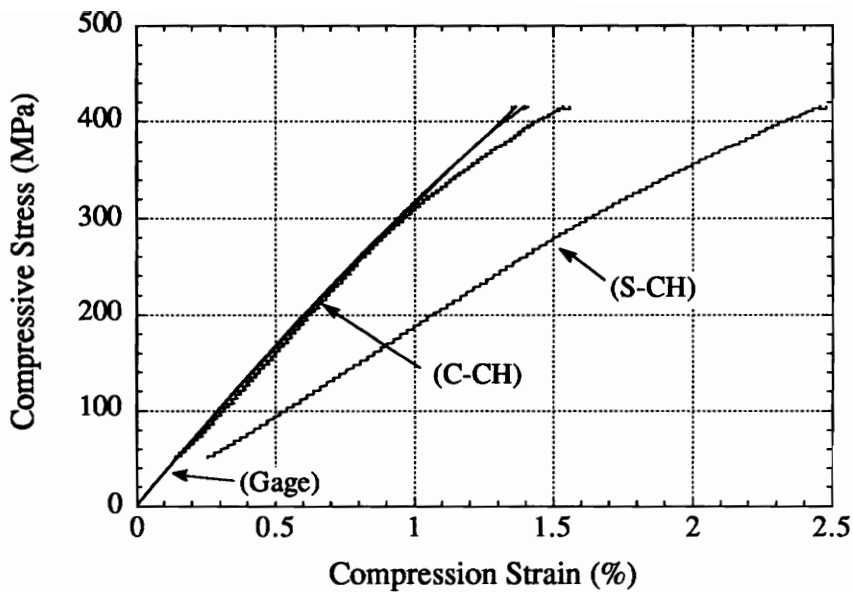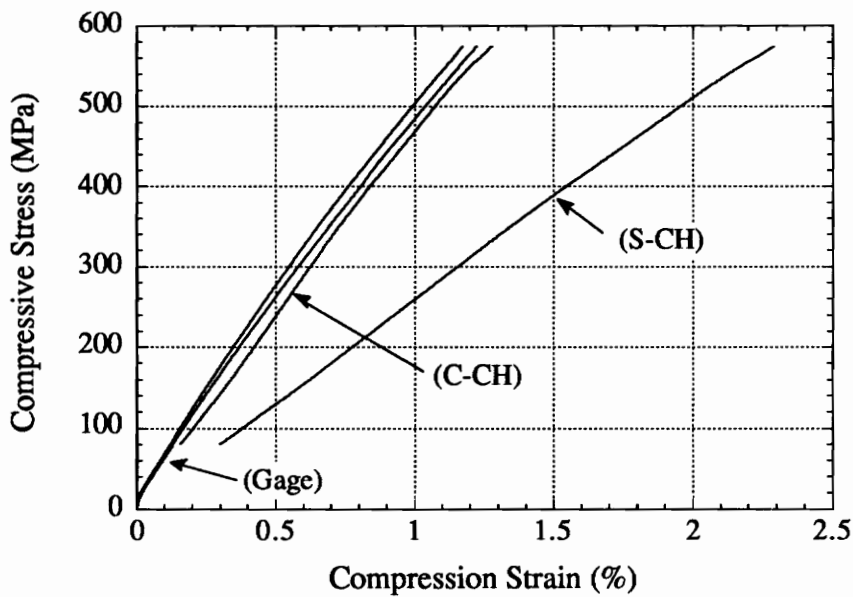
Fig. 5.6 The compressive stress-strain curves of (a) G30-500/F185 and (b) IM7/F650 specimens before impact with strains measured from strain gages (Gage), and both shifted (S-CH) and corrected (C-CH) crosshead displacement.

117
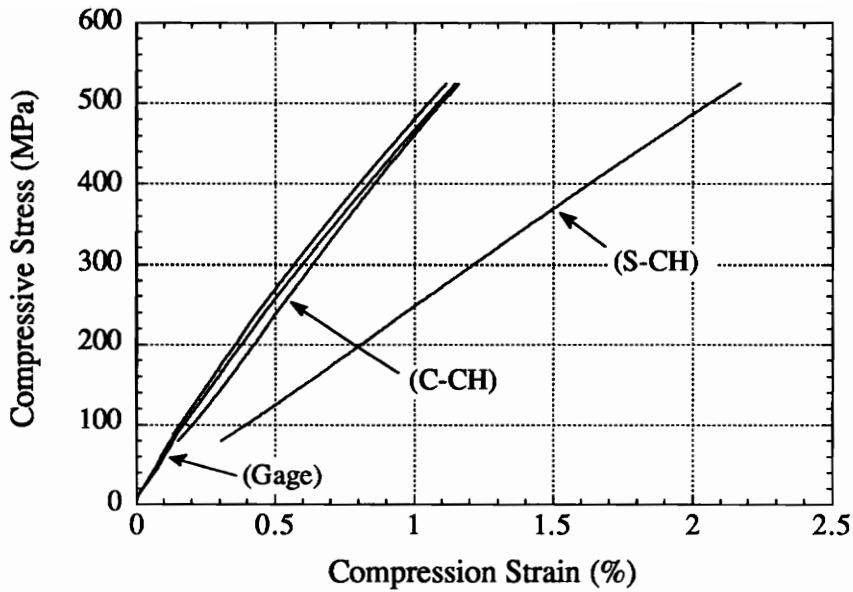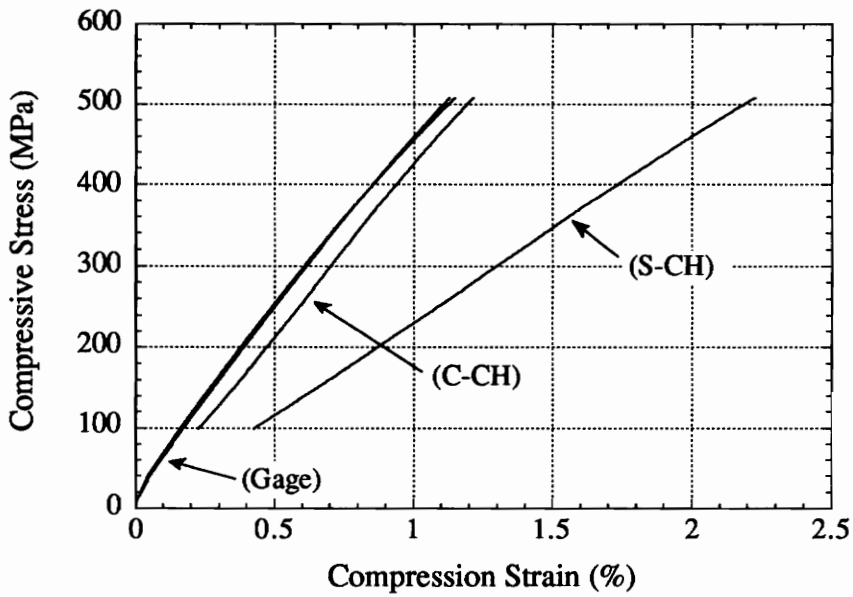
Fig. 5.7 The compressive stress-strain curves of (a) IM7/F655 and (b) IM7/F655-2 specimens before impact with strains measured from strain gages (Gage), and both shifted (S-CH) and corrected (C-CH) crosshead displacement.

118
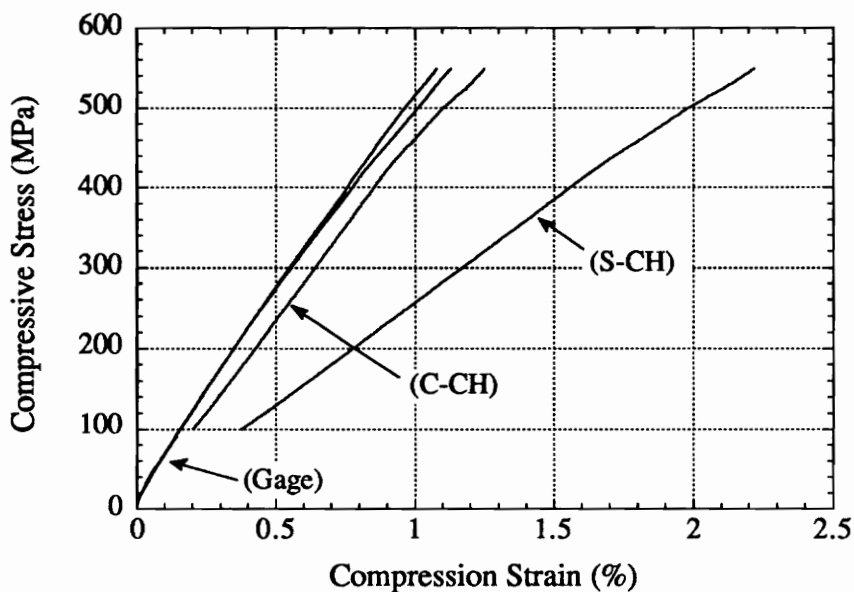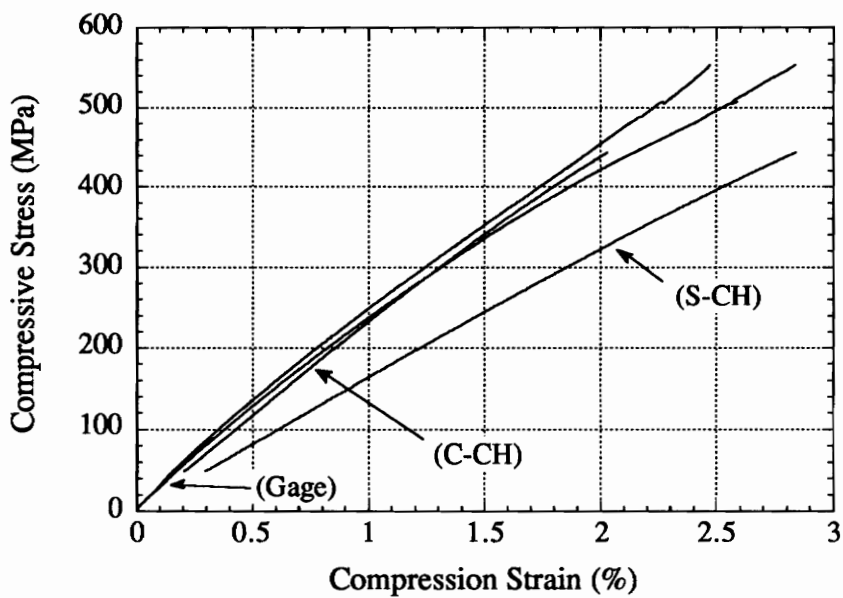
Fig. 5.8 The compressive stress-strain curves of (a) IM7/8551-7A and (b) S-2/8551-7A specimens before impact with strains measured from strain gages (Gage), and both shifted (S-CH) and corrected (C-CH) crosshead displacement.

119
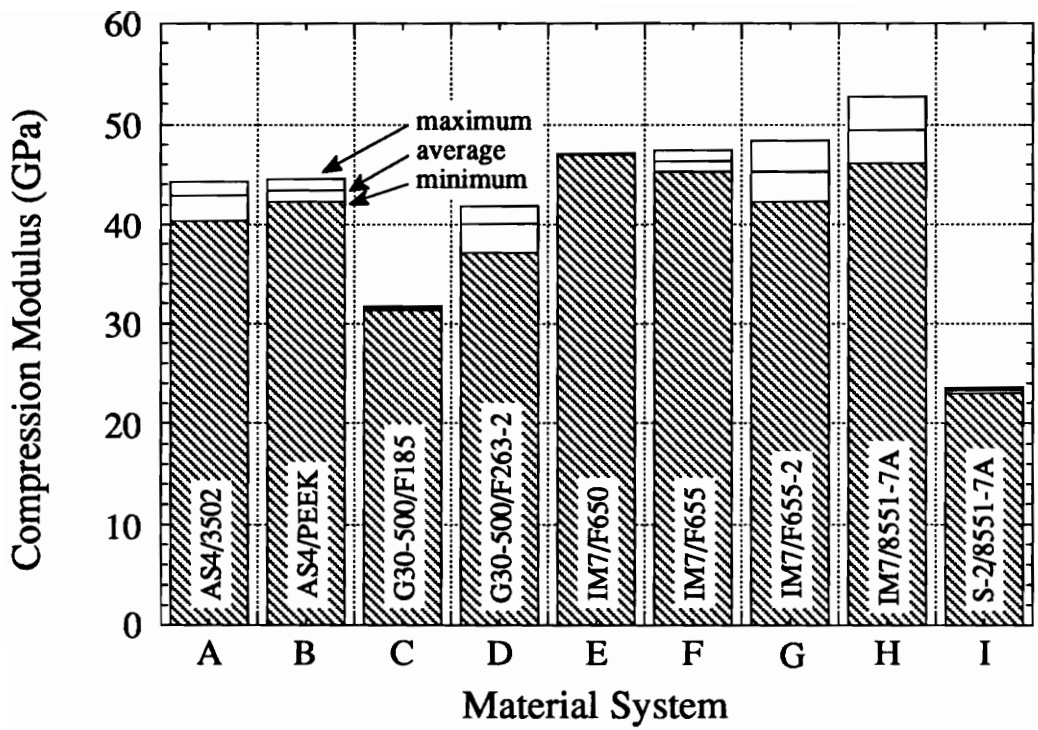
Fig. 5.9 Compressive modulus of each material system.
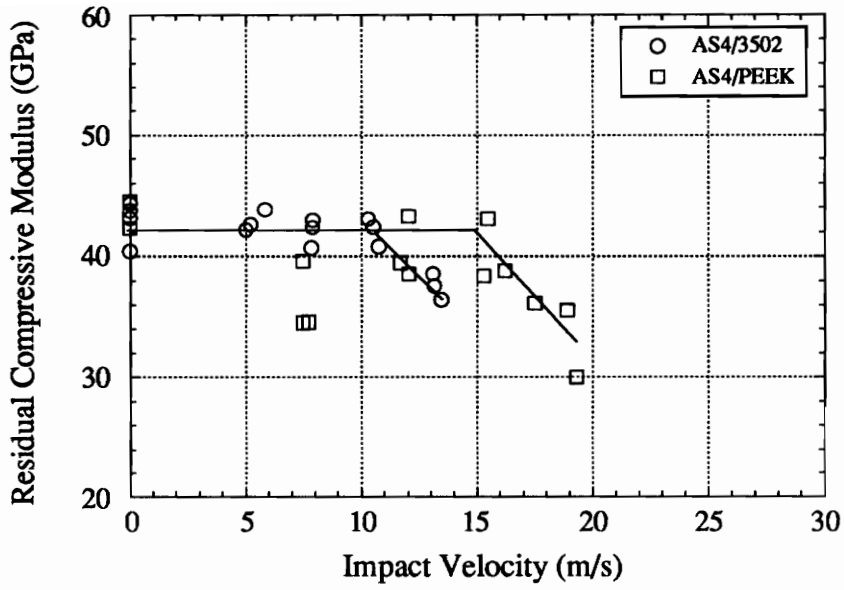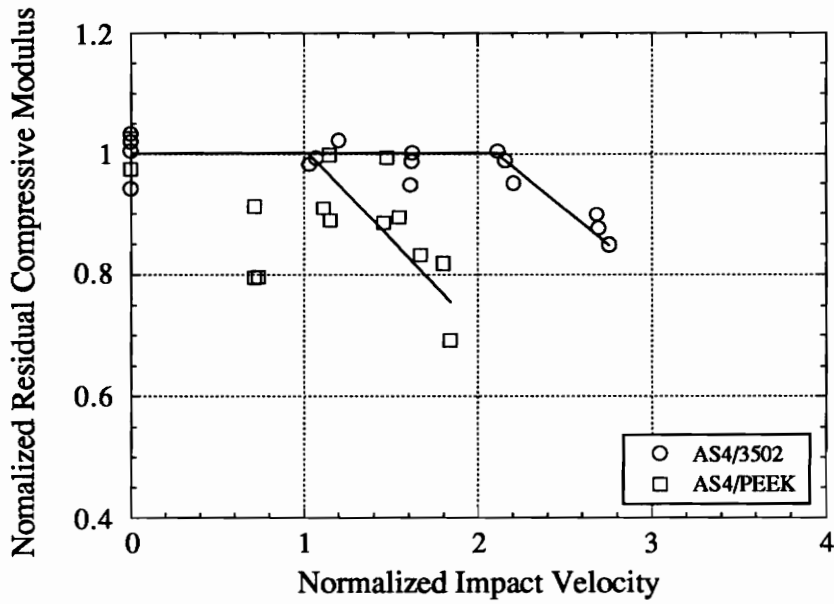
Fig. 5.10 Variation of (a) residual compressive modulus with impact velocity and (b) normalized residual compressive modulus with normalized impact velocity for AS4/3502 and AS4/PEEK.
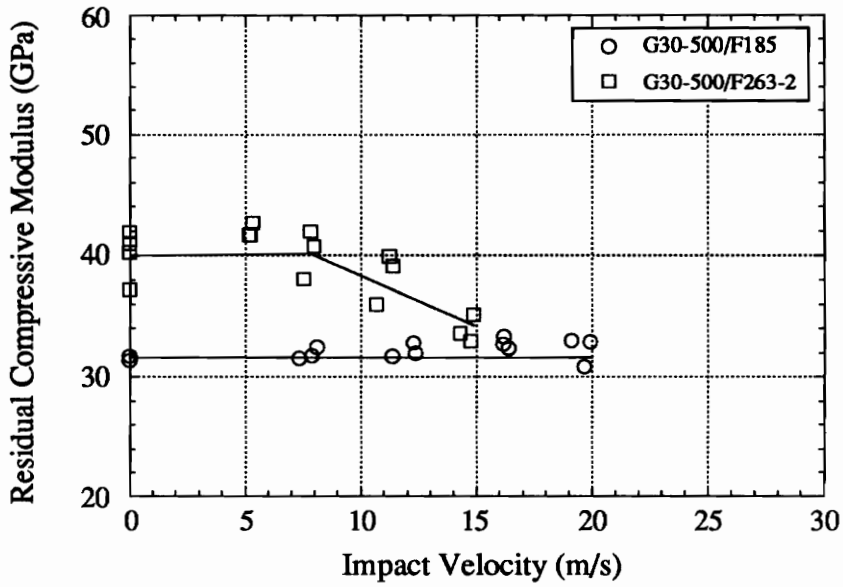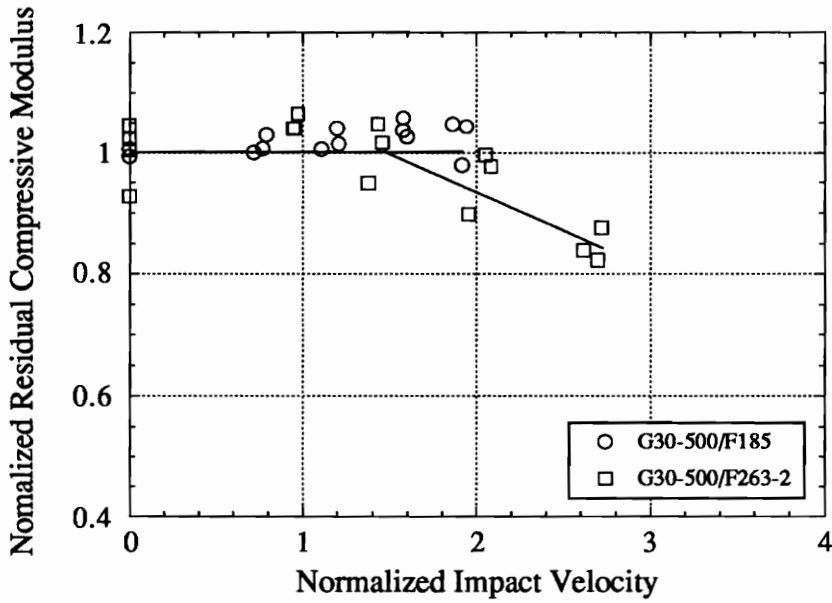
Fig. 5.11 Variation of (a) residual compressive modulus with impact velocity and (b) normalized residual compressive modulus with normalized impact velocity for G30-500/F183 and G30-500/F263-2.
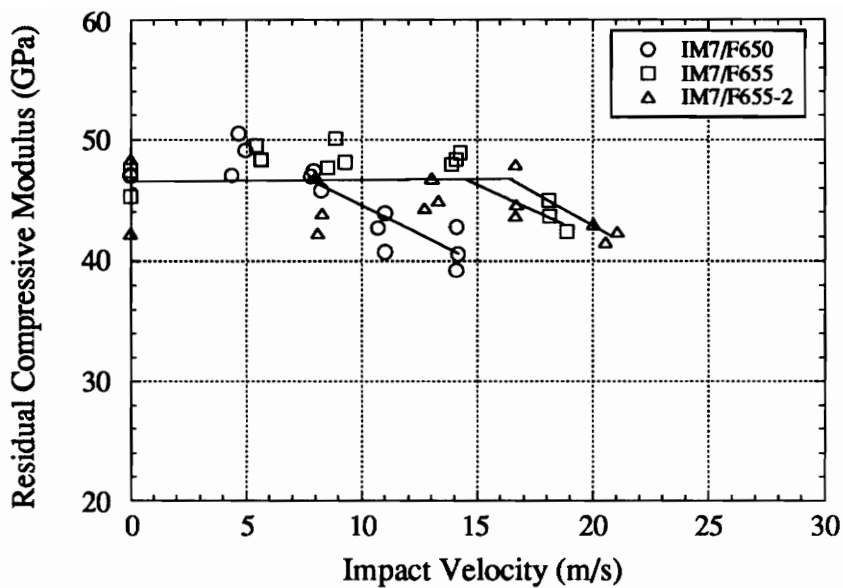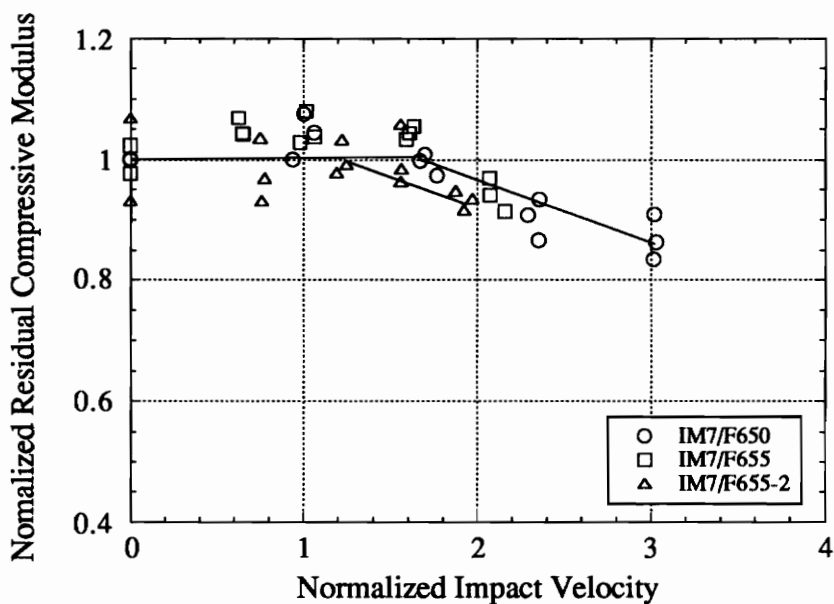
Fig. 5.12 Variation of (a) residual compressive modulus with impact velocity and (b) normalized residual compressive modulus with normalized impact velocity for IM7/F650, IM7/F655, and IM7/F655-2.
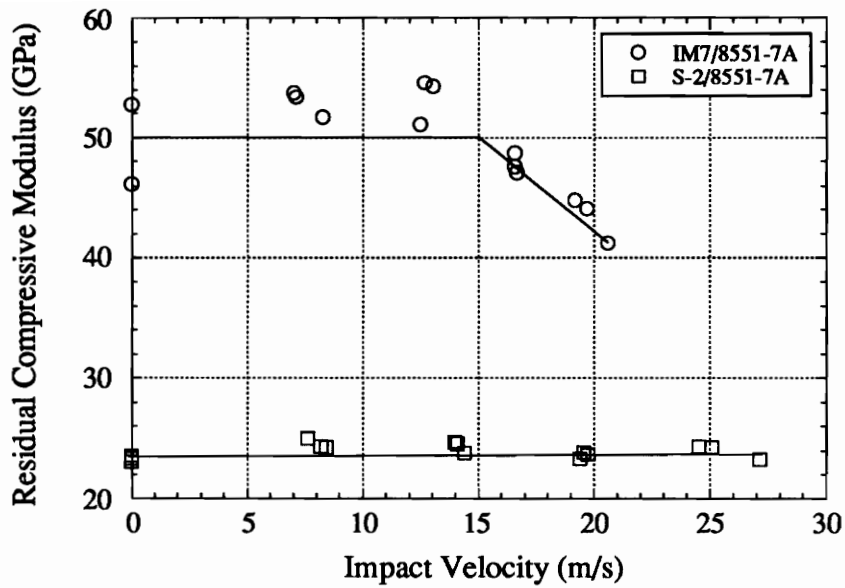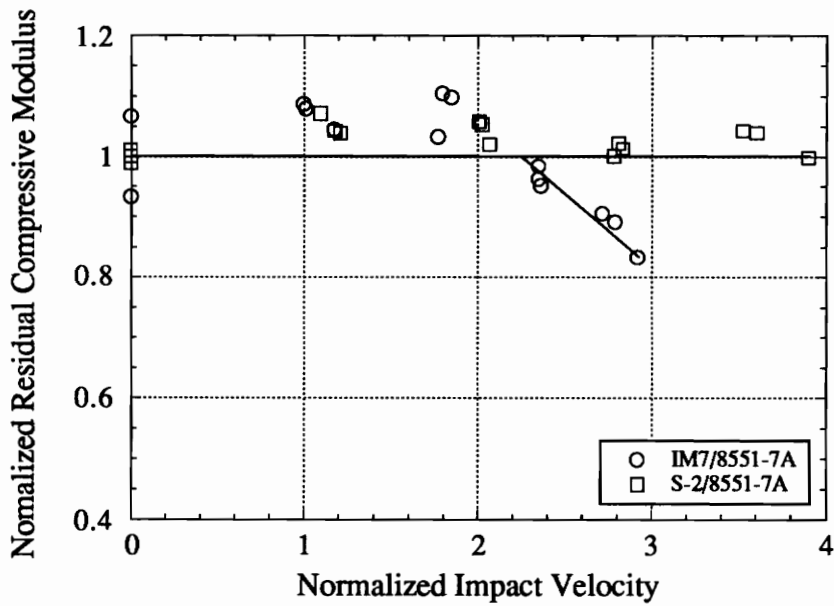
Fig. 5.13 Variation of (a) residual compressive modulus with impact velocity and (b) normalized residual compressive modulus with normalized impact velocity for IM7/8551-7A and S-2/8551-7A.

124
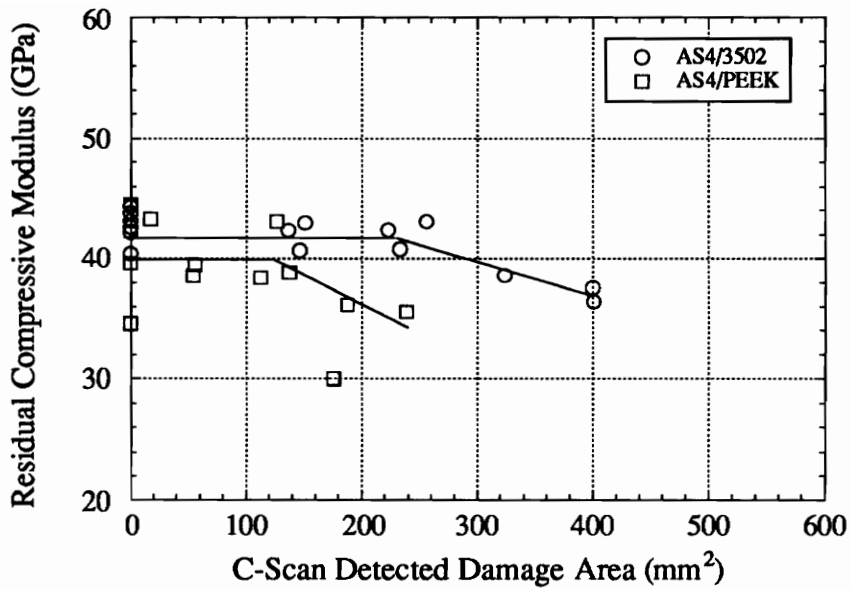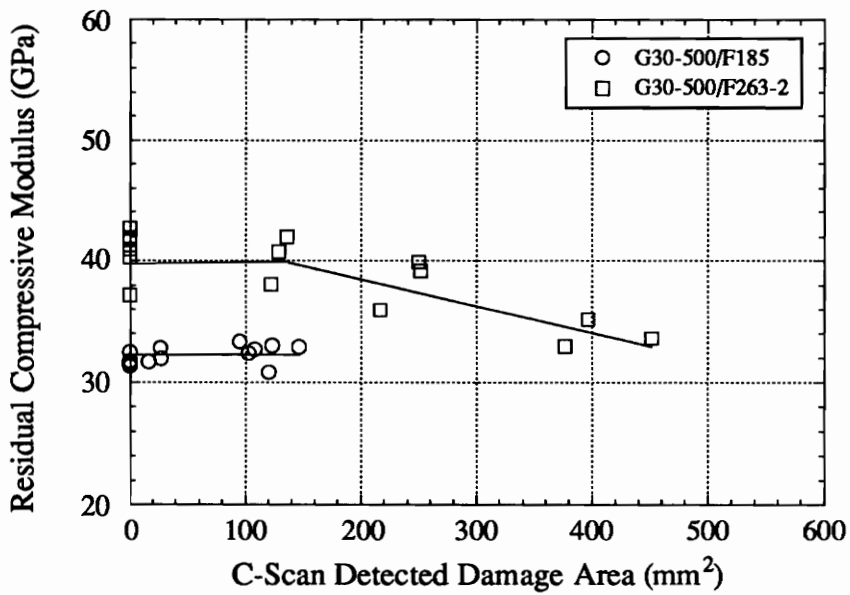
Fig. 5.14 Variation of residual compressive modulus with C-scan detected damage area for material systems with (a) AS4 and (b) G30-500 fibers.

125
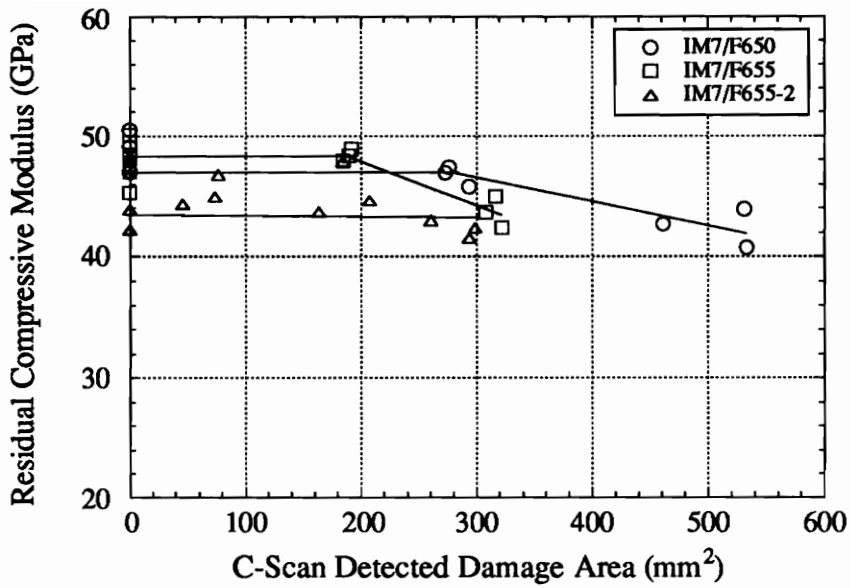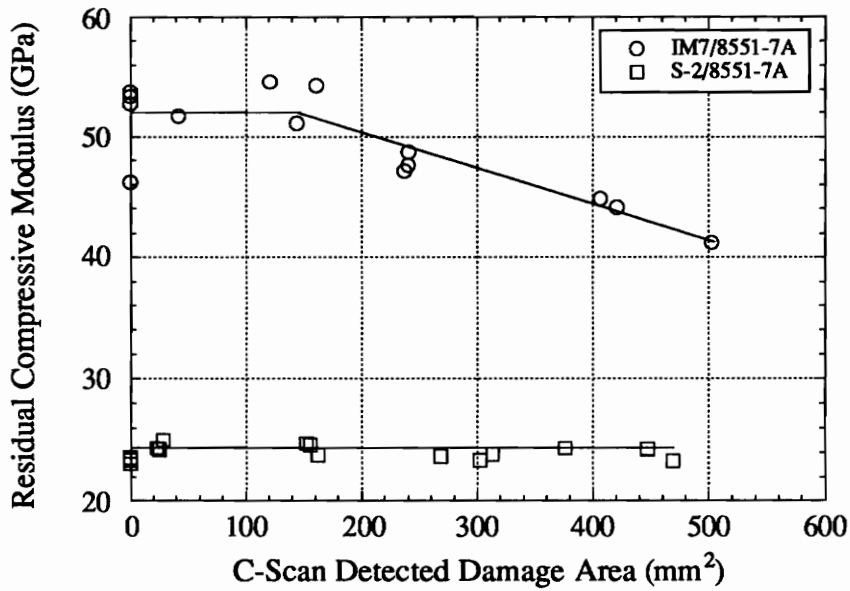
Fig. 5.15 Variation of residual compressive modulus with C-scan detected damage area for (a) bismaleimide and (b) rubber toughened epoxy systems.
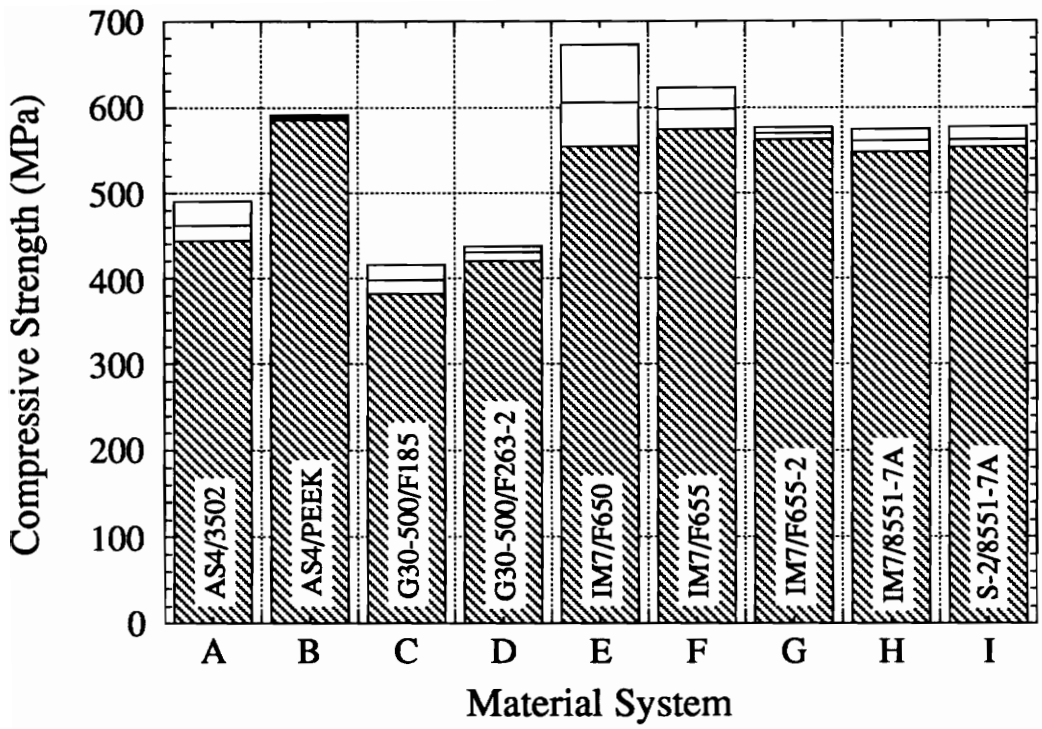
Fig. 5.16 Compressive strength of each material system.
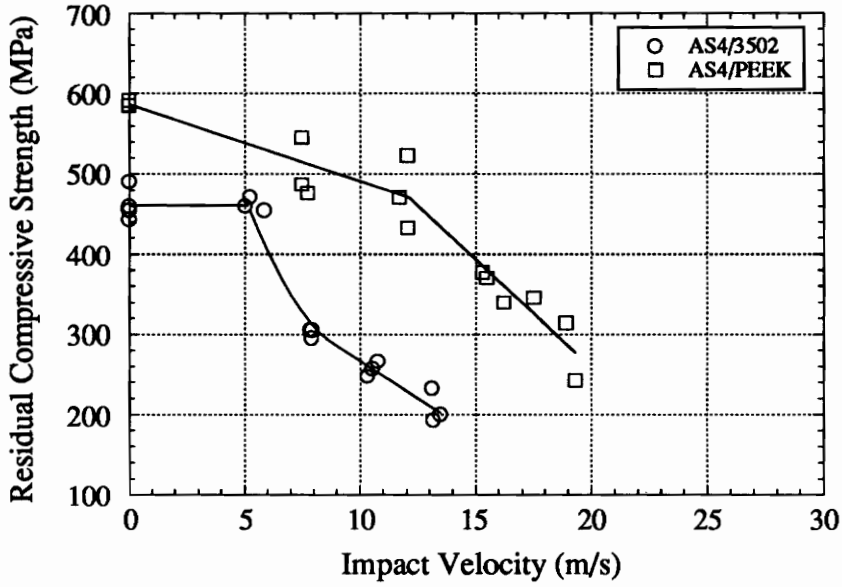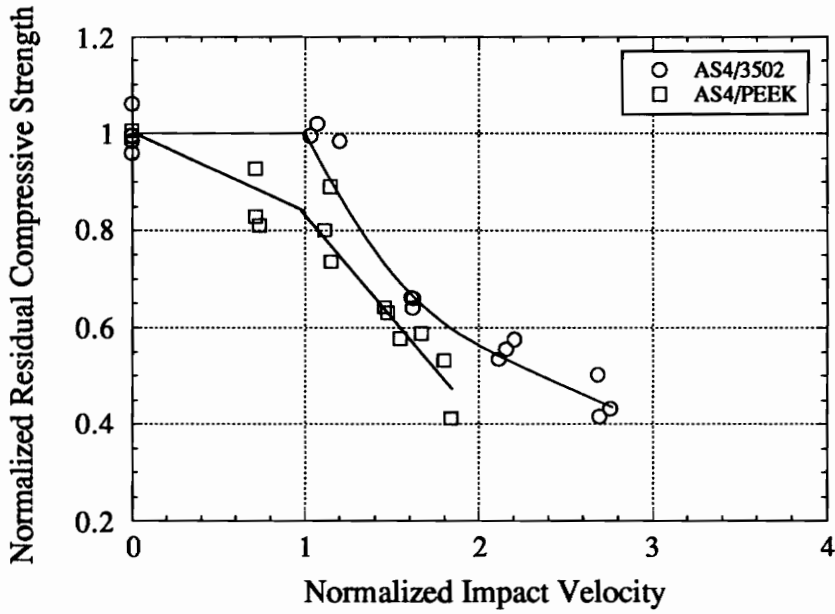
Fig. 5.17 Variation of (a) residual compressive strength with impact velocity and (b) normalized residual compressive strength with normalized impact velocity for AS4/3502 and AS4/PEEK.
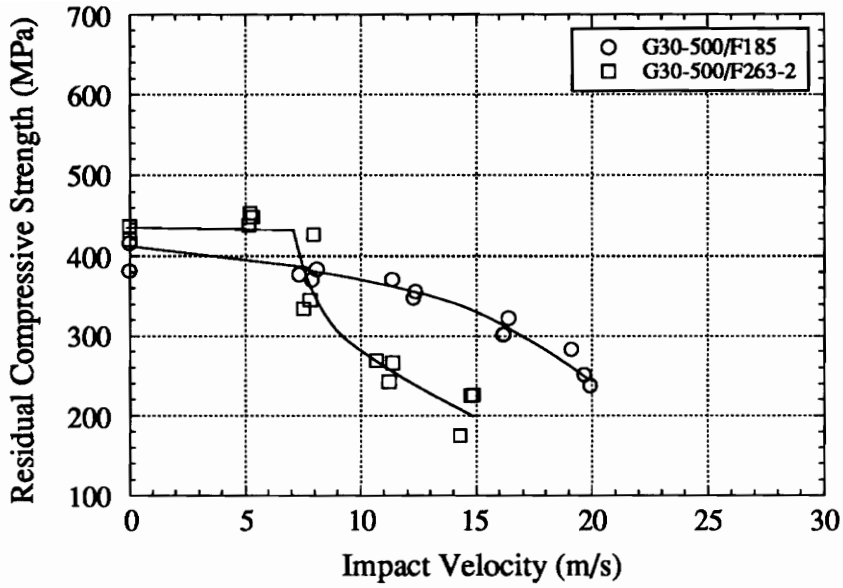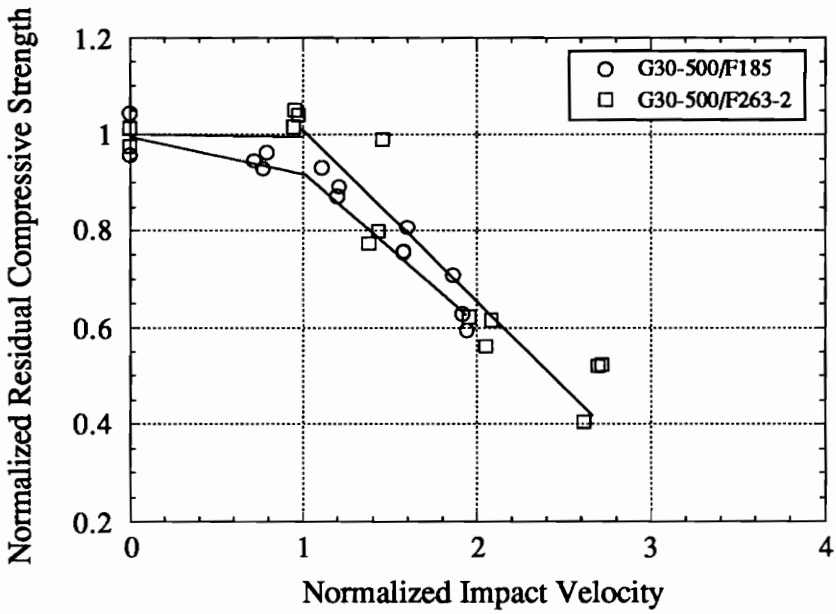
Fig. 5.18 Variation of (a) residual compressive strength with impact velocity and (b) normalized residual compressive strength with normalized impact velocity for G30-500/F185 and G30-500/F263-2.
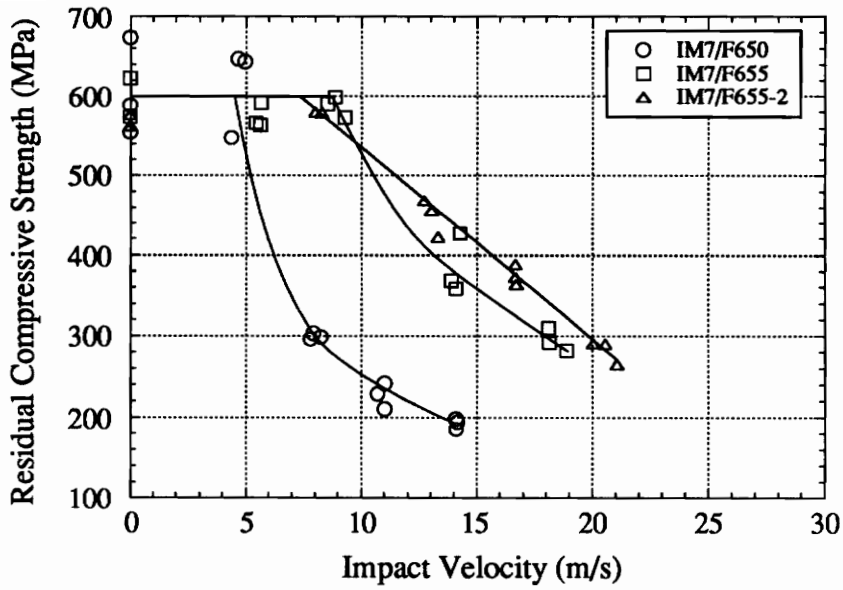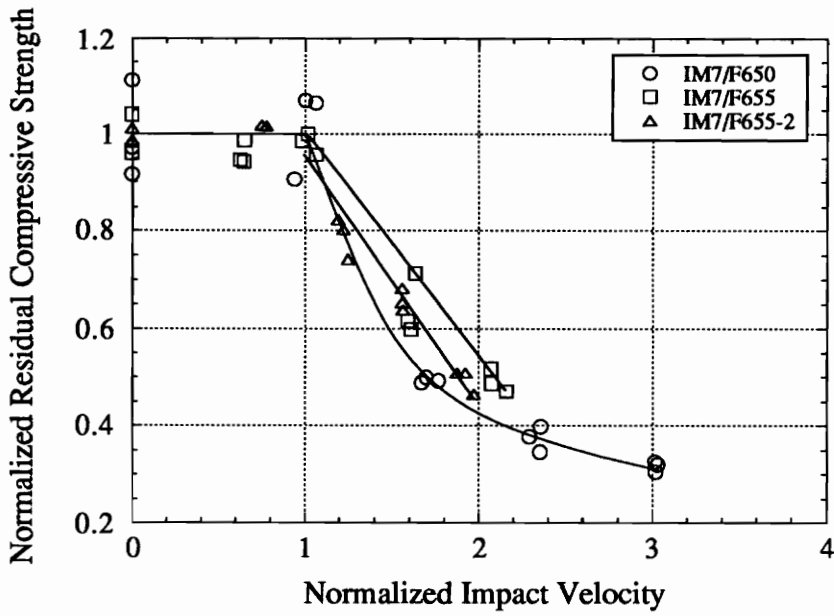
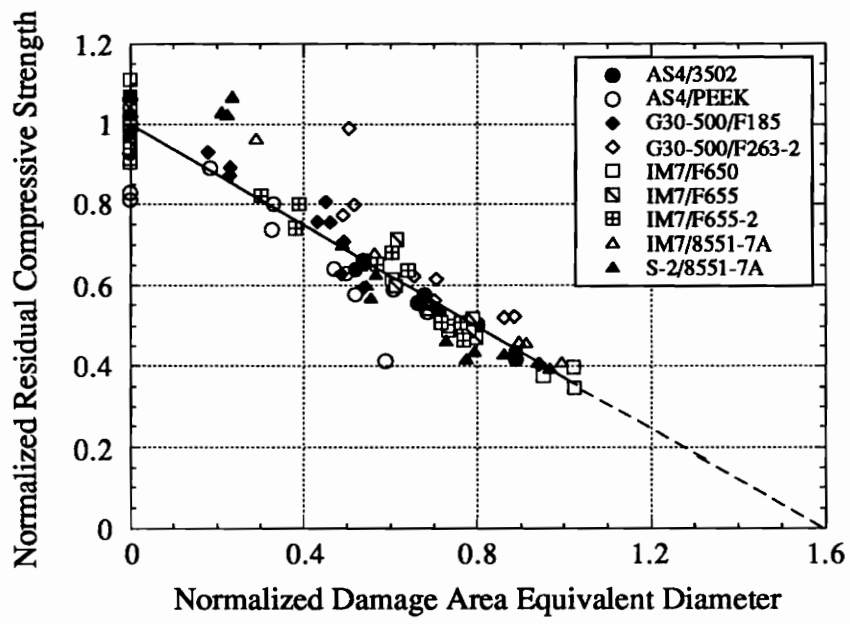**Fig. 5.19** Variation of (a) residual compressive strength with impact velocity and (b) normalized residual compressive strength with normalized impact velocity for IM7/F650, IM7/F655 and IM7/F655-2.
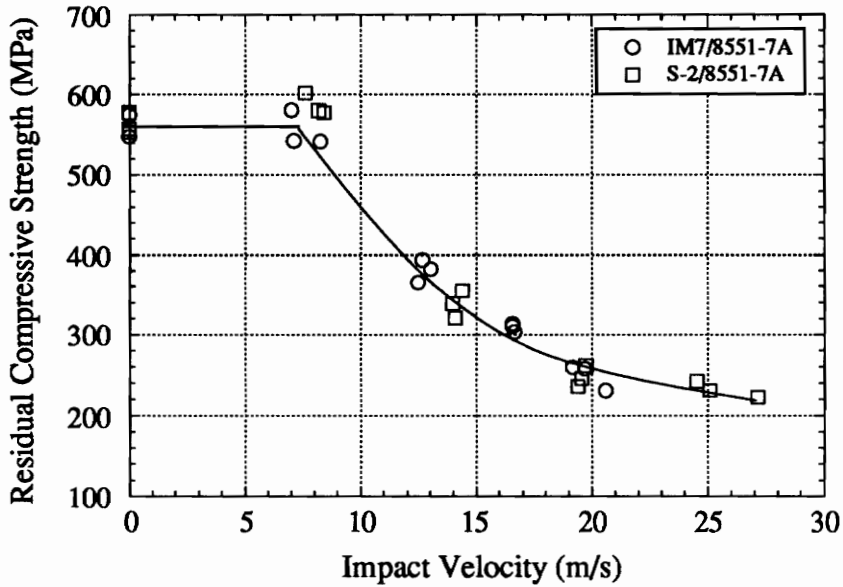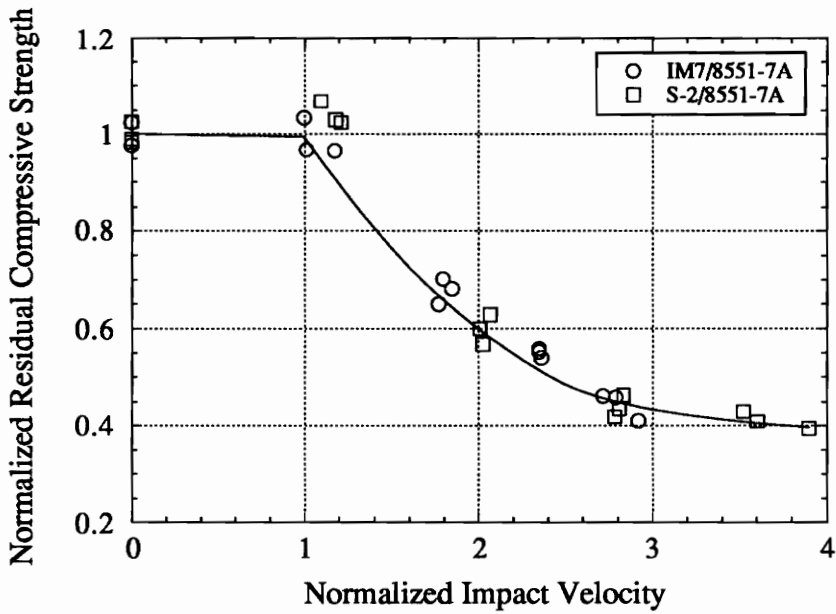
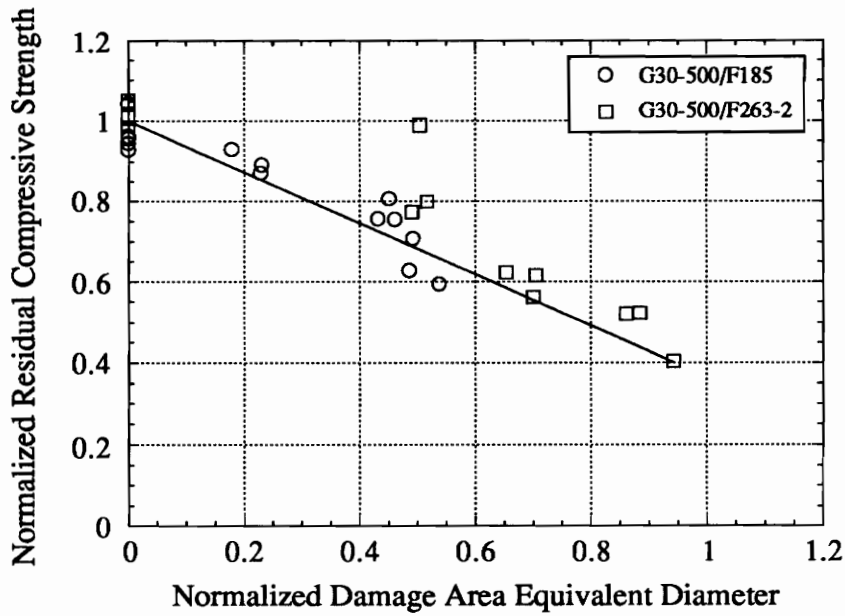**Fig. 5.20** Variation of (a) residual compressive strength with impact velocity and (b) normalized residual compressive strength with normalized impact velocity for IM7/8551-7A and S-2/8551-7A.
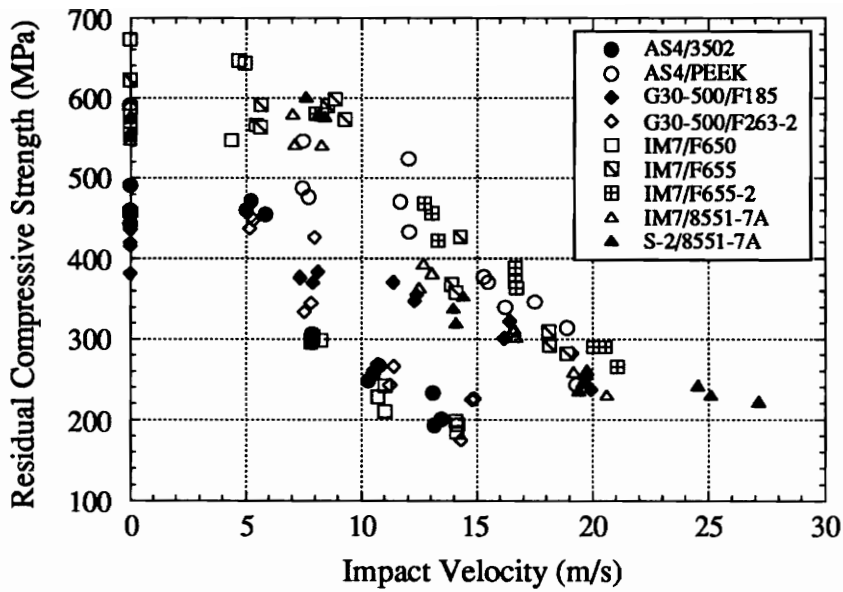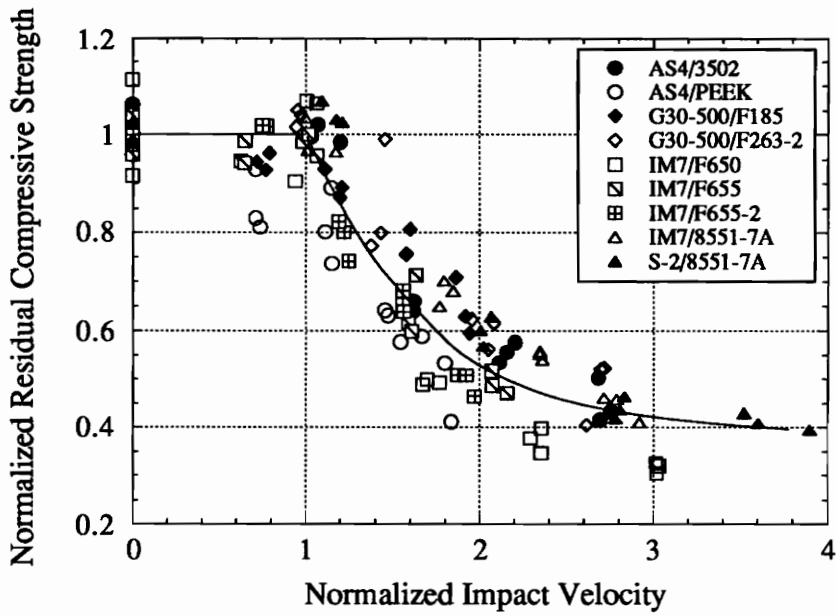
Fig. 5.21 Variation of (a) residual compressive strength with impact velocity and (b) normalized residual compressive strength with normalized impact velocity for each material system.
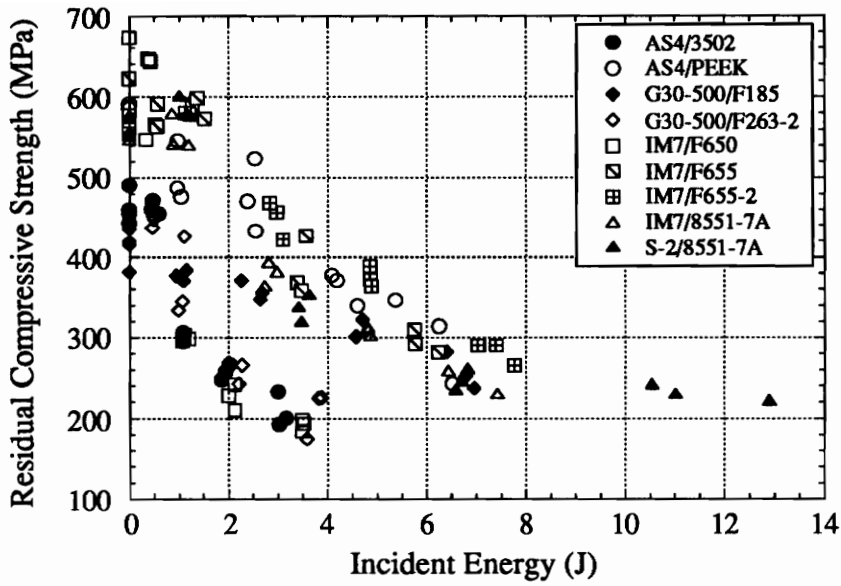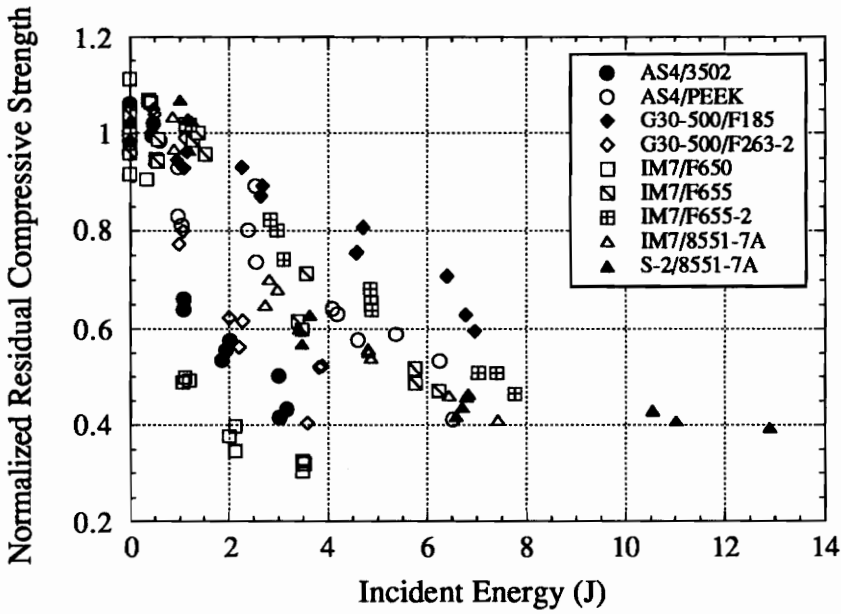
Fig. 5.22 Variation of (a) residual compressive strength and (b) normalized residual compressive strength with incident energy for each material system.
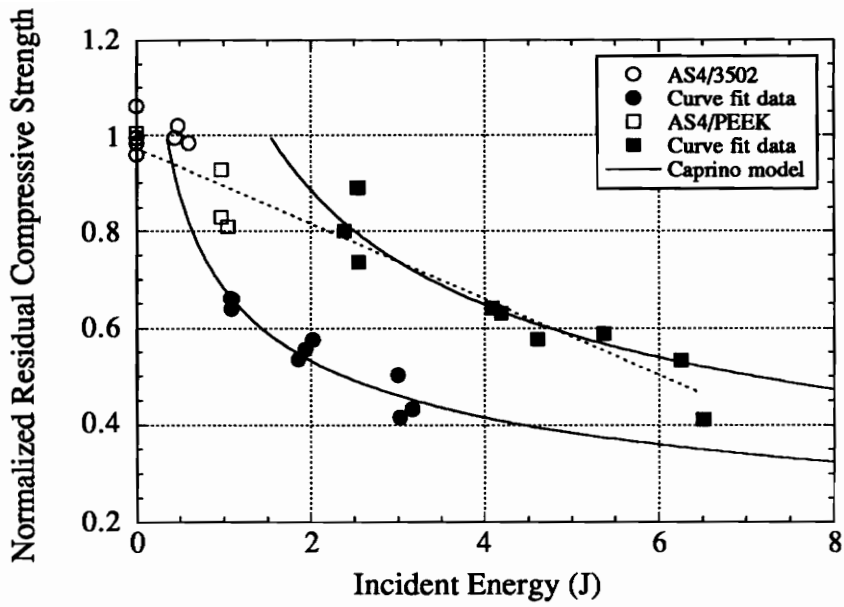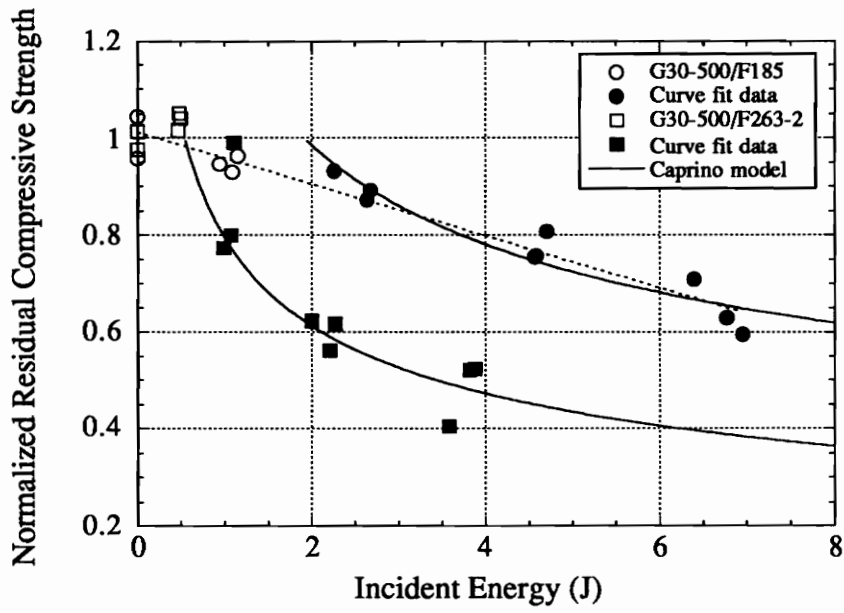
Fig. 5.23 Caprino model of normalized residual compressive strength with incident energy for (a) AS4 and (b) G30-500 fiber systems.
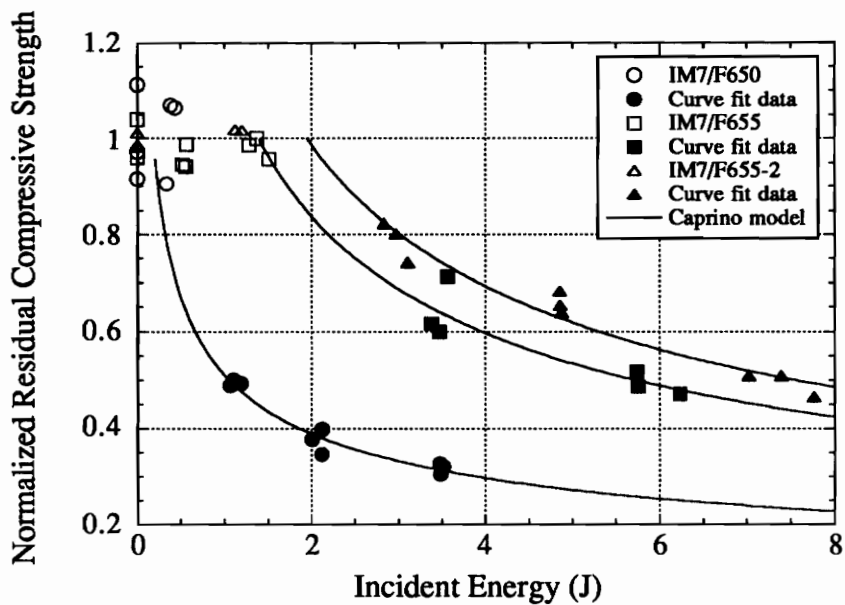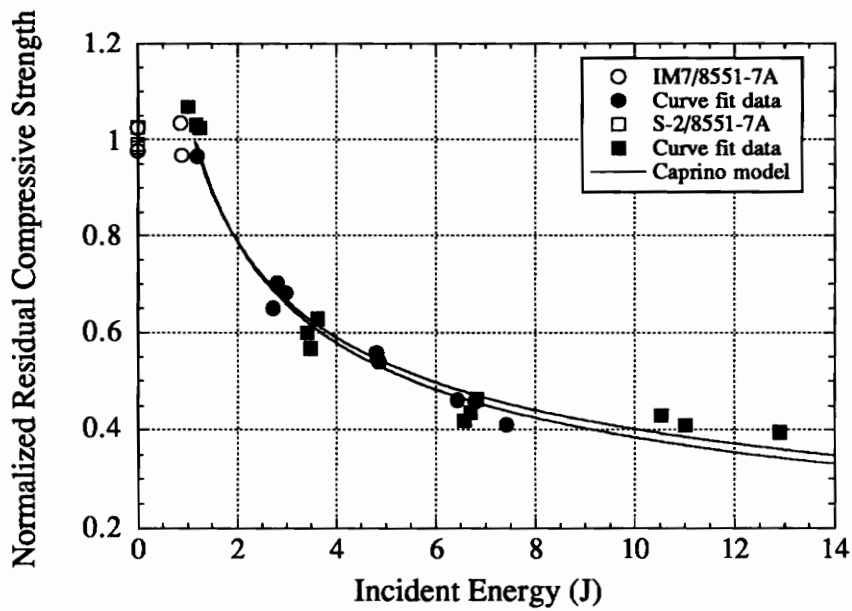
Fig. 5.24 Caprino model of normalized residual compressive strength with incident energy for (a) BMI and (b) rubber toughened epoxy systems.

135
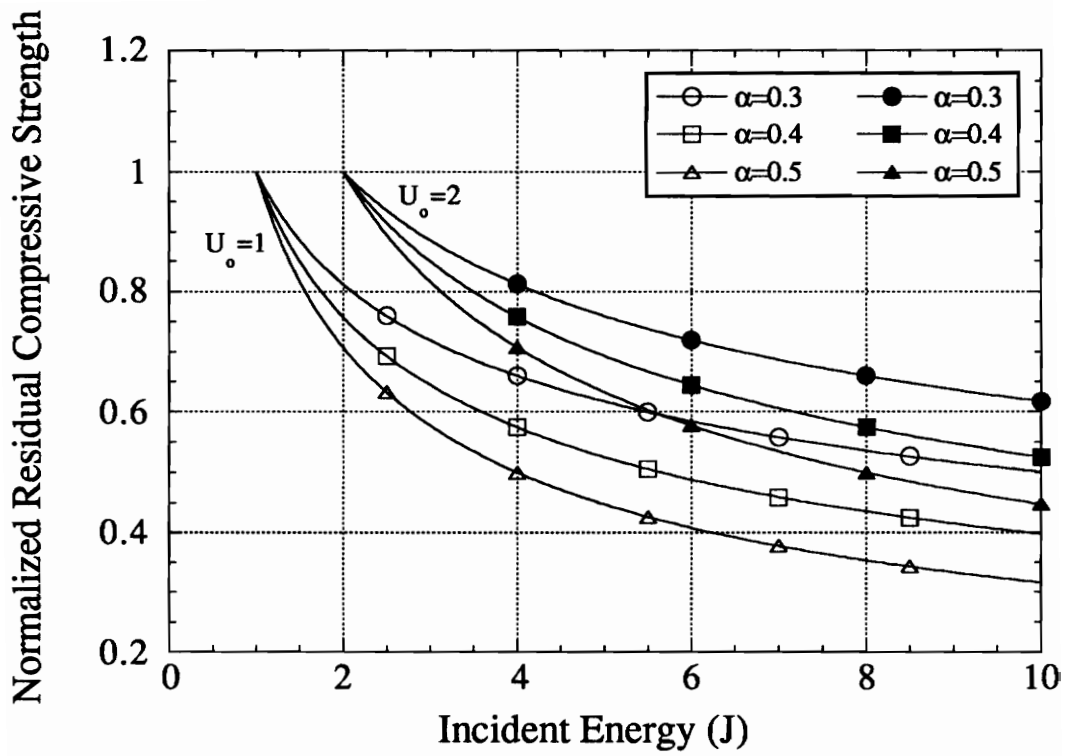
Fig. 5.25 Effects of U_o and α of Caprino model.

136
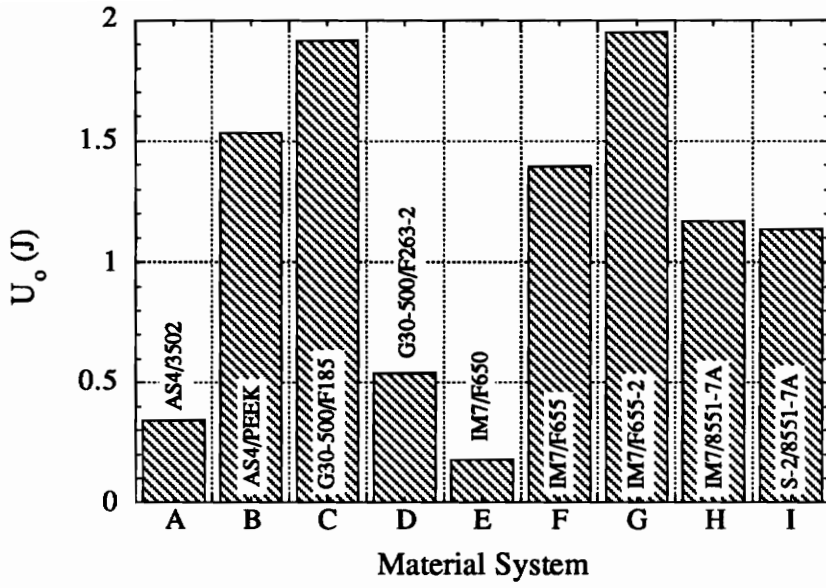
(a)
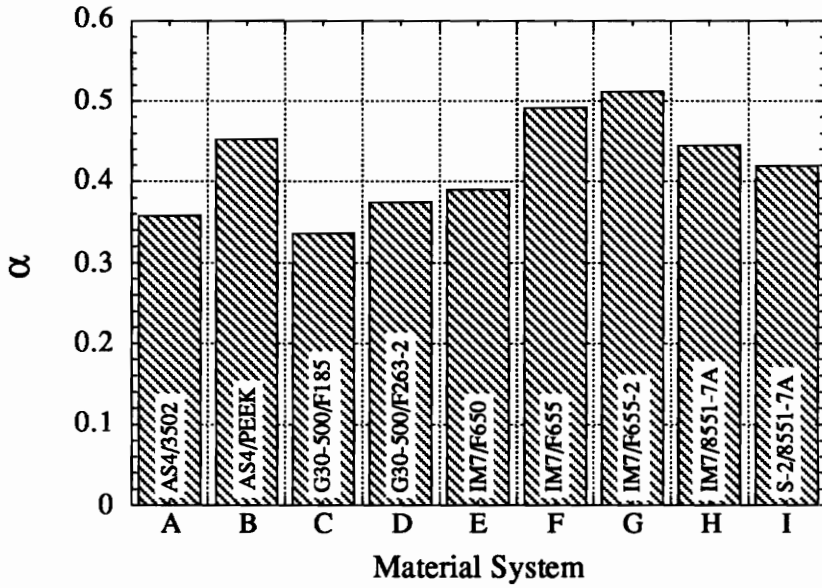
(b)

Fig. 5.26 Caprino model constants (U_o and α) of each material system.

137
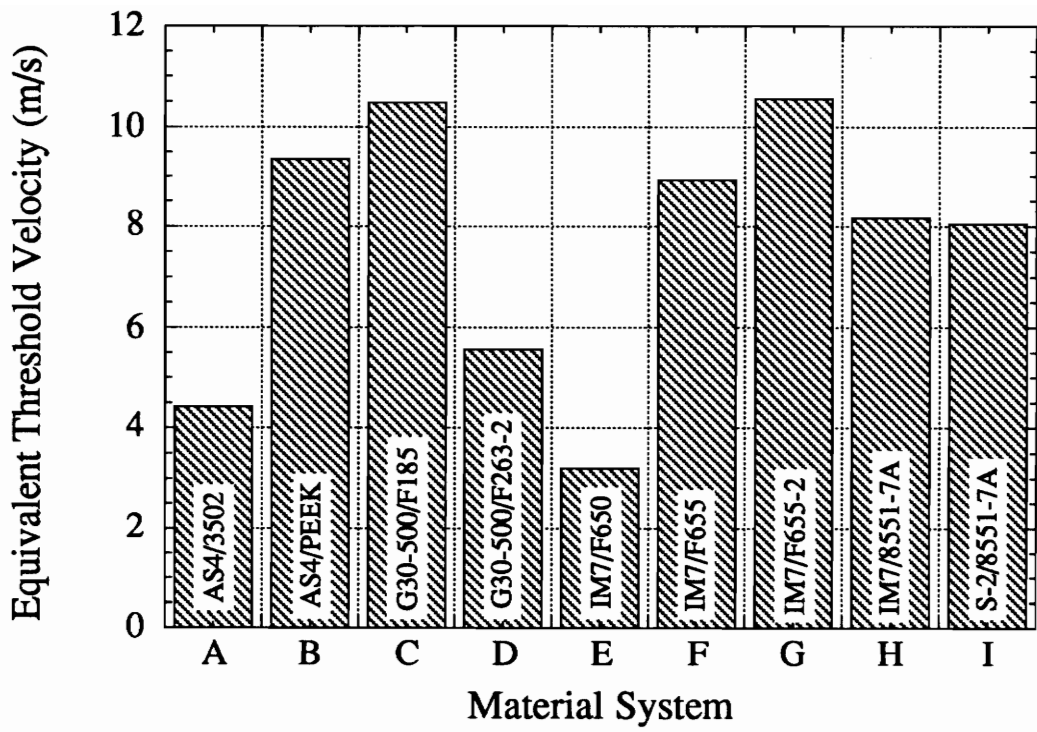
Fig. 5.27 The equivalent threshold velocity of each material system predicted by Caprino model.
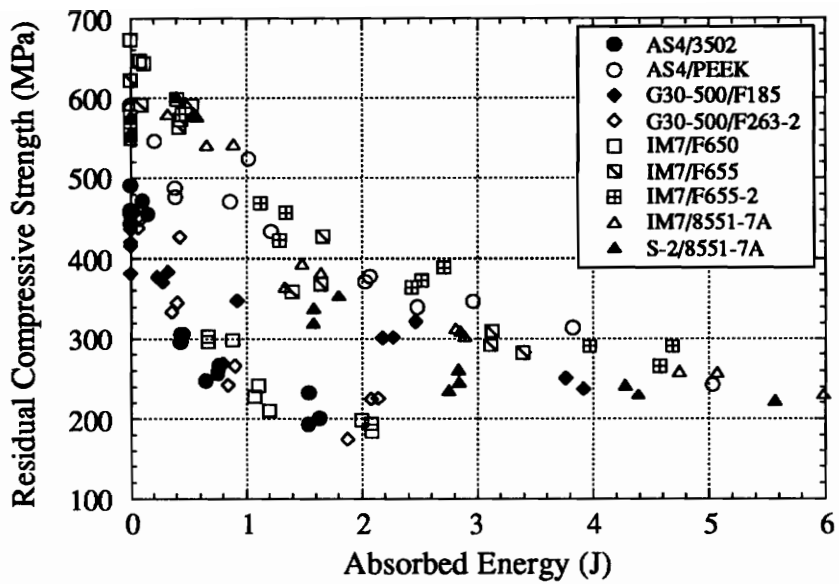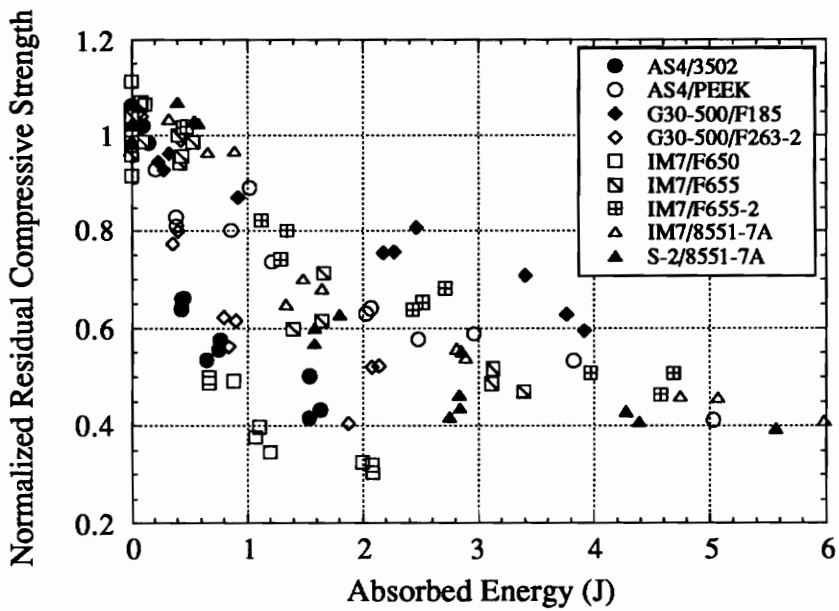
Fig. 5.28 Variation of (a) residual compressive strength and (b) normalized residual compressive strength with absorbed energy for each material system.
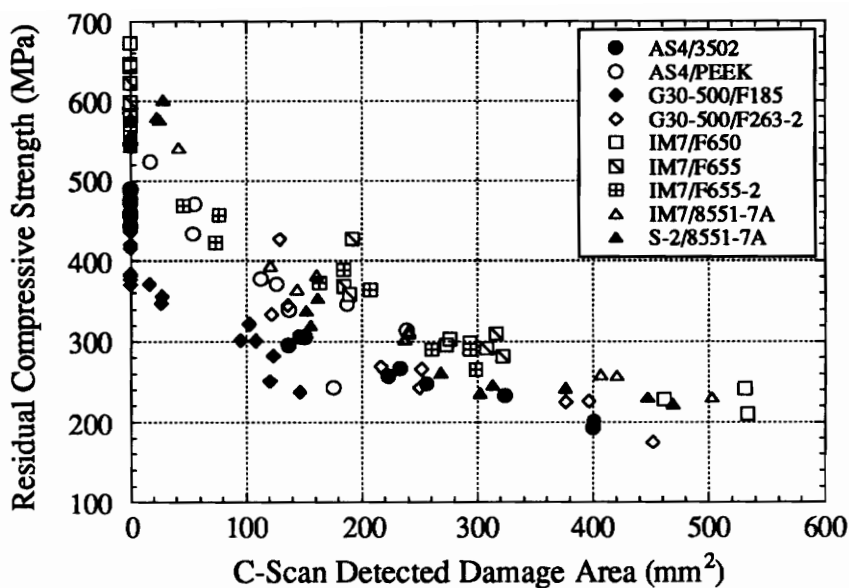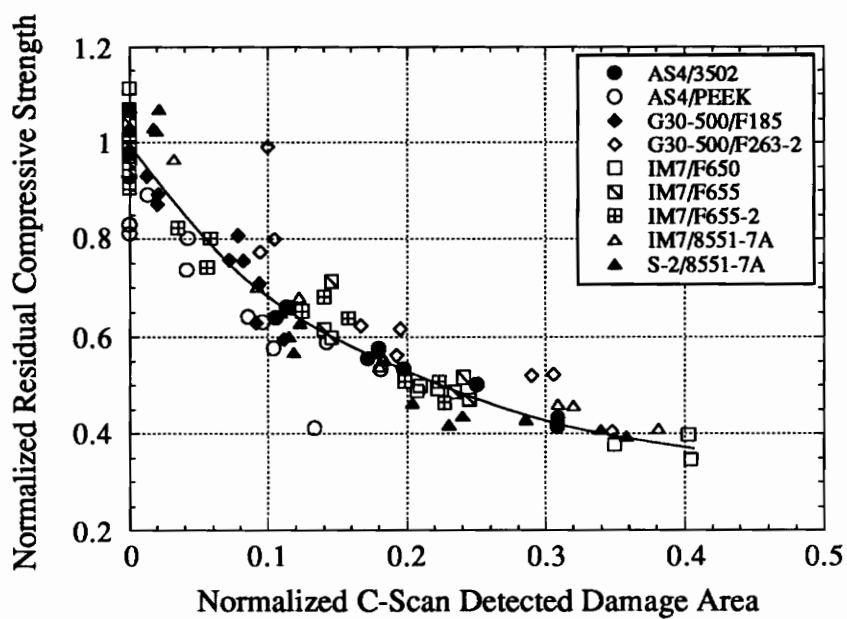
Fig. 5.29 Variation of (a) residual compressive strength with C-scan detected damage area and (b) normalized residual compressive strength with normalized C-scan detected damage area for each material system.
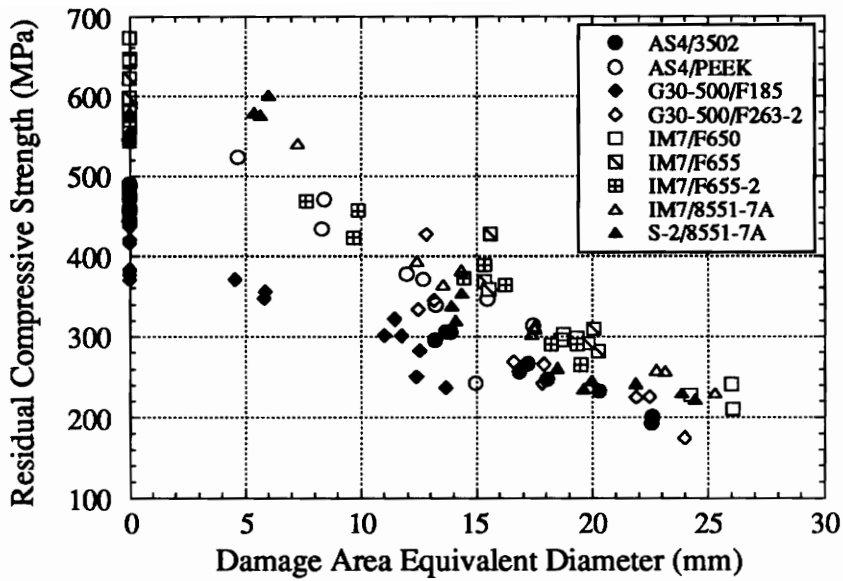
Fig. 5.30 Variation of (a) residual compressive strength with damage area equivalent diameter and (b) normalized residual compressive strength with normalized damage area equivalent diameter for each material system.
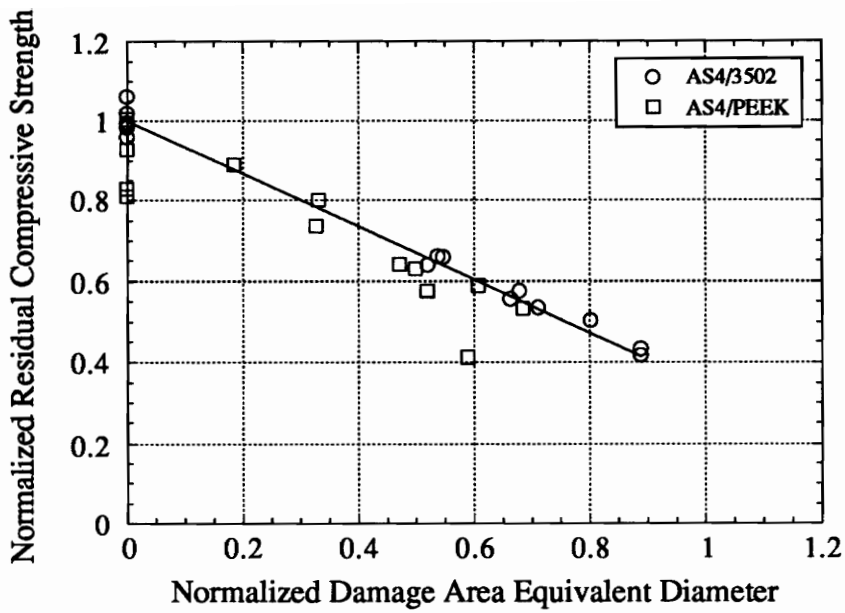
Fig. 5.31 Variation of normalized residual compressive strength with normalized damage area equivalent diameter for (a) AS4 and (b) G30-500 fiber material systems.
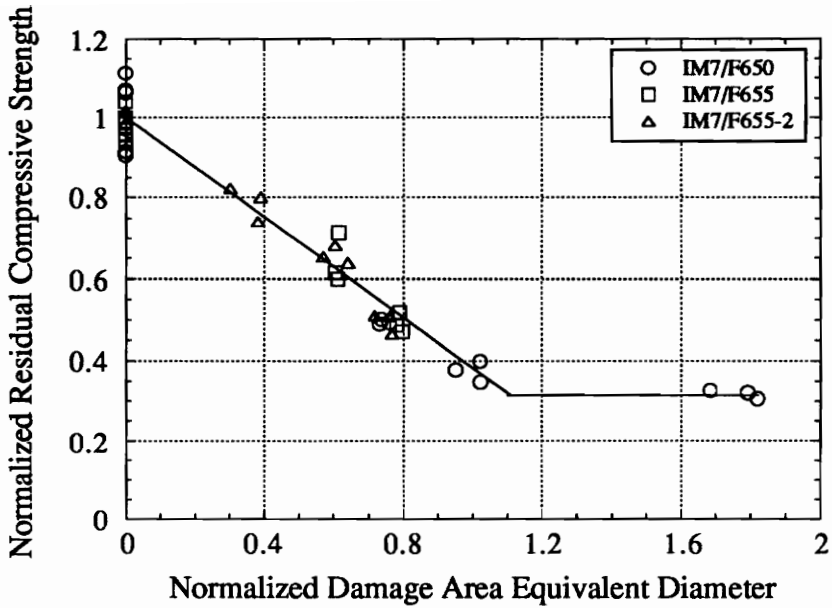
(a)
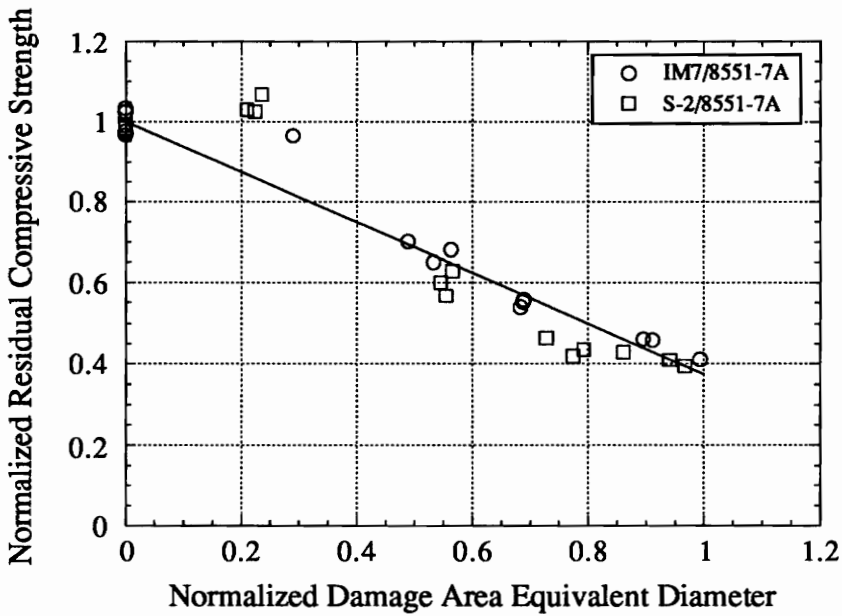
(b)

Fig. 5.32 Variation of normalized residual compressive strength with normalized damage area equivalent diameter for (a) BMI and (b) rubber toughened epoxy matrix material systems.

143
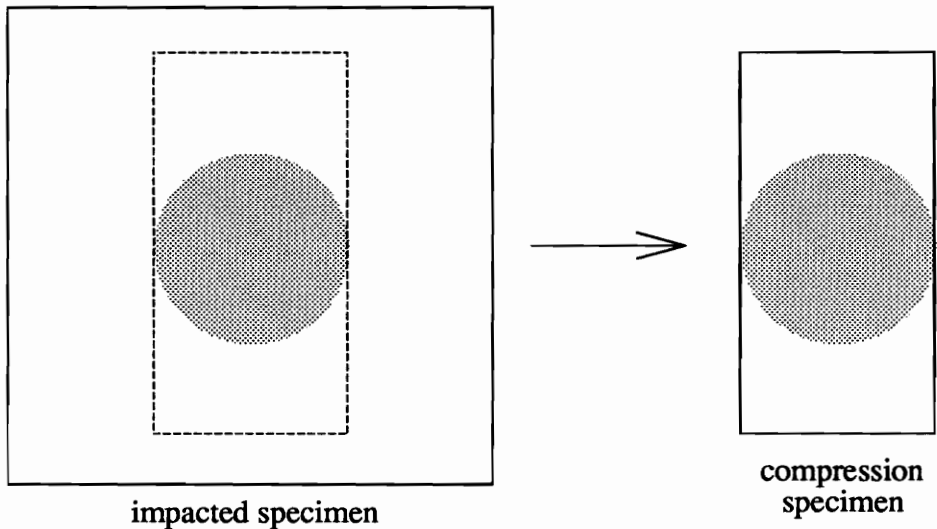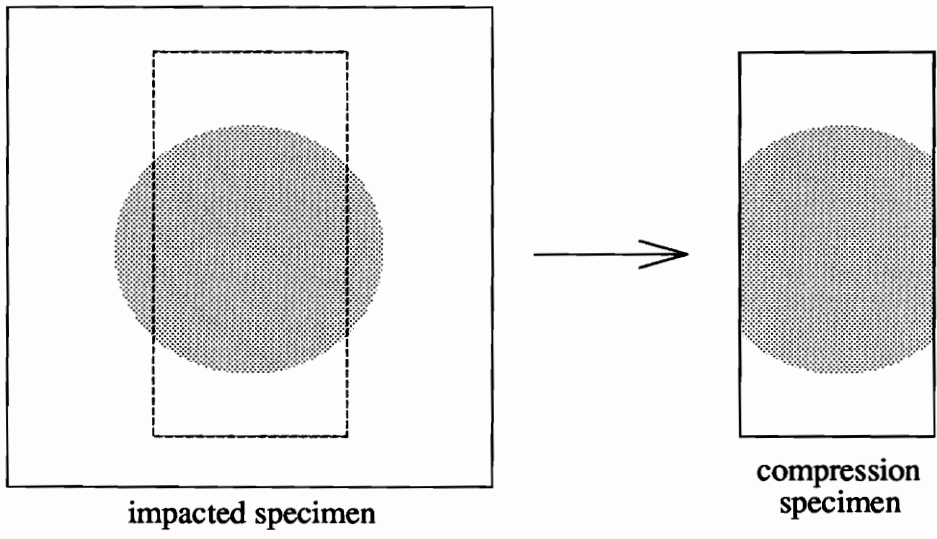
Fig. 5.33 The width of damage (delamination) size in compression specimens which are cut from impacted specimens after impacted with (a) lower and (b) higher velocities.
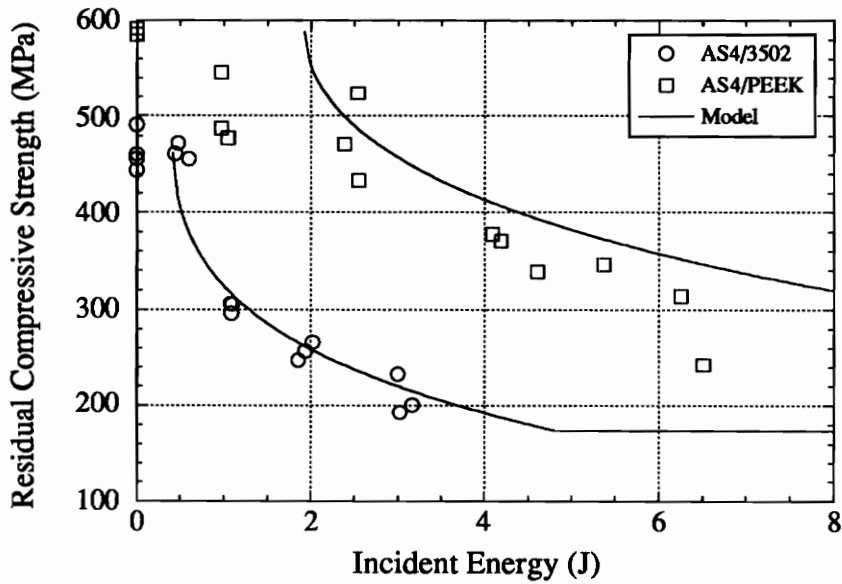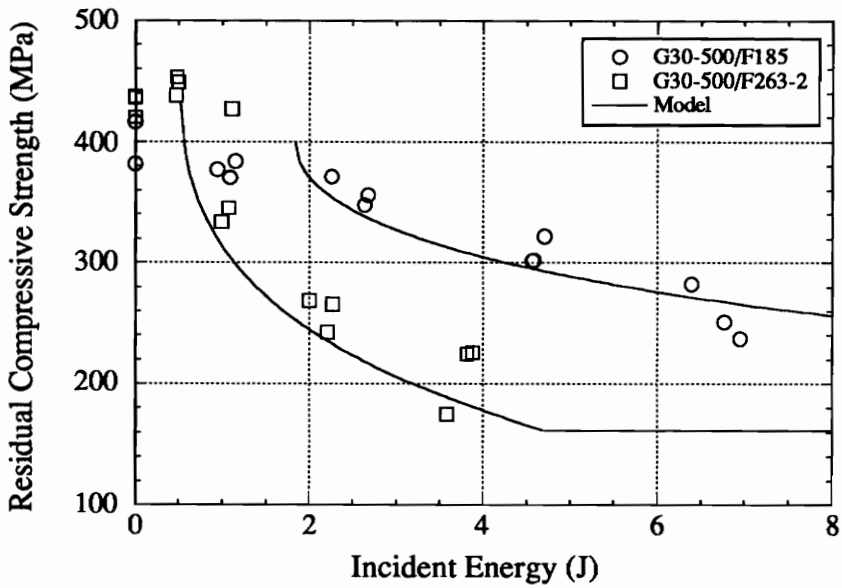
Fig. 5.34 Model prediction of residual compressive strength with incident energy for (a) AS4 and (b) G30-500 fiber material systems.
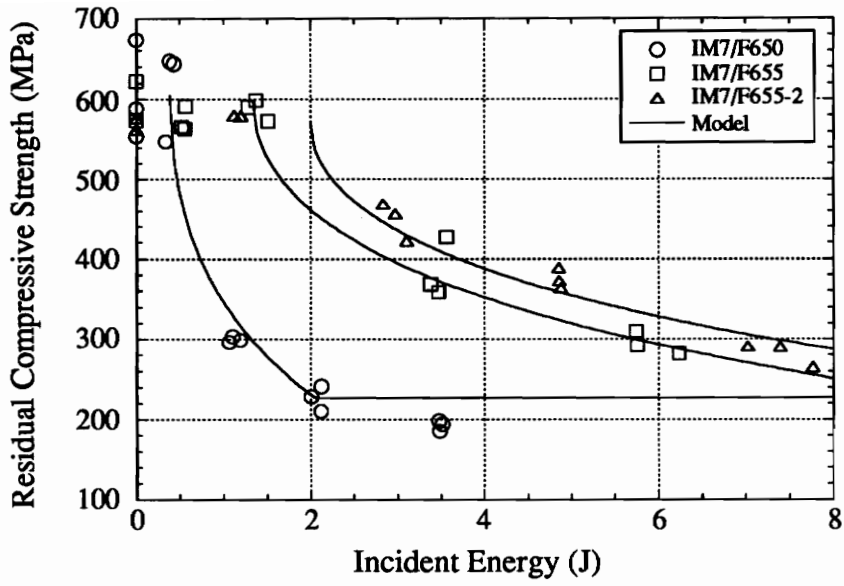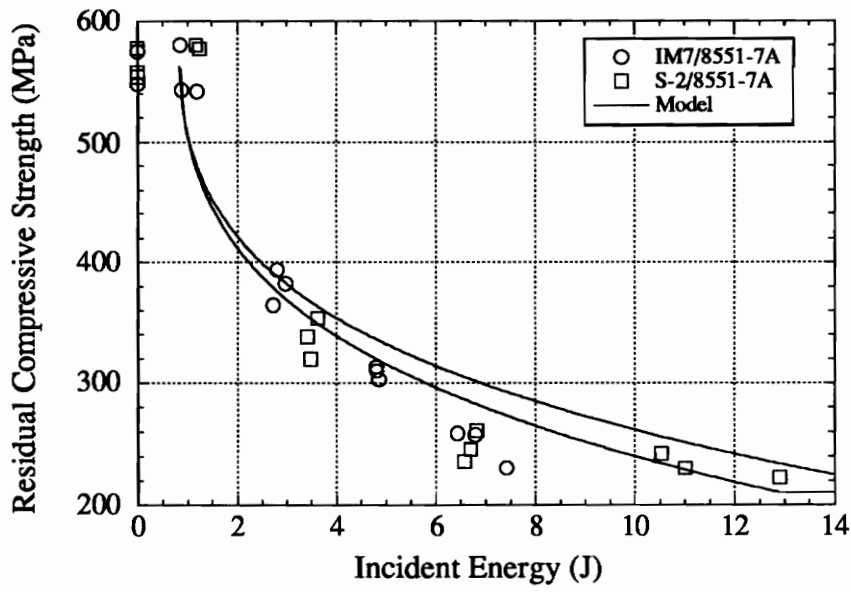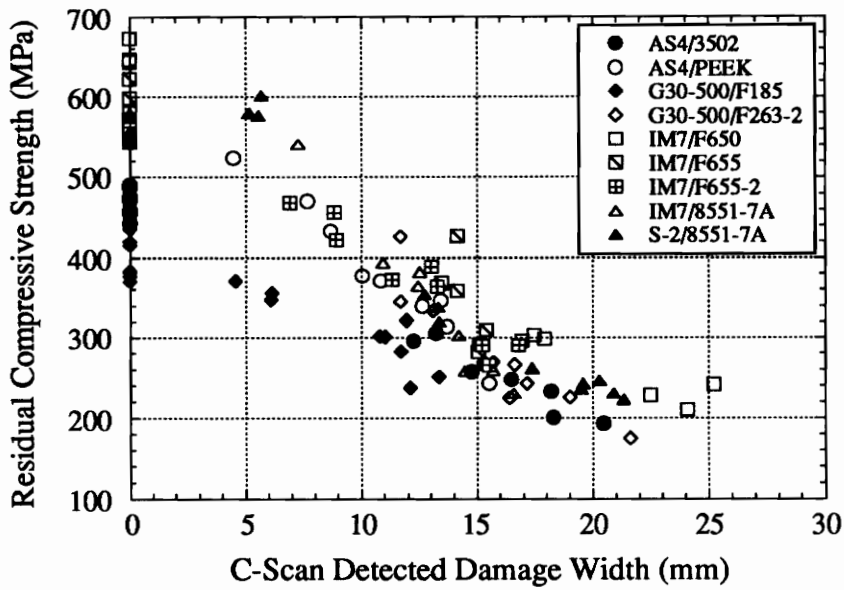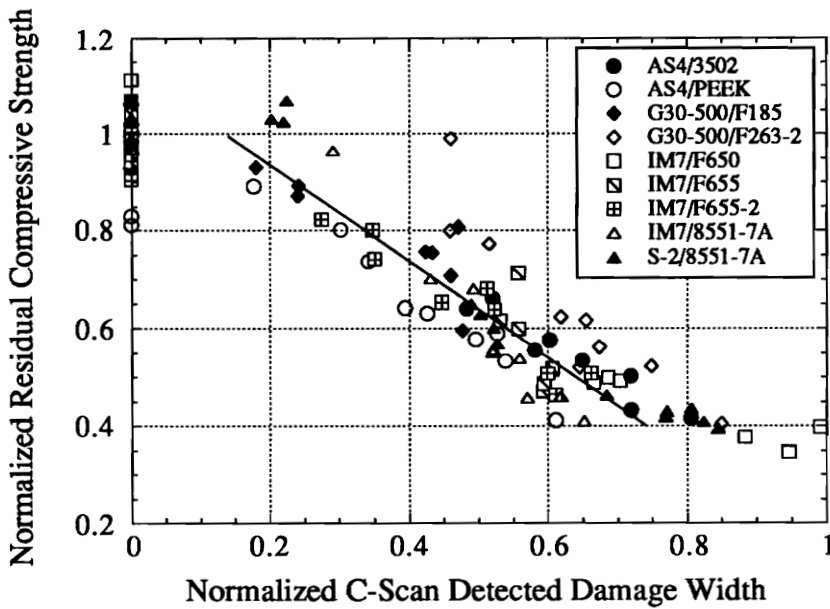
Fig. 5.35 Model prediction of residual compressive strength with incident energy for (a) BMI and (b) rubber toughened epoxy matrix material systems.
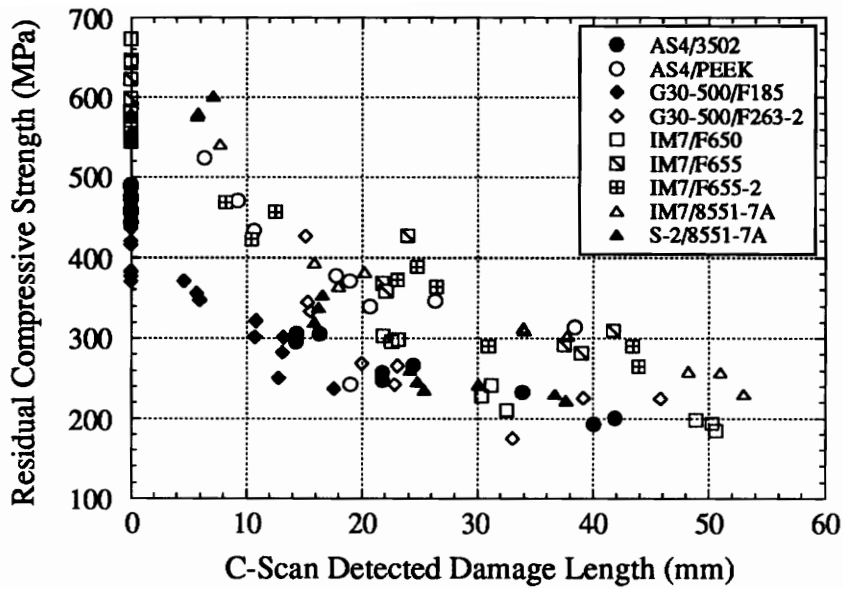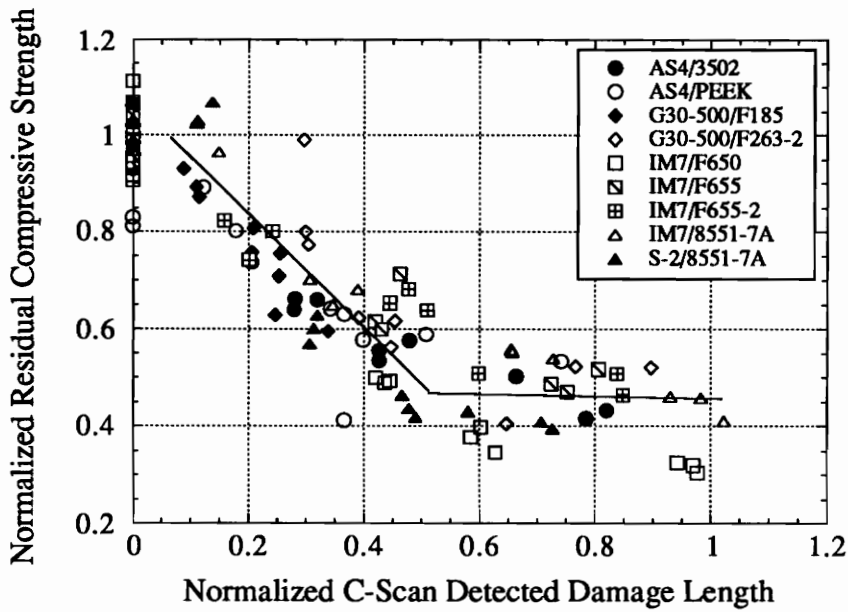
Fig. 5.36 Variation of (a) residual compressive strength with damage width and (b) normalized residual compressive strength with normalized damage width for each material system.

Fig. 5.37 Variation of (a) residual compressive strength with damage length and (b) normalized residual compressive strength with normalized damage length for each material system.
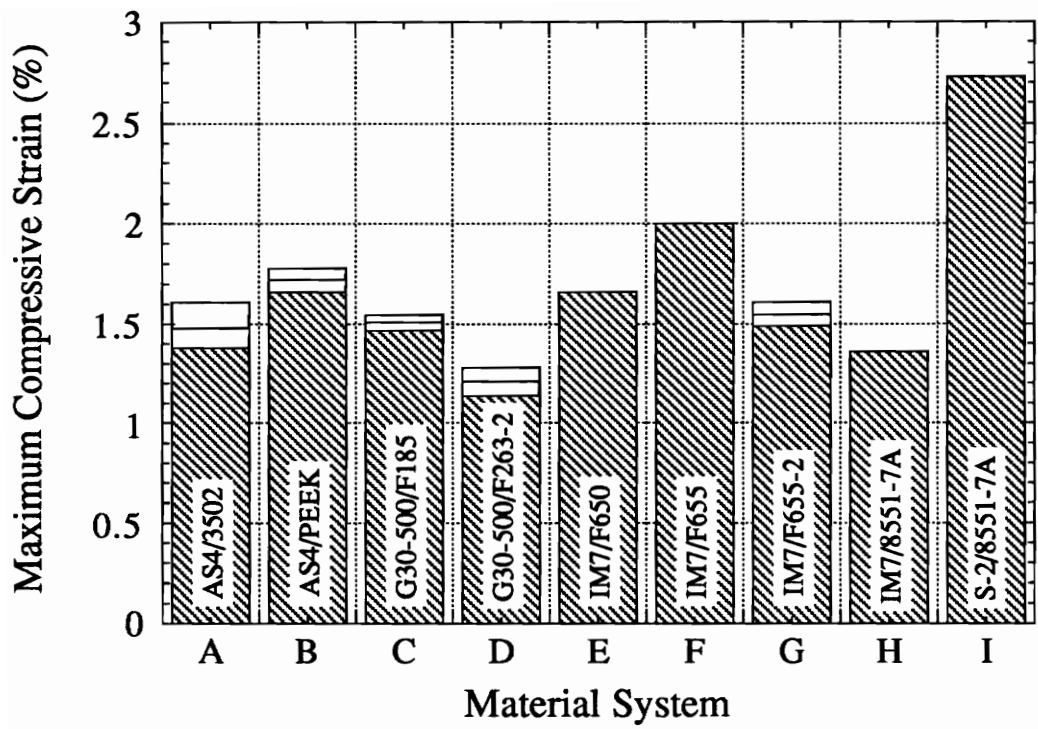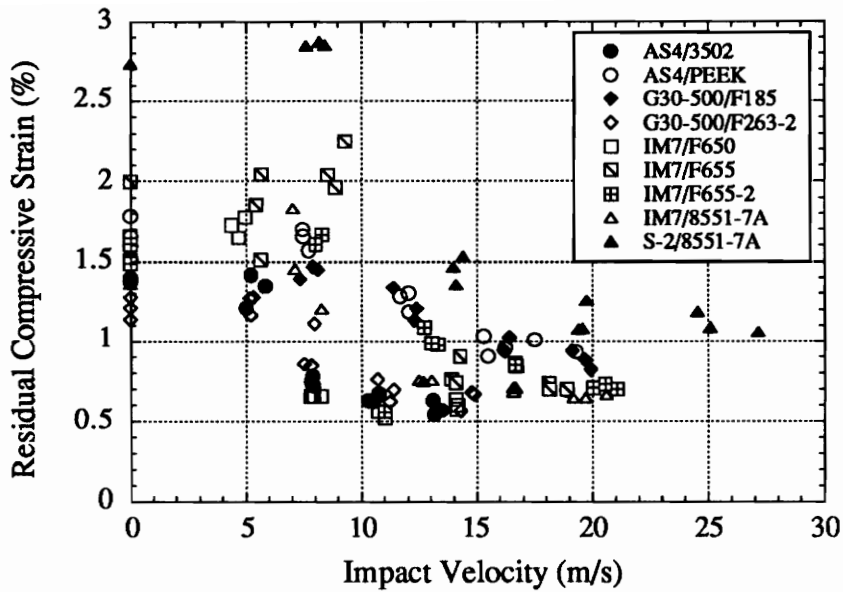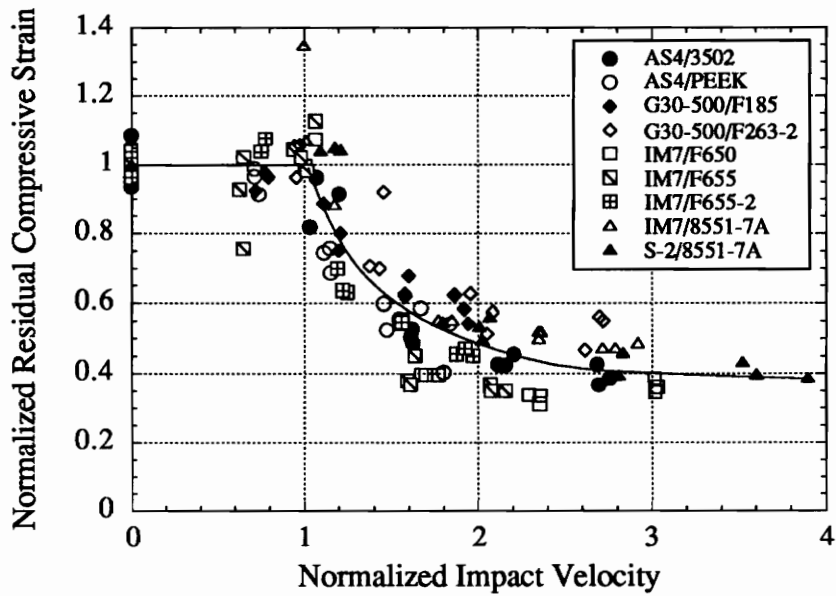
Fig. 5.38 Maximum compressive strain of each material system.

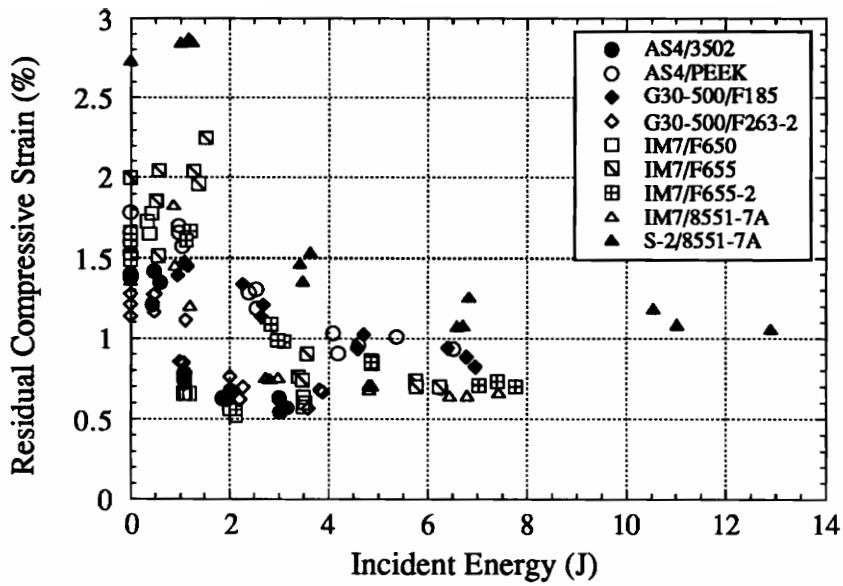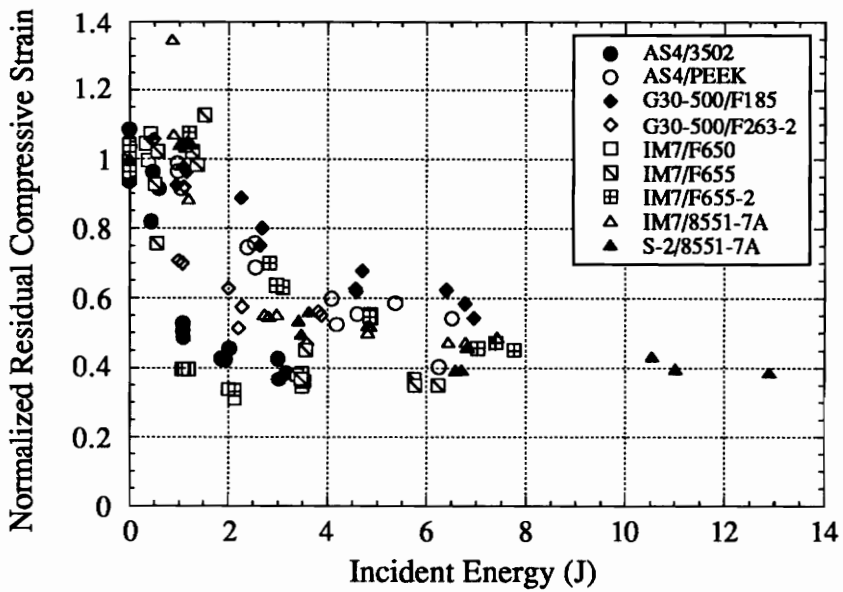**Fig. 5.39** Variation of (a) residual compressive strength with impact velocity and (b) normalized residual compressive strain with normalized impact velocity for each material system.
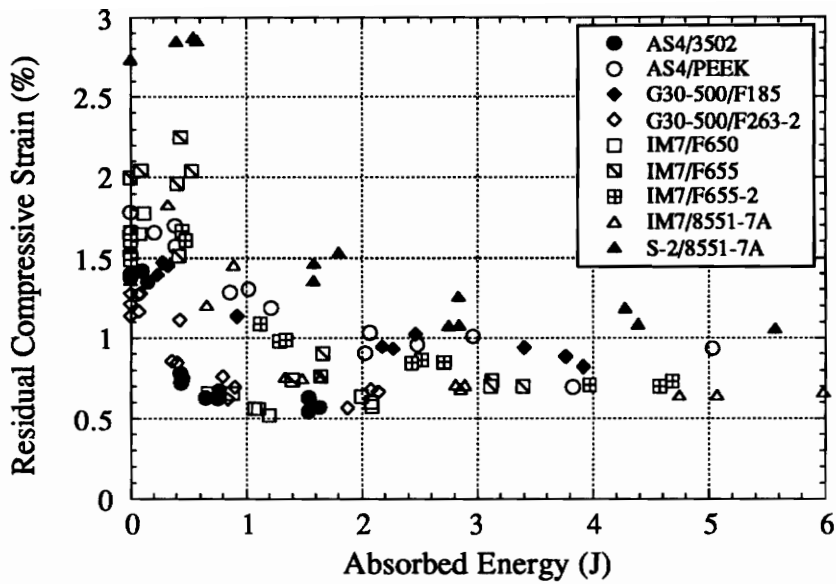
150

Fig. 5.40 Variation of (a) residual compressive strain and (b) normalized residual compressive strain with incident energy for each material system.
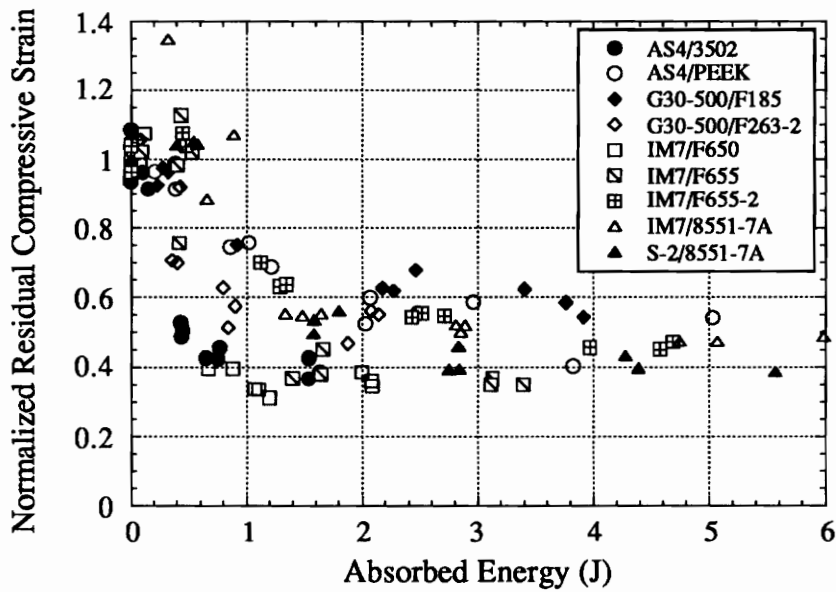
151

Fig. 5.41 Variation of (a) residual compressive strain and (b) normalized residual compressive strain with absorbed energy for each material system.

152
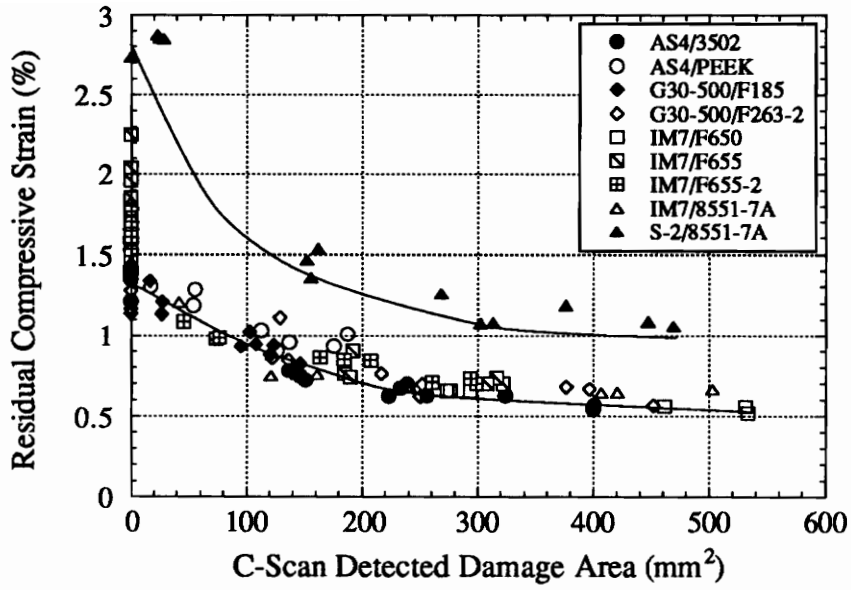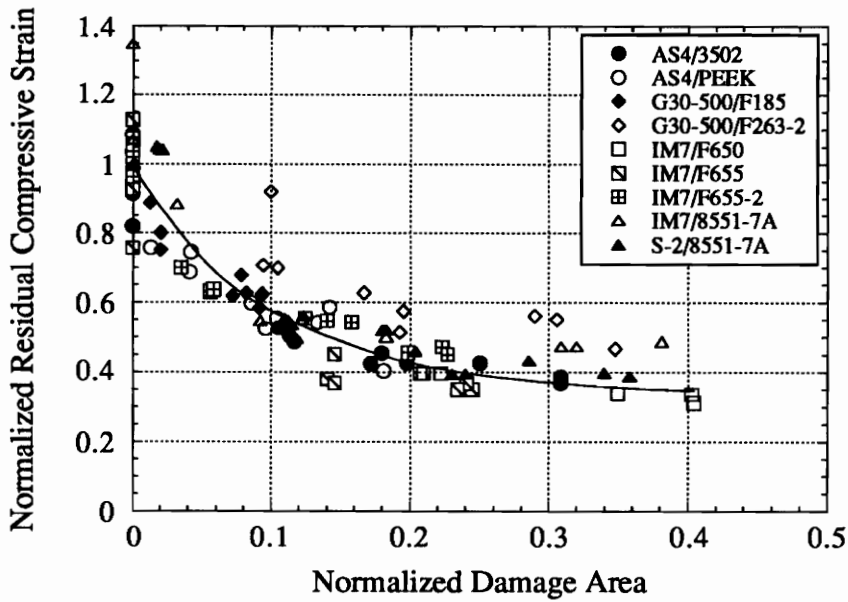
Fig. 5.42 Variation of (a) residual compressive strain with C-scan detected damage area and (b) normalized residual compressive strain with normalized damage area for each material system.

Fig. 5.43 Variation of (a) residual compressive strain with damage area equivalent diameter and (b) normalized residual compressive strain with normalized damage area equivalent diameter for each material system.

154
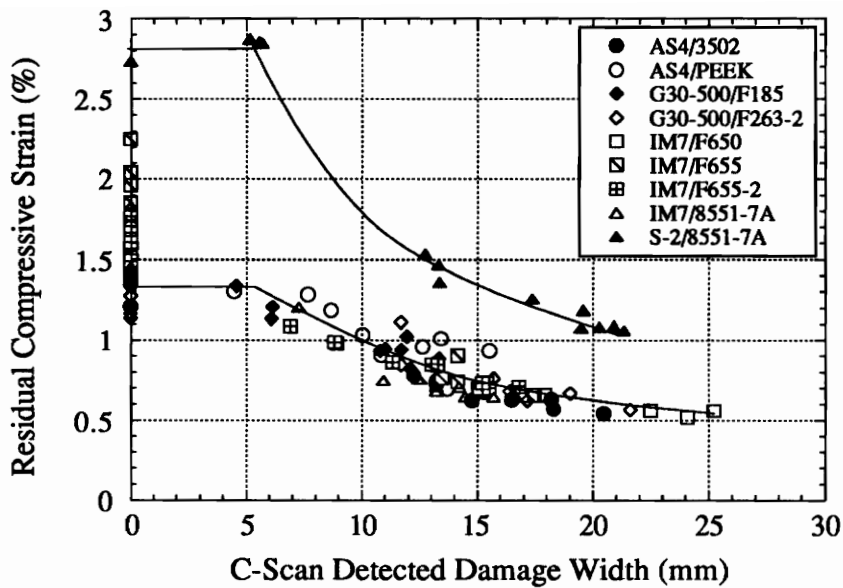
(a)
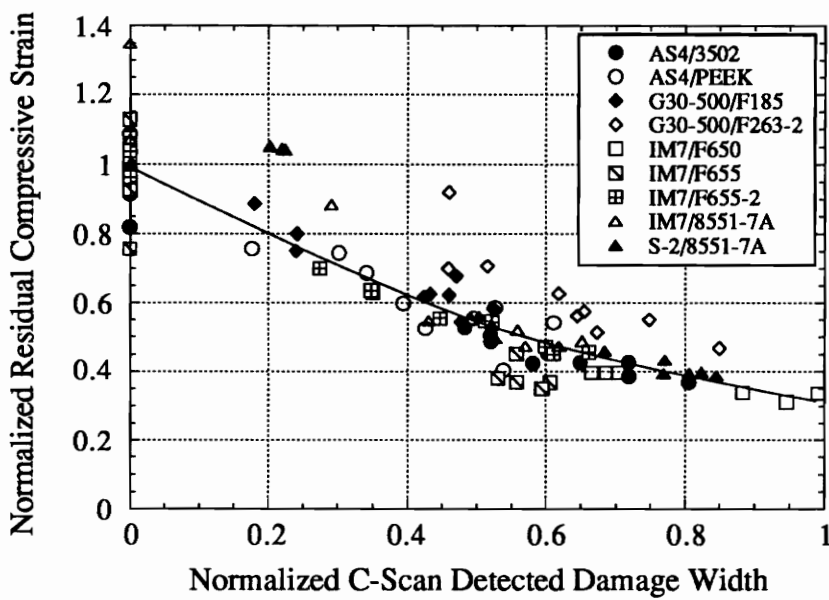
(b)

Fig. 5.44 Variation of (a) residual compressive strain with C-scan detected damage width and (b) normalized residual compressive strain with normalized C-scan detected damage width for each material system.
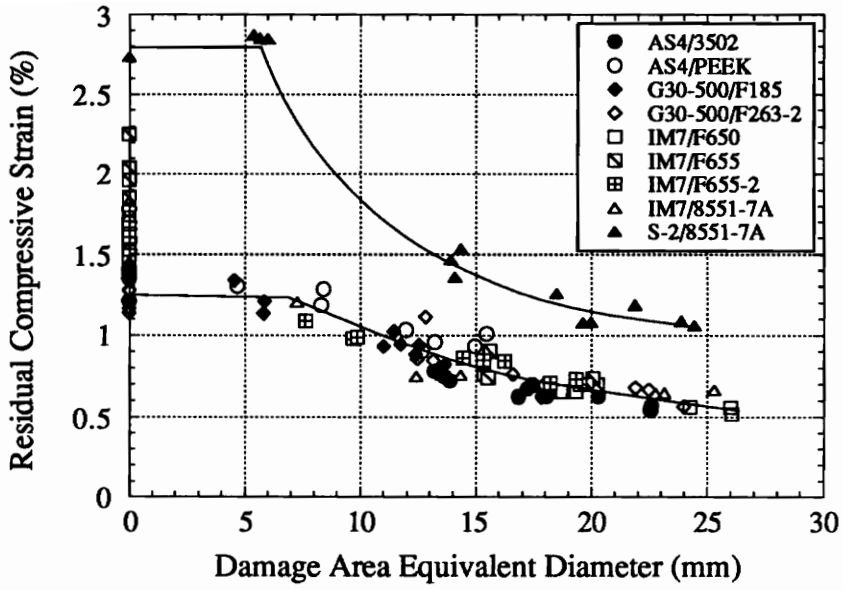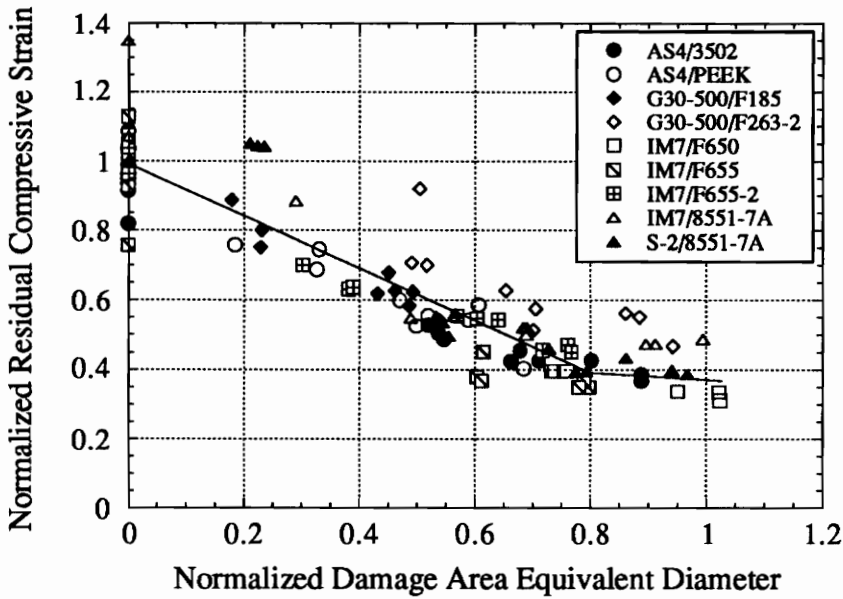
155
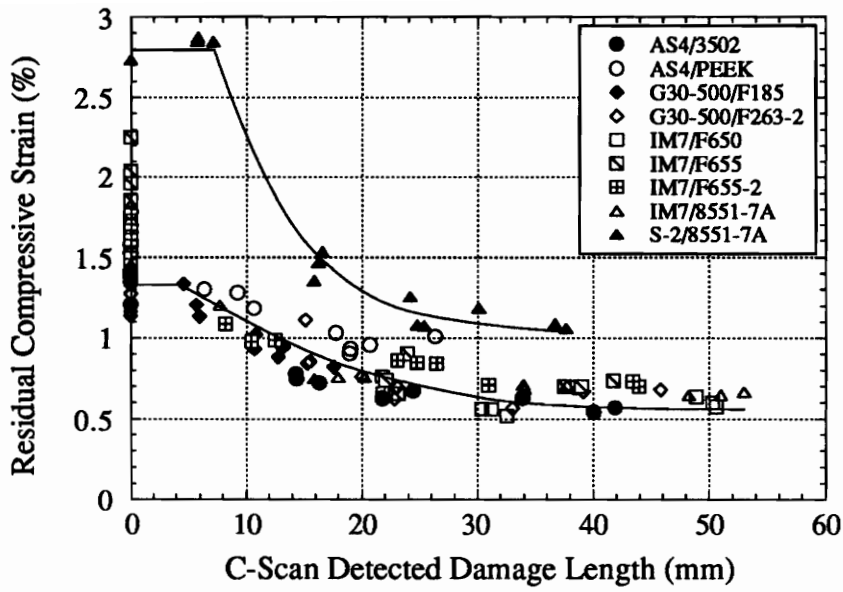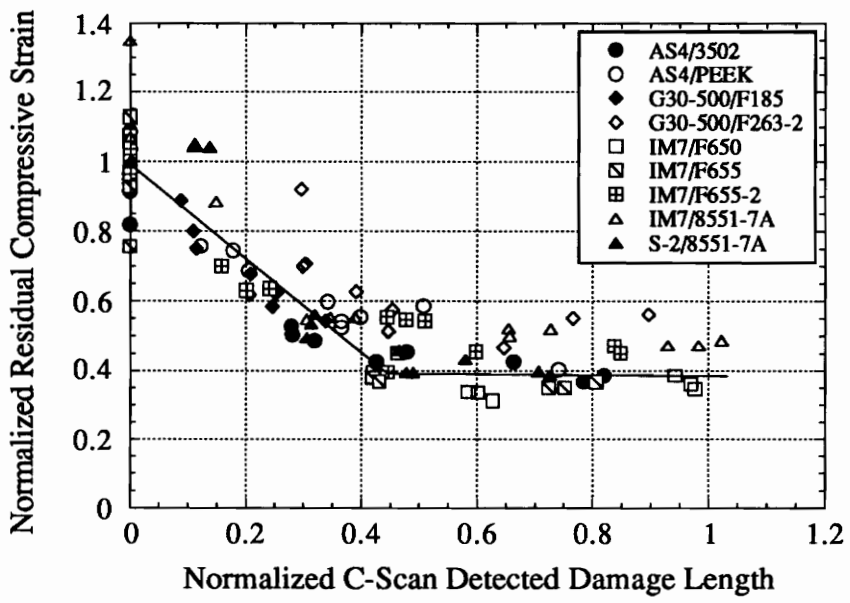
Fig. 5.45 Variation of (a) residual compressive strain with C-scan detected damage length and (b) normalized residual compressive strain with normalized C-scan detected damage length for each material system.

Indentation Force

Indentor (Impactor Head)
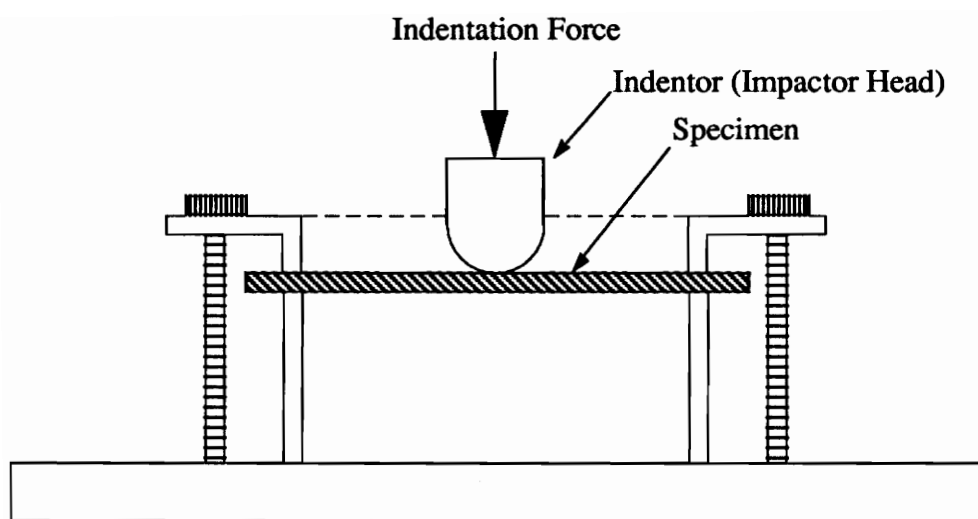
Specimen

Fig. 6.1 Schematic diagram of the quasi-static indentation test setup.
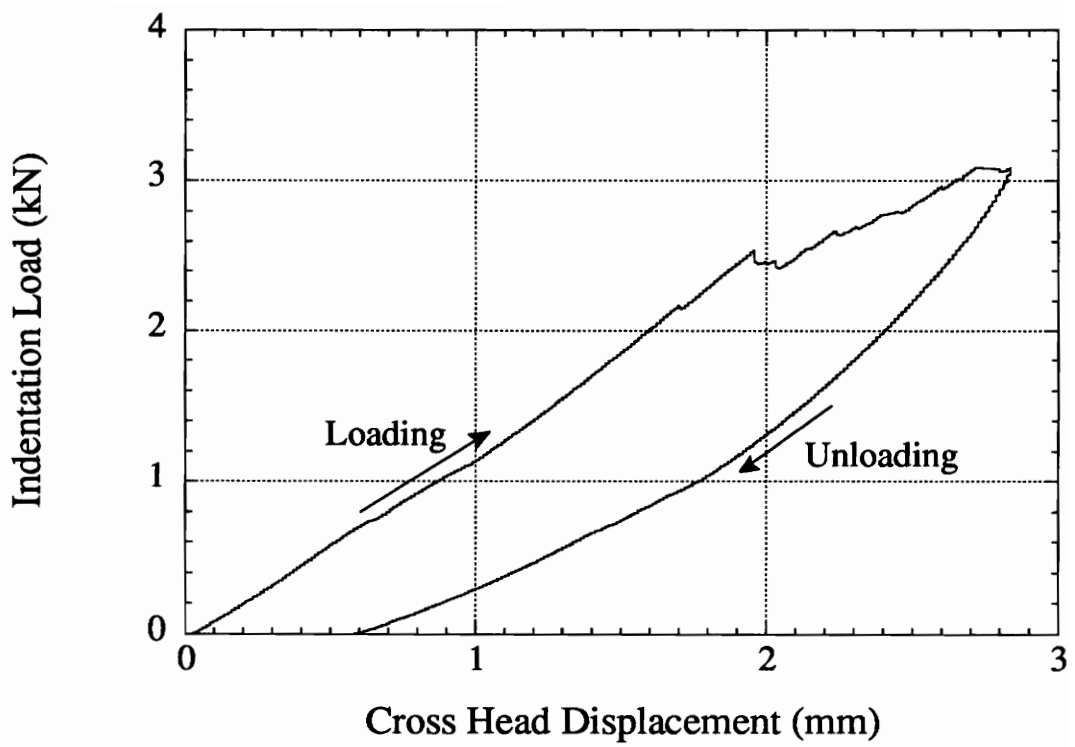
Fig. 6.2 The original recorded indentation load-crosshead displacement curve of a AS4/PEEK specimen.

158
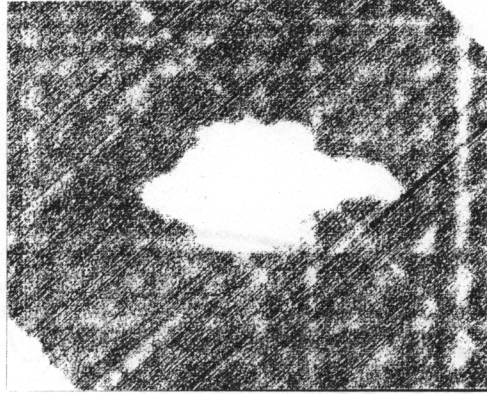
(a)
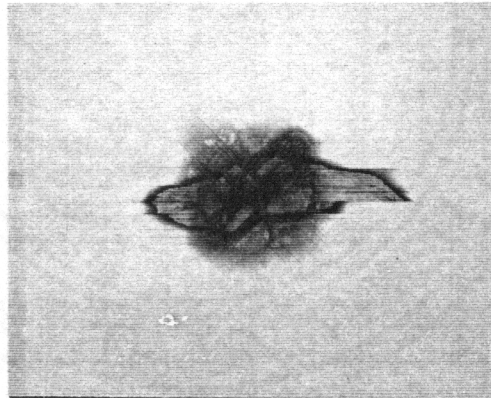
(b)

Fig. 6.3 (a) Ultra-sonic C-scan image and (b) X-ray radiograph of AS4/3502 specimen after quasi-static loaded to 2.4 kN. The surface 0° ply is in horizontal direction.

159
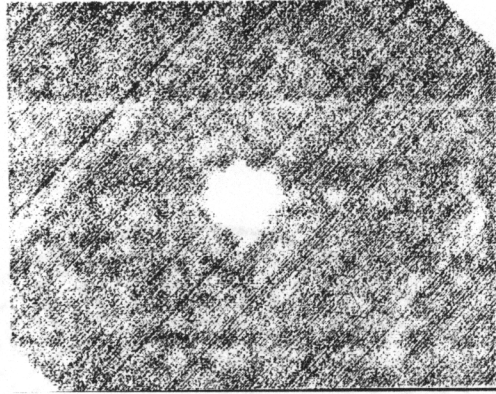
(a)
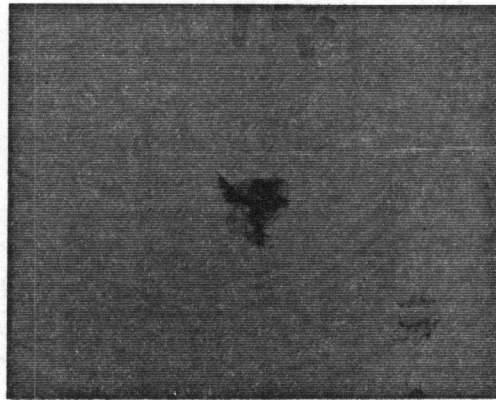
(b)

Fig. 6.4 (a) Ultra-sonic C-scan image and (b) X-ray radiograph of AS4/PEEK specimen after quasi-static loaded to 3.1 kN. The surface 0° ply is in horizontal direction.
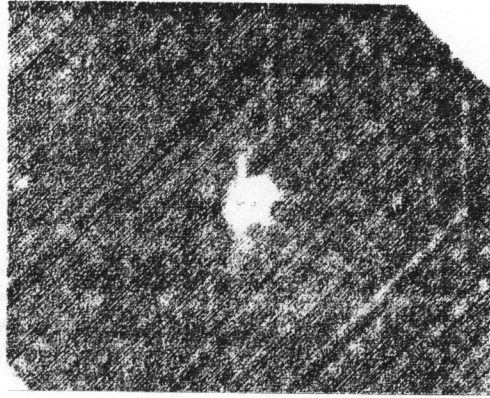
(a)
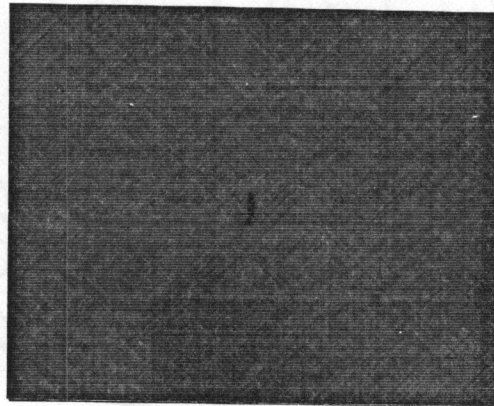
(b)

Fig. 6.5 (a) Ultra-sonic C-scan image and (b) X-ray radiograph of G30-500/F185 specimen after quasi-static loaded to 3.1 kN. The surface 0° ply is in horizontal direction.

161
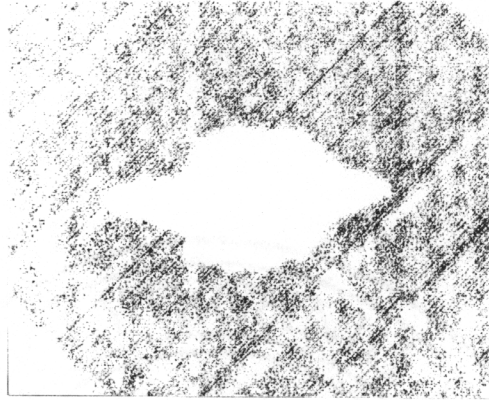
(a)
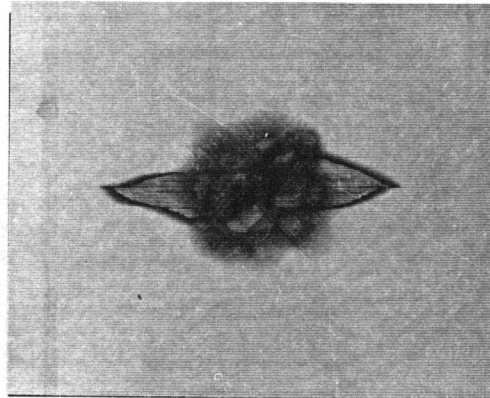
(b)

Fig. 6.6 (a) Ultra-sonic C-scan image and (b) X-ray radiograph of G30-500/F263-2 specimen after quasi-static loaded to 2.9 kN. The surface 0° ply is in horizontal direction.
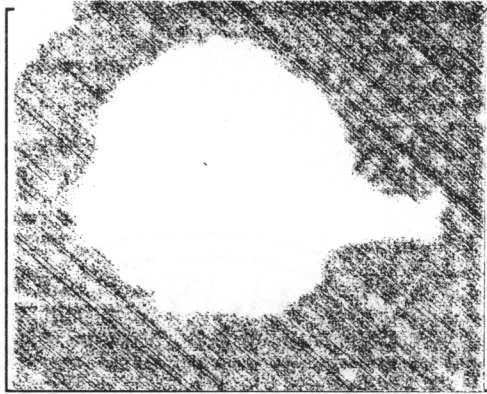
(a)
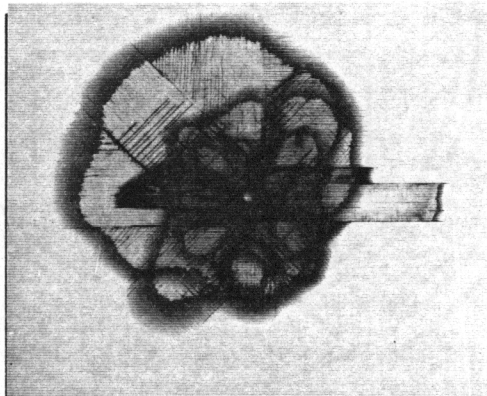
(b)

Fig. 6.7 (a) Ultra-sonic C-scan image and (b) X-ray radiograph of IM7/F650 specimen after quasi-static loaded to 3.1 kN. The surface 0° ply is in horizontal direction.
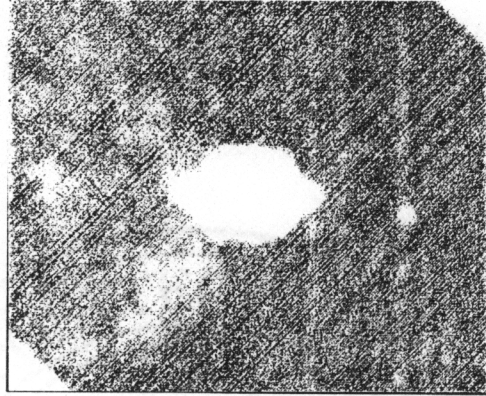
(a)
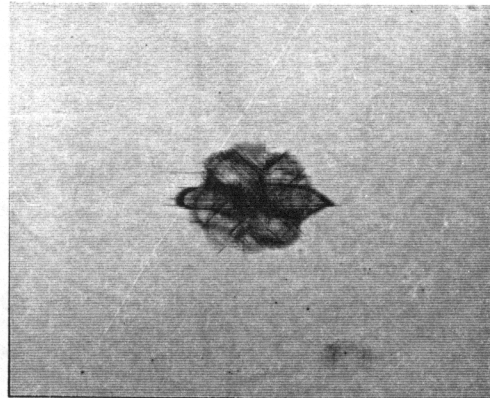
(b)

Fig. 6.8 (a) Ultra-sonic C-scan image and (b) X-ray radiograph of IM7/F655 specimen after quasi-static loaded to 3.1 kN. The surface 0° ply is in horizontal direction.
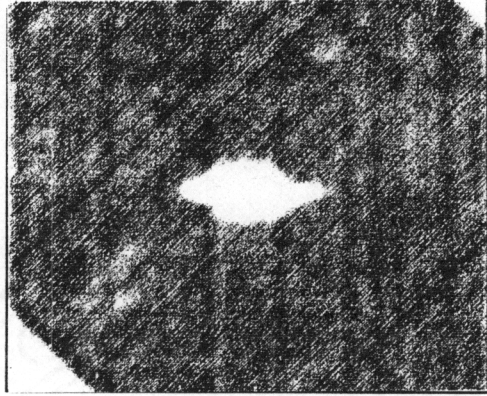
(a)
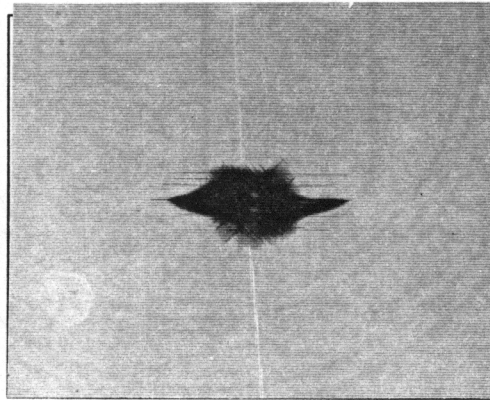
(b)

Fig. 6.9 (a) Ultra-sonic C-scan image and (b) X-ray radiograph of IM7/F655-2 specimen after quasi-static loaded to 3.1 kN. The surface 0° ply is in horizontal direction.

165
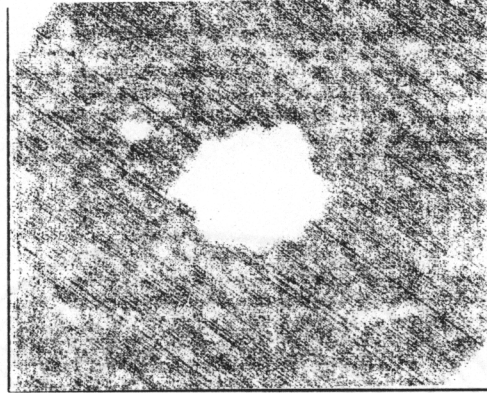
(a)
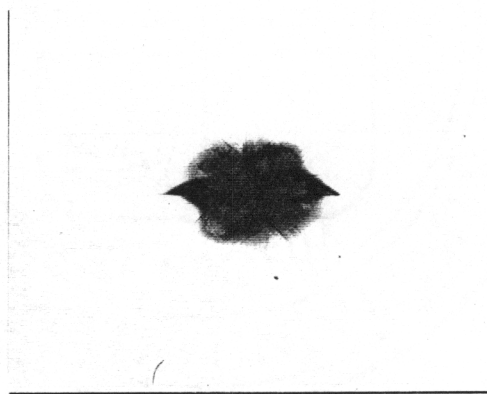
(b)

Fig. 6.10 (a) Ultra-sonic C-scan image and (b) X-ray radiograph of IM7/8551-7A specimen after quasi-static loaded to 3.1 kN. The surface 0° ply is in horizontal direction.
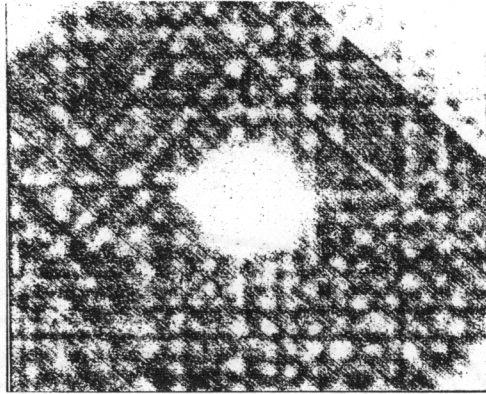
(a)
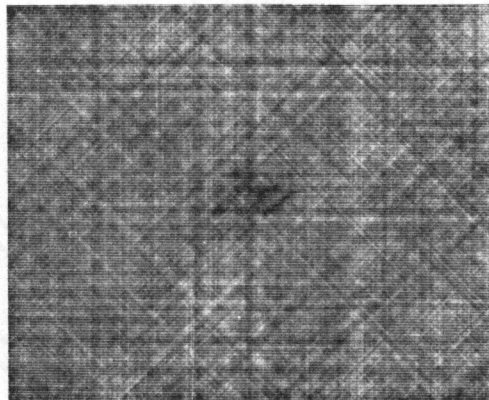
(b)

Fig. 6.11 (a) Ultra-sonic C-scan image and (b) X-ray radiograph of S-2/8551-7A specimen after quasi-static loaded to 3.1 kN. The surface 0° ply is in horizontal direction.
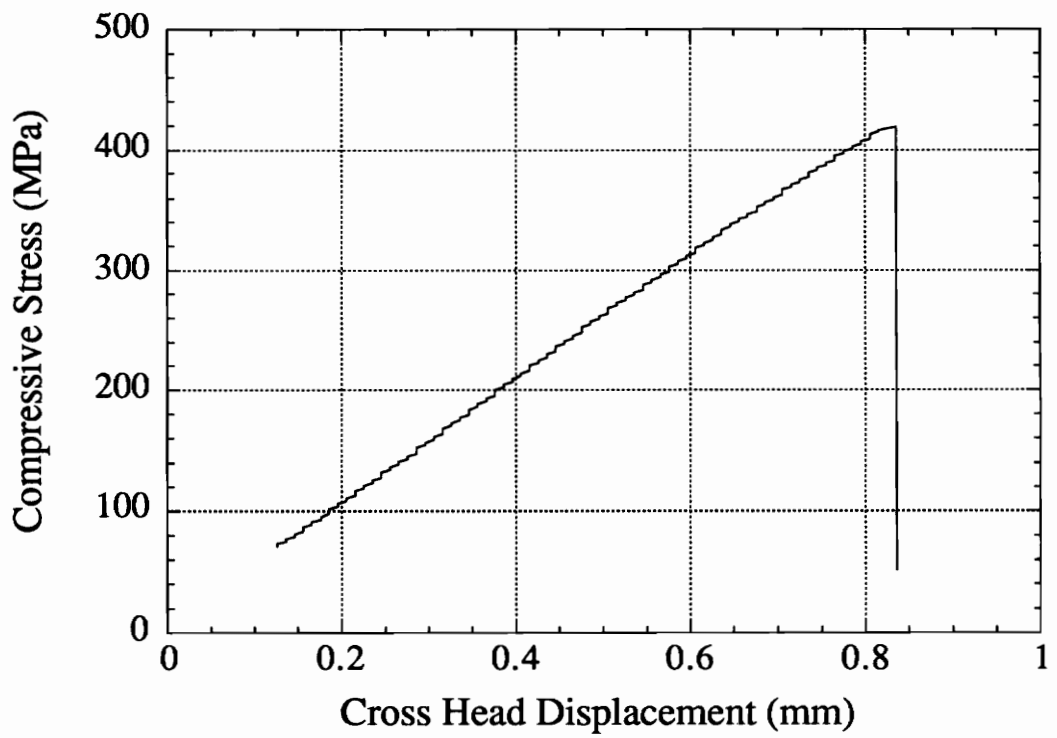
**Fig. 6.12** The compressive stress-crosshead displacement curve of AS4/PEEK after quasi-static indentation loading of 3.1 kN.
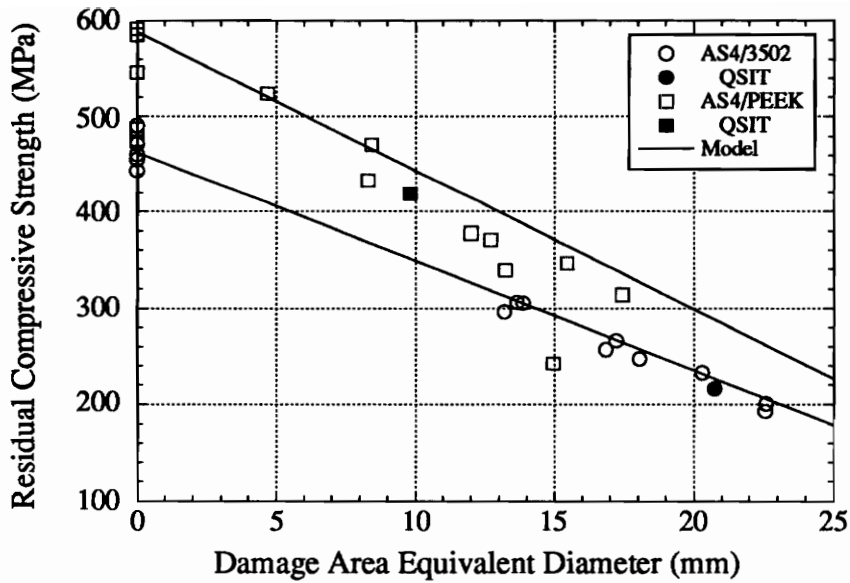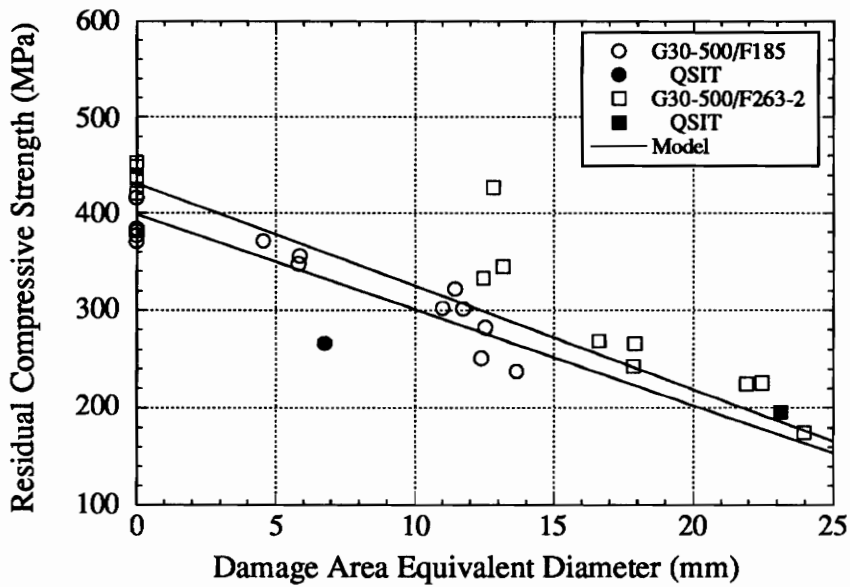
Fig. 6.13 Variation of residual compressive strength with damage area equivalent diameter resulted from impact and quasi-static indentation test (QSIT) for (a) AS4 and (b) G30-500 fiber material systems.
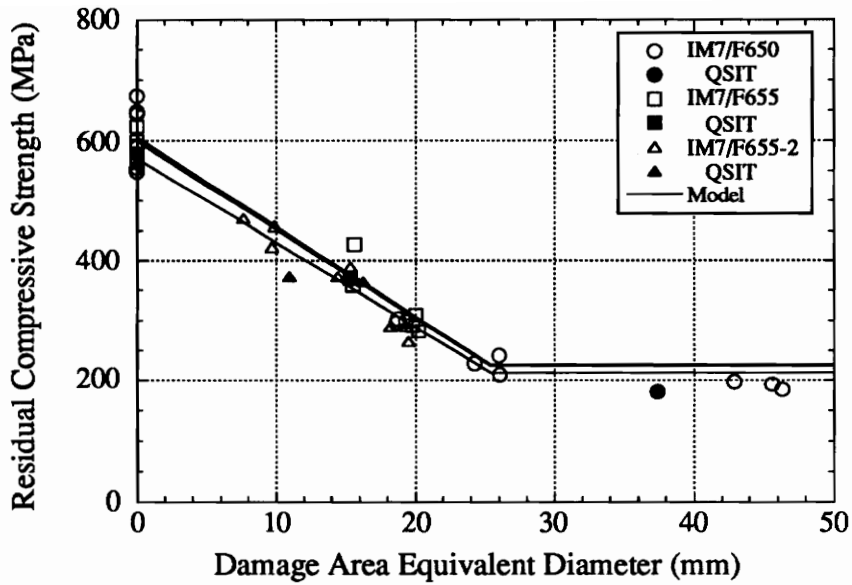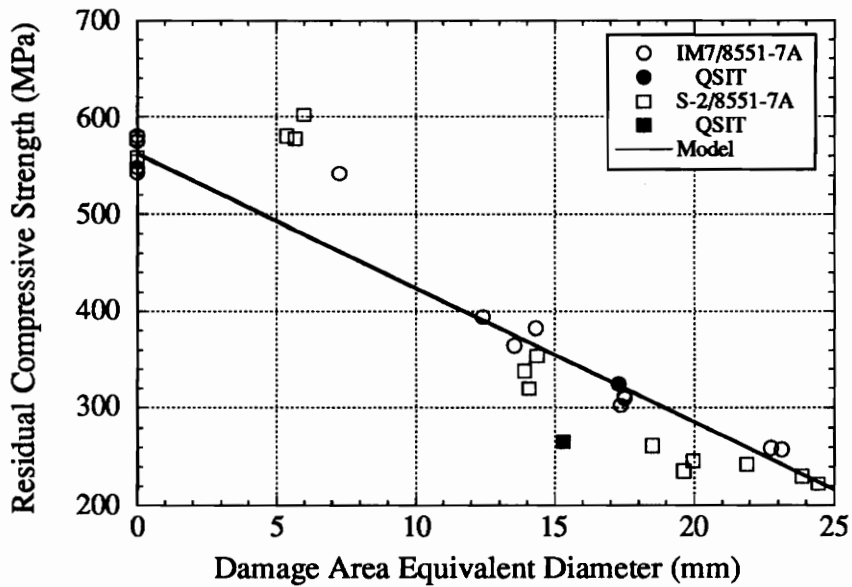
Fig. 6.14 Variation of residual compressive strength with damage area equivalent diameter resulted from impact and quasi-static indentation test (QSIT) for (a) BMI and (b) rubber toughened epoxy matrix material systems.

170

Table 3.1 Material systems in the impact program.

Material System	Fiber/Matrix	Laminate Thickness, mm
A	Hercules AS4/3502	2.07
B	AS4/PEEK (ICI APC-2 Thermoplastic)	2.09
C	BASF Celion G30-500/Hexcel F185 Epoxy	2.85
D	BASF Celion G30-500/Hexcel F263-2 Epoxy	2.18
E	IM7/Hexcel F650 Bismaleimide	2.16
F	IM7/Hexcel F655 Bismaleimide	2.39
G	IM7/Hexcel F655-2 Bismaleimide	2.46
H	IM7/Hercules 8551-7A Epoxy	2.24
I	S-2 Glass/Hercules 8551-7A Epoxy	2.26

Table 4.1 The experimental data for compressive strengths after impact and damage sizes of bismaleimide systems from Ref. 37.

Material System	Incident Energy* (J)	CAI Strength* (MPa)	Damage Diameter* (cm)	Damage Area (cm^2)	Damage Area Ratio
IM7/F650	30.5	96.9	10.7	89.9	10.5
IM7/F655	30.5	243.0	3.9	11.9	1.4
IM7/F655-2	30.5	313.4	3.3	8.6	1

* Data from Ref. 37.

Table 5.1 Compressive modulus of each material system before impacts.

Material System	Compressive Modulus (GPa)				Average (GPa)	CLT[b] (GPa)
A	44.3	43.1	40.4	43.8	42.9±5.8%	55.6
B	44.5	42.3			43.4±2.6%	51.8
C	31.3	31.7			31.5±0.6%	37.4
D	41.0	37.2	40.3		40.1±7.2%	50.3
E	*30.5*[a]	47.0	47.1		47.0±0.1%	55.8
F	47.4	45.3			46.4±2.3%	-----
G	48.4	42.2			45.3±6.8%	51.2
H	52.8	46.2			49.5±6.7%	57.8
I	23.1	23.6	23.3		23.3±1.1%	28.1

a This data is not used to calculate the average value of compressive modulus.

b Calculated using classical lamination theory (CLT) with material tensile properties.

Table 5.2 Compressive strengths of each material system before impacts.

Material System	Compressive Strength (MPa)				Average (MPa)
A	444	460	491	455	463±6.1%
B	585	591			588±0.5%
C	381	416			399±4.3%
D	436	437	420		431±2.5%
E	555	588	673		605±11.2%
F	575	623			599±4.0%
G	563	577			570±1.2%
H	575	548			561±2.4%
I	558	578	554		563±2.6%

Table 5.3 Maximum compressive strains of each material system before impacts.

Material System	Maximum Compressive Strain (%)				Average (%)
A	1.40	1.38	1.60	1.52	1.47±8.5%
B	1.66	1.78			1.72±3.7%
C	1.47	1.55			1.51±2.7%
D	1.28	1.21	1.14		1.21±5.9%
E	----	1.66	----		1.66
F	2.00	----			2.00
G	1.49	1.61			1.55±3.8%
H	1.36				1.36
I	2.73	2.74	----		2.73

Table 6.1 Damage area and the equivalent impact velocity resulting from a quasi-static indentation loading of each material system.

Material System	Maximum Indentation Load (kN)	Damage Area (mm^2)	Equivalent Impact Velocity (m/s)
A	2.4	338	12.7
B	3.1	76	13.5
C	3.1	36	12.7
D	2.9	420	14.5
E	3.1	1098	18.0
F	3.1	185	14.1
G	3.1	94	13.8
H	3.1	235	16.4
I	3.1	184	15.4

Table 6.2 Residual compressive strength with the damage area equivalent diameter due to quasi-static indentation of each material system.

Material System	Damage Area Equivalent Diameter (mm)	Residual Compressive Strength (MPa)
A	20.8	216
B	9.8	419
C	6.8	266
D	23.1	196
E	37.4	181
F	15.3	372
G	11.0	372
H	17.3	324
I	15.3	266

References

[1]   "Foreign Object Impact Damage to Composite," ASTM STP 568, 1975.

[2]   Abrate, S., "Impact on Laminated Composite Materials," Applied Mechanics Review, Vol. 44, No. 4, 1991, pp. 155-190.

[3]   Cantwell, W. J., and Morton, J., "The Impact Resistance of Composite Materials - A Review," Composites, Vol. 22, No. 5, Sep. 1991, pp. 347-362.

[4]   Greszczuk, L. B., "Response of Isotropic and Composite Materials to Particle Impact," ASTM STP 568, 1975, pp. 183-211.

[5]   Starnes, J. H., Jr., Rhodes, M. D., and Williams, J. G., "Effect of Impact Damage and Holes on the Compressive Strength of a Graphite/Epoxy Laminate," Nondestructive Evaluation and Flaw Criticality for Composite Materials, ASTM STP 696, 1979, pp. 145-171.

[6]   Caprino, G., "Residual Strength Prediction of Impacted CFRP Laminates," Journal of Composite Materials, Vol. 18, 1984, pp. 508-518.

[7]   Griffin, C. F., "Damage Tolerance of Toughened Resin Graphite Composites," Toughened Composites, ASTM STP 937, 1987, pp. 23-33.

[8]   Morton, J. and Godwin, E. W., "Impact Response of Tough Carbon Fibre Composites," Composite Structures, Vol. 13, 1989, pp. 1-19.

[9]   Cantwell, W. J. and Morton, J., "Comparison of the Low and High Velocity Impact Response of CFRP," Composites, Vol. 20, No. 6, 1989, pp. 545-551.

[10]   El-Zein, M. S., "Strength in Notched and Impact Laminates," Ph.D Dissertation, Virginia Tech, 1989.

[11]   Cantwell., W. J., and Morton, J., "Impact Perforation of Carbon Fibre Reinforced Plastic," Composite Science and Technology, Vol. 38, 1990, pp. 119-141.

[12]   Ghasemi Nejhad, M. N., Parvizi-Majidi, A., "Impact Behaviour and Damage Tolerance of Woven Carbon Fibre-Reinforced Thermoplastic Composites," Composites, Vol. 21, No. 2, 1990, pp. 155-168.

[13]   El-Zein, M. S. and Reifsnider, K. L., "On the Prediction of Tensile Strength after Impact of Composite Laminates," Journal of Composites Technology & Research, Vol. 12, No. 3, 1990, pp. 147-154.

[14]   Dost, E. F., Ilcewicz, L. B., Avery, W. B., and Coxon, B. R., "Effects of Stacking Sequence on Impact Damage Resistance and Residual Strength for Quasi-Isotropic Laminates," Composite Materials: Fatigue and Fracture (Third Volume), ASTM STP 1110, 1991, pp. 476-500.

[15]   Robinson, P. and Davies, G. A. O., "Impactor Mass and Specimen Geometry Effects in Low Velocity Impact of Laminated Composites," International Journal of Impact Engineering, Vol. 12, No. 2, 1992, pp. 189-207.

[16]   Srinivasan, K., Jackson, W. C., Smith, B. T., Hinkley, J. A., "Characterization of Damage Modes in Impacted Thermoset and Thermoplastic Composites," Journal of Reinforced Plastics and Composites, Vol. 11, October 1992, pp. 1111-1126.

[17]   Doyle, J. F., "An Experimental Method for Determining the Dynamic Contact Law," Experimental Mechanics, Vol., 24, 1984, pp. 10-16.

[18]   Lal, K. M., "Low Velocity Transverse Impact Behavior of 8-ply, Graphite-Epoxy Laminates," Journal of Reinforced Plastics and Composites, Vol. 2, 1983, pp. 216-225.

[19]   Lal, K. M., "Residual Strength Assessment of Low Velocity Impact Damage of Graphite-Epoxy Laminates," Journal of Reinforced Plastics and Composites, Vol. 2, 1983, pp. 226-238.

[20]   Morris, A. W. H. and Smith, R. S., "Some Aspects of the Evaluation of the Impact Behavior of Low Temperature Fiber Composites," Fibre Science Technology, Vol. 3, 1971, pp. 219-242.

[21] Daniel, I. M., Liber, T., and LaBedz, R. H., "Wave Propagation in Transversely Impacted Composite Laminates," Experimental Mechanics, January, 1979, pp. 9-16.

[22] Joshi, S. P. and Sun. C. T., "Impact Induced Fracture in a Laminated Composite," Journal of Composite Materials, Vol. 19, 1985, pp. 51-66.

[23] Liu, D., "Impact-Induced Delamination - A View of Bending Stiffness Mismatching," Journal of Composite Materials, Vol. 22, 1988, pp. 674-692.

[24] Cantwell, W. J., Morton, J., "The Influence of Varying Projectile Mass on the Impact Response of CFRP," Composite Structures, Vol. 13, 1989, pp. 101-114.

[25] Dan-Jumbo, E., Leewood, A. R., and Sun, C. T., "Impact Damage Characteristics of Bismaleimides and Thermoplastic Composite Laminates," Composite Materials: Fatigue and Fracture, Second Volume, ASTM STP 1012, Paul A. Lagace, Ed., 1989, pp. 356-372.

[26] Hong, S. and Liu, D., "On the Relationship Between Impact Energy and Delamination Area," Experimental Mechanics, June 1989, pp. 115-120.

[27] Qian, Y., Swanson, S. R., Nuismer, R. J., and Bucinell, R. B., "An Experimental Study of Scaling Rules for Impact Damage in Fiber Composites," Journal of Composite Materials, Vol. 24, May 1990, pp. 559-570.

[28] Choi, H. Y., Wu, H.-Y. T., and Chang, F. K., "A New Approach toward Understanding Damage Mechanisms and Mechanics of Laminated Composites Due to Low-Velocity Impact: Part II - Analysis," Journal of Composite Materials, Vol. 25, August 1991, pp. 1012-1038.

[29] Jenq, S. T., Wang, S. B., Sheu, L. T., " A Model for Predicting the Residual Strength of GFRP Laminates Subject to Ballistic Impact," Journal of Reinforced Plastics and Composites, Vol. 11, October 1992, pp. 1127-1141.

[30] Jegley, D, "Impact-Damage Graphite-Thermoplastic Trapezoidal-Corrugation Sandwich and Semi-Sandwich Panels," Journal of Composite Materials, Vol. 27, No. 5, 1993, pp. 526-538.

[31] Delfosse, D, Pageau, G., Bennett, R., and Poursartip, A., "Instrumented Impact Testing at High Velocities," Journal of Composite Technology & Research, Vol. 15, No. 1, 1993, pp. 38-45.

[32] Lagace, P. A., Williamson, J. E., Tsang, P. H. W., "A Preliminary Proposition for a Test Method to Measure (Impact) Damage Resistance," Journal of Reinforced Plastics and Composites, Vol. 12, 1993, pp. 584-601

[33] Finn, S. R., He, Y.-F., and Springer, G. S., "Delaminations in Composite Plates under Transverse Impact Loads - Experimental Results," Composite Structures, Vol. 23, 1993, pp. 191-204.

[34] Kumar, P., and Rai, B., "Delaminations of Barely Visible Impact Damage in CFRP Laminates," Composite Structures, Vol. 23, 1993, pp. 313-318.

[35] "Instrumented Impact Testing of Plastics and Composite Materials," ASTM STP 936, 1987.

[36] Morton, J., "Scaling of Impact-Loaded Carbon-Fiber Composites," AIAA Journal, Vol. 26, No. 8, August 1988, pp. 989-994.

[37] Olesen, K. A., Falabella, R. and Buyny, R. A., "Mechanical Behavior of Three Generations of Bismaleimide Composite Prepregs," Proceeding of the 37th International SAMPE Symposium, March, 1992.

[38] Gürdal, Z. and Starbuck, J. M., "Compressive Characterization of Unidirectional Composite Materials," Analytical and Testing Methodologies for Design with Advanced Materials, 1988, pp. 337-347.

[39] Caprino, G., "On the Prediction of Residual Strength for Notched Laminates," Journal of Material Science, Vol. 18, 1983, pp. 2269.

[40]   Teh, K. T., Morton, J., de Souza, J. P., and Baird, D. G., "Impact Damage Studies in AS4/PEEK and PEKK/HX1000," to be published in the ICCM-9 Proceedings, 1993.

Appendix A   Material Properties

Unidirectional and ±45° angle ply laminates were used to measure the material properties of G30-500/F185, G30-500/F263-2, IM7/F650, IM7/F655-2, IM7/8551-7A, and S-2/8551-7A laminae. Both IM7/F650 and IM7/F655-2 specimens were provided by the manufacturer and the rest were cured from the prepreg tapes in the manufacturing facility of the Center of Composite Materials and Structures. No IM7/F655 specimens were available for material properties measurement. The data of both AS4/3502 and AS4/PEEK were obtained from other sources.

The longitudinal tensile modulus E_1, Poisson's ratio v_{12}, and longitudinal tensile strength were measured from 8-ply 0° unidirectional specimen with the width of 12.7 mm (0.5 in); whereas the transverse tensile modulus E_2, and the transverse tensile strength were measured from 8-ply 90° unidirectional specimen with the width of 25.4 mm (1.0 in) except for IM7/F650 and IM7/F655-2 where 16-ply specimens were used. The shear modulus G_{12} was measured from 8-ply $[\pm 45°]_{2S}$ specimen with the width of 25.4 mm (1.0 in). The 0° and ±45° specimens were instrumented with 2-element 90° 'tee' rosette to measure the strains in the longitudinal and transverse directions. A single element strain gage was used for 90° specimens to measure the longitudinal strain only.

All specimens were loaded in tension to failure by using an Instron 4204 screw driven testing machine with a constant crosshead displacement rate of 1.27 mm/min (0.05 in/min). Typical stress-strain curves for $[0]_8$, $[90]_8$, and $[\pm 45]_{2S}$ IM7/8551-7A specimens are shown in Figs. A.1-3, respectively.

The tensile stress σ_x is calculated as

$$\sigma_x = \frac{T}{A} \tag{A.1}$$

where   T   = tensile load

A   = cross section area of the specimen

183

The longitudinal tensile modulus E_1 was measured from the slope of the stress-strain curve in Fig. A.1

$$E_1 = \frac{\Delta\sigma_x}{\Delta\varepsilon_x} \qquad (A.2)$$

and the Poisson's ratio v_{12} was calculated as

$$v_{12} = -\frac{\varepsilon_y}{\varepsilon_x} \qquad (A.3)$$

The transverse tensile modulus E_2 was measured from the slope of the stress-strain curve in Fig. A.2. From Fig. A.3, the shear stress τ_{12} and shear strain γ_{12} are calculated as

$$\tau_{12} = \frac{\sigma_x}{2} \qquad (A.4)$$

$$\gamma_{12} = \varepsilon_x - \varepsilon_y \qquad (A.5)$$

and the shear modulus G_{12} was measured from the slope of the shear stress-strain curve in Fig. A.4.

The results of E_1, E_2, G_{12}, v_{12}, tensile strengths of 0°, 90°, and ±45° specimens of each material system are presented in Tables A.1-7, respectively.
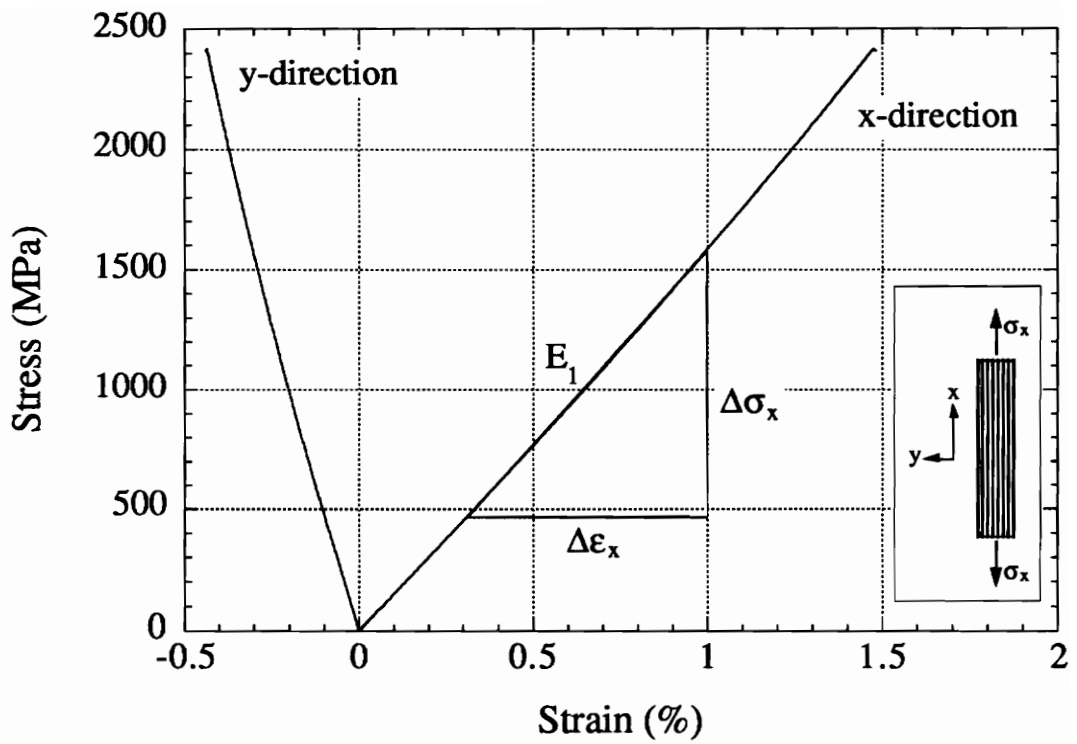
Fig. A.1 Tensile stress-strain curves for [0°]$_8$ IM7/8551-7A. The strains in x and y directions are the longitudinal and transverse strains of the specimen.

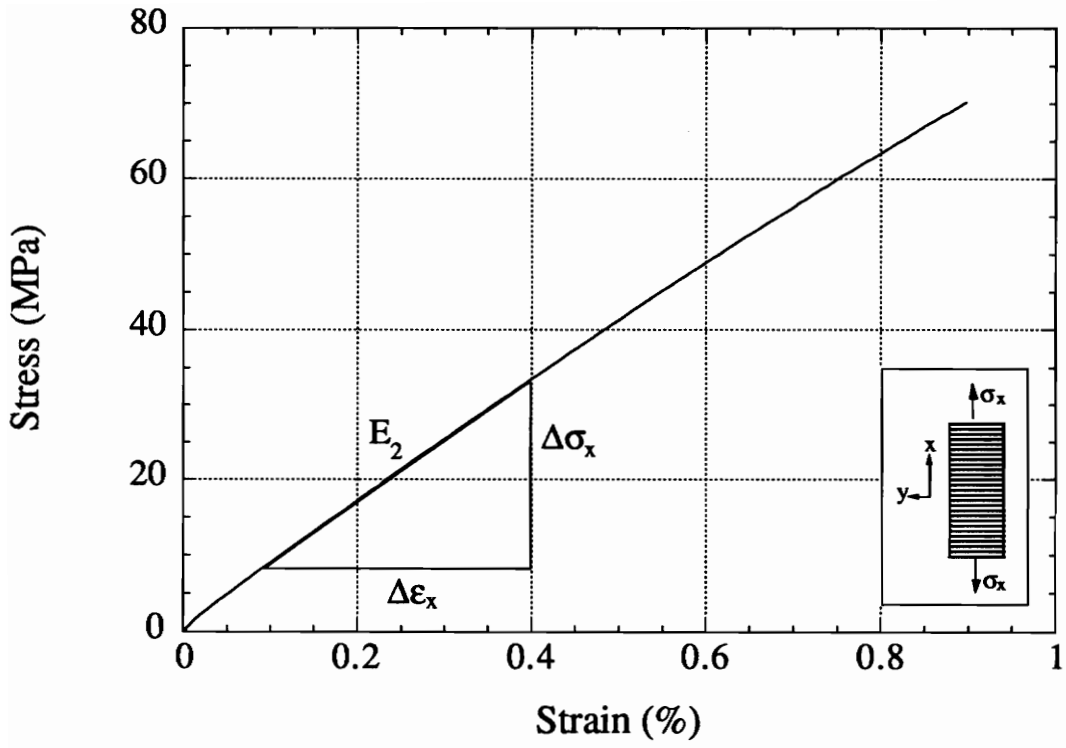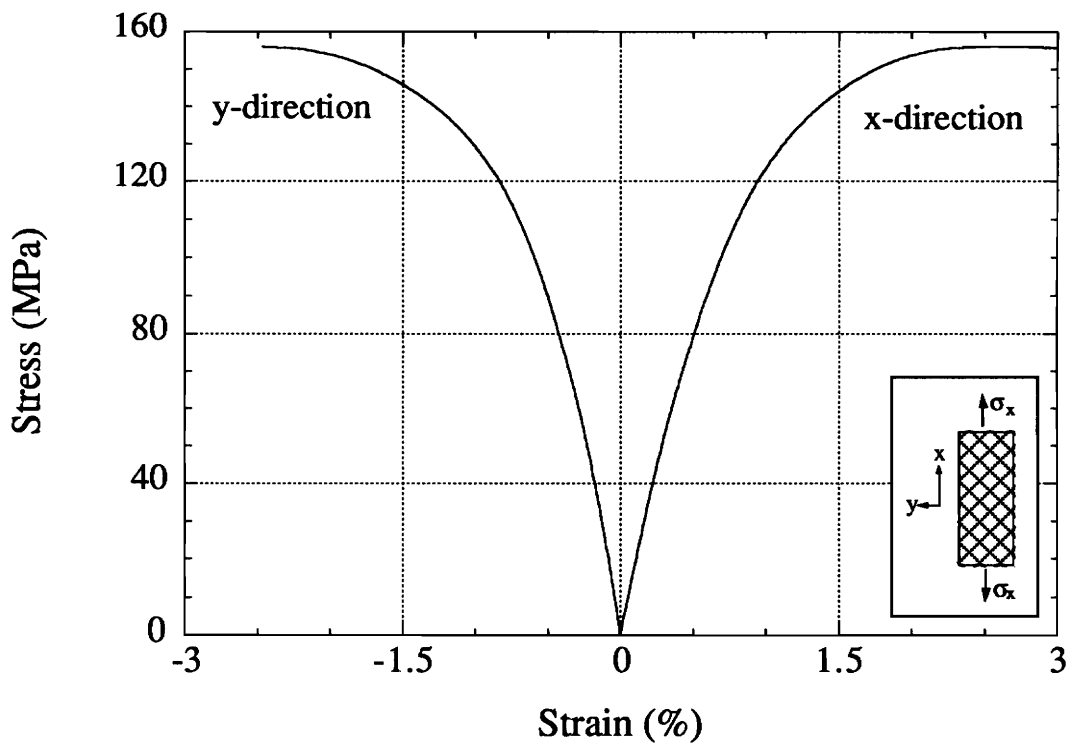**Fig. A.2** Tensile stress-strain curve for [90°]$_8$ IM7/8551-7A.

Fig. A.3 Tensile stress-strain curves for [±45°]$_{2S}$ IM7/8551-7A. The strains in x and y directions are the longitudinal and transverse strains of the specimen.
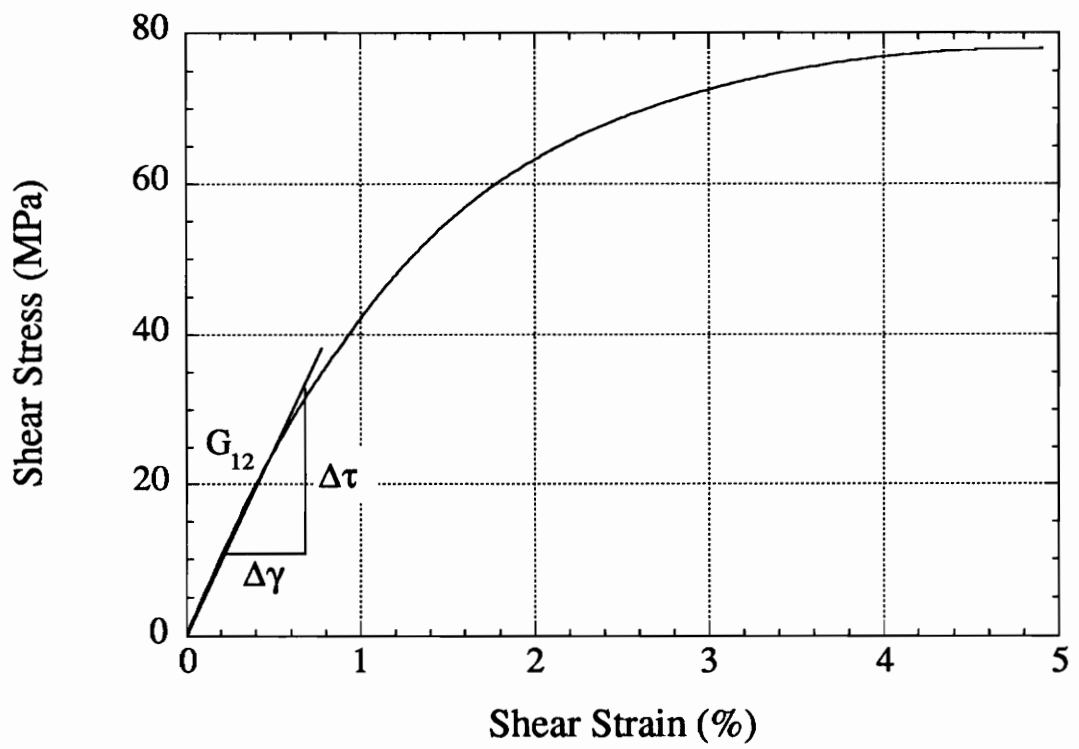
187

Fig. A.4 Shear stress-strain curve for IM7/8551-7A.

Table A.1 Tensile modulus (E_1) of $0°$ unidirectional laminate of each material system.

Material System	Tensile modulus of $0°$ laminate, E_1 (GPa)			Average
AS4/3502				142
AS4/PEEK				134
G30-500/F185	98.6	99.2	102	100
G30-500/F263-2	131	125	120	125
IM7/F650	144	146		145
IM7/F655				----
IM7/F655-2	133	133		133
IM7/8551-7A	151	152	151	152
S-2/8551-7A	49.5	50.1	48.9	49.5

Table A.2 Tensile modulus (E_2) of 90° unidirectional laminate of each material system.

Material System	Tensile modulus of 90° laminate, E_2 (GPa)			Average
AS4/3502				12.2
AS4/PEEK				8.89
G30-500/F185	5.76	5.88	5.73	5.79
G30-500/F263-2	9.16	9.49	9.14	9.26
IM7/F650	8.43	8.25	8.25	8.31
IM7/F655				----
IM7/F655-2	8.29	8.32	8.27	8.29
IM7/8551-7A	8.41	8.28	8.23	8.31
S-2/8551-7A	9.3	8.8	8.8	9.0

Table A.3 Shear modulus (G_{12}) of ±45° laminate of each material system.

Material System	Shear modulus of ±45° laminate, G_{12} (GPa)			Average
AS4/3502				5.31
AS4/PEEK				5.10
G30-500/F185	2.54	2.72	2.65	2.64
G30-500/F263-2	5.60	5.37	5.62	5.53
IM7/F650	5.77	6.14	5.50	5.80
IM7/F655				----
IM7/F655-2	5.00	4.88	5.14	5.01
IM7/8551-7A	5.22	5.85	5.54	5.54
S-2/8551-7A	7.21	6.76	6.91	6.96

Table A.4 Poisson's ratio (ν_{12}) of $0°$ unidirectional laminate of each material system.

Material System	Poisson's ratio of $0°$ laminate, ν_{12}			Average
AS4/3502				0.30
AS4/PEEK				0.28
G30-500/F185	0.32	0.32	0.36	0.33
G30-500/F263-2	0.30	0.33	0.28	0.31
IM7/F650	0.31	0.34		0.33
IM7/F655				----
IM7/F655-2	0.32	0.32		0.32
IM7/8551-7A	0.31	0.34	0.32	0.32
S-2/8551-7A	0.26	0.26	0.26	0.26

Table A.5 Tensile strength of 0° unidirectional laminate of each material system.

Material System	Tensile strength of 0° laminate (GPa)			Average
AS4/3502				1.85
AS4/PEEK				2.13
G30-500/F185	1.45	1.44	1.50	1.46
G30-500/F263-2	1.93	1.98		1.95
IM7/F650	2.25	2.29		2.27
IM7/F655				----
IM7/F655-2	2.17	2.26		2.22
IM7/8551-7A	2.42	2.32	2.43	2.39
S-2/8551-7A	1.82	1.80	1.79	1.80

Table A.6 Tensile strength of 90° unidirectional laminate of each material system.

Material System	Tensile strength of 90° laminate (MPa)			Average
AS4/3502				61.2
AS4/PEEK				80.0
G30-500/F185	51.3	53.0	52.3	52.2
G30-500/F263-2	59.3	64.1	56.0	60.0
IM7/F650	64.2	63.7	56.6	61.5
IM7/F655				----
IM7/F655-2	71.5	72.4	61.7	68.6
IM7/8551-7A	70.6	66.9	72.8	70.1
S-2/8551-7A	61.9	64.5	62.7	63.0

Table A.7 Tensile strength of ±45° laminate of each material system.

Material System	Tensile strength of ±45° laminate (MPa)			Average
AS4/3502				----
AS4/PEEK				----
G30-500/F185	211	229	226	222
G30-500/F263-2	176	176	179	177
IM7/F650	171	169	170	170
IM7/F655				----
IM7/F655-2	264	260	249	258
IM7/8551-7A	165	152	152	156
S-2/8551-7A	208	199	204	204

Appendix B   Material Microstructures

A sample was sectioned from a quasi-isotropic laminate specimen used in impact test to measure the fiber diameter and fiber volume fraction of each composite material system. The laminate was sectioned through the thickness along the surface ply fiber direction. The samples were then mounted and polished. The 0.05 micron Gamma Alumina Powders were used for the final polishing.

The micrographs shown in Figs. B.1-9 are the full thickness of a 90° ply of each laminate (micrographs (a)), and the cross sectional view of fibers in 90° ply at a higher magnification (micrographs (b)) taken from the polished samples using an optical microscope. The 0° and 45° are above and below the 90° ply shown in micrographs (a) of these figures where the fibers in 45° ply are in elliptical shape. The ply thickness for each composite material system was measured from the thickness of the 90° ply shown in micrographs (a) in Figs. B.1-9.

The ply thickness and fiber diameter of each composite material system are presented in Table. B.1.
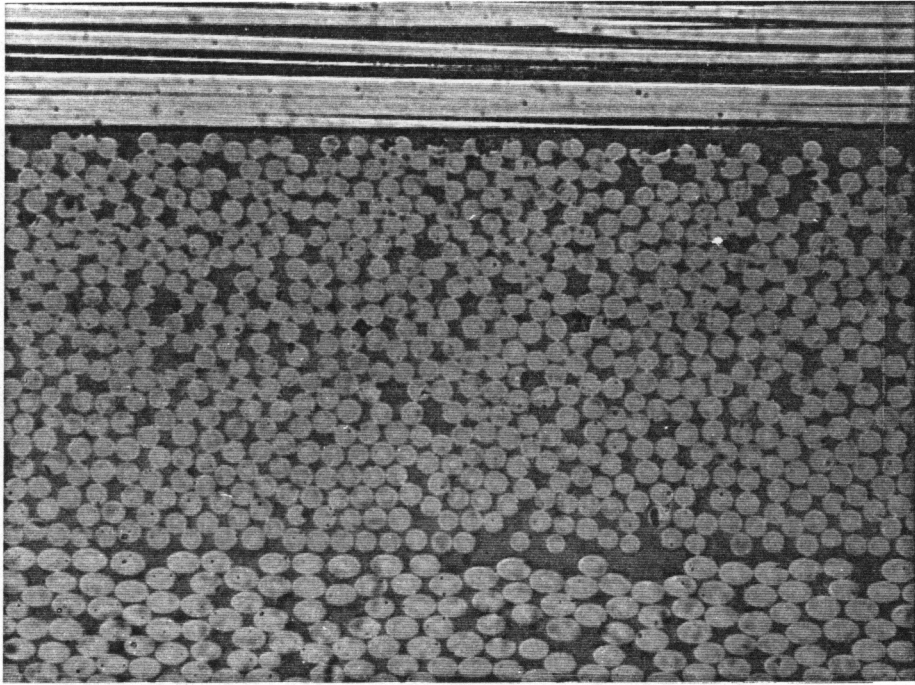
(a)
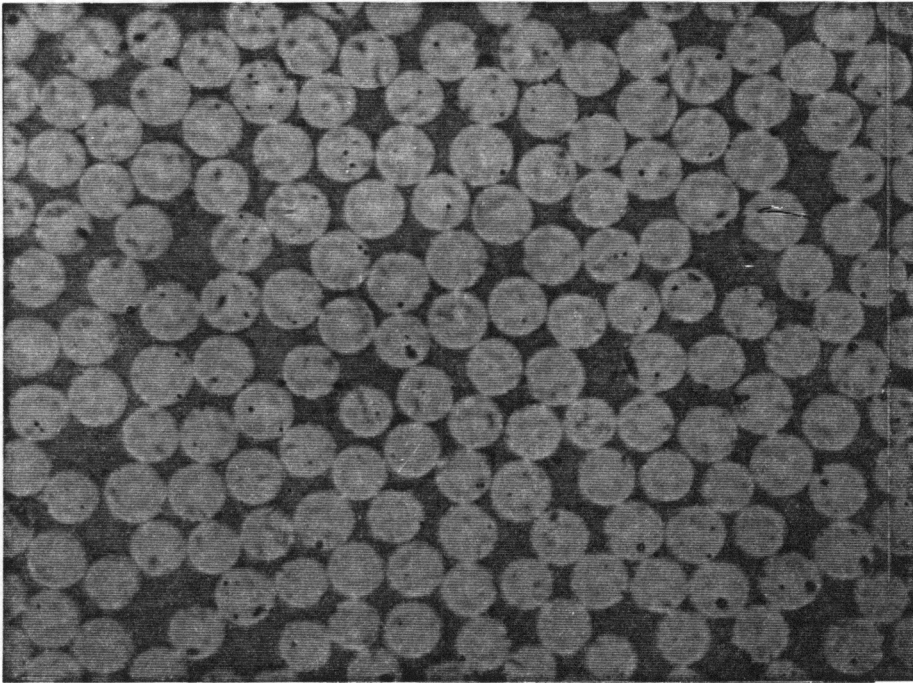
(b)

Fig. B.1 Micrographs of AS4/3502 laminate at (a) 422X and (b) 1060X magnifications.
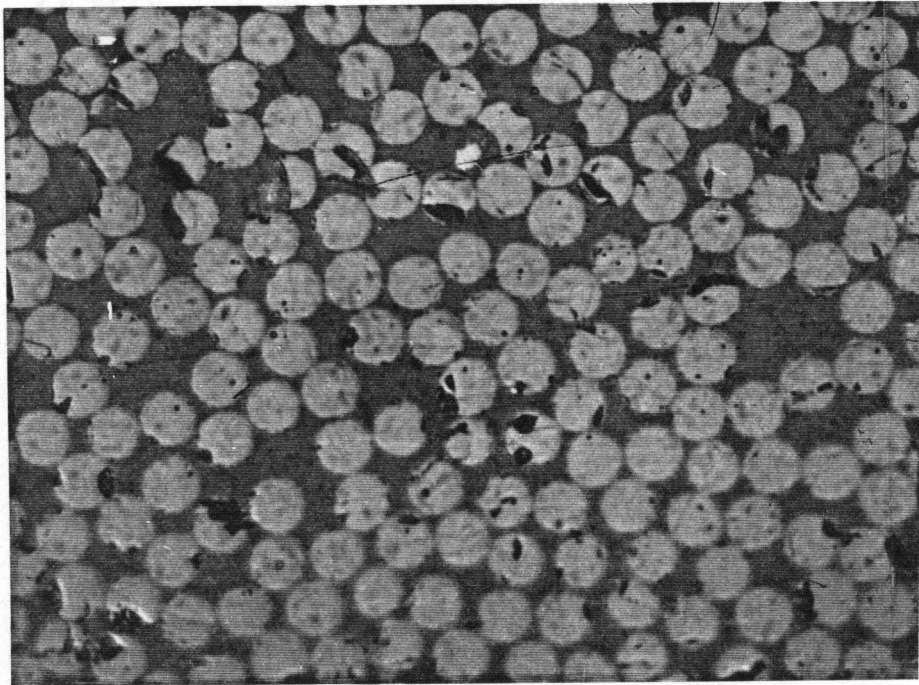
197
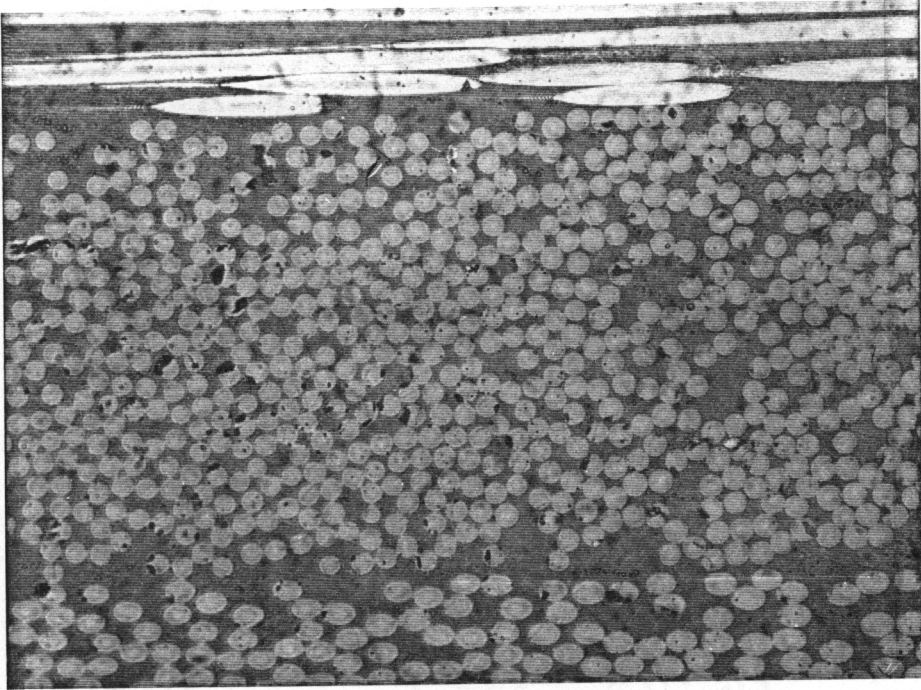
(a)
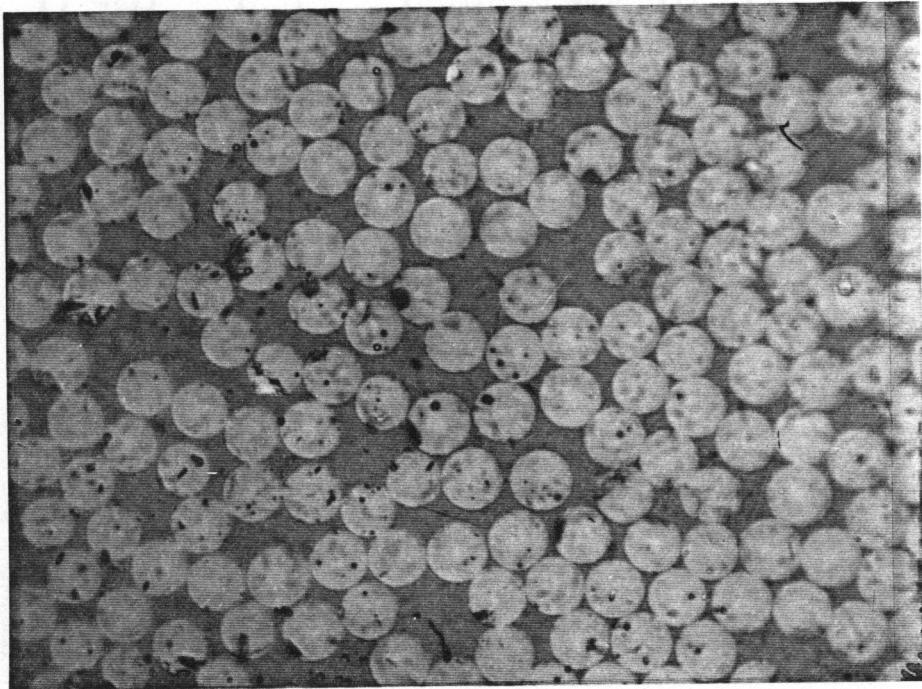
(b)

Fig. B.2 Micrographs of AS4/PEEK laminate at (a) 422X and (b) 1060X magnifications.
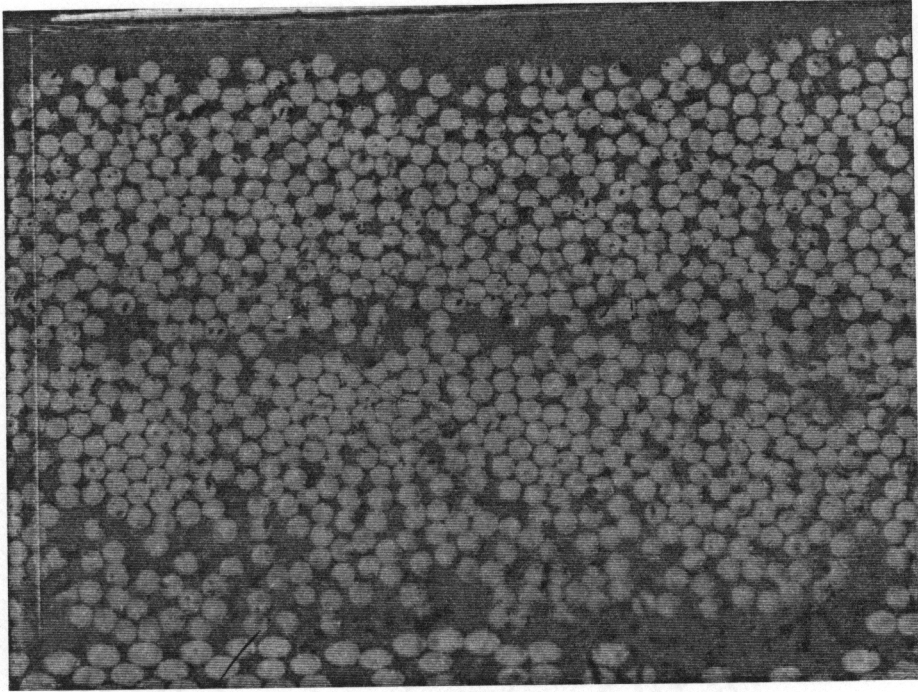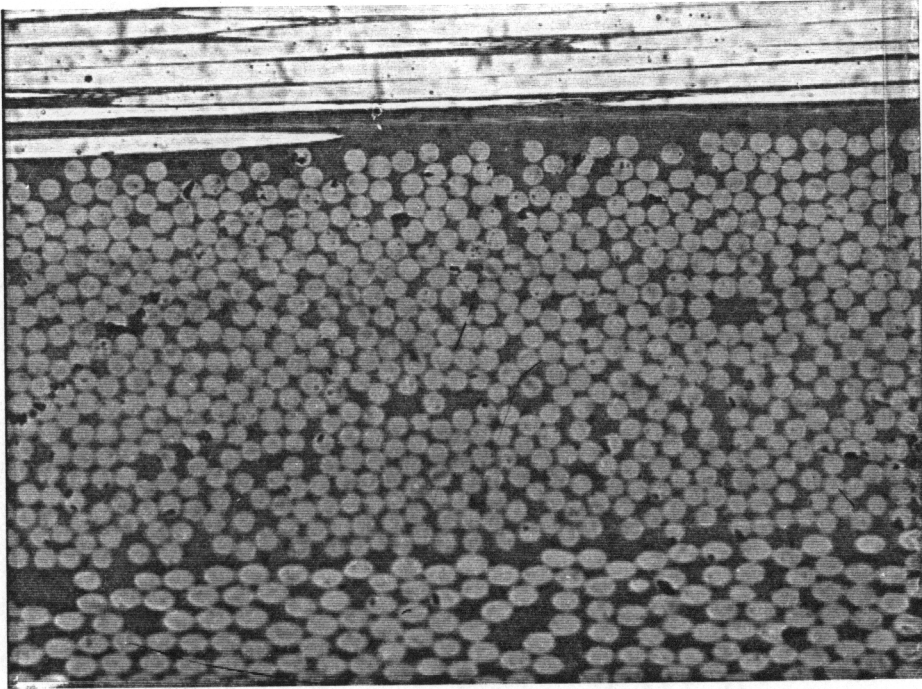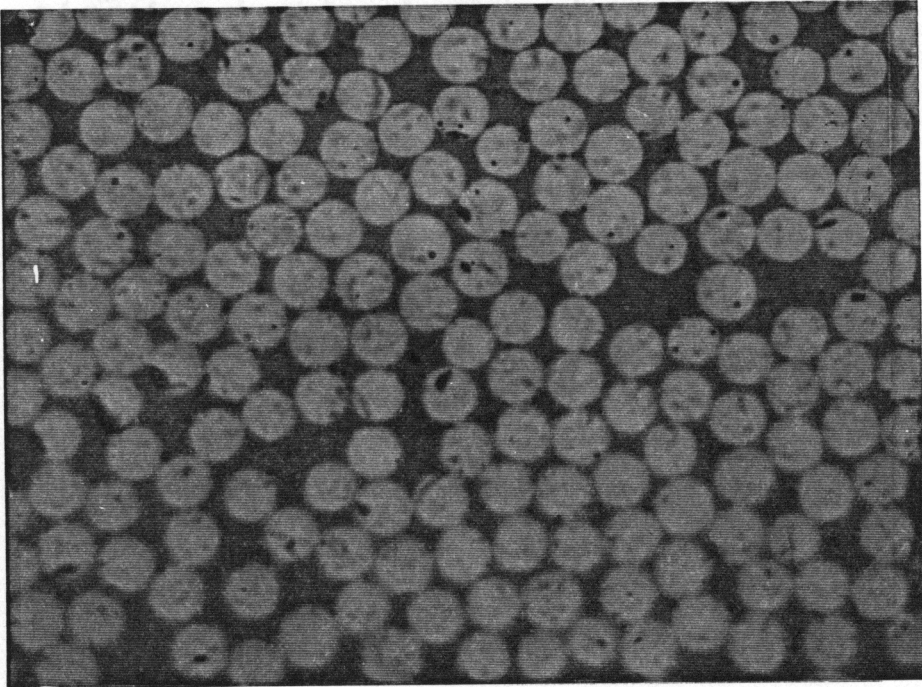
(a)

(b)

Fig. B.3 Micrographs of G30-500/F185 laminate at (a) 422X and (b) 1060X
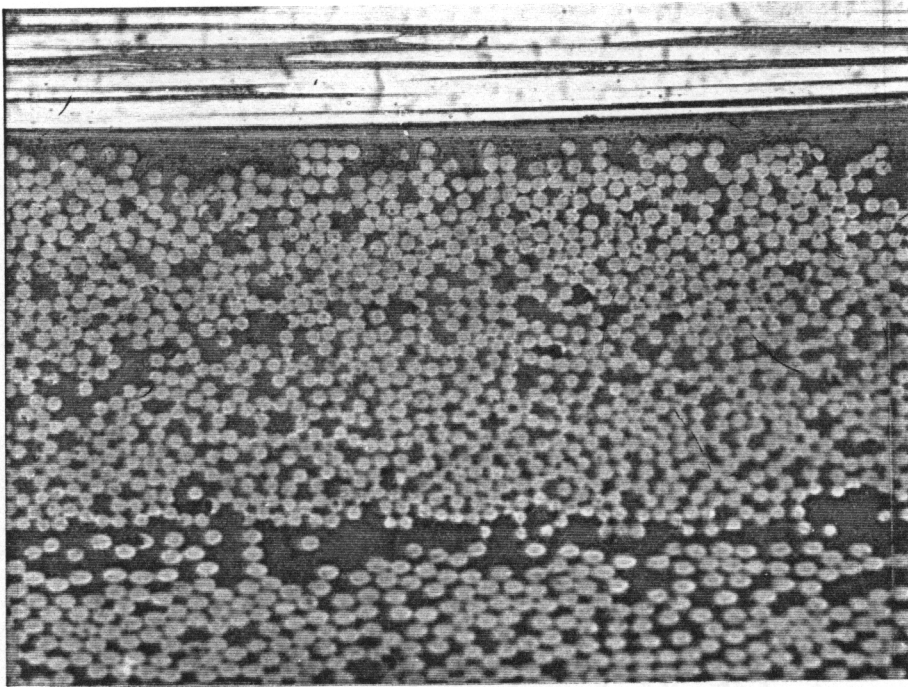magnifications.

(a)

(b)

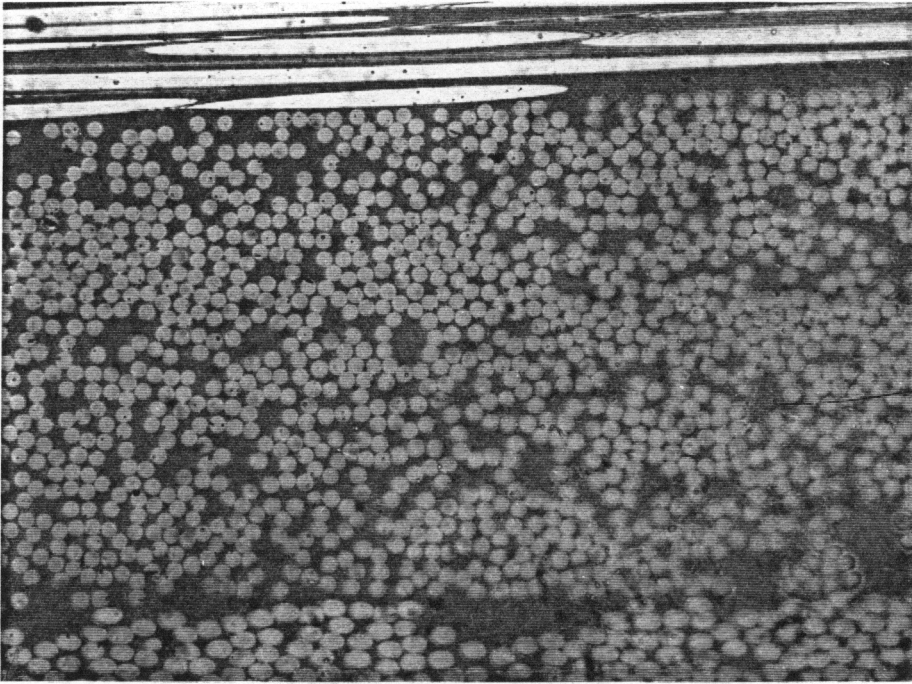**Fig. B.4** Micrographs of G30-500/F263-2 laminate at (a) 422X and (b) 1060X magnifications.

200

(a)
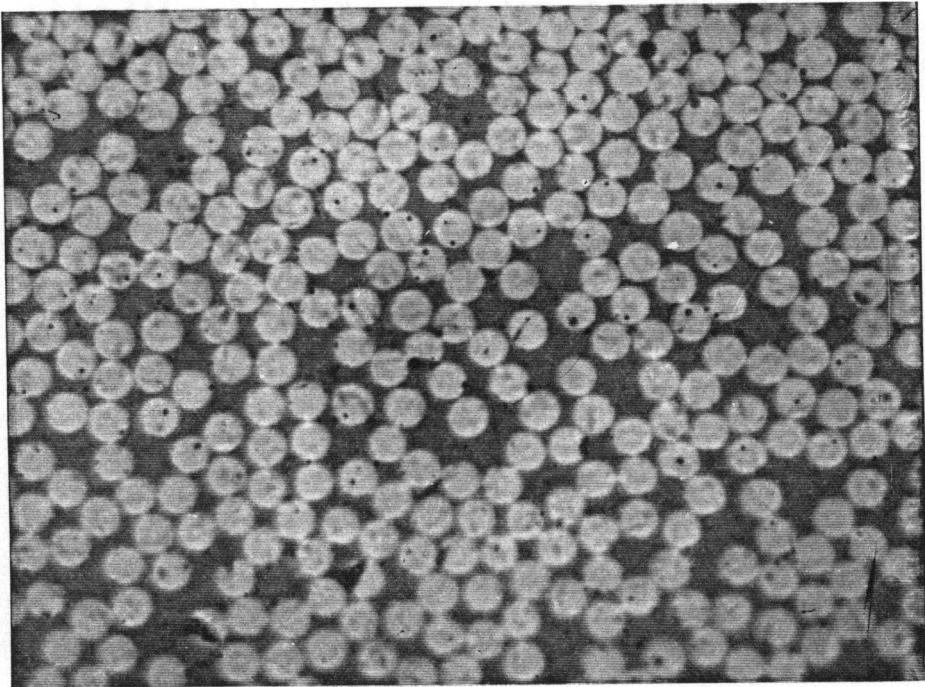
(b)

Fig. B.5 Micrographs of IM7/F650 laminate at (a) 422X and (b) 1060X magnifications.
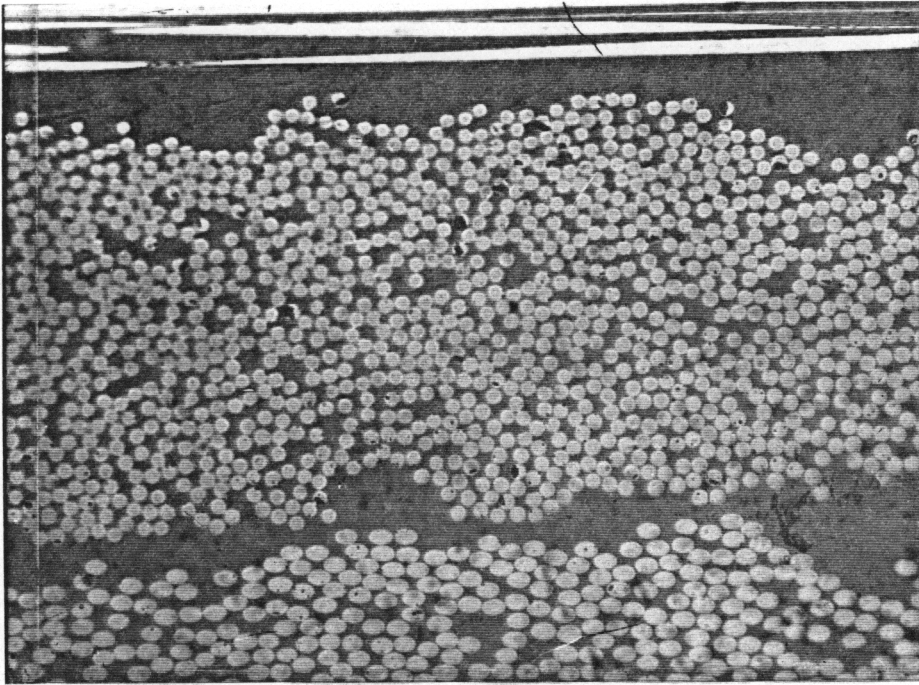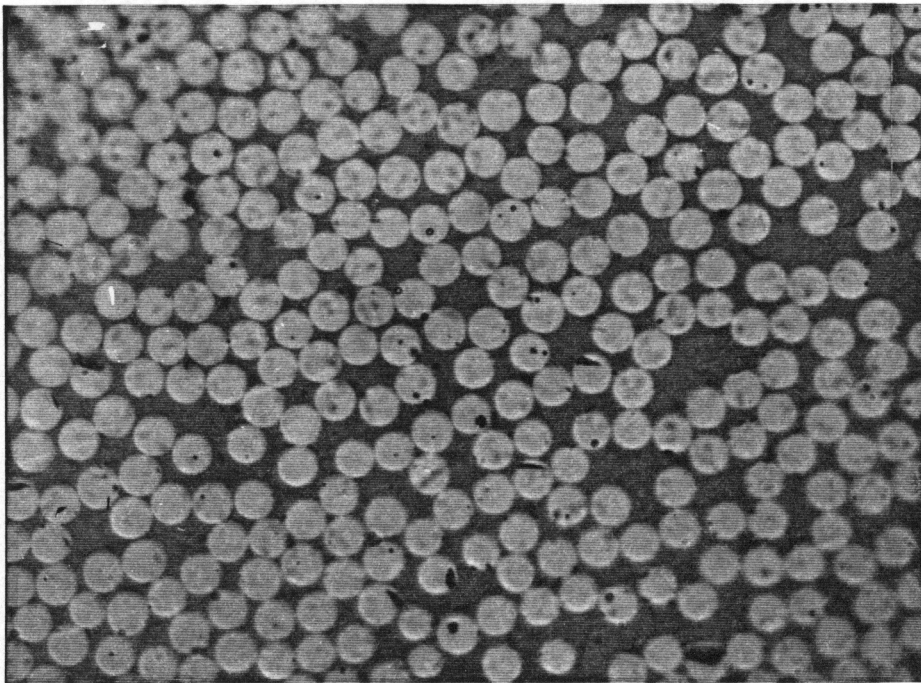
(a)
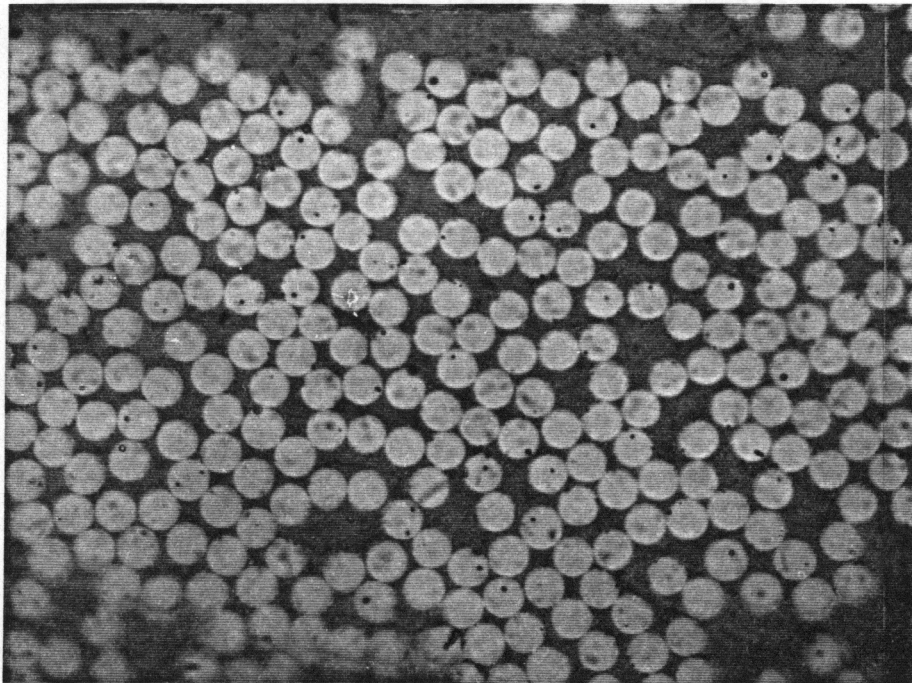
(b)

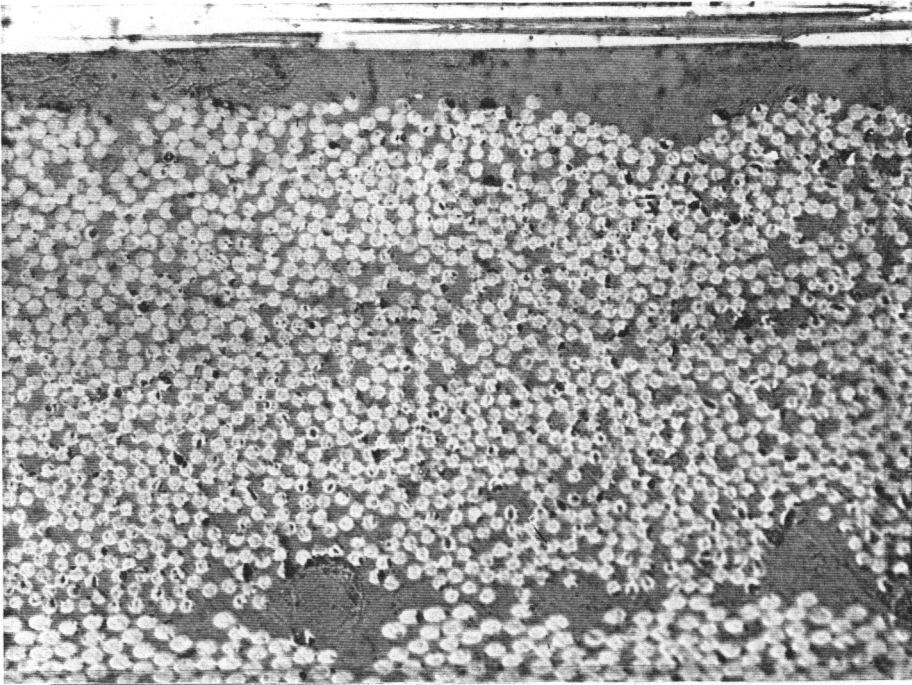**Fig. B.6** Micrographs of IM7/F655 laminate at (a) 422X and (b) 1060X magnifications.
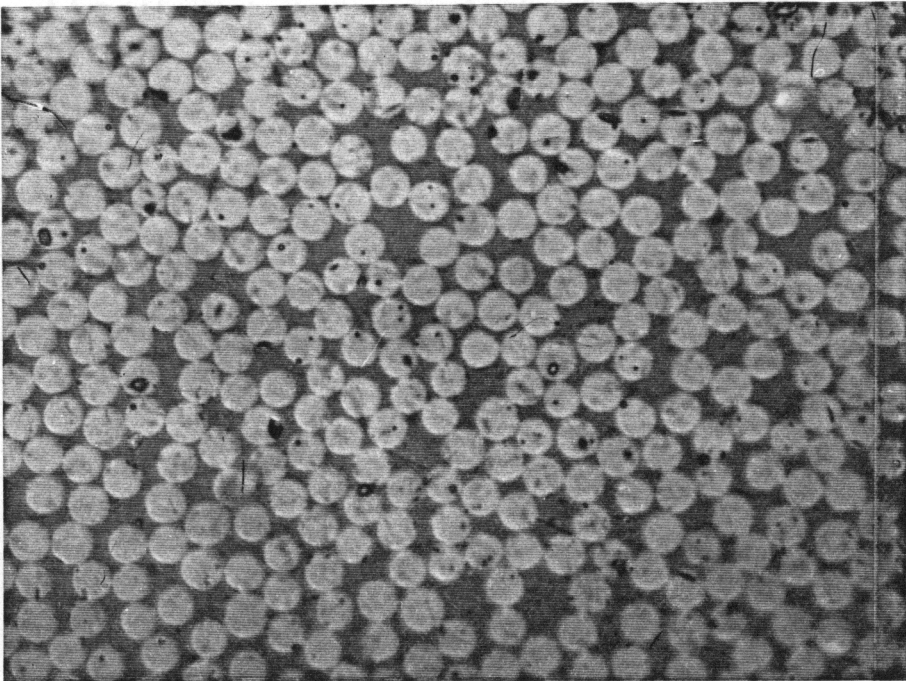
(a)

(b)

Fig. B.7 Micrographs of IM7/F655-2 laminate at (a) 422X and (b) 1060X
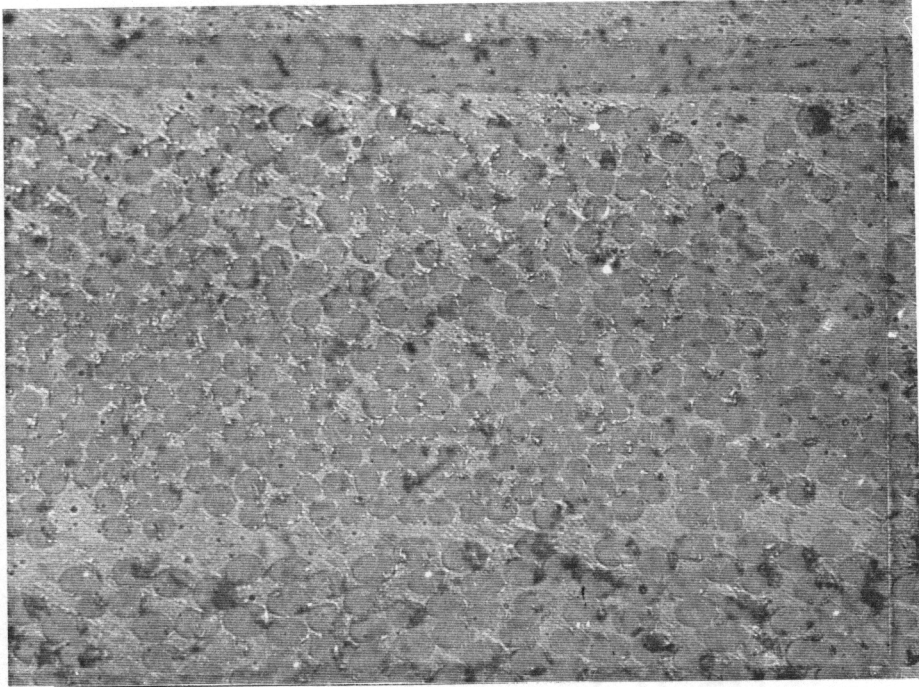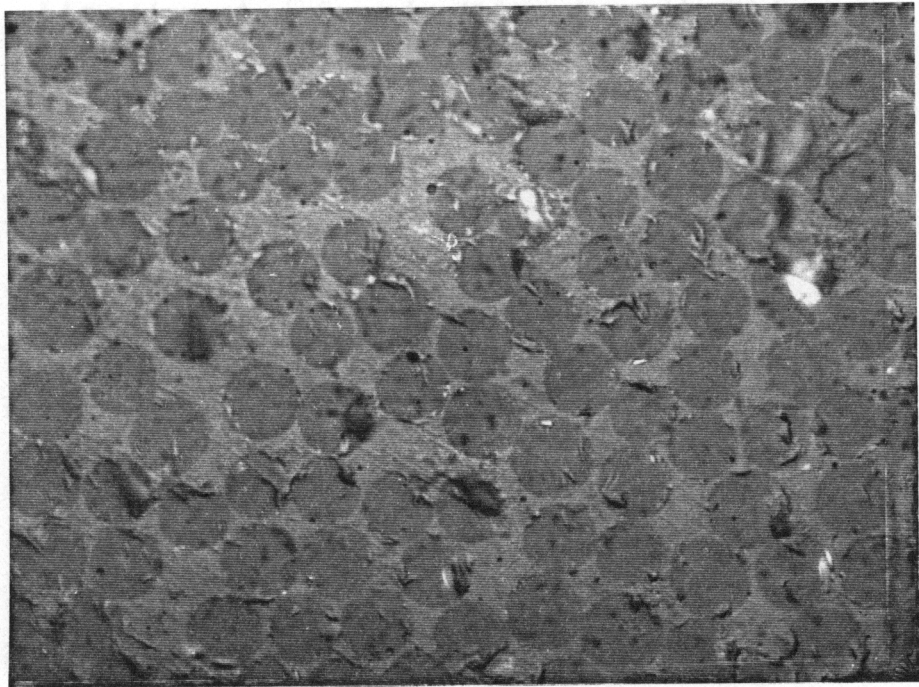magnifications.

(a)

(b)

Fig. B.8 Micrographs of IM7/8551-7A laminate at (a) 422X and (b) 1060X magnifications.

(a)

(b)

Fig. B.9 Micrographs of S-2/8551-7A laminate at (a) 422X and (b) 1060X
magnifications.

Table B.1 Ply thickness and fiber diameter of each material system.

Material System	Ply Thickness (mm)	Fiber Diameter (μm)
AS4/3502	0.13	7.6
AS4/PEEK	0.13	7.6
G30-500/F185	0.17	7.6
G30-500/F263-2	0.14	7.6
IM7/F650	0.13	5.2
IM7/F655	0.15	5.2
IM7/F655-2	0.15	5.2
IM7/8551-7A	0.14	5.2
S-2/8551-7A	0.14	9.4

Vita

Kuen Tat Teh was born in Seremban, Malaysia, in May 9, 1964. The author graduated from Chung Hua High School in Seremban, Malaysia, in 1982. In August 1983, he enrolled at Southern Illinois University at Carbondale from which he received his B.S. degree in Engineering in August 1986, B.S. degree in Mechanical Engineering in December 1986, and M.S. degree in Engineering in May 1989. In August 1989, the author started his Ph.D. program at Virginia Polytechnic Institute and State University and completed all the requirement for his Ph.D. degree in Engineering Mechanics in July 1993.